Université de Liège
Faculté des Sciences

Département d'Astrophysique, de Géophysique et d'Océanographie

COSMOGrail

Gravitationally lensed quasars:

light curves, observational constraints, modeling and the Hubble constant

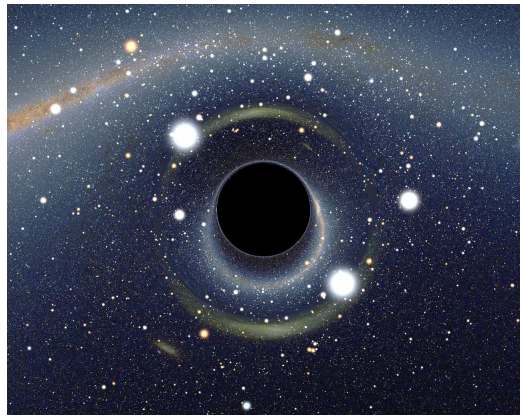

Artist view of gravitational distortions caused by a hypothetical black hole in front of the Large Magellanic Cloud. Credit: this file is licensed under the Creative Commons Attribution ShareAlike 2.5 license.

Virginie Chantry
Research Fellow, Belgian National Fund for Scientific Research (FNRS)

- December 2009 -

Astrophysique et
Traitement de l'image
Prof. Pierre Magain

Dissertation realized for the
acquisition of the grade of
Doctor of Philosophy in Space Science

Supervisor:
Pr. dr. Pierre Magain

Members of the thesis commitee:
Pr. dr. Pierre Magain
Dr. Frédéric Courbin
Pr. dr. Hans Van Winckel

Jury composed of:
Pr. dr. Jean-Claude Gérard as president
Pr. dr. Pierre Magain
Dr. Frédéric Courbin
Pr. dr. Hans Van Winckel
Pr. dr. Jean Surdej
Dr. Damien Hutsemékers
Dr. Cécile Faure
Dr. Géraldine Letawe

To dreamers.
May their wish come true.

We should do astronomy because it is beautiful and because it is fun. We should do it because people want to know. We want to know our place in the universe and how things happen.

John N. Bahcall (1934 - 2005)

Abstract

The central topic of this thesis is gravitational lensing, a phenomenon that occurs when light rays from a background source pass near a massive object located on the line of sight and are deflected. It is one of the most wonderful observational fact in favour of the General Theory of Relativity (Einstein, 1916). This phenomenon constitutes a powerful tool to probe different areas in astrophysics, including cosmology, which is our main interest. In particular we study gravitationally lensed quasars. Refsdal (1964) was the first to state that time delays between different lensed images of the same object, if this one is intrisically variable, can lead to the measurement of the Hubble constant H_0, which is related the actual expansion rate of the Universe. Up to now, only a few lensed quasars have led to H_0 and the precision on it has never reached the one obtained with other methods as the ones based on the Cosmic Distance Ladder. That is why some scientists from around the globe decided to unite their force to measure H_0 from about thirty lensed quasars. To reach that goal, these objects are being monitored with some mid-sized ground-based telescopes located in both hemispheres. This thesis is realised in the framework of this collaboration called COSMOGRAIL for *COSmological MOnitoring of GRAvItational Lenses*.

This work focuses on image processing and on several steps mandatory to obtain a measurement of H_0 from lensed quasars: the acquisiton of the light curves from which it is possible to extract the time delays and the acquisition of the observational constraints necessary to model the gravitational potential responsible for the observed configuration. The central technique of this work is the image deconvolution with the MCS algorithm (Magain, Courbin & Sohy, 1998). The main principle of this algorithm is the non-violation of the sampling theorem in trying to obtain a better resolution in the deconvolved frame instead of an infinite one. The final resolution in the deconvolved frame is chosen by the user and as it is known, every image is decomposed in a contribution from the point sources and another one from all the extended structures such as arcs, rings and galaxies.

To obtain good light curves from data coming from several telescopes, good reduction procedures are needed. That is why Vuissoz (2008) developed a semi-automated reduction pipeline including deconvolution with the MCS algorithm. In the framework of the

present thesis, we adapt it to one of the telescopes used by the collaboration whose data were never used before, i.e. the Mercator telescope. We also bring some modifications to this pipeline, e.g. concerning the estimation of the error on the magnitudes of the light curves. We apply this revised version of the reduction pipeline to HE 0435-1223, a quadruply imaged quasar with already measured time delays (Kochanek et al., 2006). Another object, the quad WFI J2026-4536, is then investigated: we obtain light curves for each of the four lensed images.

Thanks to the CASTLES project (*Cfa-Arizona Space Telescope LEns Survey*[1]), many lensed quasars have been observed with the camera 2 of NICMOS (*Near Infrared Camera and Multi-Object Spectrometer*) on board the Hubble Space Telescope. With these high resolution images, we can obtain very accurate constraints on the geometry of the lensed systems. But most of the time no star is available in the field of view to obtain a good *Point Spread Function* (PSF). That is why we develop an iterative strategy combined with the MCS algorithm: we call it *ISMCS*. This technique allows to use the lensed images themselves to improve the PSFs step by step while simultaneously deconvolving the frame to obtain better estimations of the extended structures in the image.

We first test this strategy on a quadruply imaged quasar, the Cloverleaf gravitational lens (H1413+117), and obtain relative positions precise to 1 milliarcsecond (mas). We then apply ISMCS to the quadruply imaged quasar WFI J2033-4723 in order to contribute to the estimate of the Hubble constant, as this object was monitored by our team. We then study a sample of seven lensed systems currently monitored by COSMOGRAIL and for which time delays have never been obtained. Here again, we obtain positional constraints with an accuracy of around 1 to 2 mas thanks to the application of ISMCS. We then model these systems with simple mass profiles for the main lens galaxy and obtain an estimation of the values of the time delays. Finally we apply ISMCS to a sample of eleven lensed quasars which already have measured time delays. When the delays have been remeasured by our team, in four cases until now, we also model the potential of the lens with simple mass profiles to estimate H_0.

[1] `http://www.cfa.harvard.edu/castles`

Pour tirer le meilleur parti des connaissances acquises, pour en extraire toute la richesse, il importe de ne pas s'y habituer trop vite, de se laisser le temps de la surprise et de l'étonnement.

Hubert Reeves (1932 -)

Résumé

Le sujet central de cette thèse est le phénomène de lentille gravitationnelle qui se produit lorsque des rayons lumineux émis par une source d'arrière-plan passent à proximité d'un objet massif situé sur la ligne de visée et sont déviés. Il s'agit d'un des faits observationnels les plus parlants en faveur de la théorie de la Relativité Générale (Einstein, 1916). Ce phénomène constitue un outil puissant pour investiguer différents domaines de l'astrophysique comme la Cosmologie, sujet qui nous intéresse ici. En particulier nous étudions le phénomène de lentille gravitationnelle appliqué aux quasars. Refsdal (1964) fut le premier à énoncer et prouver que les délais temporels entre différentes images-lentilles du même objet, si ce dernier est intrinsèquement variable, peuvent mener à la mesure de la constante de Hubble H_0, paramètre relié au taux actuel d'expansion de l'Univers. Jusqu'à maintenant, seulement quelques quasars subissant le phénomène de lentille gravitationnelle ont mené à H_0 et la précision obtenue n'a jamais atteint celle d'autres méthodes basées par exemple sur l'échelle Cosmique des distances. C'est pourquoi certains scientifiques originaires de différents pays ont décidé d'unir leurs forces pour mesurer H_0 à partir d'une trentaine de quasars subissant le phénomène de lentille gravitationnelle. Pour atteindre cet objectif, ces quasars sont actuellement l'objet d'un suivi photométrique grâce à plusieurs télescopes de taille moyenne situés dans les deux hémisphères. Cette thèse est réalisée dans le cadre de cette collaboration qui se nomme COSMOGRAIL (*COSmological MOnitoring of GRAvItational Lenses*).

Ce travail se concentre sur les techniques de traitement d'images et sur plusieurs étapes obligatoires pour la mesure de la constante de Hubble à partir des quasars subissant le phénomène de lentille gravitationnelle: l'obtention des courbes de lumière desquelles il est possible d'extraire les délais temporels et l'obtention de contraintes géométriques nécessaires pour modéliser le potentiel gravitationnel responsable de la configuration observée. La technique au centre de ce travail est la déconvolution d'images avec l'algorithme MCS (Magain et al., 1998). Le principe de cet algorithme est la non-violation du théorème de l'échantillonnage en essayant d'obtenir une meilleure résolution dans l'image déconvoluée et non une résolution infinie. La résolution finale dans l'image déconvoluée est choisie par l'utilisateur et, comme elle est connue, chaque image est décomposée en une contribution des sources ponctuelles et une autre des

structures étendues comme les arcs, anneaux et autres galaxies lentilles.

Pour obtenir de bonnes courbes de lumière à partir de données provenant de différents télescopes, de bonnes méthodes de réduction sont nécessaires. C'est pourquoi Vuissoz (2008) a développé un pipeline de réduction semi-automatique incluant la déconvolution avec l'algorithme MCS. Nous l'adaptons, dans le cadre de cette thèse, à l'un des télescopes utilisés par la collaboration, le télescope Mercator, dont les données n'ont encore jamais été utilisées auparavant. Nous apportons également quelques modifications à ce pipeline, par exemple concernant l'estimation de l'erreur sur les magnitudes des courbes de lumière. Nous appliquons cette version révisée du pipeline à HE 0435-1223, un quasar quadruple dont les délais ont déjà été mesurés (Kochanek et al., 2006). Un autre objet, le quasar quadruple WFI J2026-4536, est ensuite investigué: nous obtenons des courbes de lumière pour chacune des images du quasar.

Grâce au projet CASTLES (*Cfa-Arizona Space Telescope LEns Survey*[2]), beaucoup de quasars subissant le phénomène de lentille gravitationnelle ont été observés avec la caméra 2 de NICMOS (*Near Infrared Camera and Multi-Object Spectrometer*) à bord du télescope spatial Hubble. Avec ces images à haute résolution, il est possible d'obtenir des contraintes très précises sur la géométrie de ces quasars. Mais la plupart du temps, il n'y pas d'étoile dans le champ d'observation pour pouvoir ajuster la PSF (*Point Spread Function*). C'est pourquoi nous développons une stratégie itérative combinée à l'algorithme MCS, que nous appelons *ISMCS* pour *Iterative Strategy combined with the MCS algorithm*. Cette technique permet d'utiliser les images créées par effet de lentille pour améliorer pas à pas la PSF et, simultanément, de déconvoluer l'image pour obtenir de meilleures estimations des structures étendues de l'image.

Nous testons d'abord cette technique sur un quasar quadruple, c'est-à-dire comportant quatre images de la même source, le *Cloverleaf* ou *Trèfle à Quatre Feuilles* (H1413+117), et nous obtenons des positions relatives précises à la milliarcseconde (mas). Nous appliquons ensuite ISMCS au quasar quadruple WFI J2033-4723 dans le but de contribuer à l'obtention de la constante de Hubble, cet objet faisant partie de ceux suivis photométriquement par la collaboration. Nous étudions ensuite un échantillon de sept quasars subissant le phénomène de lentille et suivis par COSMOGRAIL. Certains d'entre eux n'ont jamais été étudiés en détail. Nous obtenons ici encore des contraintes de positions avec une précision de 1 à 2 mas grâce à l'application d'ISMCS. Nous modélisons ensuite ces systèmes avec des profils de masse simples pour la lentille principale et obtenons une estimation de la valeur des délais temporels. Finalement la stratégie ISMCS est appliquée à un échantillon de onze quasars dont les délais temporels ont déjà été mesurés. Dans le cas où les délais ont été remesurés par notre équipe, c'est-à-dire pour quatre systèmes jusqu'à maintenant, nous modélisons également le potentiel de la lentille pour obtenir une estimation de H_0.

[2] `http://www.cfa.harvard.edu/castles`

Contents

List of Figures

List of Tables

Nothing shocks me.
I'm a scientist.

Harrison Ford (1942 -)
as *Indiana Jones*

1 Introduction

1.1 Research context

It is no longer to be proved that gravitational lensing is a wonderful tool to study galaxies and cosmology as well as detect extrasolar planets, to determine the structure of quasars (very bright active galactic nuclei), and so on. This phenomenon is created by a massive object located on the line of sight, or not too far from it, between Earth and a distant object. As this massive foreground object curves space-time, the light does not travel in a straight line, but borrows different curved paths. Our interest goes to lensed quasars in the *strong lensing* regime: several images of the same object are observable. If this quasar is intrinsically variable, the measurement of the time delay between its lensed images allows to estimate the Hubble constant H_0 (Refsdal, 1964). This cosmological parameter, which is equal to the ratio of the recession speed of a galaxy due to the expansion of the Universe to its distance from the observer, is very important to study our Universe at large scales.

This time delay method has a first advantage: it is completely independent from classical methods based on *standard candles*. These candles are objects belonging to a same class and sharing characteristics about their luminosity and variability, which allows to estimate their distance. A good example is the period-luminosity relation of Cepheid variable stars (see Sect. 2.2 for more details). Measuring H_0 on cosmic scales with variable lensed quasars presents a second great advantage: it is basically geometrical and the theoretical support is the General Theory of Relativity (Einstein, 1916), which is now a well-established theory.

The time delay between several images of a lensed quasar has two components: a geometrical one, due to the different paths followed by light, and a potential one, due to the gravitational potential well. These components depend on the total (luminous and dark) mass distribution in the lensing object and along the line of sight. This distribution can be constrained, to a large extent, by an accurate knowledge of the geometry of the system: relative angular positions of the lensed images and of the lens

galaxy, shape of the lens galaxy and possible presence of arcs or Einstein rings. Most of the time, the main uncertainty comes from the dark matter distribution. Moreover, the redshifts of the lens and source are mandatory to obtain H_0.

From WMAP (*Wilkinson Microwave Anisotropy Probe*) data combined with distance measurements from a large sample of Type Ia supernovae (see Sect. 2.2 for details), a Hubble constant of $H_0 = 70.5 \pm 1.3$ km/s/Mpc is derived (Komatsu et al., 2009). From standard candles, the most favoured value of H_0 was obtained by Freedman et al. (2001) in the framework of the Hubble Space Telescope Key Project: $H_0 = 72 \pm 8$ km/s/Mpc. The error is of the order of 10% but is only statistical: it does not include the systematic errors. Another team, whose work is based on Hubble Space Telescope observations of Type Ia supernovae, is convinced that the actual value of the Hubble constant is actually lower: $H_0 = 62.3 \pm 1.3$ (random) ± 5.0 (systematic) km/s/Mpc (Sandage et al., 2006). Gravitational lensing constitutes another tool to obtain the Hubble constant. But until now, the precision on H_0 obtained with variable lensed quasar has never reached the one obtained with standard methods. That is why some scientists with common interests have decided to set up COSMOGRAIL.

1.2 The COSMOGRAIL project

COSMOGRAIL stands for *COSmological MOnitoring of GRAvItational Lenses*[1]. This project was born in April 2004 when some scientists from different countries decided to gather their energy in order to determine the Hubble constant with a precision below 2% and to derive constraints on the mass distribution in lensing galaxies from around 30 variable gravitationally lensed quasars. To do so, some telescopes around the globe are partially dedicated to the observation of these objects. Indeed, a crucial point is the measurement of the time delays on light curves which must be well sampled compared to the value of the delay itself.

There are five countries involved so far in this project: Switzerland, Belgium, England, Uzbekistan, more recently joined by India. Each country provides some people working on the data and science cases and/or a telescope and the necessary technical support. The mid-sized telescopes involved in this monitoring campaign are located in the Northern and Southern hemispheres:

- the 1.2m Leonhard Euler Swiss Telescope operated by the Geneva Observatory, University of Geneva (Switzerland) at La Silla in Chile;
- its twin, the 1.2m Mercator Belgian-Swiss Telescope located at the Observatorio del Roque de Los Muchachos in La Palma (Canary Islands, Spain) and operated by the Institute of Astronomy, Catholic University of Leuven (Belgium), in collaboration with the Geneva Observatory;
- the 2.0m Robotic Telescope operated by the Astrophysics Research Institute of Liverpool University (United Kingdom), also located on the island of La Palma;

[1] `http://www.cosmograil.org`

- the 1.5m telescope of Maidanak Observatory in Uzbekistan operated by the Academy of Science in Tashkent (Uzbekistan);
- the 2.0m Himalayan Chandra Telescope (HCT) located at the Indian Astronomical Observatory in Hanle, India, and remotely operated from the Center for Research and Education in Science and Technology, which depends on the Indian Institute of Astrophysics in Bangalore.

Some pictures of them are displayed in Fig. 1.1. The Liverpool telescope is not being used for our project anymore, nor is temporarily the Mercator telescope which has been recently equipped with HERMES, which stands for *High Efficiency and Resolution Mercator Echelle Spectrograph*, and is currently in commissioning phase.

1.3 What does this thesis bring to COSMOGRAIL ?

This thesis is focused on several steps leading to the measurement of H_0 from gravitationally lensed quasars.

One key point is, of course, the measurement of the time delay. To do so, well-sampled light curves over a period longer than the delay are needed. That implies a simultaneous treatment of several hundreds of images coming from different telescopes. For that purpose, a semi-automated reduction pipeline was developed by Vuissoz (2008) in the framework of her PhD thesis. In this work, we depart from her pipeline and adapt it to our work, especially to the reduction of Mercator images which is an innovation in the COSMOGRAIL project. We then apply it to two quadruply lensed quasars, also called *quads*.

Another key step of the whole process is the acquisition of accurate relative astrometry not only for the multiple images, but also for the main lens galaxy. Therefore high resolution images are needed. The first telescope that comes to mind is obviously the NASA/ESA[2]-HST or *Hubble Space Telescope*. Even if we are dealing with high resolution images, a good image processing is very important as the typical separation between lensed images of a quasar is of the order of the arcsecond. Moreover, the instrumental profile of the HST is far from being simply shaped: it contaminates any diffuse structure under but also around the point sources because of its spatial extension and special structures such as a strong first Airy ring and spikes. The technique we use is the MCS deconvolution (Magain, Courbin & Sohy, 1998). It is based on the non-violation of the sampling theorem: we try to obtain images with a better resolution instead of an infinite one. As a consequence, the user chooses the final PSF or *Point Spread Function*. The deconvolved image is then decomposed into point sources and diffuse structures. In this work, we essentially treat images acquired with NIC2, the camera 2 of the instrument NICMOS, which stands for *Near Infrared Camera and Multi-Object Spectrometer*, on board the HST. The field of view of NIC2 being quite small, in most cases no extra star is available to determine an accurate PSF. That is why we develop an iterative strategy combined with the MCS deconvolution algorithm:

[2]NASA stands for *National Aeronautics and Space Administration* and ESA for *European Space Agency*.

Figure 1.1: Telescopes partially dedicated to the COSMOGRAIL project. *Left picture*: the dome. *Right picture*: the telescope itself. *From top to bottom*: the 1.2m Euler Swiss Telescope, the 1.2m Mercator Belgian-Swiss Telescope, the 2.0m Robotic Telescope of the Liverpool University, the 1.5m telescope of Maidanak Observatory and the 2.0m Himalayan Chandra Telescope. Credit from top left to bottom right: personal collection of pictures, ESO, `http://www.ing.iac.es`, `http://www.mercator.iac.es`, personal collection of pictures, R. Smith (2005), `http://www.astrin.uzsci.net` for the next two pictures and `http://www.iiap.res.in` for the last two.

the PSF is improved step by step by estimating the background and subtracting it from the original frames. This technique allows to obtain a very accurate relative astrometry of the system, as well as to detect structures blurred in the PSFs on the original frames, such as rings, arcs and lensing galaxies.

The next and directly related step is the modeling of the potential giving birth to the mirage phenomenon. Several softwares were designed for that purpose and are available to the entire scientific community. The difficulty resides essentially in the numerous models at our disposal, but also in the lack of knowledge about the dark matter distribution. When the time delays are known, as well as the source and lens redshifts, it leads to an estimation of H_0. Our aim is to test the effects of strong positional constraints on this modeling, with simple mass profiles.

1.4 Outline of the thesis

This work is divided as follows.

Part I presents the theoretical aspects needed to go through this thesis: general notions about cosmology (Chapter 2), the history and nature of active galactic nuclei (Chapter 3), strong gravitational lensing (Chapter 4) and finally deconvolution (Chapter 5) as it is the image processing technique we mainly use in this work.

Part II presents the main methods developed in the framework of this thesis: the revised semi-automated reduction pipeline in Chapter 6 and the iterative strategy combined with the MCS deconvolution algorithm in Chapter 7. Moreover the latter is tested on a particular object, the famous Cloverleaf gravitational lens, in Chapter 8.

Part III concerns the acquisition of the light curves. The application of the semi-automated reduction pipeline to two different systems monitored by COSMOGRAIL is exposed in Chapter 9 and in Chapter 10 respectively for HE 0435-1223 and WFI J2026-4536.

Part IV presents the applications of the iterative strategy combined with the MCS deconvolution algorithm. Chapter 11 explains how we contributed to the measurement of H_0 for WFI J2033-4723 with the iterative strategy. It is then applied in Chapter 12 to a sample of seven lensed quasars arbitrarily chosen amongst the COSMOGRAIL targets with no measured time delay and most of the time no detailed study. These systems are then modeled with simple mass profiles to study the influence of strong astrometric constraints on the goodness of fit. Finally it is applied in Chapter 13 to eleven lensed quasars which already have measured time delays. Our aims are twofold for this last sample: first we want to remeasure the delay(s) and second to model the systems with the new observational constraints.

Finally, Part V contains the conclusions (Chapter 14), the bibliography, the list of publications and the acknowledgments.

Part I

Theoretical background

Change will not come if we wait for some other person or some other time. We are the ones we've been waiting for. We are the change that we seek.

Barack Obama (1961 -)

2 An overflight of modern cosmology

Contents

2.1 Introduction

Cosmology has long been associated to divinity, religion and myths. Since the oldest ages, many questions about this topic have been in the mind of human beings who, back then, found answers in their Gods. An example is given in Fig. 2.1: two representations of the Cosmos as perceived respectively by the Mayas and the Incas. According to both civilizations, the Universe was composed of three major levels: the Earth, the underworld and the skies that they pictured as a limit to the world. But the thirst of Mankind to understand where they come from and the will to define the Universe they live in have brought them to ask more and more questions and to be more and more eager to obtain rational answers instead of religious ones. Nowadays, cosmology is considered as the science that studies the Universe, i.e. the Cosmos at large scales. It thus focuses on the origins, the evolution since then and the future development of the Universe. Modern cosmology was born in the first quarter of the last century with Albert Einstein and the completion of his General Theory of Relativity (Einstein, 1916).

After the *Copernican Principle* which states that no place in the Universe is favoured (no absolute reference point), the most important assumption or working hypothesis in cosmology, supported by observations, is the *Cosmological Principle* which states that our Universe is isotropic, i.e. the same in all directions, and homogeneous, i.e. what is observed is independent of the observer position, on large spatial scales. Another very

Figure 2.1: Representation of the Cosmos as seen by the Mayas (*left image*) and by the Incas (*right image*). According to both civilizations, the Universe was composed of the Earth and the underground and delimited by the skies. Credit: original paintings by Ken Dallison, National Geographic, March 1990, "Ancient Skywatchers", revised for the Web (`http://www.edwardtbabinski.us/geocentrism/ancient\_american\_cosmology.html`) by Sharon Mooneysee.

important assumption is the *Universality of Physical Laws* with the consequence that they are applicable everywhere in the Universe.

The metric, which converts the coordinates of two points into a distance, attached to our Universe must thus also be homogeneous and isotropic as a consequence of the Cosmological Principle: this is the case of the Friedmann-Lemaître-Robertson-Walker metric, which is an exact solution of Einstein's field equations of General Relativity. This metric contains a scale factor $R(t)$, which describes how the size of the Universe changes with time. This enables a convenient choice of a coordinate system: the comoving coordinates. In this system, the grid expands along with the Universe, and objects that are moving only due to the expansion of the Universe remain at fixed points on this grid. While their coordinate distance (comoving distance) remains constant, the physical distance between two such comoving points expands proportionally to the scale factor. In summary *comoving* means "that moves with the Hubble flow". The latter is related to the *Hubble Law*, which we present in the next section, as it is the first discovery that led to the present global view of our Universe and its origins.

2.2 The Hubble Law: a first step towards the Big Bang

In 1929, Hubble discovered that all galaxies, called *nebulae* at that time, are moving away from us. He hilighted a correlation between the radial velocity of those galaxies and their distance. The radial velocity can be measured through the *redshift* in the spectrum of an object if this redshift is interpreted as resulting from a Doppler effect: it

is a shift of the wavelength of a known transition towards longer wavelengths. Moreover, for some galaxies, it is possible to estimate their distance with standard candles.

This redshift appeared to be larger for faint and presumably further objects. Edwin Hubble thus plotted the radial velocities against the distances of these nebulae and noticed a linear relation, though tainted by a considerable scatter due to peculiar velocities[1]. This proportionality relation is known as the *Hubble Law*:

$$v_r = H_0 \times D \tag{2.1}$$

where v_r is the radial velocity of the object in km/s, D is its proper distance[2] in megaparsec[3] and H_0 is the Hubble constant conventionally expressed in km/s/Mpc even though it is the inverse of a time. So, for each Mpc of distance from us, the velocity of an object appears to increase by an amount equal to H_0 km/s. As the Hubble constant varies with time, it would be more appropriate to call it the *Hubble parameter*, the subscript *0* of H_0 being used to denote the present time value ($H_0 = H(t_0)$).

The Hubble parameter $H(t)$ can be expressed as follows:

$$H(t) = \frac{dR(t)/dt}{R(t)} \tag{2.2}$$

where $R(t)$ is the scale factor at time t. Moreover $R(t)$ is related to the actual scale factor $R(t_0)$ by the expansion parameter $a(t)$ in the following way:

$$R(t) = a(t) \times R(t_0). \tag{2.3}$$

$R(t_0)$ is arbitrarily chosen as equal to unity. If D is the proper distance of an object and r_{co} the radial comoving coordinate, then:

$$D = R(t) \times r_{co} \tag{2.4}$$

with the following consequence on v_r:

$$v_r = \frac{dD}{dt} = \frac{dR(t)}{dt}\, r_{co} = \frac{dR(t)}{dt}\frac{D}{R(t)} = H(t) \times D \tag{2.5}$$

which is the Hubble Law.

[1] The *peculiar velocity* of an object is due to relative motions caused by gravitational interactions and independent of the expansion of the Universe. The error caused by these velocities becomes smaller, relative to the total speed, as the distance increases.

[2] The *proper distance* between two events is the distance measured on a hypersurface of constant proper time, i.e. the distance measured in a coordinate system where these events are simultaneous. The proper time is the time measured by a single clock between events that occur at the same place as the clock. Let us note that the comoving distance of an object is its current proper distance because $R(t_o)$ is arbitrarily chosen as equal to 1.

[3] A *parsec* (pc) is the distance of an object having an annual parallax of 1 arcsec, i.e. 1 pc = 3.086 10^{16} m = 3.26 light years. Let us recall that the annual parallax of a celestial body is the maximum apparent displacement of this body during a year resulting from the motion of the Earth around the Sun.

The redshift z is defined as follows:

$$z = \frac{\Delta\lambda}{\lambda_{em}} \tag{2.6}$$

where $\Delta\lambda = \lambda_{obs} - \lambda_{em}$, λ_{em} being the initially emitted wavelength while λ_{obs} is the observed one. The redshift is also related to the scale factor of the Universe by the following expression (not demonstrated here):

$$1 + z = \frac{\lambda_{obs}}{\lambda_{em}} = \frac{R(t_{obs})}{R(t_{em})} = \frac{R(t_0)}{R(t)} = \frac{1}{R(t)}. \tag{2.7}$$

As $t_{obs} > t_{em}$, we have $R(t_{obs}) > R(t_{em})$ and thus $\lambda_{obs} > \lambda_{em}$. That is why z is called *redshift* as the optical wavelengths are shifted towards the red part of the electromagnetic spectrum.

However, the redshift at stake here is not a true Doppler shift due to relative motions, but rather the result of the expansion of the Universe between the time the light was emitted and the time it was detected: the proper name of the apparent radial velocity is *recession velocity* and it is often talked about *cosmological redshift*. So the use of the Doppler formula to associate redshifts with velocities, i.e. $v \approx cz$ where c is the speed of light[4], is an approximation only valid for objects located at low redshifts, typically less than unity. At larger redshifts, it has to be replaced by a relation that depends on the cosmological model.

The value of H_0 initially obtained by Hubble was around 500 km/s/Mpc, and has since been radically revised because initial assumptions about stars led Hubble to underestimate the distances of nebulae. Distance measurements to nearby galaxies mainly use Cepheid variable stars as standard candles (until around 30 Mpc). A Cepheid is a pulsating supergiant star, in the core He-burning phase, known for its period-luminosity relation: at each period, which is observable, corresponds an absolute magnitude that can be translated into a distance in comparing it to the relative magnitude of the star in question. However, more distant galaxies must also be investigated: indeed, the galaxies within our reach thanks to the Cepheid variables are under the influence of the gravitational attraction of the Local Group[5]. That goal is more easily achieved nowadays than back when Hubble established his law: the development of more sophisticated techniques and technologies has considerably improved the efficiency of telescopes and has helped us to reach unprecedented deepnesses in the night sky. For farther located objects, we need brighter standard candles such as Type Ia supernovae (SNe Ia). This phenomenon happens in a binary system composed of a white dwarf star accreting matter from her companion star. When the mass of the white dwarf reaches a certain value of 1.38 $M_\odot$ called the *Chandrasekhar mass*, the star ejects its external layers in a cataclysmic explosion that is very short but very bright. In studying the shape of the light curve of the SN Ia and especially the luminosity decline after the explosion, it is possible to know the intrinsic luminosity of the object. After some corrections for the

[4] $c = 299\ 792\ 458$ km/s.

[5] The *Local Group* is a group of about 30 galaxies in gravitational interaction, including the Milky Way, Andromeda and the Magellanic Clouds.

dust reddening and in comparing the absolute magnitude to the relative one, it leads to an estimation of the distance. This is possible for distances until around 500 Mpc. Moreover, as they are calibrated with the Cepheid period-luminosity relation, they are called *secondary distance indicators*. That also means that any error in the estimation of distances with the Cepheid period-luminosity relation will propagate into distances estimated with SNe Ia. More generally, it is the case of any secondary indicators that allow to estimate larger and larger distances thanks to closer secondary indicators. All these indicators constitute the Cosmic Distance Ladder.

There exists many other ways to measure the Hubble constant: classical indicators (surface brightness fluctuations, scaling relations such as Tully-Fisher or the fundamental plane) which include Cosmic Distance Ladder as explained above, and physical indicators (Sunyaev-Zeldovich effect, gravitational lensing). Here are a few words on each aforementioned technique:

- **Surface brightness fluctuations** (Tonry & Schneider, 1988): The basic principle of this method is that all galaxies are composed of a finite number of stars. The number of stars in any *pixel*[6] of a deep image of a galaxy will vary from one to the other, creating a noise-like fluctuation in the surface brightness distribution. The working hypothesis is the following: the distribution of the number of stars N per unit area is Poissonian[7]. The observed area depends on the angular diameter distance and the solid angle. The further the galaxy, the larger is the number of stars contained in a given solid angle and the smaller are the fluctuations. Let us note that this technique requires a calibration with classical indicators.

- **Tully-Fisher relation** (Tully & Fisher, 1977): This relation is empirical and relates the intrinsic luminosity of late-type galaxies to the amplitude of their rotation curve. The velocity dispersion of the galaxy being measurable, it thus allows to estimate the absolute magnitude of the galaxy and, in comparing it to the apparent magnitude, to deduce its distance.

- **Fundamental plane** (Djorgovski & Davis, 1987): Similar to the Tully-Fisher relation, the fundamental plane is also an empirical relationship but it concerns elliptical galaxies. It relates their effective radius, central velocity dispersion and average surface brightness. The two first being measurable, the last one can lead to the distance of the galaxy through the comparison of absolute and apparent magnitudes.

- **Sunyaev-Zeldovich (SZ) effect** (Sunyaev & Zeldovich, 1970): This method is independent from any distance calibrators. The SZ effect is the result of high energy electrons, coming from hot gas in clusters, that collide with the low energy *Cosmic Microwave Background* (CMB) photons, which consitute a relic glow of the Big Bang (see Sect. 2.3 for details), yielding them some energy and thus distorting the CMB. The gain of energy by photons thanks to matter is called *inverse*

[6] The word *pixel* comes from the contraction of the words *picture* and *element*. The pixel is the basic component of an image.

[7] The standard deviation is thus equal to $\sqrt{N}$ and the number of stars per unit area fluctuates as $1/\sqrt{N}$.

Compton scattering. The distortions in the CMB are used to detect overdensities in the far Universe. The "rate" of distortion depends on the size, temperature, and density of the hot gas in the cluster. In measuring the temperature and density of the gas with X-ray observations coupled with the distortion of the CMB, the size of the gas-emitting region can be estimated. This size along with the brightness gives an estimate of the distance to the cluster, which combined to its redshift leads to H_0.

- **Gravitational lensing**: This method does not use any distance indicator. See Sect. 4.9 for details.

Nowadays there are two different schools adopting two different values of H_0: Sandage et al. (2006) obtained $H_0 = 62.3 \pm 1.3$ (random) $\pm$ 5.0 (systematic) km/s/Mpc from the Cepheid-calibrated luminosity of Type Ia supernovae in the *SN Ia HST Calibration Program* while Freedman et al. (2001) concentrated on obtaining accurate primary distance indicators (Cepheids) and derived a value of $H_0 = 72 \pm 8$ km/s/Mpc, the currently most popular value, in the framework of the Hubble Space Telescope Key Project. The latter value is supported by WMAP (*Wilkinson Microwave Anisotropy Probe*) data combined with distance measurements from Type Ia supernovae: $H_0 = 70.5 \pm 1.3$ km/s/Mpc (Komatsu et al., 2009). To account for this uncertainty on H_0, it is conventional to define a dimensionless parameter : $h = H_0/(100$ km/s/Mpc).

Let us finish this section about the Hubble Law with noticing that astronomical redshifts are extremely isotropic and homogenous, thus supporting the Cosmological Principle. Moreover, according to the Copernican Principle, the expansion cannot be centered on the solar system: the Universe is uniformly expanding everywhere, unregarding any fixed central point. This universal expansion was predicted from General Relativity by Alexander Friedmann, a Russian mathematician, in 1922 and by Georges Lemaître, a Belgian physicist and Roman Catholic priest, in 1927, well before Hubble established his linear law in 1929. This Hubble Law is one of the master ideas that led to the *Big Bang theory*: if the distance between galaxies or, more exactly, clusters of galaxies is increasing today, everything must have been closer together in the past. This is the central topic of the next section.

2.3 The Big Bang theory

Fig. 2.2 presents a cartoon of the birth of our Universe and its evolution until now. Let us go through the main different phases.

According to the so-called *Standard Model of cosmology*[8], also called the *Concordance Model*, our Universe started around 13.7 billion years ago in a very dense and hot state, the *Big Bang*, also called the *original singularity* and where all known physical laws break down. It is still unknown whether this singularity is a physical reality or just a mathematical extrapolation of General Relativity beyond its limits of applicability. The resolution of this issue depends on a theory of quantum gravity, which is not currently available.

[8]The *Standard Model of cosmology* is the most commonly accepted model of cosmology.

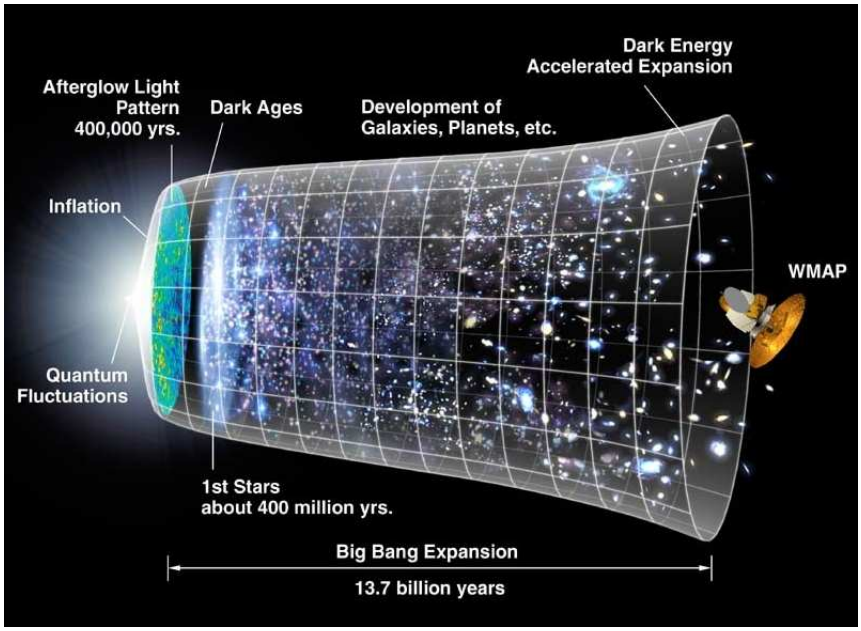

Figure 2.2: Evolution of the Universe according to the Bing Bang model. Credit: NASA/WMAP Science Team.

When space-time began to expand, our Universe was radiation-dominated. The next phase is an exponential expansion called the *inflation* (Guth, 1981) and driven by the energy of the vacuum which has a negative pressure. This rapid expansion increased the linear dimensions of the early Universe by a factor of at least 10^{28} but most likely around 10^{50}, in about 10^{-32}s. The first mentioned value allows to solve for the so-called *horizon problem*. Indeed, as no information can travel faster than light, some regions were not in causal contact in the past considering the distances between them. There is thus a horizon beyond which we cannot observe anything. Nevertheless, some properties, e.g. the temperature, are common between those regions. Without an inflationary phase to enlarge the horizon length, this would not be possible. The inflation is also the solution to the flatness of the Universe: any initial curvature of the Universe would have flattened out. Let us note that this inflationary scenario is not yet fully understood: one major theoretical issue concerns the mecanisms responsible for the end of the exponential expansion.

Only a few minutes after the Big Bang, the primordial nucleosynthesis by nuclear fusion between protons and neutrons created atomic nuclei until the temperature was not high enough to allow fusion anymore. At that time, there were about three times more H than ^{4}He (regarding the mass) and only traces of some light nuclei. Approximately 400 000 years after the Big Bang, the electrons got captured by nuclei to form electrically neutral atoms: this is called the *recombination*.

Thanks to these uncharged particles who could no longer interact efficiently with

the thermal radiation, the *decoupling* of matter and photons happened. The Universe was no longer opaque: it became transparent for the first time. The mean path of photons became so long that most of them have not scattered ever since: they are still propagating. This is the source of a relic glow, better known as the *Cosmic Microwave Background*, or CMB (Penzias & Wilson, 1965), which is a "picture" of the Universe at the decoupling epoch. We can still observe it today as the thermal radiation of an almost perfect black body. But as the Universe expands, the CMB photons are redshifted: the observed temperature of the black body has cooled down to 2.725 ± 0.002 K since the decoupling and the spectrum peaks in the microwave range frequency of 160.2 GHz, corresponding to a 1.9 mm wavelength. Let us note that the nearly perfect isotropy of the CMB radiation is explained by the inflationary phase. Indeed, thanks to it, the diverse regions in the sky where the CMB is observed were in physical contact.

After the decoupling, ordinary matter was able to fall into the dark matter clumps previously created. 400 million years after the Big Bang were born the first quasars and hypothetical *Population III stars*[9], which started the process of turning the light elements that were already formed into heavier ones.

Several hypotheses, illustrated on Fig. 2.3, have been made concerning the future of our Universe. Here are the four main scenarios:

- *Big Crunch*: This scenario is very unlikely as it requests a closed Universe which is currently not favoured by observations. If that was the case, the strength of the gravitational force would slow down the expansion until it stops to eventually reverse. The Universe would recollapse and contract until it reaches a very hot and very dense state.

- *Big Bounce*: The *Big Crunch* scenario is also proposed in an oscillatory version. When the Universe would reach a dense state, a new Big Bang would occur until the expansion stops and reverses, and so on. This suggests that we might be living in the first of all universes but we might also be living in the 700^{th} one.

- *Big Freeze*: At a certain precise critical density called ρ_{crit}, the Universe would asymptotically approach a zero expansion rate, but never collapse. Considered as a likely scenario, it will occur if the expansion continues forever as it has been until now. Over a time scale of the order of 10^{14} years, existing stars will die and new stars will not be created anymore.
  If a cosmological constant (see next section for more details) accelerates the expansion of the Universe, clusters of galaxies will rapidly be driven away from each other, leaving observers in different clusters unable to either reach each other or sense each other's presence in any ways. That will result in the *heat death* of the Universe: the temperature will lower nearly until the absolute zero and the Universe will approach a state of maximal entropy over a very long time period. It will finally turn dark.

[9]The stars belonging to the *Population III* are extremely massive stars ($M > 100$ M$_\odot$) that would have a very low metallicity ($Z < 10^{-6} \times Z_\odot$), i.e. they likely hardly contain elements heavier than H and He.

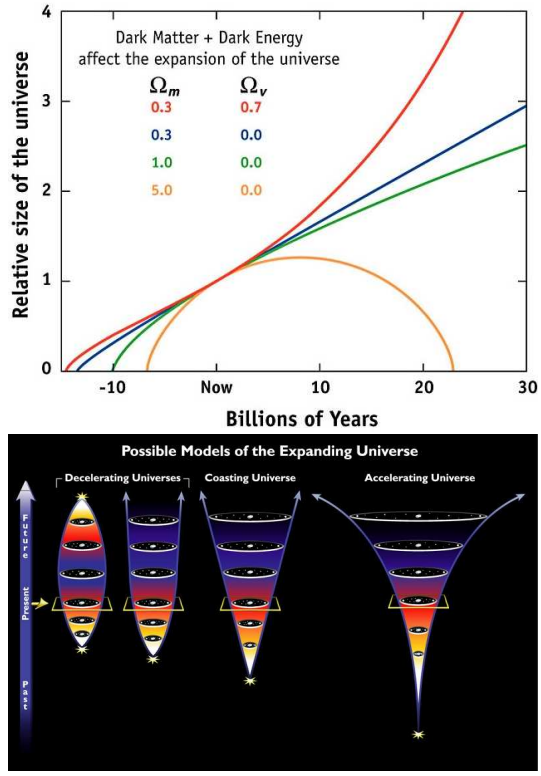

Figure 2.3: Diverse options for the future of our Universe. *Top*: diagram of the relative size of the Universe against time in billions of years (see next section for a definition of Ω_m and Ω_V which is equal to Ω_Λ). Credit: NASA/WMAP Science Team. *Bottom*: cartoon representing a portion of the Universe evolving as a function of the chosen model. *From left to right of this cartoon*: Big Crunch (orange curve on the top diagram), Big Freeze (green curve on the top diagram), Coasting Universe (blue curve on the top diagram) and Big Rip (red curve on the top diagram). Credit: `http://physics.uoregon.edu/~jimbrau/astr123/Notes/Exam2rev.html`.

- *Coasting Universe*: This kind of Universe will expand forever with a strictly linear evolution of the scale factor: there is no acceleration or deceleration of the expansion rate. Even if, apparently, this kind of model can explain a host of observations, it is not very popular, however still studied by some cosmologists.

- *Big Rip*: Another likely scenario is the *Big Rip*. It is the newest one as it appeared with the interpretation of the cosmological constant as being related to a so-called *dark energy*. It is supported by some observations of relatively distant supernovae. It is possible if the density of dark energy increases indefinitely. As a consequence, the expansion rate of the Universe will increase with no limit. Gravitationally bounded systems will be torn apart. Over a certain treshold, the expansion rate will be so high that even the electromagnetic force will not be able to hold molecules, atoms and, finally, even nuclei together. The Big Rip scenario is considered as the *New Standard Model*.

2.4 The Concordance Model

The *Concordance Model*, also called Λ-*CDM* which stands for *Lambda Cold Dark Matter*, is the currently most popular and most commonly used cosmological model. According to that model, our Universe is spatially flat (or really close to perfect flatness) as a consequence of the inflation phase. It is composed mainly of CDM, i.e. slowly moving massive particles (in opposition to HDM or *Hot Dark Matter*, composed of nearly relativistic massive particles), presumably non-baryonic, dissipationless and collisionless, with the consequence of a *bottom-up* formation of the structures: small objects collapsed into larger ones until they assembled into *clusters*, *superclusters* and larger structures such as *sheets*, *filaments* and finally *walls*. The motion-induced pressure of the CDM particles is insignificant regarding the one, non-negligible, created by photons because of their relativistic velocities. The non-zero cosmological constant Λ in Einstein's field equations of General Relativity can be interpreted as a negative pressure associated to the vacuum energy which has a repulsive effect on matter with the consequence that our Universe is expanding at an increasing rate. It is better known as *dark energy*. Its real nature is still a matter of speculation.

This Λ-CDM model has several crucial parameters including the density parameter Ω_x which is the ratio of the density ρ_x to the critical one ρ_{crit}. The subscript x can be replaced by b for baryons, dm for dark matter, m for total matter (light + dark), r for radiation and Λ for dark energy:

$$\Omega_b = \frac{\rho_b}{\rho_{crit}},\ \Omega_{dm} = \frac{\rho_{dm}}{\rho_{crit}},\ \Omega_m = \frac{\rho_m}{\rho_{crit}},\ \Omega_r = \frac{\rho_r}{\rho_{crit}},\ \Omega_\Lambda = \frac{\rho_\Lambda}{\rho_{crit}}. \tag{2.8}$$

Let us note that, in the absence of a cosmological constant, if the density of matter equals the critical density ρ_{crit}, the Universe is flat (zero curvature) but still presumably infinite, if the density is less than ρ_{crit}, the Universe is open, i.e. infinite, and hyperbolic (negative curvature), while if the density is larger than ρ_{crit}, the Universe is closed (finite) and spheric (positive curvature). The critical density corresponds roughly to five hydrogen atoms per cubic meter. The vacuum we can create on Earth for our experiments is far from that value. The total density at the present time is obviously defined as follows:

$$\Omega_0 = \Omega_m + \Omega_\Lambda + \Omega_r\,. \tag{2.9}$$

Here are some of the latest results of the *Wilkinson Microwave Anisotropy Probe* team (WMAP) obtained by Komatsu et al. (2009). That publication is part of a serie of seven papers on the analysis of the WMAP 5-year data. WMAP is a satellite aiming at measuring the spectrum of the CMB with high angular resolution to study its anisotropies. In fitting a model to the fluctuations in temperature of the CMB photons, believed to trace the fluctuations in the density of matter back at the decoupling epoch, Komatsu et al. (2009) obtained constraints on the cosmological parameters. In combining their results with the ones obtained e.g. from Type Ia supernovae, they obtained

with a 68% confidence level:

$$\Omega_{b,0} = 0.0456 \pm 0.0015, \tag{2.10}$$
$$\Omega_{dm,0} = 0.228 \pm 0.013, \tag{2.11}$$
$$\Omega_{\Lambda,0} = 0.726 \pm 0.015, \tag{2.12}$$
$$\Omega_0 = 1.0050\ ^{+0.0060}_{-0.0061}, \tag{2.13}$$
$$t_0 = 13.72 \pm 0.12 \text{ Gyr}, \tag{2.14}$$

Ω_0 coming from Hinshaw et al. (2009) also part of the serie of seven papers. Moreover they do not find any deviation from a spatially flat universe.

Let us conclude this section on the Concordance Model and, more generally, on our overflight of cosmology with the following questions. Have we really entered an era of high accuracy cosmology ? Or are the new challenges that constitute dark matter and dark energy only crutches just waiting for the next scientific revolution to fall to pieces? Some think the answer is clear, while some others, only a few though, think the answer is not yet within our reach.

Something unknown is doing we don't know what.

Arthur Eddington (1882 - 1944)

3 Active galactic nuclei

Contents

3.1 Introduction

This section is mainly based on the following works: Binney & Merrifield (1998), Krolik (1999) and Letawe (2006).

Some galaxies show a strange behaviour. What differs from classical ones is the presence in their center of a nucleus releasing a huge quantity of energy by non-nuclear processes (unlike what happens in stellar interiors): these objects produce very high luminosities, up to ten thousand times the typical luminosity of classical galaxies, in tiny volumes. They are called *AGN*, which stands for *Active Galactic Nuclei*, or simply *active galaxies*. A cartoon is shown in Fig. 3.1: it represents an artist view of an AGN.

The spectral distribution of normal galaxies is composed of contributions from the different stellar populations. It consists in thermal radiations, redder if the stars are cooler, but mainly in the optical and near-IR. Unlike these normal galaxies, AGN are observable in a wide range of wavelengths, from radio to X-ray. Moreover, they present emission and sometimes absorption lines reaching a flux of several percent of the continuum, in the optical and UV. Most AGN are non-periodically variable in the optical,

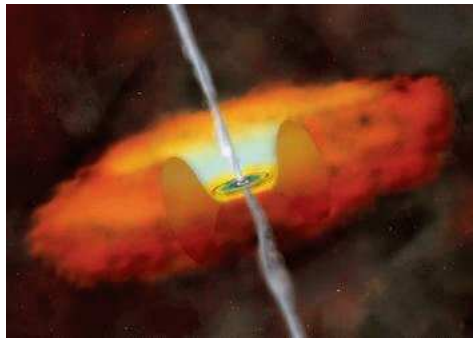

Figure 3.1: Artist view of an AGN. The central black hole is surrounded by a disk composed of hot gas and a huge belt composed of colder gas and dust. The latter is called the *torus*. We can also see two jets of high energy particles (see hereafter for details). Credit: CXC/M.Weiss.

some more violently than others. Moreover, their light is often slighlty polarized due to the interstellar medium crossed before reaching us.

AGN can be sorted out in four main categories: Seyfert galaxies, radio galaxies, blazars and quasars. These latter are the main subject of this chapter. Let us explain briefly what the other types consist in.

3.2 Seyfert galaxies

Since galaxies are studied, some scientists have been observing objects with unusual shapes. The best example is probably Carl Seyfert who made a catalog, back in 1943, with galaxies looking like spirals but having a very bright region at their center, i.e. a very bright nucleus, that often shows quite broad emission lines of high excitation.

A very interesting characteristic of such galaxies, called without surprise *Seyfert galaxies*, is the tiny size of their nucleus. Indeed, this very bright part is highly variable on periods of less than a year. That deserves a short explanation. Let us assume that the luminosity of an extended object of size a doubles. These variations have to occur simultaneously on the entire nucleus: there must be an exchange of information between the different points of this nucleus. The observed brightness of the object adjusts to the new level in a time $\tau \simeq a/c$, i.e. in the time that light takes to travel from the back of the object to the front. It implies, as periods of several months are observed, that the maximal size of the nucleus cannot be larger than several light months, which is really small compared to the size of the entire galaxy.

Seyfert galaxies are classified in two groups depending on the aspect of their spectrum. *Type I Seyfert galaxies* emit an intense continuum and the permitted spectral lines have very broad wings while the forbidden lines are narrow because the velocities involved are weaker and so is the velocity dispersion. In *Type II Seyfert galaxies*, only the narrow lines are observable.

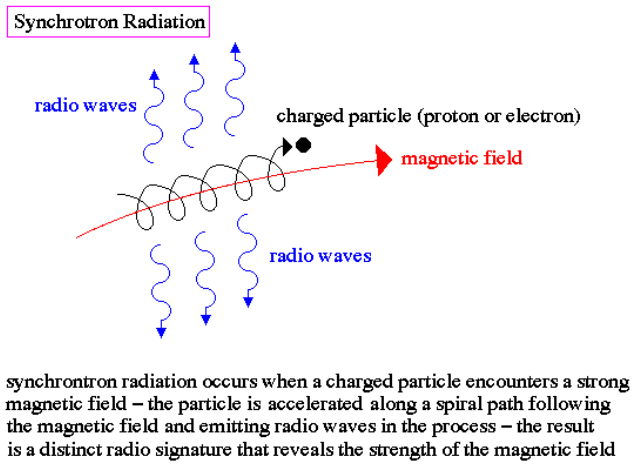

Figure 3.2: Illustration and explanation of the synchrotron radiation phenomenon. Credit: `http://blueox.uoregon.edu`.

3.3 Radio galaxies

Radio galaxies constitute another type of AGN. They differ from Seyfert galaxies because their nucleus is not necessarily visible. These objects, which most of the time look like normal elliptical galaxies, are characterized, as their name tells us, by strong and extended radio emissions, 10 000 times superior to those of classical galaxies.

These radio waves are produced by highly energetic electrons moving in a magnetic field[1], i.e. by synchrotron radiation. This phenomenon is illustrated in Fig. 3.2 and can be explained as follows: a relativistic charged particle, most of the time an electron, moving in a magnetic field is accelerated along a field line. In spiraling around the latter, it emits a radiation called *synchrotron*. Most of the radio flux generally comes from two huge regions called the *radio lobes* and located on either side of the nucleus. Their size may be about 10 times larger than the one of the galaxy and can reach several megaparsecs. High resolution radio images reveal that these lobes are often tied to the nuclear source by thin relativistic filaments called *radio jets* (see Fig. 3.3). Sometimes, along with the compact emission of the core, a jet can be visible at optical frequencies, as it was discovered by Geoffrey Burbidge in 1956 in the giant elliptical galaxy M87 (see Fig. 3.4).

Radio galaxies can be sorted out in two categories according to their optical spectrum:

- *narrow-line radio galaxies* or NLRGs, which show only the narrow emission lines that we find in Type II Seyferts;

[1] This magnetic field is created by particles moving in the accretion disk of the supermassive black hole (see next section).

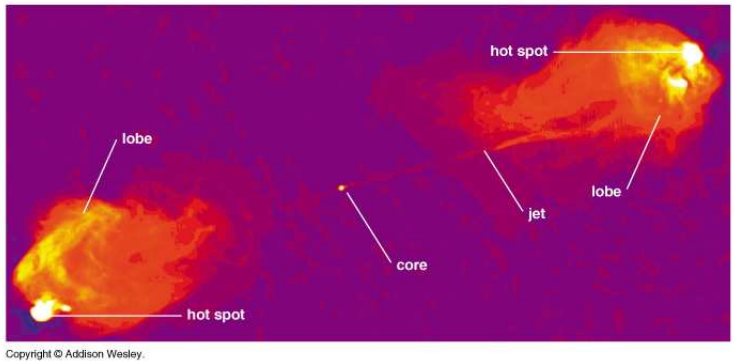

Figure 3.3: Radio lobes tied to the galactic nucleus by thin relativistic jets. Credit: Addison Wesley.

- *broad-line radio galaxies* or BLRGs, which also show the broad lines observed in Type I Seyferts.

These galaxies can also be classified according to their radio morphology: the ones whose emissions are dominated by the compact nucleus are called *FR-I radio galaxies* while the intensity of the emissions from *FR-II radio galaxies* increases outwards. Let us note that *FR* stands for *Fanaroff-Riley*, after the two astronomers who highlighted this characteristic (Fanaroff & Riley, 1974).

3.4 Blazars

The word *blazars* derives from *BL Lacertae*, the prototype of this class of objects, and obviously from the term *quasar* itself (see next section). Blazars are radio emitters and appear to be point-like, very bright and dramatically variable objects: their brightness can change by large factors on timescales of a few weeks. Moreover, their light is relatively highly polarized in the optical.

Blazars can be sorted out in two categories: *BL Lac* objects and OVV which stands for *Optically Violent Variables*. The difference resides in the fact that OVV show broad but weak optical emission lines in their spectra, which is characteristic of quasars, while BL Lac objects do not, which makes it difficult to measure their redshift. Let us mention that the separation between these two types is quite fuzzy. Depending on the epoch of observation, a blazar can even switch from one category to the other.

At first it was believed that the object BL Lacertae was some kind of extremely variable star. But in 1974, Adams highlighted its AGN nature: the bright point source is actually surrounded by a faint nebulosity, i.e. an elliptical galaxy. The spectra revealed a redshift of 0.07 (Miller, French & Hawley, 1978).

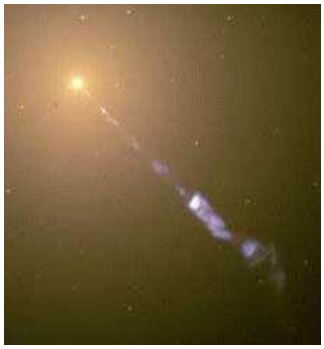

Figure 3.4: The giant elliptical galaxy M87, located at 50×10^6 light years, is an AGN. It corresponds to the radio source 3C 274. The galaxy itself appears to be red: it is composed of old and relatively cold stars. The blue radio jet, made of high energy electrons, comes from the nucleus and is around 6500 light years long. Credit: NASA/STScI.

3.5 Once upon a time...

The neologism *quasar* stands for *QUAsi-Stellar Astronomical Radio source* and was born in the late 1950s. This word was introduced when very loud radio sources were discovered. For some of them, no visible counterpart other than a stellar-like object was observed. It was believed that quasars were some strange and new kind of stars belonging to the Milky Way. But their spectra showed very clear emission lines corresponding to no usual chemical element. This mystery was solved in 1963 by the Dutch astronomer Maarten Schmidt who studied a particular quasar, 3C 273, observed during the Survey of Radio Sources III carried out at Cambridge University. According to him, quasars are very distant and very bright sources. Therefore the emission lines are strongly redshifted and most of them simply correspond to hydrogen. It means that 3C 273, with a redshift of 0.16, is receding at a rate of around 47 000 km/s. More generally it shows that quasars are far from being located in our galaxy.

Later, it was found that many similar objects were radio-quiet, i.e. did not emit radio waves. These were called *Quasi-Stellar Objects* or QSOs. Nowadays, the term *quasar* is often used for all of them even if only about 10 % of the QSOs known to date have been proved to radiate at least 0.1% of their total luminosity in the radio range.

Some spectral similarities to Type I Seyferts were also pointed out. It is now agreed that QSOs are no stars of the Milky Way at all, but objects located at the center of distant galaxies. Their nucleus is so optically bright that it can outshine the whole surrounding galaxy. They are located so far away that their optical angular size is comparable to the resolution of ground-based observations. Indeed, the angular size of an average galaxy with redshift $z \approx 1$ amounts only to 1 arcsecond[2]. The luminosity

[2]Typically, 1 arcsecond, also written $1''$, is the size of the seeing disk of a ground-based image even in good conditions. Let us recall that the *seeing* is the blurring and twinkling of objects observed with a ground-based telescope. It is caused by a combination of temperature differences and turbulence in the Earth's atmosphere crossed by the light before reaching the mirror of the telescope.

of the nucleus completely drowns the stellar light and the object appears to us as an unresolved point. Only under good observing conditions can the host galaxies of QSOs be observed.

All host galaxies of QSOs which are strong radio emitters, i.e. *radio-loud* quasars, seem to be giant elliptical. It is less clear for QSOs which are not strong radio emitters, i.e. *radio-quiet* quasars: the distribution of luminosity of the host is better represented by an exponential law, typical of spiral galaxies. For AGN with a redshift larger than 1, it was quite rare to observe the host galaxy: the visible light we receive comes from the ultraviolet in the rest frame and most galaxies are weak in these bands. Moreover, at such redshifts, the luminosity contrast between the host and the nucleus is very large. But nowadays, more and more host galaxies are detected thanks to technological progress and its impact on the telescopes and their efficiency.

Let us mention that the distinction between Seyferts and quasars is also quite fuzzy. To make it easier, it has been decided that AGN with absolute magnitudes brighter than $M_v \sim -23$ are considered as QSOs, and fainter radio-quiet objects as Seyferts. Another distinction is often made: if the host galaxy is visible we talk about a Seyfert galaxy. If none is visible, we talk about a quasar. Let us insist on the fact that this last distinction depends mostly on the background level of the observed image and on the instrument performances but is somehow correlated to the luminosity of the object.

3.6 The Unified Model of AGN

In the 1980s, unified models of AGN were developed. Nowadays a standard theoretical model is generally accepted to explain the existence of the whole AGN family. It is simply called the *Unified Model* (see Fig. 3.5). The basic principle is the following: every type of AGN is the same phenomenon, at various luminosities, observed with different viewing angles, which, combined with the anisotropy of the AGN radiation and possible dust obscuration, can cause the apparent differences. Let us go a little bit further in this theory.

It is believed that matter falling into a *Super Massive Black Hole* (SMBH) of between 10^6 $M_\odot$ and 10^9 $M_\odot$ is responsible for the huge energy release of AGN. As the angular momentum must be conserved, the matter flattens into an accretion disk (see Fig. 3.6). This matter is heated by friction and becomes a plasma which emits a strong continuum in the optical, UV and X-ray bands. This radiation is responsible for the excitation of the layers surrounding the black hole. The energetic process at stake here is much more efficient than nuclear reactions occuring in stars: an AGN can be as bright as several galaxies. That is why we can observe such objects even if they are located very far away from our galaxy.

The accretion disk is surrounded by a region containing clouds of gas orbiting around the black hole. These clouds are responsible for the spectral lines observed in active galaxies, which are, of course, affected by the Doppler broadening as they orbit around the center. Moreover, the area around the black hole is divided in two different regions: the *broad-line region* (BLR), within the *torus* (see next paragraph), and the *narrow-line region* (NLR), further from the black hole, which may have the shape of a cone on each

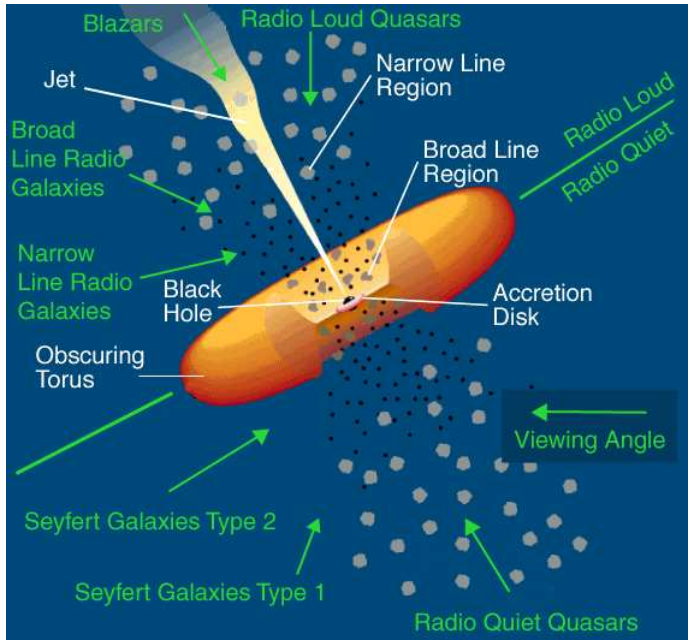

Figure 3.5: Schematic representation of an active galactic nucleus in the context of the Unified Model. The subcategory of classification of the AGN depends on the angle under which it is observed. Credit: M. Polletta, ITESRE/CNR, Bologna, Italy.

side of the accretion disk (see Fig. 3.5). Indeed, clouds with a shorter orbital radius move faster than clouds with a larger one. As a consequence, their velocity dispersion is larger and so is the broadening of their emission lines.

The *torus* is a region surrounding the fast clouds but located in the same plane as the accretion disk. It consists in a thick belt of gas and dust, with a diameter of about 10^4 Astronomical Units[3]. This region is opaque to visible or UV radiation.

The high density fast rotating clouds are visible only if the line of sight is situated along a cone around the axis of symmetry of the torus. The smaller the angle between the line of sight and the orbital plane, the less core emission reaches us because of the presence of the dust torus. When the broad-line region is observable, we are dealing with a QSO or a Type 1 Seyfert depending on the luminosity. If the line of sight is close to the dust torus plane as illustrated on Fig. 3.7), the broad-line region and the continuum are unobservable: we are in the presence of a Type II Seyfert or a Type II quasar, depending on the luminosity of the nucleus. However, a part of the continuum still reaches us. Indeed, some photons coming from the high density region can be polarize and scattered in our direction by free electrons orbiting outside the dusty and obscure zone: these photons broaden the wings of the narrow emission lines.

[3]An *Astronomical Unit* (AU) is the length of the semi-major axis of Earth's orbit around the Sun, i.e. 1 AU = 149 597 870 km.

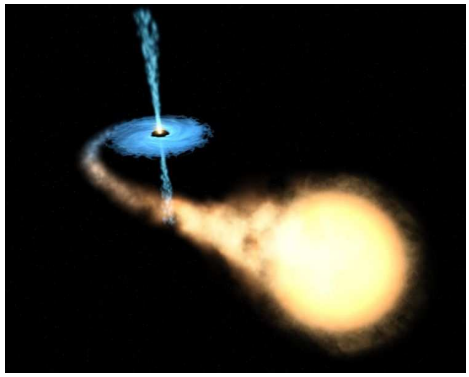

Figure 3.6: Artist view of a black hole accreting the external layers of a star. Credit: ESA, NASA and Felix Mirabel (French Atomic Energy Commission and Institute for Astronomy and Space Physics/Conicet of Argentina).

Perpendicular to the orbital plane and along the rotation axis, some particles may be accelerated by a magnetic field to velocities close to the speed of light, as already explained above. These relativistic particles form very long and thin jets responsible for the radio emission of some active galaxies. When these particles encounter some matter they are decelerated and we can observe *radio lobes*. In such a case the AGN is *radio-loud*. On the contrary, if no jets are observable, the AGN is *radio-quiet*. The reasons for the presence or absence of jets are still obscure.

In blazars a jet is pointing towards us and only a region with a small radius is observable. In radio galaxies, the line of sight does not pass right down the jets but they are seen sideways. It is obvious thus why blazars are much less frequent than radio galaxies. Here also we can distinguish between NLRG and BLRG, respectively *narrow-line* and *broad-line radio galaxies*.

Let us look deeper into what really causes the AGN phenomenon, as first suggested by a British scientist, Donald Lynden-Bell, in 1969: supermassive black holes. To produce a luminosity typical of that of a quasar, i.e. 10^{40} W, a SMBH would have to consume a quantity of matter equivalent to 10 stars like the Sun per year. For the brightest specimens this amount increases to 100 $M_{\odot}$. It is very likely that active nuclei turn off and on, depending on their surroundings. That suggests that, when a quasar has consumed all the matter in its sphere of influence, it will become an invisible object and its host an ordinary galaxy. That explains the absence of nearby AGN and why they appear to have been much more common in the early Universe. That also means that most galaxies, including ours, could have gone through an active stage. They would be quiet now because the SMBH would not be accreting significant amounts of matter anymore. But if a galaxy with a quiet supermassive black hole enters in collision with another galaxy, some fresh material can enter the sphere of influence of the black hole and the quiet galaxy can turn back to the state of AGN. There may even be a connection between the brightness of an active galactic nucleus and the time since it was last gravitationally disturbed.

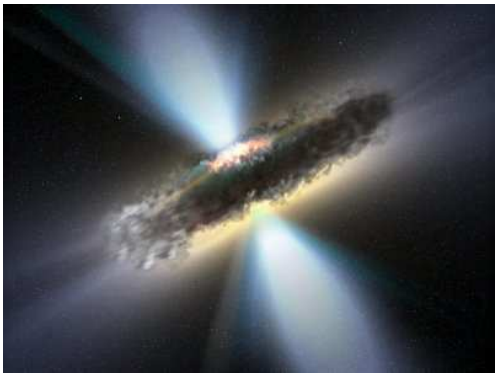

Figure 3.7: This artist illustration shows the thick dust torus surrounding a supermassive black hole. As the line of sight is in the plane of the torus, most of the light emitted by the accretion disk and the BLR is blocked from our view. Credit: ESA/V.Beckmann (NASA-GSFC).

To end this section it is worth mentioning several important dark zones in the understanding of AGN. First of all the physics in accretion disks is not fully understood. Then it is not really known why some AGN are active and others are not, and exactly which processes are responsible for that. Finally the origin of such black holes is quite unclear. Stars massive enough to collapse and give birth to such objects have never been observed. However, it could be the result of a massive star that would have collapsed into a black hole, then the latter, merging with other such black holes, would have become larger and larger to finally form a supermassive black hole.

3.7 Some properties of quasars

Nowadays, more than 60 000 quasars are known. The redshifts extracted from their spectra range from 0.06 to 6.43 (CFHQS J2329-0301, Willott et al., 2007). That means that quasars are located at distances from 240 Mpc (780×10^6 light years) to around 4 Gpc (13×10^9 light years). It is not astonishing that they represent, to the eyes of the astrophysicists, a fascinating tool to probe the past of our Universe.

The galaxies containing the brightest quasars, usually called *host galaxies of quasars*, are often found to be early-type galaxies.

As quasars, though located far away from us, are observable, they have to be very bright. In fact they appear to be the most luminous objects known to date. Their luminosity can reach 10^{12} $L_\odot$. The quasar with the brightest apparent magnitude is 3C 273 in the constellation of Virgo. Its average apparent magnitude is 12.8 and its absolute magnitude is -26.7. It means that, located at a distance of 10 pc, 3C 273 would almost shine like the Sun. This quasar is about 100 times more luminous than average galaxies such as the Milky Way.

A quasar spectrum presents an intense continuum from the X-ray to the IR range. In the optical and UV bands it shows narrow and broad emission lines. It was also pointed

out that their spectrum is non-thermal: their emission law does not follow Planck's Law for black bodies. A typical spectrum of a Type 1 quasar is shown on Fig. 3.8.

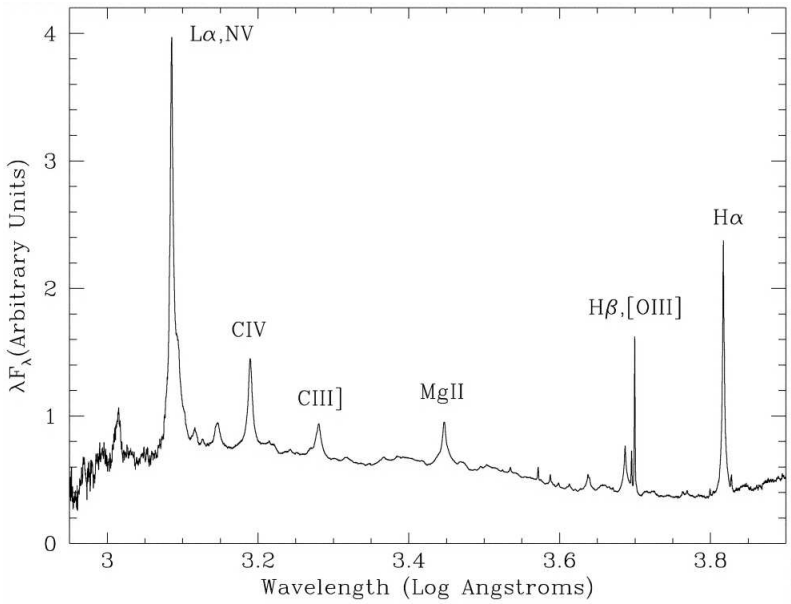

Figure 3.8: Typical spectrum of a Type 1 quasar. At short wavelengths, i.e. on the bluer side of the spectrum, the continuum is more intense. The emission lines H_α and H_β correspond to the redshifted lines of hydrogen from the Balmer serie[4]. We can see that they are broad compared to the narrow [OIII] emission line. Credit: Brotherton et al. (2001).

[4]The *Balmer serie* is a serie of emission or absorption lines in the visible spectrum of light due to the presence of hydrogen. Four wavelengths are observed: they are due to transitions between the second (or first excited) state and higher energy states of the hydrogen atom.

The shortest distance between two points is under construction.

Noelie Altito

4 Strong gravitational lensing

Contents

4.1 Introduction

This theoretical section is inspired by Schneider, Ehlers & Falco (1992), Binney & Merrifield (1998), Courbin (1999), Burud (2001), Courbin & Minniti (2002) and Eigenbrod (2008).

Another point making AGN so interesting for the scientific community is a phenomenon called *gravitational lensing*. Basically it is the bending of light rays coming from a distant bright source, such as a quasar, by a foreground object called *the lens* which creates a gravitational potential well (see Fig. 4.1). The distorted and sometimes multiple images of such a distant source can be used to infer, amongst others, the total mass distribution of the lens through its gravitational potential and to estimate its

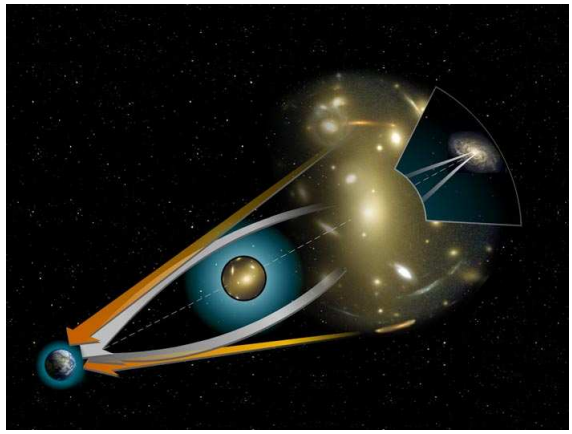

Figure 4.1: Illustration of the gravitational lensing phenomenon: the rays of light coming from a distant source are bent in the vicinity of a massive object. The white arrows show the path of the light coming from the true source. In general several images of the source are observed in directions corresponding to the tangents of the real light rays, as shown by the orange arrows. Credit: NASA/ESA.

amount of dark matter. Lensing can also be used as a *gravitational telescope*: a lens magnifies the total amount of light received from very faint and distant background objects, making them appear brighter (it is called the *magnification effect*, see Sect. 4.5 for further information) and therefore more easily observable. Let us notice that gravitational lensing is not restricted to optical wavelengths and acts equally on all kinds of radiation: it is achromatic.

There are three classes of lensing:

1. *Strong lensing*: the distortions are particularly obvious. Also called *macrolensing*, it occurs when, e.g. a quasar is lensed and multiply imaged by a foreground galaxy. Arcs, arclets and Einstein rings, i.e. very distorted images of the background object, can be observed under certain circumstances (see Sect. 4.4). However, the effects are small: a galaxy of 10^{11} $M_\odot$ will produce multiple images separated by at most a few arcseconds while galaxy clusters can produce separations of several arcminutes.

2. *Weak lensing*: the distortions of the background objects are much smaller. They can be inferred only statistically, when considering a large sample of objects. Indeed, the distortions can be seen as a stretching in a preferred direction, perpendicular to the line joining the distorted object to the center of the lensing system. For example it occurs when galaxies are lensed by a foreground galaxy cluster. In studying the distribution of distortions we can measure the shear (see Sect. 4.5) of the lensing field in any region and obtain an estimate of the mass distribution in the cluster.

3. *Microlensing*: no distortion in shape is observable but the observed flux of the

lensed object varies in time. For example it occurs when a star of our galaxy gets aligned with a massive and sufficiently compact foreground object, e.g. another star: two distorted unresolved images of the background star are created, the separation being typically of the order of the microarcsecond. That results in an observable magnification. As the source, the lens and the observer move relative to each other, the configuration changes in time and so does the magnification. Galactic microlensing is very useful to detect compact halo objects in the Milky Way or extrasolar planets. This phenomenon can also occur at cosmological scales: when a quasar is lensed by a galaxy, the stars in the lensing galaxy itself may cross the rays forming the lensed images of the quasar.

In the following sections we will concentrate on the topic under investigation in this work: multiply imaged quasars, in the strong lensing regime.

4.2 A small piece of History

The first writings about the bending of light rays by a massive object go back to 1804 when Johann Soldner, a German geodesist, mathematician and astronomer working at the Berlin Observatory, wrote an article entitled "*On the deflection of a light ray from its straight motion due to the attraction of a world body which it passes closely*". He estimated, in a Newtonian context, the deflection angle of a light ray passing close to the solar limb to $0.84''$. But before him, in the 18^{th} century, Isaac Newton had already thought about that phenomenon when he wondered "*Do not bodies act upon light at a distance, and by their action bend its rays; and is not this action strongest at the least distance?*", but without finding a way to prove its existence or validity.

In a paper of 1911, Albert Einstein discussed the influence of gravity on the propagation of light. He knew nothing about the work of Soldner, one century earlier. But at the beginning of the 20th century, the Theory of General Relativity was incomplete and he calculated, for a star in the solar limb, the same deflection angle as Soldner estimated in the Newtonian context. Renn, Sauer & Stachel (1997), in reconstructing some of Einstein's research notes, discovered that he derived the lens equation, the possibility of a doubly imaged object and the magnification of lensed images already in 1912. He finally obtained the right expression of the deflection angle when he completed his General Theory of Relativity in 1916.

The deflection angle $\hat{\alpha}$ of a light ray passing at a minimum distance ξ, also called the *impact parameter*, of a point-like object of mass M is expressed as follows:

$$\hat{\alpha}(\xi) = \frac{4GM}{c^2}\frac{1}{\xi} \tag{4.1}$$

where G is the constant of gravity[1] and c the speed of light. This is equal to twice the Newtonian value, which reflects the spatial curvature. With the solar values for the radius and mass, Einstein obtained $\hat{\alpha}_\odot \approx 1.75''$ for a light ray passing at the solar limb.

[1] $G = (6.67428 \pm 0.00067) \times 10^{-11}$ m^3 kg^{-1} s^{-2}

In 1919, this theory was confirmed by Arthur Stanley Eddington and his group who observed for the first time the apparent displacement of the position of a star close to the solar limb during a total solar eclipse (see Fig. 4.2). These results were published by Dyson, Eddington & Davidson (1920). In spite of the poor precision of the measurements, the obtained deflection could only be explained in the context of a relativistic theory for the gravitation.

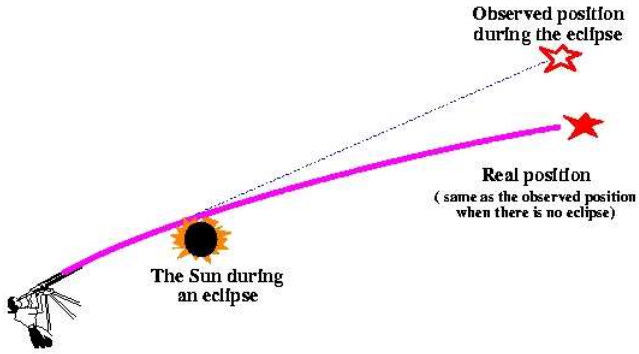

Figure 4.2: Bending of light rays coming from a star and passing through the solar limb during a total eclipse of the Sun. Credit: Jose Wudka.

Fritz Zwicky was the first to consider the case of galaxies acting as lenses in 1937. His calculations showed that this phenomenon was within the reach of observations as the probability that it could occur was of the order of 10%. Then, in the 1960's, the first quasars were discovered. A scientist called Barnothy was the first to connect them with lensing in 1965. But it was not until 1979 that the first lensed quasar, Q0957+561, was discovered by Walsh et al. They noticed that two apparently distinct quasars, separated by $6''$, had nearly identical spectra and could be two images of the same object. Later, the lensing galaxy was identified and the lensed nature of this system firmly established.

4.3 The lens equation

In the case of an extended gravitational lens, the deflection angle is not given by Eq. 4.1 anymore, which is only correct for point mass lenses. Actually, every infinitesimal mass element of the lens must be taken into account. The key is now to find a general expression for the *lens equation*, also called the *ray-trace equation*.

To give the expression of the deflection angle we must first describe the general context we work in. Most of the time, the typical distances involved in the geometrical configuration of a lensed system, such as the distance to the source, to the lens and between the lens and the source, are much larger than the size of the lensing galaxy. As a consequence, we work in the *thin lens approximation*, which means that all the deflecting matter is considered as contained in a mass sheet perpendicular to the observer-lens direction. As a consequence, the lens is located at a single distance from the observer

(and from the source). That is why we always consider a lens plane, an observer plane and a source plane as illustrated on Fig. 4.3. On the latter, O stands for *observer*, L for *lens*, S for *source* and I for *image*. D_L is the distance between the observer and the lens, D_S between the observer and the source and D_{LS} between the lens and the source. Let us note that, for cosmological distances, $D_S \neq D_L + D_{LS}$. We also define several angles from the observer point of view: α is the angle between the source and its lensed image, β is the angle between the observer-lens axis, also called *optical axis* by analogy with an optical system, and the position of the unlensed object, meaning that we would observe the source at a position β in the absence of a lens, and θ is the angle between the optical axis and the position of the lensed image. $\hat{\alpha}$ is not defined from the observer point of view: it is the deflection angle, i.e. the angle between the original source and the lensed image, from the intersection between the lens plane and the observer-image direction. Finally the impact parameter ξ is the distance, in the lens plane, from the light ray to the optical axis and η is the distance, in the source plane, between the unlensed object and the optical axis.

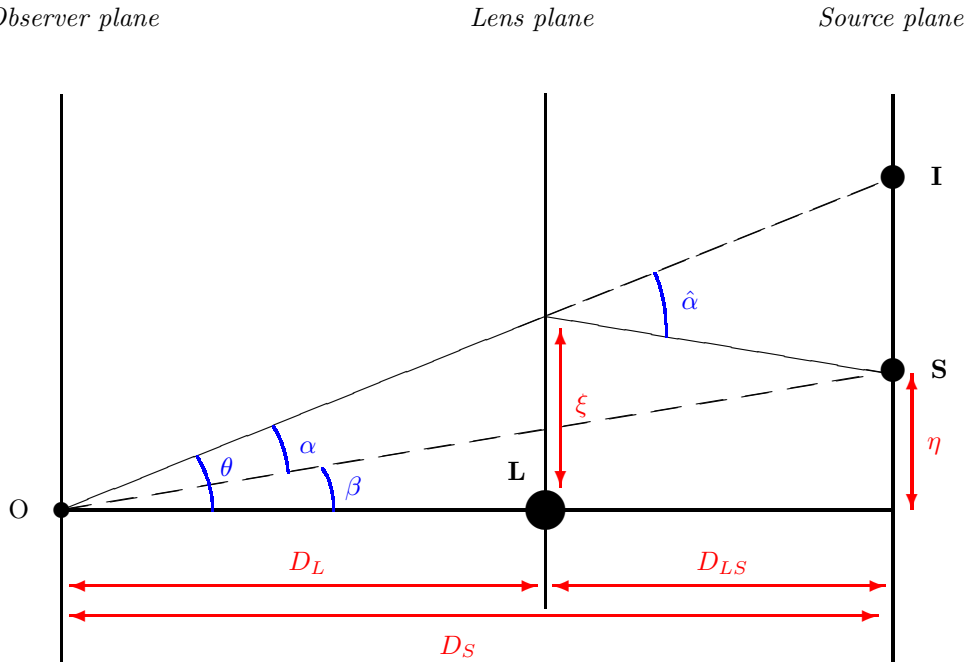

Figure 4.3: Diagram of the gravitational lens phenomenon assuming the lensing galaxy L bends the light of a background source S. As a consequence the observer O detects a lensed image I of the source. The line passing through L and O is called the *optical axis* by analogy with an optical system.

The deflection angle $\hat{\alpha}$ for a lens with circular symmetry is given by:

$$\hat{\alpha}\left(\xi\right) = \frac{4GM\left(\xi\right)}{c^2}\frac{1}{\xi} \tag{4.2}$$

where $M\left(\xi\right)$ is the mass contained in the radius ξ. A simplifying and reasonable hypothesis is to consider that the angles involved are very small: θ, β, $\hat{\alpha} \ll 1$. In using formulae from basic trigonometry, it is easy to obtain the following equation:

$$\theta D_S = \beta D_S \ + \hat{\alpha} D_{LS}. \tag{4.3}$$

The reduced deflection angle $\alpha\left(\theta\right)$ can be written as:

$$\alpha\left(\theta\right) = \frac{D_{LS}}{D_S}\ \hat{\alpha}\left(\xi\right). \tag{4.4}$$

Eq. 4.3 then becomes:

$$\beta = \theta \ - \alpha\left(\theta\right). \tag{4.5}$$

As the observer has no direct access to the source, the observable is θ and not α. If the mass distribution of the lens is not symmetric, Eq. 4.5 becomes vectorial:

$$\boldsymbol{\beta} = \boldsymbol{\theta} \ - \boldsymbol{\alpha}\left(\boldsymbol{\theta}\right). \tag{4.6}$$

In the thin lens approximation, the deflection caused by any lens can be calculated in adding the contributions from every point mass contained in the lens plane. If we consider a two-dimensional vector $\boldsymbol{\xi} = (\xi_x, \xi_y)$ in the lens plane, we obtain the following expression:

$$\hat{\boldsymbol{\alpha}}(\boldsymbol{\xi}) = \frac{4G}{c^2}\int\int \frac{\Sigma(\boldsymbol{\xi'})(\boldsymbol{\xi} - \boldsymbol{\xi'})}{|\boldsymbol{\xi} - \boldsymbol{\xi'}|^2}\ d\boldsymbol{\xi'} \tag{4.7}$$

where $\Sigma(\boldsymbol{\xi})$ is the surface mass density at position $\boldsymbol{\xi}$. As $\boldsymbol{\xi} = D_L\boldsymbol{\theta}$, we can write the reduced deflection angle as:

$$\boldsymbol{\alpha}(\boldsymbol{\theta}) = \frac{D_{LS}}{D_S}\hat{\boldsymbol{\alpha}}(D_L\boldsymbol{\theta}) = \frac{4G}{c^2}\frac{D_L D_{LS}}{D_S}\int\int \frac{\Sigma(\boldsymbol{\theta'})(\boldsymbol{\theta} - \boldsymbol{\theta'})}{|\boldsymbol{\theta} - \boldsymbol{\theta'}|^2}\ d\boldsymbol{\theta'}. \tag{4.8}$$

For a finite circular lens with constant surface mass density Σ, we obtain:

$$\alpha\left(\theta\right) = \frac{4\pi G\Sigma}{c^2}\frac{D_L D_{LS}}{D_S}\ \theta. \tag{4.9}$$

Let us define the critical surface mass density:

$$\Sigma_{cr} = \frac{c^2}{4\pi G}\frac{D_S}{D_{LS}D_L}\ . \tag{4.10}$$

Eq. 4.7 finally becomes:

$$\alpha\left(\theta\right) = \frac{\Sigma}{\Sigma_{cr}}\ \theta = \kappa\ \theta. \tag{4.11}$$

where κ is called *the convergence*. For general mass distributions, κ depends on $\boldsymbol{\theta}$ and some multiple images are produced if $\Sigma \geq \Sigma_{cr}$, i.e. $\kappa \geq 1$. In short, the challenge is to solve Eq. 4.11. Two situations can occur:

- for a given mass distribution, we want to know the configuration of the images of a background source;
- we try to find which mass distribution can be responsible for an observed configuration of lensed images.

Finally let us define a two-dimensional deflection potential $\hat{\psi}$, which verifies $\hat{\boldsymbol{\alpha}} = \boldsymbol{\nabla}\hat{\psi}$:

$$\hat{\psi}(\boldsymbol{\xi}) = \frac{4G}{c^2} \int\int \Sigma(\boldsymbol{\xi'})\ ln|\boldsymbol{\xi} - \boldsymbol{\xi'}|\ d\boldsymbol{\xi'}. \tag{4.12}$$

This potential is related to the convergence of the lens by the Poisson equation:

$$\boldsymbol{\nabla}^2\hat{\psi}(\boldsymbol{\xi}) = 2\kappa(\boldsymbol{\xi}). \tag{4.13}$$

Here again, we can define a reduced potential ψ which will depend on θ and with $\boldsymbol{\alpha} = \boldsymbol{\nabla}\psi$:

$$\psi(\boldsymbol{\theta}) = \frac{1}{\pi} \int\int \kappa(\boldsymbol{\theta'})\ ln|\boldsymbol{\theta} - \boldsymbol{\theta'}|\ d\boldsymbol{\theta}. \tag{4.14}$$

The general lens equation (see Eq. 4.6) can finally be expressed as follows:

$$\boldsymbol{\beta} = \boldsymbol{\theta} - \boldsymbol{\nabla}\psi(\boldsymbol{\theta}). \tag{4.15}$$

4.4 Einstein rings

Unlike an optical lens, a gravitational one has no single focal point. As a consequence, in the case of a circularly symmetric lens, if the observer, the massive lens and the background object are aligned, the latter will appear as a perfect ring surrounding the lens (see Fig. 4.4 for an example). This phenomenon was first mentioned by Chwolson in 1924 but then quantified by Einstein in 1936. That is why it is called an *Einstein ring*.

In such a case, $\boldsymbol{\beta}$ is equal to 0 and the lens equation (Eq. 4.6) is simplified and becomes scalar:

$$\theta_E = \alpha\left(\theta_E\right) = \hat{\alpha}\left(\xi_E\right)\frac{D_{LS}}{D_S} \tag{4.16}$$

where θ_E is the angular radius of the Einstein ring and ξ_E the corresponding impact parameter. Introducing the expression of the deflection angle for a point mass lens given in Eq. 4.1 and $\xi_E = D_L\theta_E$, the previous equation can also be written as follows:

$$\theta_E = \sqrt{\frac{4GM}{c^2}\frac{D_{LS}}{D_L D_S}}. \tag{4.17}$$

This can lead to the measurement of the mass of the lens inside the Einstein radius. For an axisymmetric mass distribution, the mean surface mass density inside θ_E is:

$$\Sigma(\theta_E) = \frac{M}{\pi\ (D_L\theta_E)^2} \tag{4.18}$$

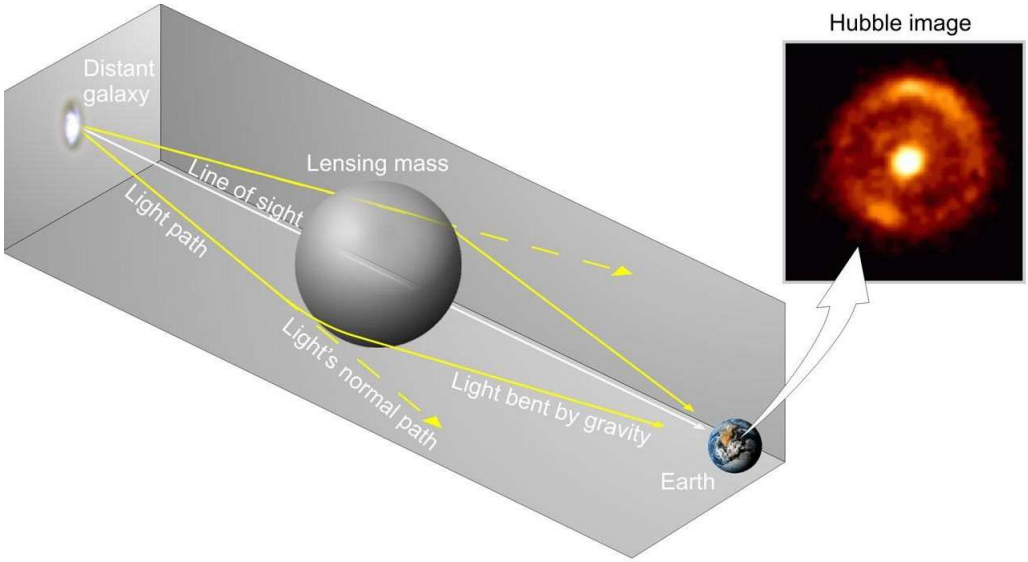

Figure 4.4: Illustration of the Einstein ring phenomenon and the necessary conditions to observe it. The image of the Einstein ring of B1938+666 was obtained with NICMOS or *Near Infrared Camera and Multi-Object Spectrometer* on board the Hubble Space Telescope, in 1998. Credit: L. J. King (University of Manchester).

which is exactly equal to Σ_{cr}. The mass inside θ_E can thus be expressed as follows:

$$M(\theta_E) = \Sigma_{cr}\pi \ (D_L\theta_E)^2 \tag{4.19}$$

where D_L and θ_E are observable.

In the case that interests us, the background source cannot be considered as a point source: it is indeed a quasar with a host galaxy, which has a certain spatial extension depending on the wavelength of observation. The radio lobes of the quasar being more extended, Einstein rings are more often observed at radio wavelengths. They can be complete or partial, depending on the configuration of the system and how the source, lens and observer are aligned. At very high resolution it is even possible to resolve details of it and to reconstruct the original source.

Let us note that in most cases the lensing galaxy is not located on the line-of-sight to the source, which creates a number of images according to the potential of the lens and the relative positions of the observer, the lens and the source. Even in that case, it is still possible to obtain constraints on the mass of the lens.

4.5 Magnification

When light emitted by a background source is bent by a lens, the flux received is amplified or deamplified compared to the one that we would observe if no lens were

present: gravitational lensing conserves the surface brightness of a source but not the solid angle under which the object is observed. That is why a lensed image of a source can be brighter than the source itself.

The magnification factor μ, i.e. the amplification of the image brightness compared to the one of the source, is thus equal to the ratio between the surface of the image and the surface of the source. For a circularly symmetric lens, it can be written as:

$$\mu = \frac{\theta d\theta}{\beta d\beta}. \tag{4.20}$$

For a point mass lens, Eq. 4.3 is a second degree equation and thus easy to solve. Combining it with Eqs. 4.1 and 4.17, we obtain:

$$\theta^2 - \beta\theta - \theta_E^2 = 0\,. \tag{4.21}$$

This equation has two solutions with opposite signs:

$$\theta_\pm = \frac{1}{2}\left(\beta \pm \sqrt{\beta^2 + 4\theta_E^2}\right). \tag{4.22}$$

Differentiating Eq. 4.22 and taking Eq. 4.20 into account, we obtain the expression of the magnification for each image:

$$\mu_\pm = \frac{1}{4}\left[\frac{\sqrt{\beta^2 + 4\theta_E^2}}{\beta} \;+\; \frac{\beta}{\sqrt{\beta^2 + 4\theta_E^2}} \;\pm\; 2\right]. \tag{4.23}$$

Let us introduce the impact parameter u which is defined as the angular separation between the source and the lens in units of angular radius of the corresponding Einstein ring, i.e. $u = \beta/\theta_E$. Eq. 4.23 then becomes:

$$\mu_\pm = \frac{u^2 + 2}{2u\sqrt{u^2 + 4}} \;\pm\; \frac{1}{2}\,. \tag{4.24}$$

The total flux magnification is obtained in adding the absolute values of the magnification of the two images:

$$\mu = |\mu_+| + |\mu_-| = \frac{u^2 + 2}{u\sqrt{u^2 + 4}}\,. \tag{4.25}$$

In the case of an unspecified mass distribution, μ is expressed as follows:

$$\mu(\boldsymbol{\theta}) = \left[\det\frac{\partial\boldsymbol{\beta}(\boldsymbol{\theta})}{\partial\boldsymbol{\theta}}\right]^{-1} = \frac{1}{(1-\kappa)^2 - \gamma^2}\,. \tag{4.26}$$

where κ is called the *convergence* as aforementioned and γ the *shear*. The images are distorted both in size and shape: the term involving the convergence magnifies the image by isotropically increasing its size while conserving surface brightness and the term involving the shear, i.e. the tidal gravitational field, not only acts as the convergence but also stretches the image tangentially around the lens. Let us note that

any galaxy located along the line of sight or in the environment of the lens will create a distortion in the lensed images through a tidal gravitational field. It is called the *external shear* and it has to be taken into account in the modeling of the lensed system. We define the total shear γ as:

$$\gamma = \gamma_{int} + \gamma_{ext} \tag{4.27}$$

where γ_{int} is due to the main lensing galaxy, and where γ_{ext} is due to the environment of the lens. Fig. 4.5 illustrates the effect of the convergence and the shear on a circularly symmetric source.

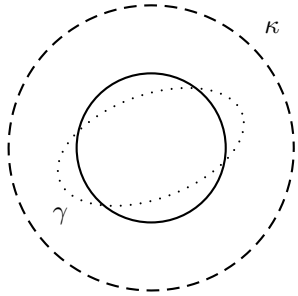

Figure 4.5: Effects of the convergence κ (dashed lines) and the shear γ (dotted lines) on a circularly symmetric source (solid line).

As expressed by Eq. 4.26, the magnification factor is the inverse of the Jacobian of the lens mapping ($\boldsymbol{\theta} \rightarrow \boldsymbol{\beta}$). But, as the unlensed source is not observable, its intrinsic properties are unknown and so is the magnification factor. However, the flux ratios of different images can be measured and then used to model the lensed system (see hereafter). Of course, to obtain the magnification of an extended source, Eq. 4.26 must be integrated over the source.

4.6 Time delays

A strong lens produces several images of the same background object. So the light reaching Earth has followed different paths and there is a delay between the arrival times of photons emitted simultaneously but having borrowed different ways. Assuming the source, in our case a quasar, is sufficiently variable, a long-term photometric monitoring allows to obtain the light curves of the lensed images, i.e. the magnitude of each lensed image in function of time. These light curves, as they come from images of the same source, should be identical apart from a shift in time, called the *time delay*, and a shift in magnitude caused by the magnification factor.

The arrival time τ, which is the light travel time, can be expressed as follows (to know how it is derived, see e.g. Narayan & Bartelmann (1996)):

$$\tau(\boldsymbol{\theta}) = \frac{1}{2}(\boldsymbol{\theta} - \boldsymbol{\beta})^2 - \psi(\boldsymbol{\theta}), \tag{4.28}$$

one of its properties being:

$$\boldsymbol{\nabla}\tau(\boldsymbol{\theta}) = 0 \tag{4.29}$$

which leads to the lens equation:

$$\boldsymbol{\beta} = \boldsymbol{\theta} - \boldsymbol{\nabla}\psi(\boldsymbol{\theta}). \tag{4.30}$$

According to that property, the lensed images will only occur at stationary points of the arrival time $\tau(\boldsymbol{\theta})$. This is in fact called the *Fermat's Principle* which states that the optical path length must be stationary, i.e. minimal, maximal or a saddle point[2]. Let us note that the arrival time, as a function of the image positions, defines a two-dimensional surface called the *arrival-time surface*.

There are two contributions to $\tau(\boldsymbol{\theta})$. The first one is the obvious geometrical contribution, due to the difference in optical length between the different paths:

$$\tau_{geom}(\boldsymbol{\theta}) = \frac{1}{2c}(1+z_L)\frac{D_L D_S}{D_{LS}}(\boldsymbol{\theta}-\boldsymbol{\beta})^2 \tag{4.31}$$

where z_L is the redshift of the lens. The second contribution is relativistic and is due to the so-called *Shapiro effect*. It occurs when light rays are under the influence of different gravitational potentials: the stronger the potential, the more the light will be slowed down. It is exactly what happens to light emitted by a quasar and passing near a galaxy: different rays travel through different parts of the potential well. Here is the expression of this potential contribution to the arrival time:

$$\tau_{Shap}(\boldsymbol{\theta}) = -\frac{1}{c}(1+z_L)\ \hat{\psi}(\boldsymbol{\xi}) + C \tag{4.32}$$

where C is a constant. The total arrival time can thus be expressed as follows:

$$\tau_{tot}(\boldsymbol{\theta}) = \frac{1}{c}(1+z_L)\frac{D_L D_S}{D_{LS}}\left\{(\frac{1}{2}\boldsymbol{\theta}-\boldsymbol{\beta})^2 - \psi(\boldsymbol{\theta})\right\} + C. \tag{4.33}$$

The difference in propagation times associated with an image pair, A and B:

$$\Delta t_{AB} = \tau_B - \tau_A = \frac{1+z_L}{c}\frac{D_L D_S}{D_{LS}}\left((\boldsymbol{\theta}_B-\boldsymbol{\beta})^2 - (\boldsymbol{\theta}_A-\boldsymbol{\beta})^2 - \psi(\boldsymbol{\theta}_B) + \psi(\boldsymbol{\theta}_A)\right). \tag{4.34}$$

Δt_{AB} is called the *time delay* between image A and image B and is measurable. Let us note that in most publications another convention is adopted: $\Delta t_{AB} = t_A - t_B$.

As the Universe is expanding and might even have a non-zero curvature, the notion of distance is not uniquely defined, as it is the case in a Newtonian context. There are thus several definitions all based on quantities that are supposed to be observable such as the apparent luminosity or the angular size of an object on the sky. The distances at stake in Eq. 4.34 are different from our intuitive comprehension of the notion of distance and are defined as follows:

$$D_A = \frac{R_T}{\delta}, \tag{4.35}$$

[2]A *saddle point* is also called *point of inflexion*. It is a point of a function or surface which is not extremal but still stationary.

where R_T is the tranverse size of the object and δ its angular size as viewed from the Earth. D_A is called the *angular diameter distance*. It is a good indicator of the distance of an object when it emitted the light that we now receive. It can also be expressed in terms of the comoving distance D_M, if the source is located at a redshift z:

$$D_A(z) = \frac{D_M}{1+z}. \tag{4.36}$$

Let us recall that the comoving distance between two events is the current proper distance between them: the distance measured on a hypersurface of constant proper time, i.e. the distance measured in a coordinate system where these events are simultaneous. It tells us where the objects of interest are now rather than where they were when they emitted the light that we observe.

The angular diameter distance D_{ij} of an object j located at a redshift z_j and measured by an observer i located at a redshift z_i can be expressed as follows:

$$D_{ij} = \frac{2c}{H_0} \frac{(1-2q_0)(G_i - G_j) + (G_i G_j^2 - G_i^2 G_j)}{(2q_0)^2(1+z_i)(1+z_j)^2} \tag{4.37}$$

with

$$G_i = \sqrt{1+2q_0 z_i}\ , \tag{4.38}$$

q_0 being the current deceleration parameter (negative in the Concordance Model). As D_{ij} is inversely proportional to H_0, so is the time delay Δt_{AB}. In resolving the lens equation, knowing the source and lens redshifts and the time delay between the lensed images, it is thus possible to estimate H_0. Let us recall that this method has first been proposed by Refsdal (1964).

4.7 Properties of images

Eq. 4.26 can lead to further considerations about the lensed images. The determinant in the expression of μ can have either sign. If it is positive, the image is said to have a *positive parity*. If it is negative, the image has a *negative parity*: it is mirror inverted compared to the original source. If the determinant is equal to zero, μ diverges. That does not mean that the magnification factor is infinite. Indeed, real sources are extended: the magnification is thus the weighted mean of μ over the whole source and it is then finite. Moreover, we are working in the symplifying hypothesis of optical geometry. In taking into account the wave effects, the magnification factor is finite even in the case of a point-like source.

Images only occur at stationnary points of the arrival time surface $\tau(\boldsymbol{\theta})$, as explained above. Three types of image with different properties are thus possible:

- maximum, i.e. $(1-\kappa)^2 > \gamma^2$ and $\kappa > 1$ thus $\mu > 0$, positive parity and the largest time delay;
- minimum, i.e. $\gamma < 1-\kappa \leq 1$ thus $\kappa < 1$ and $\mu \geq 1$, positive parity and the smallest time delay;

- saddle point, i.e. $(1-\kappa)^2 < \gamma^2$ thus $\mu < 1$, and negative parity.

For example, in a doubly lensed quasar, the image outside the ring defined by the Einstein radius associated to the main lens is a minimum and has a positive parity while the one inside is a saddle point with a negative parity.

We can now highlight some special parts of the image plane and lens plane. In the first one, the *critical curves* are composed of points where the magnification $\mu(\boldsymbol{\theta})$ diverges. They thus separate regions with minima, saddle points and maxima. These curves are closed and smooth. If we map them back to the source plane, we obtain the *caustic curves* or simply *caustics*. These notions, illustrated on Fig. 4.6, are very helpful to qualitatively understand the deflection mapping. If a source crosses a caustic, a pair of images, one with a positive parity, the other one with a negative parity, either appears or disappears, depending on the direction of the crossing. Moreover, an image near a caustic is highly amplified and distorted. Caustics are not necessarily smooth and can be composed of stable singularities called *cusps*. At these points, three images merge into one unique extended image. The smooth parts of a caustic are called *folds*.

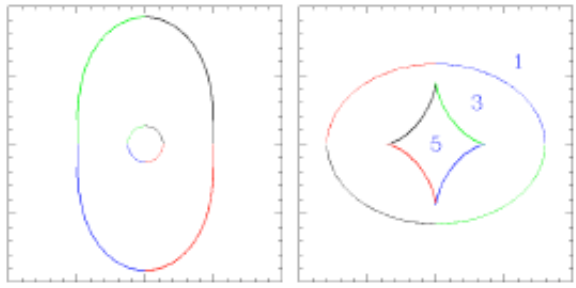

Figure 4.6: *Left*: critical cruves for an elliptical lens. *Right*: corresponding caustics and number of observed images. The inner caustic is called *astroid caustic* while the outer one is called *radial caustic*. When the source crosses one of them, the number of images change. The inner caustic corresponds to the outer critical curve and vice-versa. Credit: taken from the PhD thesis of C. Vuissoz (EPFL/LASTRO).

The number of images is thus not random and obeys to a law called the *odd-number theorem*. It states that "*Any transparent mass distribution with finite total mass and with a weak gravitational field produces an odd number of images*" (Burke, 1981), if the source is not located on a caustic. Fig. 4.7 shows different image configurations according to the location of the source relative to the folds and cusps of the caustics. In reality, we never observe an odd number of lensed images: we only observe quads and doubles. Indeed, the third or fifth image, which is always a maximum of the arrival time surface, is highly demagnified and mixed with the main lensing galaxy. Beyond four images, we observe arcs and rings.

Another interesting property, established by Schneider (1984), states that amongst lensed images, one has always a positive parity with $\mu \geq 1$, so one image will always be at least as bright as the original source.

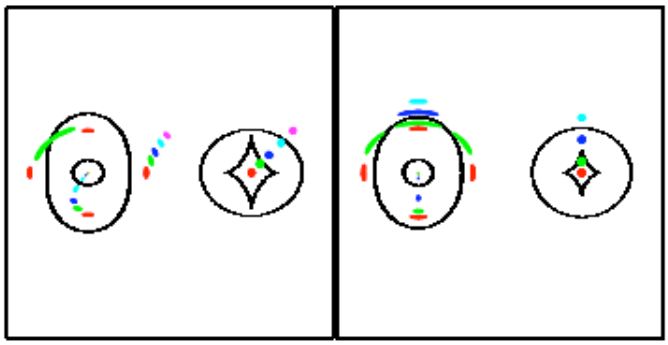

Figure 4.7: Illustration of different image configurations. *Left*: when the source crosses the fold of a caustic. *Right*: when the source crosses the cusp of a caustic. The right part of each cartoon shows the position of the source relative to the caustics while the left part shows the resulting image configuration and the critical curves. Images outside the two critical curves correspond to minima of the arrival time while images between the two critical curves are saddle points and images inside the inner critical curve are maxima. Credit: Narayan & Bartelmann (1996).

4.8 Lens modeling

4.8.1 Introduction

Most of the applications of gravitational lensing require the modeling of the lensed system under investigation. The measurement of H_0 from lensed quasars is amongst them and that is why we review the main mass distributions. In Sect. 4.8.2, mainly inspired by Keeton (2001a), we present some parametric models, while Sect. 4.8.3 gives an overview of the non-parametric modeling.

To model strong lenses, several observational constraints are necessary (the more, the better...). For a N-times imaged source, we have:

- 2(N-1) independent constraints from the image positions,
- 2 more constraints from the position of the main lens,
- N-1 constraints from the flux ratios,
- N-1 constraints from the time delays;

for a total of 4N-2 constraints. Sometimes, the flux ratios cannot be used e.g. because of microlensing effects caused by stars in the lens. Moreover, if H_0 is not held fixed, we lose one time delay as a constraint, which makes a total of 4N-3 constraints at most. For quads, this number seems quite reasonable while it seems little for doubles (5 constraints at most). Sometimes, the ellipticity and effective radius can be constrained by observation, if we assume that the total mass distribution follows the light distribution.

In any case, there is a problem: different models can reproduce the exact same observed configuration. This is called the *mass-sheet degeneracy* (Falco, Gorenstein & Shapiro, 1985): there exists a special transformation of the mass distribution that leaves unchanged the image positions and flux ratios. The transformation is the following:

$$\kappa_\lambda(\boldsymbol{\theta}) = (1-\lambda) + \lambda\ \kappa(\boldsymbol{\theta}) \tag{4.39}$$

where λ is a parameter and $\kappa(\boldsymbol{\theta})$ is a good fit to the different observational constraints. The first term consists in adding a sheet of constant mass density to the actual mass distribution while the second term consists in rescaling the actual mass distribution. For any κ_λ, the lens equation has the same form as for κ and the previous equation also gives a good fit to the constraints: there is no mean to decide between one or the other of these models. This transformation has three consequences: it moves the estimated position of the original source, which is undetectable, it scales the magnification factor, which is also undetectable because only the flux ratios are measurable, and finally it scales the value of H_0 through a change in the time delays, which is a real problem when trying to estimate H_0. But if H_0 is known from an independent technique, we can determine the absolute surface mass density and then the mass-sheet degeneracy is broken. Another possibility is to constrain the surface mass density by independent techniques such as stellar dynamics studies, or to set an absolute flux or size scale on the source. Moreover, when there are at least two sources located at different redshifts and lensed by the same object, a transformation as in Eq. 4.39 would change the image configuration: the mass-sheet degeneracy no longer exists.

4.8.2 Parametric modeling

Singular isothermal sphere and ellipsoid

The *Singular Isothermal Sphere* (SIS) is the simplest model and so a good point to start from: it describes a circular mass distribution. This model has a flat rotation curve outside the core, accounting for the motions observed e.g. in the Milky Way[3]. It also gives a constant velocity dispersion profile, characteristic of elliptical galaxies. Physically, in such a model, all the stars and other mass components in the galaxy are considered as self-gravitating particles plunged in an ideal isothermal gas.

The density of the SIS model is expressed as follows:

$$\rho(r) = \frac{\sigma_v^2}{2\pi G r^2} \tag{4.40}$$

where r is the radius and σ_v the one-dimensional velocity dispersion, while the surface mass density is given by:

$$\Sigma(\xi) = \frac{\sigma_v^2}{2G}\frac{1}{\xi}\,. \tag{4.41}$$

[3]The flat rotation curve observed in our Galaxy is one of the evidences for the existence of dark matter.

The projected mass within radius ξ is then:

$$M(\xi) = 2\pi \int_0^{\xi} \Sigma(\xi')\xi' d\xi' = \frac{\pi\sigma_v^2 \xi}{G}\,. \tag{4.42}$$

As a consequence, the deflection angle (see Eq. 4.1 on p. 33) does not depend on the impact parameter:

$$\hat{\alpha}(\xi) = 4\pi \frac{\sigma_v^2}{c^2} \tag{4.43}$$

and two colinear images are created on each side of the lens.

A few remarks can be made about this model. First the SIS profile is unphysical because of a singularity at the center, that is why it is called *singular*. This can easily be solved by introducing a finite core radius. Moreover its total mass is infinite (it increases with the radius) but it has no influence on images located at small radii. And finally an SIS alone cannot produce quads, as there is no angular contribution.

As galaxies are rarely perfectly round, it is logical to introduce an ellipticity in the SIS model. That model is called the SIE model or *Singular Isothermal Ellipsoid*.

De Vaucouleurs

The *de Vaucouleurs* model (de Vaucouleurs, 1948) is a profile with a constant mass-to-light ratio, i.e. the mass distribution of the galaxy follows the one of the light. This empirical law for the light distribution is well suited for elliptical galaxies, as well as bulges of spiral ones. Its projected surface mass density is the following:

$$\Sigma(\xi) = \Sigma_e \, \exp\left\{-k\left[(\xi/R_e)^{\frac{1}{4}} - 1\right]\right\} \tag{4.44}$$

where $k = 7.66925001$, R_e is the *effective radius*, i.e. the radius of the circle enclosing half the total light or mass of the galaxy, also called the *half-light radius* and Σ_e is the *effective surface brightness*, i.e. the surface brightness at $\xi = R_e$.

Exponential disk

An *exponential disk* is a model adapted to the light distribution of a typical late-type galaxy. When viewed in projection on the sky, it has an elliptical symmetry and the surface mass density is given by:

$$\Sigma(\xi) = q^{-1}\Sigma_0 \, \exp\left[-\xi/R_d\right]. \tag{4.45}$$

This represents a thin circular disk, seen in projection with an axis ratio $q = |\cos i|$, i being the inclination angle (0° means face-on and 90° means edge-on), with intrinsic central density Σ_0 and a scale length of R_d.

Navarro, Frenk & White

In running cosmological N-body simulations, Navarro, Frenk & White (1996) found that dark matter halos all have the same shape, regardless the initial conditions, the mass

and the value of the cosmological parameters chosen in the simulations. Moreover, they found a cusp at the center of these halos. This universal density profile can be expressed by the following empirical formula:

$$\rho(r) = \frac{\rho_s}{r/r_s \left(1 + r/r_s\right)^2} \tag{4.46}$$

where ρ_s is a characteristic density and r_s is the scale radius at which the slope of the profile changes from $\rho(r) \propto r^{-1}$ in the inner region to $\rho(r) \propto r^{-3}$ in the outer region. This model is called without surprise *NFW*. An argument independent from the simulations in favour of a sharply-peaked central density comes from the lack of observed central images: no third or fifth image has ever been observed. A flat core is thus less likely than a cuspy core, the latter creating a highly demagnified central image.

In a more general version of the NFW model, the slope of the cuspy region is an arbitrarily chosen power law: $\rho(r) \propto r^{-\gamma}$. This model is called the *cuspy NFW* model.

External perturbations

A galaxy is unlikely to be isolated: it is very often plunged into a group or a cluster. Tidal perturbations created by the gravitation of neighbouring galaxies or objects along the line of sight should be taken into account in the modeling as an angular contribution to add to the main lens potential. This contribution is called the *external tidal shear* and is analytically represented by γ and θ_γ which are respectively the strength of the shear and its direction angle. The latter points towards the mass responsible for the shear.

There are thus two angular contributions to the potential: one from the elliptical shape of the main lens galaxy and the other from the external shear. It is difficult to disentangle them: they are degenerated. One should then be very careful before drawing conclusions on the shear and ellipticity.

Let us note that an external shear is sufficient in the modeling if the perturbations created by other objects are weak. If not, the potential of these objects should be added to the one of the main lens through models as those explained above.

4.8.3 Non-parametric modeling

For more complicated systems, it is possible to combine more than one type of model in two different ways. First to account for an object with a more complicated structure, different models can be used at the same position. Second to account for different lenses, several models can be introduced at different positions. In such cases, the elliptical symmetry that we generally and reasonably assume for a lensing galaxy is broken. However, it is still possible to model the potential as a sum of circular and elliptical contributions. But these models are not completely general: some assumptions are made about the shape of mass distributions. That is why Saha & Williams (1997) and Williams & Saha (2000) developed a new approach to reproduce the observed configuration of lensed images with non-parametric models in an algorithm called *PIXELENS* (Saha, 2004).

The main principle is to divide the lens into around a thousand pixels, each one of them containing a certain amount of mass which is to be determined. That is why these models are also referred to as *pixelized*. This problem has a high number of degrees of freedom: it is then underconstrained. Some additional criteria, also called *priors*, are used to reduce the number of possible models, such as a positive surface mass density or a certain smoothness in the mass distribution. However, the number of plausible models is still high. One could argue that some of them are probably not consistent with the stellar dynamics of such galaxies. But all these possible models can be used statistically to obtain e.g. a probability distribution of the Hubble constant.

4.9 The Hubble constant from lensed quasars

Sjur Refsdal was the first to consider the possibility of using time delay measurements to derive H_0. That was in 1964. At that time he wanted to use lensed galaxies for that purpose, which seemed unrealistic. Thanks to the discovery of quasars in 1963 by Schmidt, another possibility came up: derive H_0 from lensed quasars. But the first multiply imaged quasar, the double QSO 0957+561, was not discovered until 1979 by Walsh et al.. It was also the first one with a measured time delay (Vanderriest et al., 1989).

Let us summarize what is required to obtain H_0 from lensed quasars:

- the redshift of the quasar and the one of the lens,
- the relative astrometry of the lensed images and the lens,
- the flux ratio(s) of the images,
- if available, more constraints on the lens,
- the time delay(s) between the different images.

These data must be put into a code which allows to model the mass distribution that reproduces the gravitational potential creating the observed configuration. The outputs are diverse: the position and flux of the original source, the external shear, and also, when the time delays are known, the Hubble constant. The code we use in this work (see Chapters 12 and 13) is the LENSMODEL software package (Keeton, 2001b). Let us note that, as shown in Eq 4.37 on p. 42, the time delays also slightly depend on the density parameters (through the deceleration parameter) which are now well constrained (see Sect. 2.4 in Chapter 2).

But obtaining accurate values of H_0 from time delays is far from being easy. A first reason is that quasars rarely show very sharp variations. Photometric monitoring over long periods, longer than the time delay, is then necessary. A second one is caused by microlensing of stars in the lensing galaxy as illustrated on Fig. 4.8. The microlensing variations will affect differently and independently the individual light curves. If they occur on short time scales, they can be considered as an extra source of noise. On the contrary, if they occur on long time scales, they introduce global trends into the light

curves. The most critical case is probably when the microlensing variations occur on similar time scales as the quasar intrinsic variations. In any case it is complicated to get rid of these variations. That is why the temporal sampling step of the monitoring should be chosen carefully.

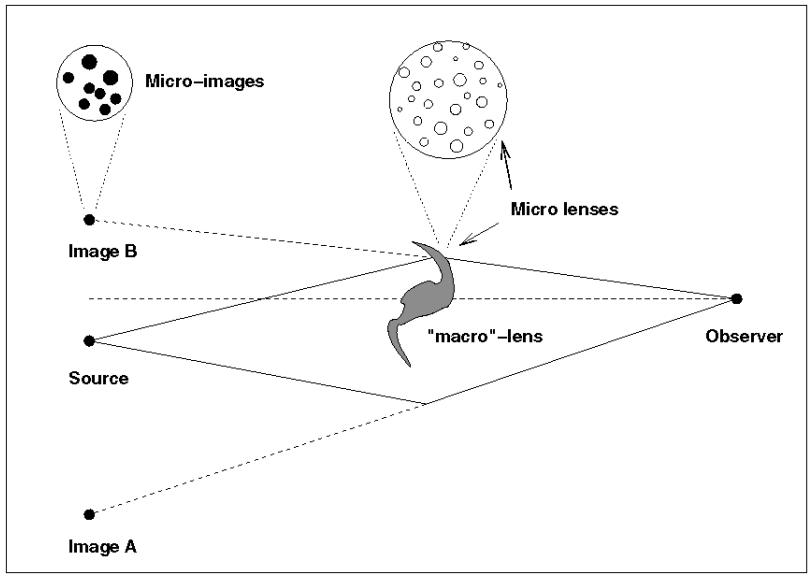

Figure 4.8: Illustration of the microlensing phenomenon which occurs when stars or compact objects in motion in the lens, in this case a spiral galaxy, cross the rays forming the lensed images and affect the fluxes of these images: some unresolved micro-images are created and result in a magnification of the flux. Credit: Courbin & Minniti (2002).

Let us note that microlensing in itself is also an achromatic phenomenon. But the magnification depends on the source size if the latter is comparable to or larger than the Einstein radius of the microlenses. A quasar is composed of different regions with different sizes and emitting at different wavelengths as seen in a previous chapter (see Chapter 3). These regions are then differently magnified by a same microlens and the phenomenon is then chromatic. The flux ratios of multiple images can then change with the spectral band.

A third reason why it is not easy to obtain H_0 comes from the different sources of error: the time delay measurement, the astrometry of the quasar images, the modeling of the lens, microlensing events or even some unknown systematic source of error, every case being different. So, to obtain a reliable value of H_0, it is better to monitor several systems than to concentrate on a single one.

Gravitationally lensed quasars can also be used the other way around. Indeed, if the Hubble constant is known from an independent method, the time delays can be used to constrain the total mass profile and so to study the dark matter distribution.

The possibility to probe our Universe and to study cosmology with lensed quasars has made them very famous and popular amongst the scientific community. However,

time delays and the measurement of the Hubble constant are not the only reason. Indeed, there are many other applications of gravitational lensing such as the study of the mass distribution in clusters or the structure of quasar accretion disks, the search for extrasolar planets or compact objects through microlensing of background Galactic or Magellanic stars, the statistical study of the distribution of foreground galaxies through weak lensing, and so on. No wonder gravitational lensing is still in vogue and will be so probably for a long time...

To live a creative life, we must lose our fear of being wrong.

Joseph Chilton Pearce (1926 -)

5 Deconvolution

Contents

5.1 Introduction

The theoretical notions hereafter come mainly from the following PhD theses: Courbin (1999), Burud (2001) and Letawe (2006).

Higher and higher resolution images are always demanded by scientists. Indeed, the more detailed are the observations, the more information they can provide. That is why it is very fashionable to build larger and larger telescopes and even to send some to space. But numerical techniques can also be used to improve data acquired with a not so big mirror, in not so good atmospheric and/or optical conditions. Deconvolution is one of these techniques allowing to recover information from blurred images in clearing them from the influence of the optical system that has collected the light and possibly from the effects of the atmospheric turbulence. The interest of deconvolution in the

astronomical community has grown after the launch of the Hubble Space Telescope because of the strong optical aberrations discovered in the primary mirror.

Every observation $\mathcal{D}(\vec{x},t)$ is sampled on a detector, $\vec{x}$ representing a pixel on the CCD, i.e. *Charge-Coupled Device*[1], and may depend on time t. It can be decomposed as follows:

$$\mathcal{D}(\vec{x},t) = \Big(\mathcal{F}(\vec{x},t) * \mathcal{T}(\vec{x},t)\Big) \; + \; \mathcal{N}(\vec{x},t) \tag{5.1}$$

where $\mathcal{F}(\vec{x},t)$ represents the original signal, $\mathcal{T}(\vec{x},t)$ stands for the instrumental profile and $\mathcal{N}(\vec{x},t)$ is the noise, $*$ being the convolution operator. Convolution, when applied to two functions f and g[2], produces a third function which is defined as the integral of the product of the two functions after one is reversed and shifted:

$$\big(f * g\big)(x) = \int_{-\infty}^{+\infty} f(\xi)\; g(x-\xi)\; d\xi\,. \tag{5.2}$$

In Eq. 5.1, $\mathcal{T}(\vec{x},t)$ is also called the total PSF (*Point Spread Function*). It is the instrumental diffraction shape of a theoretical point source of light through the whole optical system and possibly through atmospheric layers if the observations are ground-based. The noise $\mathcal{N}$ is mainly due to the readout of the CCD and to the statistical character of the counting of photons. The lower the signal-to-noise ratio (S/N) is, the poorer our estimation of the original signal will be.

To make it easier we will consider a unique observed image which does not depend on time. Eq. 5.1 can then be written as follows:

$$\mathcal{D}(\vec{x}) = \Big(\mathcal{F}(\vec{x}) * \mathcal{T}(\vec{x})\Big) \; + \; \mathcal{N}(\vec{x})\,. \tag{5.3}$$

Our aim is to recover the signal $\mathcal{F}(\vec{x})$ and to highlight high frequency components in the data in spite of the noise. It is obvious that we are dealing with an inverse problem and, especially in the presence of noise, with an ill-posed problem: it has no unique solution. Regularization, a process consisting in introducing additional information about the problem, is then necessary in order to select a solution amongst the set of all light distributions compatible with the observation, within the error bars.

Many different deconvolution techniques have been elaborated, each one being based on a different regularization criterion. Most of them present some weaknesses: at some level they all produce deconvolution artifacts, which add to the deconvolved image information that does not exist in the original signal. This often prevents from obtaining reliable astrometric and photometric measurements. The next section will expose briefly three of the most common techniques and their problems.

[1] A *Charge-Coupled Device* (CCD) is an electronic chip sensitive to light. It consists in an integrated circuit containing an array of coupled capacitors, each one of them representing a pixel. Under the control of an external circuit, the charges of a pixel can be shifted to another one. This way, the charges are transferred row by row to a serial output register. The picture is the display of the electronic distribution.

[2] For simplicity we assume that they are both defined from $-\infty$ to $+\infty$.

5.2 The common methods and their weaknesses

5.2.1 Wiener deconvolution

The foundations of deconvolution techniques and time-series analysis were largely built by Norbert Wiener in a book that he wrote during but published after World War II. *Wiener deconvolution* is a linear procedure based on the application of the *Wiener filter* to reduce the noise problems inherent to deconvolution.

By the convolution theorem, which states that a convolution product in the image space becomes a simple product in the Fourier space, we can apply the Fourier transform to Eq. 5.3 such that we obtain:

$$D(\vec{\nu}) = F(\vec{\nu}) \cdot T(\vec{\nu}) + N(\vec{\nu}) \tag{5.4}$$

where $\vec{\nu}$ is the variable in the Fourier space and where $D(\vec{\nu})$, $F(\vec{\nu})$, $T(\vec{\nu})$ and $N(\vec{\nu})$ are the Fourier transforms of $\mathcal{D}(\vec{x})$, $\mathcal{F}(\vec{x})$, $\mathcal{T}(\vec{x})$ and $\mathcal{N}(\vec{x})$ respectively.

What comes then to mind is to invert Eq. 5.4 to directly obtain the original signal in the Fourier space:

$$F(\vec{\nu}) = \frac{D(\vec{\nu}) - N(\vec{\nu})}{T(\vec{\nu})} \tag{5.5}$$

which is valid if $T(\vec{\nu})$ differs from zero. However, the term $N(\vec{\nu})/T(\vec{\nu})$ diverges at high frequencies, precisely the ones we try to recover.

A step towards the solution to this problem was found by Wiener: before inverting the observed signal, one can apply a special filter to the data which will attenuate high frequencies. That filter can be written as follows in the Fourier Space:

$$\Phi(\vec{\nu}) = \frac{|B(\vec{\nu})|^2}{|B(\vec{\nu})|^2 + |N(\vec{\nu})|^2} \tag{5.6}$$

where $B(\vec{\nu}) = F(\vec{\nu})\ T(\vec{\nu})$. If there is no noise, the filter becomes equal to unity and has no effect on the observed signal. Of course, nor $N(\vec{\nu})$ neither $B(\vec{\nu})$ are known, but $|N(\vec{\nu})|^2$ and $|B(\vec{\nu})|^2$ can be estimated by separating the contributions from the noise and the actual data in the power spectrum of the data $|D(\vec{\nu})|^2$.

5.2.2 The maximum entropy method

Here again we are willing to obtain a deconvolved signal that will be the best representation of the original signal in a *least square*[3] sense. We are thus trying to minimize the following expression:

$$\left(\frac{\mathcal{D}(\vec{x}) - [\mathcal{F}(\vec{x}) * \mathcal{T}(\vec{x})]}{\sigma(\vec{x})} \right)^2 . \tag{5.7}$$

[3]The *least square* minimization technique is an approach used in statistics, curve fitting and signal processing amongst others. For a given data set, the least square values of the unknown factors of a model are the values minimizing the sum of squared deviations, obtained in comparing the data to the model predictions.

Let us assume that our CCD has only one dimension. We can write the previous expression in terms of a χ^2:

$$\chi^2 = \sum_{i=1}^{N} \left[\frac{d_i - \left(\Sigma_{j=1}^{N} t_{ij} f_j\right)}{\sigma_i} \right]^2 \tag{5.8}$$

where N is the total number of pixels, σ_i an estimated value of the standard deviation of the signal acquired in the i^{th} pixel, d_i the measured value in the i^{th} pixel of the observed image, t_{ij} the intensity in pixel j of the PSF centered on pixel i and f_j the original signal in pixel j.

Just before the 1950s, Shannon showed that the average amount of information contained in a probability distribution p_i is measured by the entropy:

$$\mathcal{H} = -\sum_{i=1} p_i ln\ p_i. \tag{5.9}$$

The maximum entropy principle states that, amongst all the solutions to an inverse problem, the one with the highest entropy and, thus, the minimum amount of information, should be chosen. To apply it to image processing, we assume that the intensity distributions are normalized, e.g.:

$$\sum_{i=1}^{N} f_i = 1 \tag{5.10}$$

so that f_i can be viewed as a probability, i.e. the probability that the next photon will be emitted in the region of the sky corresponding to pixel i on the detector.

The maximum entropy method consists in minimizing the following function which depends on N variables (the f_i):

$$\Phi = \chi^2 - \lambda\mathcal{H} \tag{5.11}$$

where χ^2 is given by Eq. 5.8 and where λ is a Lagrange parameter introduced to modulate the weight of $\mathcal{H}$, which can be seen as a smoothing term. The maximum entropy image is the flattest image compatible with the data, in other words, the closest to a constant. This method automatically constrains every f_i to be positive as expected for a detected number of photons.

5.2.3 The Richardson-Lucy algorithm

The Richardson-Lucy algorithm, introduced by Richardson in 1972 and theoretically developed by Lucy in 1974, is an iterative and non-linear procedure which basic idea is to calculate the most likely f_j, given the observed d_i and known t_{ij}. If the noise is neglected in a first approximation, some manipulations of Eq. 5.3 lead to the following expression:

$$f_j^{(n+1)} = f_j^{(n)} \sum_{i=1}^{N} \frac{d_i}{c_i} t_{ij} \tag{5.12}$$

where $f_j^{(n)}$ is the n^{th} estimation of f_j and

$$c_i = \sum_{k=1}^{N} t_{ik} f_k^{(n)}. \tag{5.13}$$

d_i/c_i is thus the ratio of the value acquired in pixel i and the value, in the same pixel, of the deconvolved image but reconvolved by the instrumental profile. This ratio is then convolved by the normalized PSF t_{ij} to get rid of the details with higher frequencies than the instrumental profile. This modified ratio is then used to correct the first estimate of the deconvolved image and obtain a new estimate of f_j which can be used as a starting point for the next iteration. If this process converges, it converges to the maximum likelihood solution for f_j. Usually $f_j^{(0)}$ is the measured value in pixel j.

Let us notice that for positive data, a positive PSF, and a positive first approximation of the deconvolved image, every following estimate of f_j will also be positive.

5.2.4 Their weaknesses

Mainly there are three problems encountered by these classical methods. The first one is related to the sampling theorem, the second one to the smoothing parameter and the last one to the positivity constraint. Hereafter we develop the three of them.

- **The sampling theorem**

  The *sampling theorem*, or the *Nyquist-Shannon theorem* states that "*A function that contains no frequencies higher than* ν_0 *is completely determined by giving its ordinates at a serie of points spaced* $(2\nu_0)^{-1}$ *seconds apart*" (Shannon, 1949). It means that a signal, continuous in time, can be reconstructed from a sampled version only if it is band-limited, e.g. its Fourier transform is equal to zero above a certain finite frequency ν_f, and if the sampling rate exceeds ν_c (*cut-off* frequency) which is equal to twice ν_f. When the sampling frequency is too low, all the components of frequencies higher than ν_c are badly represented by the chosen sampling step and superimposed on frequencies between $-\nu_c$ and ν_c. This artifact is called *aliasing* (see Fig. 5.1). Let us insist on the fact that, even if $\mathcal{D}(\vec{x})$ is well sampled, it does not imply that $\mathcal{F}(\vec{x})$ will be well sampled too. The simplest example of a violation of the sampling theorem is a perfect deconvolution of an image containing a point source (e.g. a star): it would give an image of the point source narrower than the sampling step and this is not feasible.

  The problem of classic algorithms is that they attempt to reach an infinite resolution. That would be possible only if the pixel size was infinitely small, which is far from being the case. This is thus in complete contradiction with the sampling theorem. As a consequence, the *Gibbs phenomenon*, i.e. rings surrounding point-like objects, will appear in the deconvolved frame. This phenomenon, also known as *ringing artifacts*, comes from the fact that the signal is band-limited. We will not give more details about this particular topic. Let us just insist on the fact that these artifacts are caused by high frequencies contained in the data (and

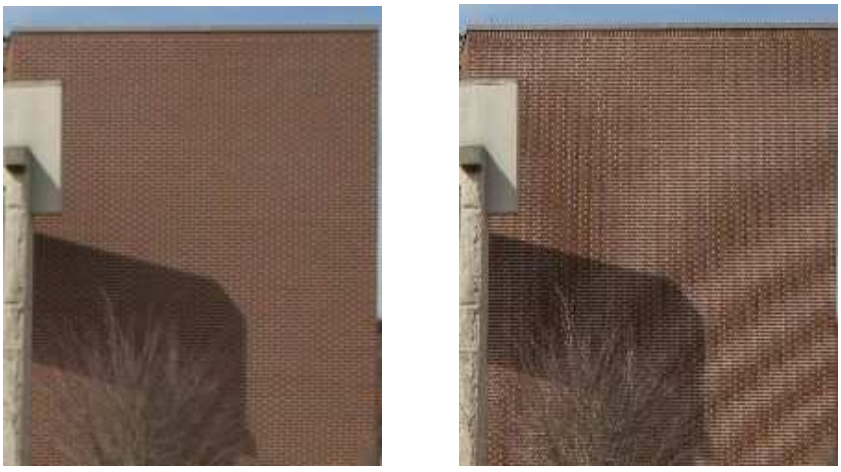

Figure 5.1: Example of the aliasing phenomenon. *Left*: properly sampled image of a brick wall. *Right*: effect of a bad sampling (undersampling) on the same image. The aliasing phenomenon is obvious. Credit: `http://www.wikipedia.org`.

in particular in the point sources). For those who are interested, here is a good reference of a PhD thesis developing that subject: Blanchet (2006).

- **The smoothing parameter**

  Usual algorithms select the smoothest solution amongst the ones compatible with the observed light distribution, according to different criteria: it allows to attenuate the amplification of the noise and the Gibbs' oscillations. But choosing the smoothest image is in complete contradiction with our expectations. Indeed, our intuition tells us that an astronomical observation is far from being smooth: we want to detect objects like stars, planets, quasars, and other structures. We often expect bright points on a faint diffuse background.

- **The positivity constraint**

  To be efficient, the positivity constraint must be applied to an image with no sky background. But most of the time after sky subtraction, the photon noise implies many pixels with a negative value. In algorithms such as Richardson-Lucy, one has to put to zero these negative values before deconvolution, in the observed frame as well as in the PSF. That modifies consequently the shape and the intensity of faint objects, as well as the wings of the instrumental profile.

A first step towards the solution was made by Lucy in 1993. He developed a technique based on the Richardson-Lucy algorithm and he called it the *PLUCY algorithm*. Its particularity resides in the decomposition of the deconvolved frame in two images, one containing the point sources and the other one the diffuse background. High frequencies are thus treated separately which leads to a deconvolved image less contaminated by ringing artifacts. This algorithm works better than the Richardson-Lucy method.

However, a fundamental weakness persists: the algorithm tries to obtain a deconvolved image with an infinite resolution, which is completely forbidden by the sampling theorem. Moreover, by construction, the point sources are exactly centered on the pixels, which severly limits the accuracy of the results.

5.3 The MCS algorithm and its advantages

5.3.1 Principle

The basis of the MCS algorithm, which stands for Magain, Courbin & Sohy (1998), is the respect of the sampling theorem in trying to improve the spatial resolution of images instead of trying to obtain an infinite one. To do so we do not deconvolve the image by the total PSF $\mathcal{T}(\vec{x})$ but by a narrower one, $\mathcal{S}(\vec{x})$, so that the deconvolved frame has its own resolution, the final PSF $\mathcal{R}(\vec{x})$, compatible with its own sampling step:

$$\mathcal{T}(\vec{x}) = \mathcal{R}(\vec{x}) * \mathcal{S}(\vec{x})\,. \tag{5.14}$$

Practically, $\mathcal{R}(\vec{x})$ is chosen so that the deconvolved data are well sampled: the image of a point source on the final image must have a full-width-at-half-maximum (hereafter FWHM) of at least 2 pixels. Moreover the size of the pixels used to represent the deconvolved image is also chosen by the user. Usually we adopt either the original pixel size or, more often, half the original (linear) pixel size in order to allow for a better accuracy and improvement in spatial resolution.

There are two important consequences of Eq. 5.14. First of all, the deconvolved image will be well sampled and its spatial resolution can be strongly improved. Second, the final profile of a point source, $\mathcal{R}(\vec{x})$, is known and even chosen by the user (generally a Gaussian function).

Every astronomical image is thus decomposed in a sum of M point sources and a numerical background containing the diffuse structures, the shape of the point sources in the deconvolved frame being known. However, their intensity a_k and their center $\vec{c}_k$ remain to be determined. So, if the image contains N pixels, there are $3M+N$ variables: one intensity and two coordinates per point source plus one value of the background per pixel. The deconvolved image can thus be written as:

$$\mathcal{F}(\vec{x}) = \mathcal{H}(\vec{x}) + \sum_{k=1}^{M} a_k r(\vec{x} - \vec{c}_k) \tag{5.15}$$

where $\mathcal{H}(\vec{x})$ is the diffuse background and $r(\vec{x})$ is the value of function $\mathcal{R}$ at a position $\vec{x}$ relative to its center. Practically, the algorithm has to minimize the following function:

$$\begin{aligned} \mathcal{K} &= \sum_{i=1}^{N} \frac{1}{\sigma_i^2} \Big[\sum_{j=1}^{N} s_{ij} \Big(h_j + \sum_{k=1}^{M} a_k r(\vec{x}_j - \vec{c}_k) \Big) - d_i \Big]^2 \\ &+ \lambda \sum_{i=1}^{N} \Big[h_i - \sum_{j=1}^{N} r_{ij} h_j \Big]^2, \end{aligned} \tag{5.16}$$

d_i being the value registered in pixel i on the CCD, h_j the value of the deconvolved background in pixel j and s_{ij} the intensity in pixel j of the partial PSF $\mathcal{S}(\vec{x})$ centered on pixel i. The parameter λ allows the user to adjust the value of the χ^2 so that the deconvolved frame is statistically compatible with the observed data. Indeed, a least square minimization is considered successful if $\chi^2 = 1$ per degree of freedom. In other words, λ gives a weight to the smoothing term. The latter contains all the frequencies of the diffuse background higher than the one of $\mathcal{R}(\vec{x})$. Every structure with such a frequency is not physical and has to be minimized. Finally, the length scale of the smoothing is not arbitrary, as it is the case with most methods, but directly related to $\mathcal{R}(\vec{x})$ and, as a consequence, local.

The user is guided by the value of the χ^2 but also by the *residual map*. The residual map $\mathcal{Z}(\vec{x})$ of an observation is expressed in units of standard deviation. It is defined as follows:

$$\mathcal{Z}(\vec{x}) = \frac{\mathcal{M}(\vec{x}) - \mathcal{D}(\vec{x})}{\sigma(\vec{x})} \tag{5.17}$$

where $\mathcal{M}(\vec{x})$ stands for the solution reconvolved by the partial PSF $\mathcal{S}(\vec{x})$[4]. It represents the deviation of the model compared to the original image, measured in units of the standard deviation.

It is also practical to work with the *reduced chi square* χ^2_r measured on what we call the *reduced residual map*. Actually the latter expression is a misuse of language introduced to ease the communication. The reduced chi square of an image with N pixels is mathematically defined as follows:

$$\chi^2_r = \frac{1}{N} \sum_{\vec{x}} \left(\frac{\mathcal{M}(\vec{x}) - \mathcal{D}(\vec{x})}{\sigma(\vec{x})} \right)^2 . \tag{5.18}$$

Theoretically the χ^2_r must be close to unity. That would be the case for a perfect deconvolution executed with a perfect PSF. If it is lower than 1, the model follows too closely the data and the deconvolution is noisy. This is called *overfitting*. On the contrary, if the χ^2_r is much larger than 1, the model does not correctly represent the data and we are in the presence of *underfitting*.

To end this section, let us mention that, as the MCS method is an iterative procedure, the user has to estimate the initial intensity and position of every point source in the image. The algorithm will adjust them during the process. Moreover, the MCS method preserves the astrometric and photometric properties of the observed objects. For interested readers, we suggest the original paper of Magain, Courbin & Sohy (1998).

5.3.2 The analytical model

The MCS algorithm has other features that we have not mentioned yet. Amongst them, one is of great interest to us: the possibility of introducing an analytical model (considered as a part of the diffuse background) to fit the luminosity profile of a galaxy.

[4]The solution must be reconvolved by $\mathcal{S}(\vec{x})$ and not by the total PSF $\mathcal{T}(\vec{x})$ because the deconvolved frame has its own PSF $\mathcal{R}(\vec{x})$.

We have two possibilities: a *de Vaucouleurs* model (de Vaucouleurs, 1948) well suited for elliptical galaxies, i.e. bulge systems, and an *exponential* luminosity profile (Freeman, 1970) well adapted to spiral galaxies, i.e. disk systems.

The light profile G of a galaxy with elliptical isophotes can be expressed as follows, if the ellipse is centered on $(0, 0)$:

$$G'(x', y') = I_0 \; e^{-(Ax'^2 + By'^2 + Cx'y')^{\alpha}} \tag{5.19}$$

where I_0 is the central intensity of the galaxy, A, B and C are parameters of the model and where α is equal to 0.125 in the case of a de Vaucouleurs profile and to 0.5 in the case of an exponential profile.

If we choose the ellipse axes as the coordinate axes:

$$G(x, y) = I_0 \; e^{-\left(\frac{x^2}{a} + \frac{y^2}{b}\right)^{\alpha}} \tag{5.20}$$

where a is the semi-major axis and b the semi-minor axis of the ellipse. There are other important parameters: the angle θ between the orientation of the observed frame and the orientation of the ellipse, and the ellipticity e with $e = 1 - b/a$. The angle θ leads to the *position angle* or PA which is the angle that folds back the semi-major axis of the ellipse on the direction of the North.

These parameters are related to the coefficients A, B and C:

$$a^2 = \frac{2cos(2\theta)}{(A + B)\; cos(2\theta) + A - B} \tag{5.21}$$

$$b^2 = \frac{2cos(2\theta)}{(A + B)\; cos(2\theta) + B - A} \tag{5.22}$$

$$\theta = \frac{1}{2}\; arctg\Big(\frac{C}{B - A}\Big) \tag{5.23}$$

$$e = \frac{B - A}{(A + B)\; cos(2\theta)}\,. \tag{5.24}$$

5.3.3 Optimal image combination

The MCS algorithm has another considerable advantage: it allows the user to simultaneously deconvolve several images of the same field of view, if they have the same resolution and orientation. Each image has its own PSF. The extended structures and the positions of the point sources are forced to be equal in each frame, except for a common flux scale factor and a spatial shift. For the intensity of the sources, the user can choose whether to force them to be proportional in each frame or not. If the data have been acquired consecutively during a short time period then, most of the time, there is no physical reason to let the intensity vary from one deconvolved frame to the other. On the contrary, if the images were acquired over a long time period and with the purpose of determining the variations of flux, then it is essential to let the source intensity vary from one frame to the other. The best example is probably the deconvolution of images of gravitationally lensed quasars in order to determine a time delay.

In the case of a simultaneous deconvolution of L images $\mathcal{D}_1(\vec{x})$, $\mathcal{D}_2(\vec{x})$, ..., $\mathcal{D}_L(\vec{x})$, each one of them having its own PSF $\mathcal{S}_1(\vec{x})$, $\mathcal{S}_2(\vec{x})$, ..., $\mathcal{S}_L(\vec{x})$, the function to minimize is the following:

$$\begin{aligned}
\mathcal{K} &= \sum_{i=1}^{N} \frac{1}{\sigma_{1,i}^2} \left[\sum_{j=1}^{N} s_{1,ij} \Big(\alpha_1 h(\vec{x}_j + \vec{\delta}_1) + \beta_1 + \sum_{k=1}^{M} a_{1,k}\ r(\vec{x}_j - \vec{c}_k + \vec{\delta}_1) \Big) - d_{1,i} \right]^2 \\
&+ \sum_{i=1}^{N} \frac{1}{\sigma_{2,i}^2} \left[\sum_{j=1}^{N} s_{2,ij} \Big(\alpha_2 h(\vec{x}_j + \vec{\delta}_2) + \beta_2 + \sum_{k=1}^{M} a_{2,k}\ r(\vec{x}_j - \vec{c}_k + \vec{\delta}_2) \Big) - d_{2,i} \right]^2 \\
&\ \ \vdots \\
&+ \sum_{i=1}^{N} \frac{1}{\sigma_{L,i}^2} \left[\sum_{j=1}^{N} s_{L,ij} \Big(\alpha_L h(\vec{x}_j + \vec{\delta}_L) + \beta_L + \sum_{k=1}^{M} a_{L,k}\ r(\vec{x}_j - \vec{c}_k + \vec{\delta}_L) \Big) - d_{L,i} \right]^2 \\
&+ \lambda \sum_{i=1}^{N} \left[h_i - \sum_{j=1}^{N} r_{ij} h_j \right]^2 . \qquad (5.25)
\end{aligned}$$

Each one of the L first terms is related to a particular image while the last one is the smoothing term. $d_{l,i}$ is the value of the observed data in pixel i of the l^{th} image, $\sigma_{l,i}$ its standard deviation and $s_{l,ij}$ the value of the PSF of image l, centered on pixel i and measured in pixel j. We can notice that three new parameters are introduced: α_l, β_l and $\vec{\delta}_l$. The first one, α_l, is the flux scale factor of the background: it corrects possible effects from differences in exposure times or in the transparency of the atmosphere in the case of ground-based observations, but also imposes the extended structures to have the exact same shape in each frame. The second new parameter, β_l, is an additive term introduced in order to get rid of errors in the sky subtraction that could have occurred during the reduction of the images. In this equation no constraint is applied to the intensities $a_{l,k}$ of the sources: they are free to vary from one image to the other. In the case of non-varying intensities, $a_{l,k}$ is multiplied by the factor α_l so that the ratio between the intensities of the sources and the background is the same in every image. The last parameter, $\vec{\delta}_l$, is introduced to take into account a spatial offset between two different exposures. This technique is called *dithering* and is highly recommended to get rid of bad pixels or cosmic ray[5] hits. Practically the first image of the data set is considered as the reference frame: $\alpha_1 = 1$, $\beta_1 = 0$ and $\vec{\delta}_1 = 0$.

A de Vaucouleurs or an exponential profile can also be used in the simultaneous deconvolution of several frames in order to account for a galactic light distribution. It is considered as a part of the background so it will also be affected by the parameters α_l, β_l and of course $\vec{\delta}_l$.

[5] *Cosmic rays* are highly energetic particles originating from outer space: those arising in astrophysical sources are called *primary cosmic rays*. They can then interact with interstellar matter to create *secondary cosmic rays*. When penetrating the atmosphere of the Earth, they collide with molecules, mainly oxygen and nitrogen, to produce a cascade of lighter particles.

In short, after a simultaneous deconvolution, the user obtains a unique and optimally constrained deconvolved image, which is compatible with and based on all the images of a same object taken in different observational conditions but in a given instrument configuration, e.g. through a given filter. That means that all the data are used to constrain the parameters. It is always preferable to deconvolve simultaneously many dithered images than one combined frame. This method is particularly well suited to detect underlying and relatively faint structures such as lensing galaxies or Einstein rings as explained in Courbin, Lidman & Magain (1998).

Let us now conclude this section in stating the advantages of the MCS algorithm:

- This algorithm is capable of improving the resolution but also the sampling of the data set (however this does not replace a good sampling of the original observations).
- It can be applied to a single frame or to several images of the same field obtained with the same sampling and orientation.
- It naturally and efficiently separates the diffuse structures from the point sources.
- It accurately measures the position and intensity of point sources from approximate values.
- The user is guided by the χ^2 and the residual map to choose a value for the smoothing parameter and to reach the best solution.
- The algorithm does not require the positivity constraint to be efficient. One can choose whether to use it or not depending on the case treated.

5.3.4 Determination of the PSF

To optimally use the MCS algorithm, it is necessary to know the PSF $\mathcal{S}(\vec{x})$ with a high accuracy. Indeed, it is the most important step to ensure that MCS will be successful. For that purpose, an algorithm was developed, on the same basis as MCS, to determine the PSF on images consisting of possibly blended point sources (Magain et al., 2007). This method, often called *PSFsimult* to ease the conversation, works well, even in very crowded fields, when no point source is sufficiently isolated to derive an accurate PSF from standard techniques. However, it assumes that the portion of the image used to determine the PSF only contains point sources.

For a single one-dimensional image containing one point source with intensity a, centered in c and with the usual notations, the function to minimize is:

$$\mathcal{K}_{\mathcal{S}} = \sum_{i=1}^{N} \frac{1}{\sigma_i^2} \Big[\sum_{j=1}^{N} a\ r_{ij} s_j (x-c) - t_i \Big]^2 + \lambda \sum_{i=1}^{N} \Big[s_i - \sum_{j=1}^{N} w_{ij} s_j \Big]^2 \qquad (5.26)$$

where w_{ij} is a length scale for the smoothing term. Practically, we choose w_{ij} equal to r_{ij} because, if a deconvolved frame cannot contain any frequency higher than $\mathcal{R}(\vec{x})$, then neither should the PSF $\mathcal{S}(\vec{x})$ used for its construction. The parameters to modify

during the iterations of the algorithm are the following: the center of the point source, its intensity and all the pixels s_i from the partial PSF frame.

What if we have at our disposal a frame containing several possibly blended point sources ? Let us consider a single observed frame $\mathcal{D}(\vec{x})$. It can be expressed as follows:

$$\mathcal{D}(\vec{x}) = \Big(\mathcal{F}(\vec{x}) * \mathcal{S}(\vec{x})\Big) \; + \; \mathcal{N}(\vec{x}), \tag{5.27}$$

$\mathcal{S}(\vec{x})$ being the partial PSF. The usual problem is to recover $\mathcal{F}(\vec{x})$ knowing $\mathcal{D}(\vec{x})$ and $\mathcal{S}(\vec{x})$. If we consider a part of the frame which contains no numerical background but M point sources of intensity a_k and centered in $\vec{c}_k$, the deconvolved image $\mathcal{F}(\vec{x})$ can be expressed as follows:

$$\mathcal{F}(\vec{x}) = \sum_{k=1}^{M} a_k r(\vec{x} - \vec{c}_k). \tag{5.28}$$

The aim of the PSF determination program *PSFsimult* is to obtain $\mathcal{S}(\vec{x})$ while $\mathcal{D}(\vec{x})$ is known and $\mathcal{F}(\vec{x})$ is given by Eq. 5.28. If, indeed, the shape of $\mathcal{F}(\vec{x})$ is known, the intensities and positions of the point sources are considered as free parameters and must be determined at the same time as the partial PSF $\mathcal{S}(\vec{x})$. If the image contains N pixels, the function to minimize is the following:

$$\mathcal{K} \;=\; \sum_{i=1}^{N} \frac{1}{\sigma_i^2} \Big[\sum_{j=1}^{N} s_{ij} f_j - d_i \Big]^2 + \lambda \sum_{i=1}^{N} \Big[\sum_{j=1}^{N} g_{ij} s_j - s_i \Big]^2 \tag{5.29}$$

where g is a gaussian function. The width of g and the value of λ are adjusted so that $\chi^2 \approx N$, as N is approximately equal to the number of degrees of freedom.

In the case of an image composed of blended sources, a bump from a neighbouring point source can be interpreted by the program as another source or as a bump in the wings of the PSF or even as a mixture of both. We thus have to prevent the algorithm from finding an acceptable solution (for $\mathcal{S}(\vec{x})$) in terms of χ^2, but presenting bumps in the wings from the neighbouring stars. To avoid such local minima, we proceed in two steps. First the PSF is approximated by an analytical function such as a Moffat profile, which is defined as follows:

$$\mathcal{M}(x,y) = a \left[1 + b_1(x - c_x)^2 + b_2(y - c_y)^2 + b_3(x - c_x)(y - c_y)\right]^{-\beta}. \tag{5.30}$$

This profile is centered on (c_x, c_y) with an intensity a. The parameters b_1, b_2 and b_3 specify the ellipticity and orientation of the Moffat function and β controls the width of the wings. By definition, there will be no bumbs in such a PSF. But this is not sufficient to get an accurate instrumental profile: as a second step, a numerical component is added to this analytical one. And to avoid the bumps, we proceed gradually in fitting first the central regions of the PSF on the different point sources and then in gradually enlarging the modified area. In doing so, the algorithm first fits reasonably the intensity of the sources in the central regions of the PSF and does not add spurious bumps in the wings. Let us note that the smoothing term in Eq. 5.29 is only applied to the numerical part of the PSF and not to the analytical one.

In this work we also treat HST/NICMOS-2 images, HST standing for *Hubble Space Telescope* and NICMOS for *Near Infrared Camera and Multi-Object Spectrometer*. The Tiny Tim software package (Krist & Hook, 2004) allows the generation of a numerical estimation of HST PSFs for each instrument, filter and observing configuration. Moreover, it depends on the spectral type of the observed object. Most of the astrophysicists are usually satisfied with that PSF to get rid of the instrumental shape. But the actual PSF always departs significantly from this approximated version, especially in the core. And to reach the best results, we need a better estimation. That is why we apply *PSFsimult* to the HST frames. However, instead of departing from an analytic function as a Moffat profile, we start from a Tiny Tim PSF. As the Tiny Tim software computes the total PSF $\mathcal{T}(\vec{x})$, we first have to deconvolve it by the final resolution $\mathcal{R}(\vec{x})$. In practice we notice that doing this significantly improves the results. We then run the PSF determination algorithm, in order to improve the deconvolved Tiny Tim PSF in adjusting it to the point sources of the frame.

Moreover, as the MCS algorithm allows the user to oversample the deconvolved frame compared to the original data[6], the instrumental profile itself has to be oversampled by the desired factor. That is why we take advantage of the presence of several point sources on one frame: they are located on different positions on the CCD and so centered differently on the pixel grid. They can be deconvolved simultaneously, each one of them constraining the numerical component of the unique oversampled output PSF. That gives a PSF with a higher accuracy than one adjusted on a single source.

Chapter 7 presents a method which extends the one of Magain et al. (2007) to images containing point sources lying on a diffuse background. It is based on an iterative scheme, in which both the PSF and diffuse background of the frame are improved step by step.

[6]This is useful for the deconvolution of images of an object for which the position on the detector is shifted from frame to frame. Let us remind that it is called *dithering*.

Part II

Data analysis tools

Never let the future disturb you. You will meet it, if you have to, with the same weapons of reason which today arm you against the present.

Marc Aurèle (121 - 180)

6 The semi-automated reduction pipeline

Contents

6.1 Introduction

To obtain scientifically usable light curves from lensed quasars, there are several crucial conditions. First the quasar has to be variable and these changes in brightness need to be intense enough to be detected: there is no use in getting the light curves of a calm quasar, i.e. a quasar that is not variable, as it cannot lead to a measurement of the time delay (and hence, e.g. to H_0). Moreover the observations have to be well sampled in time compared to the time scale of the intrinsic variations of the quasar: the monitoring

campaign has to last longer than the time delays involved and the sampling step of the observations has to be small enough so that the variations are accurately represented on the time axis. Finally the quality of the data has to be good enough to extract accurate light curves.

The lensed images being most of the time separated by only $1''$or $2''$, a telescope such as the HST would be needed. However, it is unrealistic for such monitoring campaigns to use that kind of a telescope. What we have at our disposal is an ensemble of several mid-sized telescopes of typically 1 to 2m of diameter and a resolution of around $0.''20$ per pixel[1] at best. So, in most cases, the lensed images are highly blended and contaminated by the lensing galaxy. What could help here of course is an adequate and efficient image processing technique. That is why we introduce hereafter the semi-automated reduction pipeline which includes deconvolution with the MCS algorithm (Magain, Courbin & Sohy, 1998).

This semi-automated reduction pipeline is a tool that aims at producing light curves merging images coming from any telescope involved in the COSMOGRAIL monitoring program. It has been first developed by Christel Vuissoz in the framework of her PhD thesis (Vuissoz, 2008). It consists in different scripts and programs in various languages such as Perl[2], Fortran[3], Bash[4] and PyRAF[5]. The latter is a command language for running IRAF[6] tasks that is based on the Python scripting language[7]. Some steps also require the use of the SExtractor (*Source Extraction*) software (Bertin & Arnouts, 1996). These different scripts have to be applied to the images in a certain order with some "hand works" in between. Most of them have been modified in the framework of the present thesis, first to adapt the pipeline to our operating system, then to adapt it to the Mercator telescope which images had never been used before by the collaboration. We have also introduced a new PSF determination algorithm, *PSFsimult* (see Sect. 5.3.4). Finally we have implemented a new way to measure the error bars on the final light curves.

The main steps of this pipeline are the following:

- the pre-reduction which includes flat fielding and correction from the bias,
- the alignment of all frames on a good quality reference frame,
- the aperture photometry on several stars to calibrate the frames in flux and the aperture photometry on the whole lensed system to check the variability of the quasar,
- the preparation for the deconvolution including cosmic ray detection and the acquisition of a good PSF for each frame,

[1] $0.''19$ per pixel in the case of the camera mounted on the Mercator telescope.

[2] `http://www.perl.org/about.html`

[3] `http://www.fortran.com/`

[4] `http://www.gnu.org/software/bash/`

[5] PyRAF is a product of the Science Software Branch at the Space Telescope Science Institute.

[6] IRAF stands for *Image Reduction and Analysis Facility* and is distributed by the National Optical Astronomy Observatories, which are operated by AURA, the Association of Universities for Research in Astronomy, Inc., under cooperative agreement with the NSF, the National Science Foundation.

[7] `http://www.python.org/`

- the simultaneous deconvolution of all the frames,
- the acquisition of the light curves for each lensed image.

These light curves are shifted in magnitude and in time between one another. An algorithm to measure these shifts can then be applied.

This semi-automated pipeline has been used by C. Vuissoz to obtain light curves for two systems, SDSS J1650+4251 (Vuissoz et al., 2007) and WFI J2033-4723 (Vuissoz et al., 2008), but also by another member of COSMOGRAIL on SDSS J1001+5027 (Asfandiyarov & et al., in preparation). In Part III, we apply our improved version on the data of HE 0435-1223 (Chantry & et al., in preparation) which come from three telescopes: Mercator, Euler and Maidanak. Also included is the work done in collaboration with G. Orban de Xivry on some Euler frames of WFI J2026-4536 in the framework of his master thesis which I co-supervised (supervisor: P. Magain).

6.2 Pre-reduction

Before trying to obtain a uniform set of frames despite the different telescopes involved, the raw data have to be pre-reduced. First we modify the headers with some useful information such as the filter used and the Heliocentric Julian Day[8] at the midpoint of the exposure. The pre-reduction itself consists in trimming each frame, correcting it from the bias, flat fielding it and subtracting the sky background level. Let us note that each telescope has its own particularities concerning this pre-reduction processes which are camera-dependent. Here are the details about each step:

1. **Trimming**: It consists in rejecting the parts of the image which do not come from the observation of the sky, such as the *prescan* region (see hereafter for a definition), and which are thus unuseful in terms of scientific results, as illustrated on Fig. 6.1.

2. **Correction from the bias**: To avoid any negative value in the output image, a positive offset of around 500 to 1000 ADU[9] per pixel is artificially added to the measured values. It is called the *bias*. The signal detected in case of no exposure is thus different from zero. That effect has to be corrected. There are two different ways of doing it. If the CCD contains a part called the *prescan* or *overscan* region (or both), the bias can be estimated on these regions and then subtracted from the scientific region of the frame (see Fig. 6.1). These regions are composed of a few columns of virtual pixels which do not exist on the CCD and are thus not exposed to the flux of photons collected by the mirror: these regions are created at the beginning and at the end of the reading out of the CCD. If the device does not create such regions, some extra frames have to be aquired with the shutter

[8] The *Julian Day* (JD) is the interval of time in days and fractions of a day since January 1, 4713 BC at noon in Greenwich, United Kingdom. The *Heliocentric Julian Day* (HJD) is the same as the JD but adjusted to the reference frame of the Sun. It can thus differ from the JD by as much as 8.3 minutes.

[9] An *Analogic to Digital Unit* (ADU) is the unit of measurement of counts on the detector.

closed and a zero exposure time so that the level of the CCD bias can be recorded. Some such frames can then be averaged on a certain period of time to get rid for example of the cosmic ray impacts, but this period should not be too long so that any change in the bias level is accurately accounted for. This frame is called a *master bias* and contains all the patterns present on the frame when the CCD is not exposed to light. An example of master bias is displayed on the left frame of Fig. 6.2. For Mercator and Euler telescopes, it is better to use the overscan region, the bias level and its pattern being significantly variable during a night of observation. For Maidanak, the overscan region is too small to be used. Bias frames are thus acquired every night.

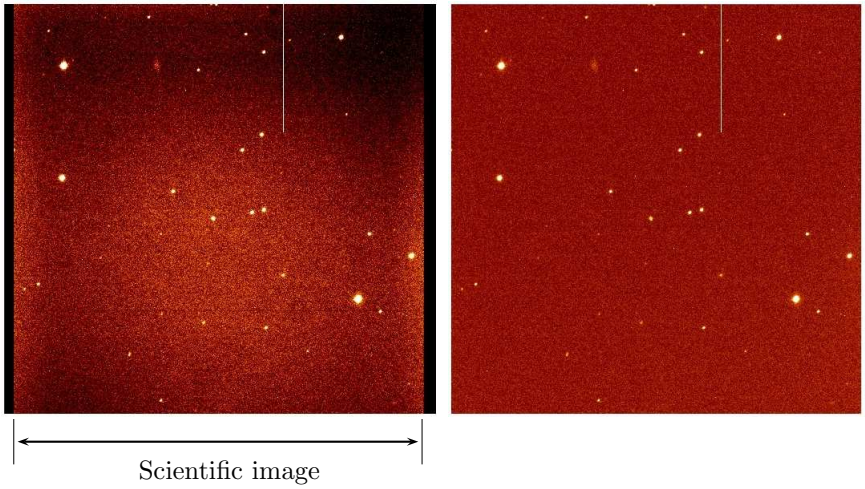

Figure 6.1: *Left*: example of a raw CCD frame from the Mercator telescope. The scientific frame is indicated. The black part to its left is the *prescan region* and the black columns to its right consitute the *overscan region*. It is also obvious that this frame has to be flat fielded. One of the columns in the right part of the image is partially white. It is caused by a very bright pixel, also called *hot pixel*, located in row number 1425 and column 1397 which contaminates the whole column during readout. *Right*: same frame after trimming, bias correction and flat fielding. The background, which is now uniform, still needs to be subtracted.

3. **Flat fielding**: Any CCD is not perfectly uniform. The behaviour of the pixels in terms of sensitivity, linearity, and so on, is variable across the detector. Moreover, the observed images can also be contaminated by vignetting, i.e. the light falling near the borders of the CCD can be partially lost. The frame is then brighter towards its center than towards its edges. Some dust particles can also be present for example on the filter and can then appear strongly defocused on the detector. These effects must be corrected for. That is why some flat fields are acquired on every night of observation. To obtain them, the CCD has to be illuminated with a light as spatially uniform as possible (flat distribution). A certain illumination

level must be reached, in order to have a good quality image of high S/N[10]. This can be done with the natural light from the sky after the sunset and before the astronomical night begins or between the end of the astronomical night and the sunrise. These are called *twilight flat fields*. It can also be done in observing a screen illuminated by an artificial and uniform light, the dome being closed. In that case, these frames are called *dome flat fields*. The obtained flat fields are then trimmed, bias corrected, cleaned from possible faint stars and cosmic ray hits and then averaged into a *master flat field* to reduce the noise. Every frame is then divided by this master flat field image, which has been previously normalized to a mean of 1. An example of master flat field is shown on the right frame of Fig. 6.2.

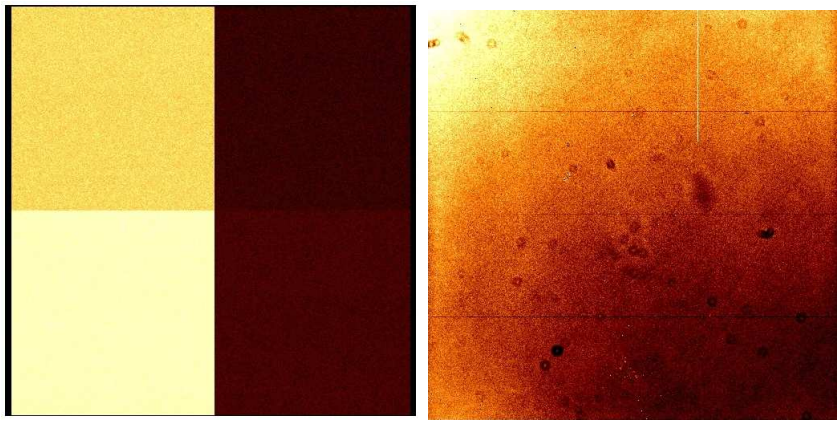

Figure 6.2: *Left*: example of a master bias for the SI camera mounted on the Maidanak telescope. *Right*: example of a master flat for the Merope camera mounted on the Mercator telescope.

4. **Sky subtraction**: Every astronomical image is composed of an undesired signal, between and underneath the interesting objects, coming from what is called the *sky background*. It is composed of scattered photons from the Earth atmosphere, sometimes from the zodiacal light[11], but also photons from very far and faint unresolved sources. The presence and phase of the moon can also cause this background level to be higher. The longer the exposure time of a frame is, the higher the sky level will be. SExtractor is thus applied to every frame to estimate this background level. To do so, a grid of cells is created on each frame, a median filter is applied on a scale of a cell of a few pixels to get rid of the stars. The background level in a cell is then estimated by the mean in this cell after a sigma-clipping at $\pm 3\sigma$[12]. This way, we construct one background map per frame that we can subtract from the corresponding image.

[10] Let us recall that S/N stands for *signal-to-noise ratio*.

[11] The *zodiacal light*, stronger in the mid-IR, is caused by the scattering of sunlight by dust particles revolving around the sun. These particles are likely to originate from comets and asteroids.

[12] A *sigma-clipping at* $\pm 3\sigma$ means that every pixel with a value deviating from the mean by 3σ or more is rejected and thus not taken into account in the final estimate of the mean in the cell.

Our data set is now composed of trimmed, bias corrected, flat fielded and sky subtracted images, but still possibly with different sizes, resolutions and orientations. However, before going any further in the process, it is necessary to check the image quality. SExtractor is applied to our data set to create a catalog of the objects present on each frame: with a fit of a Gaussian on the point sources of every frame we obtain the FWHM and ellipticity of each star in each frame. The seeing of the image is then set to the one of the star with the fifth best FWHM. This avoids any problem that would come from an abnormally small FWHM measured by SExtractor on an object that might not be a star. All the images with a seeing above $2\farcs5$ and/or a large ellipticity are visually checked. If one of them is identified as bad due to technical problems (telescope out of focus, troubles with the guiding star, ...) or to bad observing conditions (clouds, moon, ...), it is rejected from the data set. Fig. 6.3 shows two frames, acquired with the Merope camera on the Mercator telescope, that have to be rejected.

Figure 6.3: Example of two Mercator/Merope frames that have to be rejected because of technical problems during the exposure. *Left*: the PSF has a very special triangular/heart-shaped form, as highlighted by a zoom on two stars particularly affected. This is due to a change in shape and position of the primary mirror in its cell. Usually these parameters are kept constant and stable with pressurized air pads, unregarding the pointing position. *Right*: the quality of this frame is undoubtedly bad considering the elongated shape of what should appear as point sources. This is caused by a loss of the guiding star.

6.3 Alignment of the frames

The MCS deconvolution algorithm that we want to apply simultaneously to all the frames of one object requires the alignment of these frames with one another. In the case of data coming from one telescope it can be quite easy to do. It gets more complicated when the data come from different telescopes. In such a case, one of the telescopes as to be considered as the reference. The frames from other telescopes thus also need

to be transformed to the sampling of the images of the reference telescope. It seems reasonable to choose the telescope with the lower resolution as the reference one to avoid dividing the pixels of its detector into smaller ones.

Here are the different steps of this alignment phase:

1. **Reference frame and reference stars**: The first step is to choose a frame as the reference on which every other frame will be aligned. It is mandatory to pick an image of good quality, i.e. with a good seeing and a reasonably low PSF ellipticity, and to check it visually (no remnant sky background, not too noisy, ...). In case of different telescopes, the reference frame should be chosen amongst the reference telescope data set. Moreover, the object of interest should not be located too close to the edges of this reference frame to avoid any problem of alignment and any damaging border effect. Then, around ten stars have to be chosen in the reference frame. They are going to be used for the alignment and flux calibration. These reference stars should be well distributed across the field and isolated. Also they should not be too bright (far from the saturation level of the CCD), nor too faint (a relatively high signal-to-noise ratio is required), nor too far from the object of interest (so that they are present on every frame). Their coordinates and flux are then accurately measured with SExtractor and stored in a file.

2. **Telescope transformations**: In case of images acquired with another telescope than the reference one, some extra geometrical transformations might have to be applied. Indeed, the camera might be oriented differently on the sky so a *rotation* and a *mirror transformation* might have to be performed. The next step consists in obtaining frames with the same sampling as the reference frame, by rebinning each image in both directions (x and y) by the ratio between the reference and image pixel sizes. The images are then all trimmed to the size of the reference frame. That should be done carefully to try and keep the area of interest at the center of the frames.

3. **Remnant geometrical transformation**: Now that all the frames have the same sampling and roughly the same orientation, we want to perfectly align them on the reference frame. But first, we have to know the coordinates of the reference stars in every frame. To do so, we proceed as explained hereafter.

   A rough estimation of the shift is first found thanks to a cross-correlation between chosen subframes in the image to align and in the reference frame. Let us note that this operation is really time consuming. The peak in the cross-correlation image is supposed to be equal to the shift that would superimpose the two images. The next step is to apply this shift to the reference stars of the reference image, and to compare these new coordinates with every star in the catalog[13] of the image to align. We measure the distance between these stars and the new coordinates of the reference stars and then search for the minimum for each reference star. If these minimum distances are too large, then we know the cross-correlation has

[13]This catalog was created earlier by SExtractor.

failed. This happens quite often and the user has to remeasure the first estimate of the shift by hand. On the contrary, if the difference in position between the new coordinates of the reference stars from the reference frame and the corresponding stars found in the catalog of the image to align is small, then we have found the real reference stars coordinates in our non-reference frame.

Finally, in comparing these two sets of positions, a special IRAF task is capable of finding the best geometrical transformation to superimpose the image on the reference frame. It includes shifts, rotations and a possible scaling. We can then apply this transformation to our frame to obtain an image aligned on the reference frame. This process must be applied to each image of the data set.

6.4 Preliminary light curves

Our aim here is to obtain a light curve of the whole lensed system, i.e. the total flux coming from the lens and the two or four quasar images in the case of a double or a quad respectively, in order to check the global variability of the object. To do so we first need to compare the flux in each frame to the flux in the reference frame, thanks to some stars in the field, the reference stars, which flux is supposed to be constant. Indeed, as we want to use differential photometry accounting for the variations of brightness of the quasar in time and as every frame was acquired under different weather conditions and different airmasses[14], with different telescopes and sometimes different exposure times, a flux calibration is mandatory.

SExtractor is thus applied to the whole set of aligned frames to obtain the fluxes of the reference stars in a fixed aperture of around 20 to 40 pixels depending on the telescope, so that the radius of this aperture constitutes at least 3 times the seeing of most images. Let us note that at this stage, the seeing of an image is estimated by the lowest FWHM of the reference stars in the frame. To find the scale parameter of the calibration, the flux of each reference star of the frame is plotted against the flux of the corresponding star in the reference frame. These points are supposed to form a straight line (as the CCD has a linear response to light when far from saturation) passing through the origin (as a null flux will remain null in every frame). A linear regression on these points will thus give us the slope of the straight line, i.e. the calibration factor. The flux in every frame can now be divided by this scale parameter.

Let us note that the brightest reference stars have the largest weight in this regression so they must be chosen very carefully: far from the saturation of the CCD and not variable. To check if the stars are really constant, it is necessary to display their light curves to visually check them. If a star is variable, it is put aside and the linear regression has to be redone. When a point deviates too much from his neighbours, for example because of a cosmic ray hit, the corresponding frame is identified, visually checked and possibly removed from the data set.

Now that the flux of each frame is corrected by the calibration factor, we can check the variability of the total lensed system on the preliminary light curves, as shown in

[14]The *airmass* is proportional to the optical path length travelled by the light of celestial bodies through Earth's atmosphere before reaching a telescope.

magnitude on Fig. 6.4. The magnitude m is connected to the flux f by the following definition:

$$m = -2.5 \log_{10}(f) + C \tag{6.1}$$

where C is an arbitrary constant. This graph has been drawn for the Euler frames of the lensed quasar HE 0435-1223 (see Chapter 9). Each point on this graph corresponds to the mean value of an epoch of observation, the total number of frames being 856 for 172 epochs of observation. The light curves of the reference stars as well as the *mean star* (mean per epoch of all the reference stars) are also displayed. The photometric precision is estimated from the standard deviation of the global average of this mean star and is about 0.002 magnitude while the lensed system clearly varies over a magnitude scale of around 0.5. However, this variability does not represent the quasar intrisic variability as the curve was plotted from the flux of the complete system, i.e. from all the lensed images and the main lens galaxy.

We now have a set of pre-reduced, aligned and flux calibrated images.

6.5 Deconvolution

Before the simultaneous deconvolution of all the frames, there are a few more steps to complete. The first one consists in extracting the zone of interest, i.e. a square area surrounding the lensed quasar, from the full frames and in creating the sigma map that goes along. The second one consists in removing the cosmic ray hits thanks to an algorithm called L.A.Cosmic (van Dokkum, 2001). After that, the PSFs have to be created thanks to some stars selected in the field. We thus have to extract subimages containing these stars as well as their standard deviation maps. And they must also be cleaned from cosmic ray impacts as these could affect the PSF shape. Only then can the simultaneous deconvolution be performed.

6.5.1 Image extraction and creation of the sigma maps

The zone of interest, i.e. the lensed quasar, is extracted in an image of 64×64 pixels, which is a sufficient size to contain all the information needed, but not too large so that the running time of the deconvolution algorithm is kept reasonable. For each extracted image, we need to construct a standard deviation map which is going to be used in the deconvolution process to give a weight to each pixel. The noise in each pixel can be written as follows:

$$\sigma_i = \sqrt{\frac{I_i}{g} + \sigma_{sky}^2}\,. \tag{6.2}$$

The first term under the square root represents the photon noise, I_i being the intensity in pixel i and g the gain of the CCD, i.e. the number of electrons per ADU. The second term, σ_{sky}^2, is the standard deviation of the sky background. We estimate it on a portion of each frame where there is no obvious source of light and with a sigma-clipping at

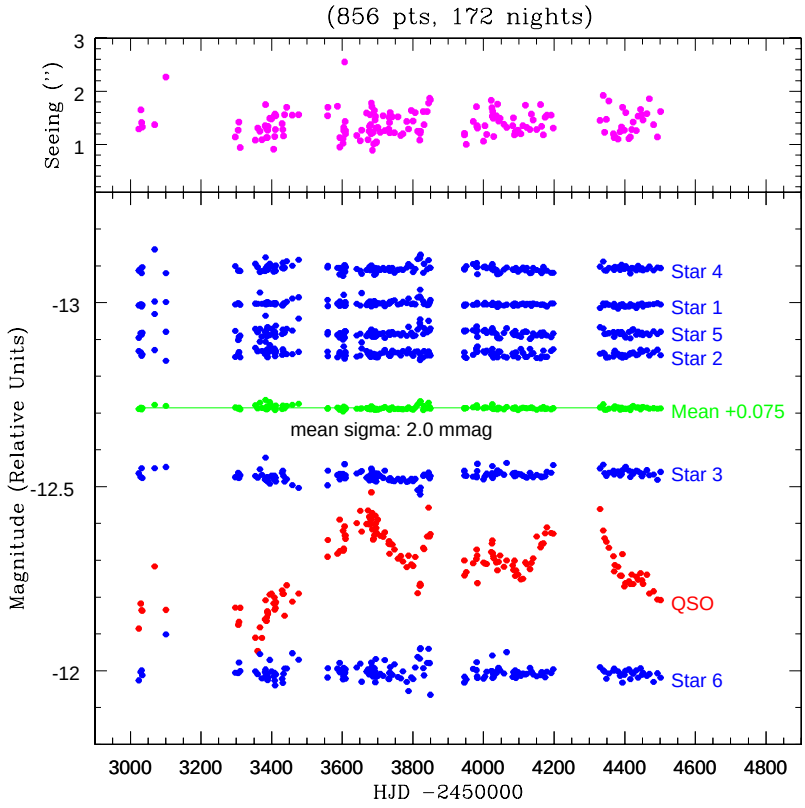

Figure 6.4: Preliminary light curves for the Euler frames of the lensed quasar HE 0435-1223 (see Chapter 9). The relative magnitude is given as a function of the HJD. Each point on this graph corresponds to the mean value of an epoch of observation. *Blue curves*: reference stars. *Red curve*: total flux of the lensed system. It is clearly variable. *Green curve*: mean per epoch of all the reference stars. *Magenta*: mean seeing per epoch.

$\pm 3\sigma$. It is defined as follows:

$$\sigma_{sky} = \sqrt{\frac{1}{N-1}\sum_{i=1}^{N}(I_i - \bar{I})^2} \tag{6.3}$$

where $\bar{I}$ is expressed as follows:

$$\bar{I} = \frac{1}{N}\sum_{i=1}^{N} I_i \,. \tag{6.4}$$

We then invert the sigma maps so that we can put to zero the inverted sigma value of any contaminated pixel (for example by a cosmic ray hit, see next section). This way,

such a pixel will have no weight in the deconvolution process and thus no influence at all on the final result.

6.5.2 Cosmic ray removal

Cosmic ray impacts are always very annoying on an astronomical image. There is no mean to prevent them from damaging the observations but there are means to identify them and to correct their effect or at least to ignore the damaged areas of a frame. Especially when it comes to photometric results, we must get rid of these cosmic ray hits because, if they are located on or next to an object of interest, they can seriously deteriorate the precision of the results.

We treat each frame individually with L.A.Cosmic, also called the *Laplacian Cosmic Ray Identification* algorithm, of van Dokkum (2001). This method relies on the sharpness of the edges of a cosmic ray rather than on the contrast between the entire cosmic ray hit and its surroundings. Therefore, it is able to detect cosmic ray impacts with very different morphologies and it allows a robust discrimination between the real cosmic ray hits and the undersampled point sources. The algorithm requires a few parameters such as the readout noise and gain of the CCD and the already subtracted background level. For further details, the reader is advised to check the original paper.

With that method, the image area contaminated by cosmic ray hits can be corrected, and the corresponding pixels in the inverted sigma map are set to zero so that they will not influence the results. An example of what L.A.Cosmic is capable to do is shown on Fig. 6.5. Let us note that in spite of the robustness of L.A.Cosmic it is advised to check the images with a high number of pixels considered as contaminated to be sure that the algorithm has not misclassified sources as cosmic ray impacts.

6.5.3 Acquisition of the PSFs

To create a PSF for each frame, four stars are chosen preferably amongst the reference stars, as they are constant and as we know their magnitude. Moreover, we should select them not too far from the lensed system in case of a variable PSF across the field. With four stars being differently positioned relatively to their central pixel, we can ovsersample the PSF by a factor of 2. Moreover we raise our signal-to-noise ratio. The images of the stars have to be extracted for every frame, cleaned from the possible cosmic ray hits and assembled in one image so that the algorithm *PSFsimult* (see Sect. 5.3.4) can create one PSF adjusted on the four stars at the same time. An example of this process is shown on Fig 6.6 in the case of a frame of HE 0435-1223 coming from the Mercator telescope. The residual map of the PSF determination is then visually checked for each frame to be sure that the algorithm has converged towards a reasonable solution.

6.5.4 Simultaneous deconvolution

Now that we have a PSF for each frame, we can simultaneously deconvolve all the images with the MCS deconvolution algorithm (Magain, Courbin & Sohy, 1998) as explained in Sect. 5.3. The PSFs are oversampled, and so will be the final deconvolved frame.

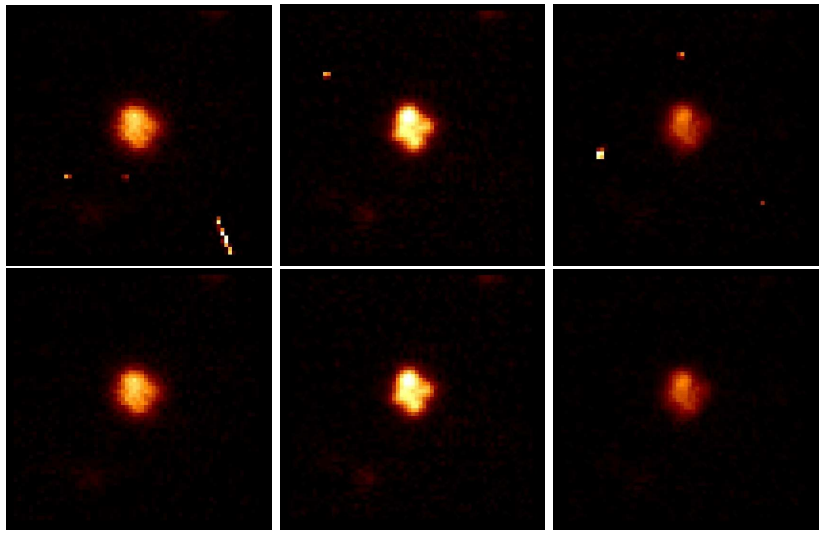

Figure 6.5: Here are some Mercator frames of the object HE 0435-1223. The original frames are displayed on the top row of the figure. We can see that these frames contain some cosmic ray hits of different shapes and sizes. The bottom row shows the same frames after cosmic ray rejection by the L.A.Cosmic algorithm.

Indeed, the dithering of the original frames allows to center the object on different parts of the detector and also on different parts of the central pixel. We can thus construct a virtual grid of pixels smaller than the original ones. An oversampling factor of 2 seems quite reasonable and generally gives good results.

First we start with a deconvolution of the reference frame only. It allows to adjust the positions of the sources and their flux. Once this is done, we simultaneously deconvolve all the frames with no numerical background, so that the intensities of the sources and the spatial shifts between the frames can be adjusted. Indeed, even if at this stage the images are aligned, there might remain a small spatial shift compared to the reference frame, due e.g. to the way the PSF has been centered on each subframe of stars. Then we restart the simultaneous deconvolution, this time with a numerical background and the previously fitted values, i.e. the spatial shifts and intensities, as starting points. We thus obtain an intensity for all the sources in all the different frames.

6.6 Final light curves

6.6.1 From MCS to physical fluxes

Before drawing the light curves, the output of the MCS algorithm needs to be turned into a real flux. Indeed, what we obtain is the maximum intensity of the point sources, i.e. I_0 in Sect. 5.3. Let us recall that every source in the final deconvolved frame is a

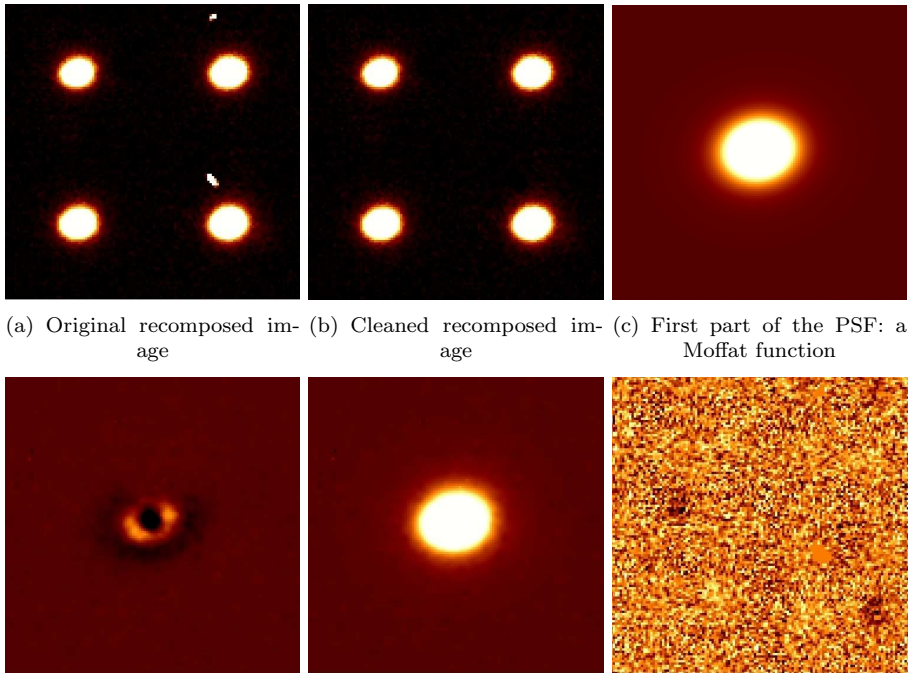

(a) Original recomposed image (b) Cleaned recomposed image (c) First part of the PSF: a Moffat function

(d) Second part of the PSF: a numerical component (e) Final PSF (f) Residual map

Figure 6.6: Example of the acquisition of the PSF for a frame acquired with the Mercator telescope, again in the framework of the monitoring of HE 0435-1223. Four stars are chosen amongst the reference ones. Their images are extracted from the frame and assembled into one single subframe as shown by *Frame a*. It is then cleaned from the cosmic ray hits (*Frame b*). Now the PSF can be created with *PSFsimult*: first a Moffat function is fitted on the four stars (*Frame c*), then a numerical component is added to this Moffat (*Frame d*). *Frame e* shows the final PSF which is the sum of *Frames c* and *d*. The last image (*Frame f*), displays the residual map in units of sigma (range: from -3σ to $+3\sigma$) which is satisfactory in this case.

Gaussian distribution which can be written as follows:

$$I(x,y) = I_0 e^{-(x^2+y^2)/2\sigma^2} \tag{6.5}$$

where σ is the standard deviation of the distribution (here proportional to the width of the point sources, see below). To obtain the total flux f_{tot}, this equation needs to be integrated. We thus have:

$$f_{tot} = \int_{-\infty}^{+\infty} \int_{-\infty}^{+\infty} I(x,y)\mathrm{d}x\mathrm{d}y = 2\pi\sigma^2 I_0 \tag{6.6}$$

where σ obeys the following relation:

$$w = 2\sqrt{2\ln 2}\ \sigma, \tag{6.7}$$

w being the FWHM of the PSF in the final deconvolved frame, i.e. 2 pixels, as chosen by the user. As we oversample by a factor of 2, one "old" pixel, also called *big pixel* (bp) is equal to four "new" pixels, also called *small pixels* (sp). We thus know that $\sigma_{sp} = 2\sigma_{bp}$ and the total flux is equal to:

$$f_{tot} = \frac{1}{2}\pi\sigma_{sp}^2 I_0 \tag{6.8}$$

$$= \frac{1}{2}\pi\left(\frac{w_{sp}}{2\sqrt{2\ln 2}}\right)^2 I_0 \tag{6.9}$$

$$= \frac{\pi}{16\ln 2} w_{sp}^2 I_0 \tag{6.10}$$

and $f_{tot} = 1.133\ I_0$ if w_{sp} is equal to 2 small pixels.

We now know the total flux for each lensed image in each frame. We then compute the mean flux per epoch that we transform in magnitude using Eq. 6.1.

6.6.2 What about the error on our measurements ?

Finally we need error bars on each flux measurement. There are typically two sources of errors. The first one is the *random* error and is due e.g. to the limited number of individuals in our sample (typically 5 frames per night) and to the photon noise. The second one is the *systematic* error and is globally affecting for example a whole night. The details are given hereafter for one lensed image.

This part of the semi-automated reduction pipeline has been completely modified from the initial version of Vuissoz (2008).

Random noise

The random noise on a flux measurement of one lensed image is estimated through the standard deviation of the mean over the epoch i of observation, the quasar being considered as constant during the fraction of the night dedicated to its observation. First we need to know the standard deviation of the population:

$$\sigma_i = \sqrt{\frac{1}{n_i - 1}\sum_{j=1}^{n_i}(f_{ij} - \bar{f}_i)}, \tag{6.11}$$

n_i being the number of frames acquired during epoch i, f_{ij} the flux of the lensed image in the j^{th} frame acquired during night i and $\bar{f}_i$ the mean flux of the lensed image in night i. σ_i is related to the standard deviation of the mean by:

$$\sigma_{mean,i} = \frac{\sigma_i}{\sqrt{n_i}}\,. \tag{6.12}$$

It has to be measured for each night. Let us note that this first component of the noise also includes some errors coming from the deconvolution process.

Systematic error

The systematic error is, as usual, not so easy to obtain. To try and estimate it, we simultaneously deconvolve the frames of a star in the field of the lensed system. The zone containing this star must be extracted from the frames, the sigma maps have to be calculated, the cosmic ray rejection to be applied and the flux calibration to be performed, just as for any other frame we use in the whole process. The chosen star has to be constant in time so we might consider picking a reference star, but not one of those used to create the PSF. This way we try to avoid a possible bias which could lead to underestimate the error.

After the deconvolution of the frames containing this star, we can calculate its mean flux per epoch i, $\bar{f}_{\star,i}$, and transform it into a magnitude as explained above, in order to obtain the light curve of this star. We then measure the standard deviation of the mean flux per night $\sigma_{\star,mean,i}$, as done above for the quasar. We also need the global mean $\bar{f}_{\star,tot}$ of this star over all nights.

To estimate the systematic error of night i, we compute the difference between the global mean and the mean of night i:

$$\sigma_{\star,tot,i} = |\bar{f}_{\star,i} - \bar{f}_{\star,tot}|. \tag{6.13}$$

This global error contains a systematic contribution but also a random one. To estimate the systematic part of it ($\sigma_{\star,syst,i}$), we have to remove the random part ($\sigma^2_{\star,mean,i}$), computed following Eqs. 6.11 and 6.12. Assuming the systematic error and the random error are statistically independent, we obtain:

$$\sigma^2_{\star,syst,i} = \sigma^2_{\star,tot,i} - \sigma^2_{\star,mean,i}. \tag{6.14}$$

This is possible only if $\sigma^2_{\star,mean,i} < \sigma^2_{\star,tot,i}$. The error $\sigma_{\star,syst,i}$ is used to estimate the systematic error $\sigma_{syst,i}$ on the quasar flux. This is valid only if we assume that the quasar and the star are affected by the same error (which is the case, e.g., if the systematic error affects the whole frame). When $\sigma^2_{\star,mean,i} \geqslant \sigma^2_{\star,tot,i}$, the systematic error is considered negligible and the total error on the quasar flux only includes the random noise.

Total error

To finally obtain the total error on the mean flux per epoch of a lensed image of a quasar, we have to quadratically add the random and systematic contributions:

$$\sigma^2_{tot,i} = \sigma^2_{mean,i} + w_i \sigma^2_{\star,syst,i} \tag{6.15}$$

where w_i accounts for the difference in flux between the star and the lensed image:

$$w_i = \left(\frac{\bar{f}_i}{\bar{f}_{\star,i}} \right)^2. \tag{6.16}$$

The whole process has to be applied to each lensed image of the quasar.

6.7 What comes next ?

When the semi-automated pipeline is applied to a data set for a lensed quasar, it allows to obtain the light curves with error bars for each lensed image. But this, of course, is not the final aim. What we really want is the time delays between these light curves. Several methods can be applied for that purpose, including the following ones:

- the minimum dispersion method of Pelt et al. (1998),
- the adjustment of a Legendre polynomial as in Kochanek et al. (2006),
- a numerical fit of the light curves as explained in Burud et al. (2001).

The first and second methods are actually being revisited and improved by M. Tewes, a PhD student at the EPFL or *Ecole Polytechnique Fédérale de Lausanne*, in the Swiss node of the COSMOGRAIL collaboration (Tewes & et al., in preparation). The third method (see Sect. 13.5) has been significantly improved thanks to the work of E. Eulaers, a PhD student at the University of Liège, in the Belgian node of the COSMOGRAIL collaboration (Eulaers, 2008; Eulaers & et al., in preparation). She is currently using the code in its newest form to obtain the delays from the already published light curves of eleven lensed quasars as explained in Chapter 13.

To be conscious that you are ignorant is a great step to knowledge.

Benjamin Disraeli (1804 - 1881)

7 ISMCS: the Iterative Strategy combined with the MCS algorithm

Contents

7.1 Why do we need a new strategy ?

To derive H_0 from lensed quasars and their time delay(s), accurate positional constraints for the sources and lens are mandatory. High resolution images are thus more than welcome. The CASTLES project (*Cfa-Arizona Space Telescope LEns Survey*[1]) aimed at characterising the geometry of every known multiply imaged quasar. That is why they acquired HST/NICMOS[2]-2 (NIC2) images of a large number of gravitationally lensed quasars. This data set is available to anyone in the HST archives. Our aim is to apply the MCS deconvolution algorithm to these images to improve their quality in getting rid of the instrumental profile, the ultimate goal being to obtain constraints as accurate as possible.

Unfortunately, as the field of view of NIC2 is not large, i.e. $19\farcs2 \times 19\farcs2$, we usually have no PSF star at our disposal on the frame, neither have we separate frames of stars acquired in the same conditions as the lensed systems. Moreover, there could be a mismatch of SED, i.e. *Spectral Energy Distribution*, between the PSF stars and the lensed quasar itself, which could modify the shape of the point sources especially through broad band filter. We thus have to use the information in the lensed images themselves.

[1] `http://www.cfa.harvard.edu/castles`

[2] Let us remind that NICMOS stands for *Near Infrared Camera and Multi-Object Spectrometer*.

Let us recall that the original version for deriving the PSF from blended point sources (Magain et al., 2007) assumes that a part of the image contains only point sources and no diffuse component, which is not the case here. Indeed, we know there may be some diffuse structures under or not far from the point sources such as arcs or rings and the lensing galaxy. The difficulty resides in separating these contributions from the point sources themselves. That is why we need a new method: the iterative strategy combined with the MCS deconvolution algorithm, also called *ISMCS* and detailed in the next section.

The first object we investigate and which we test the method on is the famous Cloverleaf gravitational lens, H1413+117, a quadruply imaged quasar (see next chapter). The iterative strategy gives astrometric and photometric measurements and reveals the primary lensing galaxy as well as a partial Einstein ring. The reliability of the method is checked on a synthetic image similar to H1413+117. In Part IV, ISMCS is applied to WFI J2033-4723, an object studied in detail by the COSMOGRAIL collaboration to obtain H_0, and to two samples of gravitational mirages. The first one is composed of seven lensed quasars currently monitored by COSMOGRAIL but with no previously measured time delays and the second one is composed of eleven lensed quasars with already measured time delays.

7.2 The method: ISMCS

The originality of the present method is that the same images are used to determine the PSF and to perform the deconvolution, i.e. to detect the diffuse background and to obtain the astrometry and photometry of the object. It works only if there are several point sources in the field: this makes it possible to distinguish the structures belonging to the PSF, and thus appearing in the vicinity of each point source, from the diffuse structures assumed not to be identical around each source.

This new method is based on an iterative strategy. We start with a first approximation of the PSF, in the case of HST images this PSF is constructed by the Tiny Tim software (Krist & Hook, 2004; see Fig. 7.1 for an example of a Tiny Tim PSF), with a sampling step two times smaller than the original one (i.e. oversampling by a factor of 2). That instrumental profile is deconvolved by the final Gaussian PSF $\mathcal{R}(\vec{x})$ in order to obtain the deconvolution kernel that we call $\mathcal{S}_0(\vec{x})$. This is a reasonable first approximation, although not accurate enough to obtain trustworthy deconvolved frames. Indeed, when using that deconvolution kernel to deconvolve the acquired signal which we call $\mathcal{D}_0(\vec{x})$, the result shows significant structures around each point source, clearly demonstrating that the Tiny Tim PSF departs from the actual one. An example is shown on Fig. 7.2: it is the simultaneous deconvolution of four frames of the Cloverleaf gravitational lens[3] through the F160W filter. The ring-like structures due to the insufficient accuracy of the Tiny Tim PSF are obvious.

For all these reasons we proceed as follows:

1. First, for each individual image, we determine an improved PSF $\mathcal{S}_1(\vec{x})$ following

[3]See Sect. 8 for details on this object.

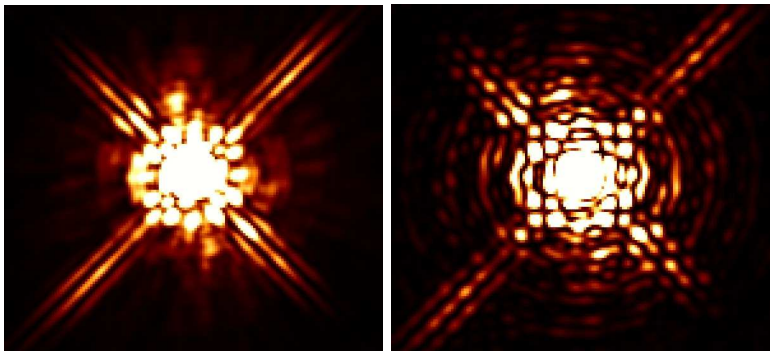

Figure 7.1: PSF constructed by the Tiny Tim software for two filters available on NIC2. They are considerably different. However, we can easily notice that they both have complex structures including spikes. *Left*: a PSF for the F160W filter, which will be defined in the next chapter. *Right*: a PSF for the F180M filter, also defined in the next chapter.

the method described in Sect. 5.3.4 (*PSFsimult*, Magain et al., 2007). This is done by adding a numerical component to the approximate PSF $\mathcal{S}_0(\vec{x})$ (here, the deconvolved Tiny Tim PSF) so that the observed image $\mathcal{D}_0(\vec{x})$ is reproduced better. But, since this method assumes that the image consists of point sources only, and since our object is supposed to contain diffuse structures, a part of them will be wrongly included in the improved PSF $\mathcal{S}_1(\vec{x})$. If the structures of the diffuse component were identical around each point source, they would be entirely included in the new instrumental profile. On the other hand, assuming that the quasar is quadruply lensed, and if the background was completely different around each of the point sources, only around 25% of it would be included in the PSF. In practice, a variable fraction of it contaminates the PSF. As long as that fraction is below 100%, our iterative procedure will allow improvements of the results.

2. We then use the once-improved PSFs $\mathcal{S}_1(\vec{x})$ to perform a simultaneous deconvolution of all the frames. Let us insist on the fact that each image has its own instrumental profile: $\mathcal{S}_1(\vec{x})$ varies slightly from frame to frame. The simultaneous deconvolution allows to obtain a first approximation of the diffuse component, $\mathcal{H}_1(\vec{x})$, which, by construction, is the same in each image. However, since a part of the smooth structures was included in the PSFs $\mathcal{S}_1(\vec{x})$, $\mathcal{H}_1(\vec{x})$ is only the remaining part of the actual background.

3. Third, we subtract $\mathcal{H}_1(\vec{x})$, reconvolved and resampled to the initial resolution, from the original images. This gives us a new version of the observed images, $\mathcal{D}_1(\vec{x})$, with point sources less contaminated by the diffuse structures. The first iteration is over.

4. To begin the second iteration, we determine a new set of PSFs $\mathcal{S}_2(\vec{x})$ on the images $\mathcal{D}_1(\vec{x})$. As they contain a lower amount of background than $\mathcal{D}_0(\vec{x})$, the new PSFs are indeed less contaminated by diffuse structures.

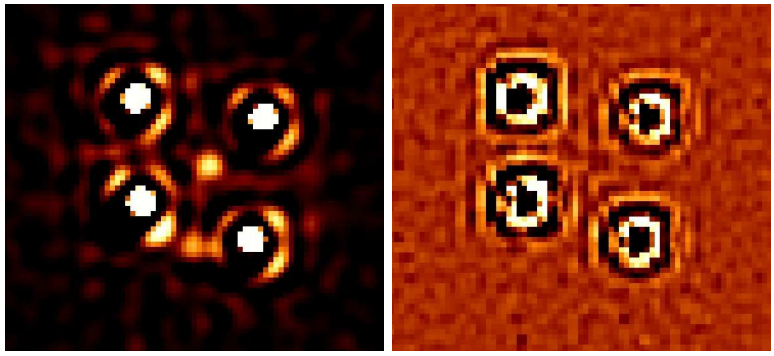

Figure 7.2: Frame of the *Cloverleaf* resulting from a simultaneous deconvolution of four HST/NIC2 frames using Tiny Tim PSFs. *L*eft: deconvolved image. *R*ight: residual map (difference between the model and the original frame in units of sigma) of the deconvolution. The remnant structures around each point source is obvious and is due to the use of inappropriate PSFs.

5. The simultaneous deconvolution of the original images $\mathcal{D}_0(\vec{x})$ with the new PSFs $\mathcal{S}_2(\vec{x})$ allows to get an improved version, $\mathcal{H}_2(\vec{x})$, of the diffuse background.

6. We subtract $\mathcal{H}_2(\vec{x})$ from the original images $\mathcal{D}_0(\vec{x})$. This closes the second iteration.

7. This iterative process is continued until no significant improvement is observed. Usually around 3 to 5 iterations are necessary, depending on the structures under the sources.

Sometimes this process needs to be adapted. For example when the diffuse background is not faint enough compared to the intensities of the sources, it is better to start with a simultaneous deconvolution of the data with deconvolved the Tiny Tim PSFs than to try and improve these PSFs on the strongly contaminated point sources. Before subtracting the background obtained thanks to the Tiny Tim PSFs from the original images, it is necessary to clean it from the artifact structures created to compensate the inaccuracies in the Tiny Tim PSFs. This demands some intuition to decide what is part of the real background and what is not. At this stage it is always better to remove too many structures than too few because it is always possible to recover them in the following iterations.

This iterative strategy, ISMCS, is tested on a real example in the next chapter and then illustrated on a few cases in Part IV.

Not to be absolutely certain is, I think, one of the essential things in rationality.

Bertrand Russell (1872 - 1970)

8 Test of ISMCS on the Cloverleaf gravitational lens

The content of this chapter along with the details of the method exposed in the previous chapter have been published in *Astronomy & Astrophysics* under the following title: "*Deconvolution of HST images of the Cloverleaf gravitational lens. Detection of the lensing galaxy and a partial Einstein ring*" (Chantry & Magain, 2007).

8.1 Introduction

Four years after its discovery in 1984 by Hazard et al., the QSO H1413+117 was identified as a gravitational lens by Magain et al. (1988). This system, consisting in four components of comparable brightness separated by around $1''$, is better known as the *Cloverleaf*. It is also one of the brightest quasars amongst the BAL, or *Broad Absorption Line*, class, with a redshift of 2.558 and an apparent visual magnitude of 17. The lensing galaxy was detected by Kneib, Alloin & Pello (1998) from a careful PSF subtraction on near-infrared HST images. Let us apply ISMCS on the same set of images and on another one which was acquired through a different filter. We will see that it permits to obtain a more accurate astrometry of the system and a better characterization of the lensing galaxy. Moreover, it will also allow the detection of additional structures, such as parts of an Einstein ring.

8.2 HST/NIC2 images

The first set of HST data (PI: E. Falco) was obtained on the 28^{th} of December 1997 by the camera 2 of NICMOS through the F160W filter, a wide band filter corresponding approximately to the near-IR H-band. We use the four calibrated images, i.e. treated by CALNICA, the HST image reduction pipeline. Each of them has an exposure time

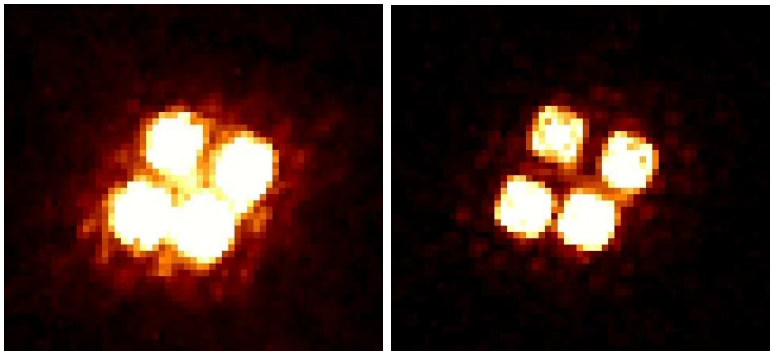

Figure 8.1: Combined HST/NIC2 images of the Cloverleaf. The structures of the PSF are obvious. North is to the top and East to the left. *L*eft: combination of the 4 calibrated and reduced images obtained with the F160W filter. *R*ight: combination of the 8 calibrated and reduced images obtained with the F180M filter.

of 640s and a mean pixel size of $0''.07510$ according to the version 6.3 of the Tiny Tim software (Krist & Hook, 2004). These images were obtained in the MULTIACCUM mode: each of them is a combination of several samples, 19 in the present case. A combination of these four images is shown on the left panel of Fig. 8.1.

The second set of frames (PI: D. A. Turnshek) was obtained on the 10^{th} of July 2003 with the same instrument but through the medium-band F180M filter. As for the F160W filter, we use the calibrated images, here eight frames, four of them being a combination of 18 samples and the other four being a combination of 16 samples. The first four have an exposure time of 576s each and the other four an exposure time of 448s each. The mean pixel size is, again according to the Tiny Tim software (Krist & Hook, 2004), $0''.07568$. A combination of these eight calibrated frames is shown on the right panel of Fig. 8.1.

The wavelength ranges of these two filters are partly superimposed: the passband of the F160W filter is $1.4\ \mu m \leq \lambda \leq 1.8\ \mu m$ while it corresponds to $1.76\ \mu m \leq \lambda \leq 1.83\ \mu m$ for the F180M filter. The latter was chosen in order to include the oxygen [OIII] forbidden line doublet (499 - 501 nm) at the redshift of the QSO.

The image reduction is divided into two parts: the image cleaning and the calculation of the sigma images, i.e. the maps of the standard deviations of the pixel intensities. The first step of the first part consists in computing the intensities in counts per pixel. The second step consists in removing the sky background, which is mostly caused by the *zodiacal light*[1] at short wavelengths and by the thermal emission from the telescope at longer ones. As the NIC2 detector is composed of four quadrants, it is necessary to subtract a different value for each of them. These four values are derived from parts of the image where no obvious light source is observed.

The second step consists in the calculation of the sigma maps. We start from the sigmas obtained by the pipeline CALNICA. Two effects are then corrected. First, we

[1]Let us recall that the *zodiacal light* is caused by the scattering of sunlight by dust particles revolving around the sun.

take into account the underevaluation of the standard deviation for the negative pixels. To do that we replace all negative intensities in the original frames by a null value and calculate a new sigma. The difference between such a sigma and a sigma calculated on the unmodified original frames is then added to the CALNICA sigma. Second, we make use of the HST flag files indicating bad pixels, e.g. cold or hot pixels. It allows us, using the inverted sigma maps, to put the statistical weight of such pixels to zero so that the information they provide has no influence on the deconvolution.

Let us mention that, at the time of these tests, we did not remove the cosmic ray impacts from the images during the reduction process. We used the deconvolution residuals (see Sect. 5.3) to spot the pixels likely contaminated by a cosmic ray hit. We then put the inverted sigma value of such pixels to zero.

8.3 Deconvolution with ISMCS

We then apply ISMCS to both sets of reduced images in order to improve their resolution and sampling and, most importantly, to detect any significant extended structure which might be hidden by the complex PSF. In order to improve the resolution while keeping a well-sampled light distribution, we use a sampling step 2 times smaller than the original pixel size and we choose, as the final PSF $\mathcal{R}(\vec{x})$, a Gaussian with a FWHM of 2 pixels in the new sampling grid[2]. Let us recall that, since the HST PSF varies e.g. with the thermal breathing of the telescope, and since the object is located on different parts of the detector at each exposure, each original frame has its own individual PSF.

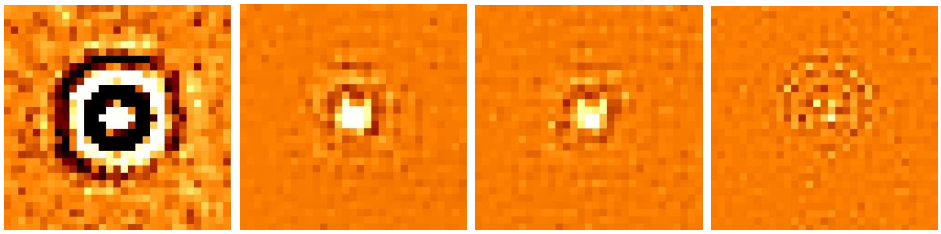

Figure 8.2: Corrections applied to the PSFs for one image of the F160W data set at different stages of the process. The colour scale goes from -1.3% (black) to +1.3% (white) of the peak intensity of the Tiny Tim PSF. *L*eft: corrections to the PSF at the first iteration, starting from the deconvolved Tiny Tim PSF. *M*iddle left: corrections at the second iteration. *M*iddle right: corrections at the fourth iteration. *R*ight: corrections at the last iteration.

For the F160W data set, seven iterations of ISMCS are necessary while, for the F180M data set, convergence is reached after three iterations. This difference is due to the fact that the diffuse background is less intense when compared to the point sources in the F180M filter. Figs. 8.2 and 8.3 illustrate the evolution of the PSF in the iterative scheme: they show the corrections applied at different stages for the two data sets. We can see that the first step of the iterative process changes significantly the PSF obtained

[2]Four pixels in the new grid correspond to one pixel on the original frame. Indeed, the oversampling is applied in both directions, x and y.

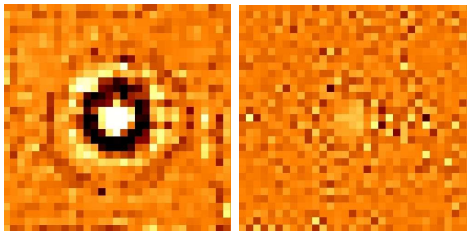

Figure 8.3: Corrections applied to the PSFs for one image of the F180M data set at different stages of the process. The colour scale goes from -4.8% (black) to +4.8% (white) of the peak intensity of the Tiny Tim PSF. *L*eft: corrections to the PSF at the first iteration, starting from the deconvolved Tiny Tim PSF. *R*ight: corrections at the last iteration.

with Tiny Tim. The next steps make smaller adjustments and correct smaller details. In the case of the F180M filter, it is obvious that three iterations are sufficient, as the corrections already become negligible after the second step. The same happens after the fifth iteration in the F160W filter.

Now that we have an idea about the evolution of the successive corrections applied to obtain a trustworthy instrumental profile, we can focus on the results of the deconvolution itself. Figs. 8.4 and 8.5 show the deconvolved frames from the last iteration, respectively for the F160W and the F180M data set. A partial Einstein ring, which is the gravitationally lensed image of the quasar host galaxy, and the lensing galaxy can be seen, for both sets, on the background frame (top right) and on the background plus point sources frame (top left). The lens galaxy appears less intense compared to the point sources in the F180M filter, which is expected as it is a medium-band filter including the [OIII] emission lines (499 - 501 nm) at the redshift of the QSO, but no emission line at the redshift of the lens. The partial Einstein ring also has a different structure: compared to the F160W filter, it appears more intense in the F180M filter close to the point sources and less intense in between them. This suggests that the NLR[3] is more compact than the global lens galaxy, which could have been expected.

The mean residual map (see bottom left panel of Figs. 8.4 and 8.5) guides us through the different steps of the iterative process. We can see that, for both sets, at the last iteration, there is some structure left under the point sources, but nothing systematic, and there is nearly no remnant structure where the ring and the lensing galaxy are located. The fact that the residuals under the four point sources have very different shapes suggests that they are not due to errors in our instrumental profile, but rather to small PSF variations from one QSO image to the other.

As already mentioned, the reduced chi square χ_r^2 is also a very helpful tool to know if the process has converged towards the best solution possible. We calculate it for each set and each iteration step in the zone of interest, i.e. in a square containing the four point sources and the extended structures (ring plus lens). In the last iterations it barely changes: the PSF is not improved significantly anymore and the iterative process has converged. We obtain a χ_r^2 of 3.845 for the F160W data set after the

[3]To learn more about the *narrow line region*, see Sect. 3.6.

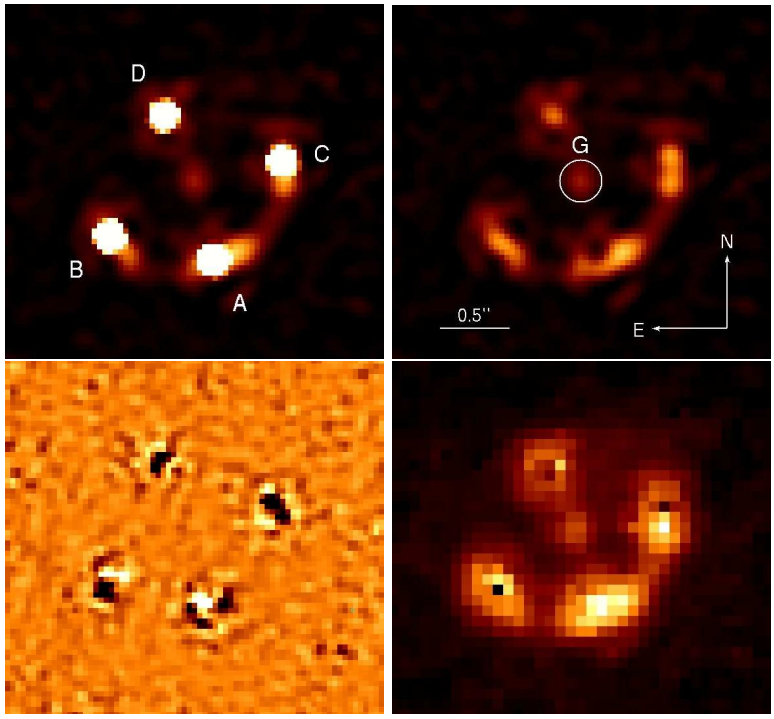

Figure 8.4: Results from the last simultaneous deconvolution for the F160W data set. *Top left*: deconvolved image, i.e. point sources plus smooth background; the point sources are labeled as in Magain et al. (1988). *Top right*: smooth background common to all images of the set where the lensing galaxy G is encircled. *Bottom left*: mean residual map of the simultaneous deconvolution, the scale ranging from -3σ in black to $+3\sigma$ in white. *Bottom right*: image of the background reconvolved to the original resolution and sampling.

seventh iteration, and a χ^2_r of 1.125 for the F180M data set after the third iteration, which is very satisfying. Let us mention that these values are computed taking into account all images of a given set, so that any slight incompatibility between some of the input images results in an increase of the χ^2 that cannot be lowered by changing the model. A final χ^2_r of 1 means that the model is perfectly compatible with all the images of the set. It implies that all images are statistically compatible with each other and that the PSFs are perfectly known. Any inaccuracy in the data acquisition or reduction will also increase the final χ^2.

8.4 Astrometry and photometry

Table 8.1 gives the relative astrometry and photometry for the quasar images as well as for the lens, in the F160W filter (top table) and the F180M filter (bottom table). The coordinates are measured in arcseconds relative to component A (see Figs. 8.4 and 8.5).

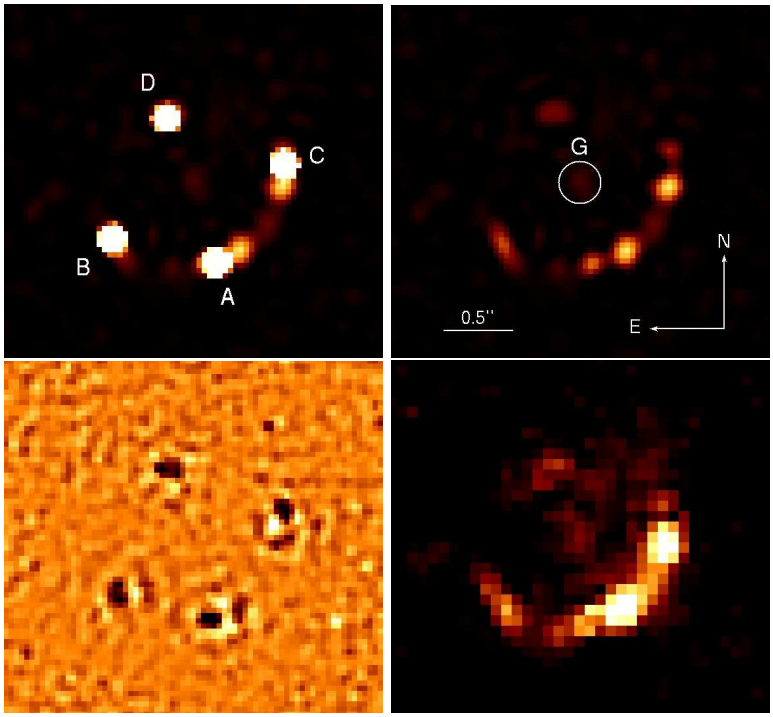

Figure 8.5: Results from the last simultaneous deconvolution for the F180M data set. The comments made in the caption of Fig.8.4 remain valid.

The apparent magnitudes are given in the Vega system.

As the geometric distortions of the camera 2 of NICMOS depend on the position of the object on the CCD, their proper corrections require an individual deconvolution of each image. We obtain the position of each point source, relative to source A, on each individually deconvolved frame and we correct them from the distortions according to the formulae given in the NICMOS Data Handbook (STScI NICMOS Group, 2007). We can then compute average values and the standard deviation of the mean for each measurement: this accounts for the errors inherent to the deconvolution, i.e. *internal error bars*, but no external systematic error is included. For the point sources, this gives more accurate results than a simultaneous deconvolution with a mean correction on the coordinates. However, this is not true for the lensing galaxy and the Einstein ring. As these objects are faint, it is better to rely on the results of the simultaneous deconvolution, where the signal in the whole set of images is used to constrain their shape. A mean geometric correction estimated from the corrections on the individual frames is applied.

The astrometric precision for the point sources is about 0.5 milliarcsecond (mas) in the F160W filter and 0.3 milliarcsecond in the F180M filter. The higher precision in the medium-band filter may be explained by the fact that the partial ring is less

	F160W		
ID	ΔRA (″)	ΔDEC (″)	Magnitude
A	0.	0.	15.760 ± 0.002
B	0.7426 ± 0.0002	0.1686 ± 0.0004	15.863 ± 0.005
C	-0.4930 ± 0.0003	0.7135 ± 0.0004	16.143 ± 0.004
D	0.3526 ± 0.0007	1.0394 ± 0.0004	16.400 ± 0.006
G	0.1365 ± 0.0024	0.5887 ± 0.0035	20.527 ± 0.037
	F180M		
ID	ΔRA (″)	ΔDEC (″)	Magnitude
A	0.	0.	15.548 ± 0.006
B	0.7458 ± 0.0003	0.1688 ± 0.0002	15.650 ± 0.009
C	-0.4917 ± 0.0003	0.7105 ± 0.0003	15.902 ± 0.004
D	0.3532 ± 0.0003	1.0400 ± 0.0002	16.218 ± 0.007
G	0.1255 ± 0.0036	0.6192 ± 0.0069	22.182 ± 0.101

Table 8.1: Relative astrometric and photometric measurements for the four components and lensing galaxy of the Cloverleaf. The results in the top table comes from the application of ISMCS to the F160W data set, while those in the bottom table come from the application of ISMCS to the F180M data set. The right ascension (RA) and the declination (DEC) are given in arcseconds relative to component A. The photometry is given in apparent magnitude in the Vega system. The internal $\pm 1\sigma$ error bars are also indicated (see text for an explanation on how they are derived).

extended than on the F160W frame and the lens galaxy appears fainter relative to the point sources: they thus have a lower contribution to the error bars.

Of course, the precision on the position of the lens galaxy is significantly lower. This is due to the facts that (1) it is a diffuse angularly small object, (2) it is much fainter than the point sources (about 4.5 mag in the F160W filter and 6.4 mag in the F180M filter) and (3) it is mixed with the PSF wings of the point sources.

Table 8.1 also shows that the results derived from both filters are not compatible within their internal error bars. As the geometry of the system is not expected to vary on the time scale of a few years, this disagreement suggests that the actual error bars are significantly larger than the internal ones. The causes may be diverse. As the two sets of data were acquired six years apart, with a different orientation of the HST and thus of the detector, and in different cycles of NICMOS (pre- and post-NCS, NICMOS Cooling System[4]), the geometrical distortions are different from the two sets and may not have been completely taken into account. The uncertainties concerning the coefficients of the formulae used to correct for the geometrical distortions, as given in the NICMOS Data Handbook (STScI NICMOS Group, 2007), account for an error of the order of 0.1 milliarcsecond in each filter, which is about ten times smaller than the total error we obtain (see next paragraph). It is thus possible that a residual distortion

[4]The instrument ran out of nitrogen coolant sooner than expected in January 1999. During a Hubble Service Mission in 2002, a cryocooler was installed on board the HST: it now cools NICMOS through a cryogenic (below 123 K) neon loop.

of the NICMOS images remains, at the 10^{-3} level of accuracy, i.e. 0.001 arcsecond per arcsecond. An imperfect separation of the partial Einstein ring from the point sources in the deconvolution process as well as some inaccuracies in the PSF recovery may also play a role.

The actual total errors are computed by comparing the point source positions derived from the two data sets. First the average difference in position between the point sources amounts to 1.4 mas. Then, assuming that the errors in both data sets contribute equally to this difference, we derive a value of $1.4/\sqrt{2} \approx 1$ mas, i.e. 0.013 pixel, for the estimated accuracy in the position of the point sources.

Our measurements are compared to those of Magain et al. (1988) and Turnshek et al. (1997) given in Table 8.2. The latter were derived from images acquired with other HST instruments, WFPC (*Wide Field Planetary Camera*) and WFPC2 (*Wide Field Planetary Camera 2*), and with a completely different image processing technique, while the first ones were obtained from much lower resolution ground-based images. For both sets of results we indicate the $\pm 1\sigma$ error bars. Let us mention that they do not appear on the original paper of Magain et al. (1988). The average difference between our results and those of Magain et al. (1988) amounts to 4 mas, which is close to the error bars on the measurements performed by these authors. The same comparison with Turnshek et al. (1997) gives an average difference of 2.6 mas, also compatible within their error bars.

	Magain et al. (1988)		Turnshek et al. (1997)	
ID	ΔRA ($''$)	ΔDEC ($''$)	ΔRA ($''$)	ΔDEC ($''$)
A	0.	0.	0.	0.
B	0.753 $\pm$ 0.006	0.173 $\pm$0.006	0.744 $\pm$ 0.003	0.172 $\pm$ 0.003
C	-0.496 $\pm$ 0.004	0.713 $\pm$ 0.003	-0.491 $\pm$ 0.003	0.716 $\pm$ 0.004
D	0.354 $\pm$ 0.004	1.043 $\pm$ 0.004	0.355 $\pm$ 0.003	1.043 $\pm$ 0.012

Table 8.2: Relative astrometry of the Cloverleaf from Magain et al. (1988) and from Turnshek et al. (1997). The two coordinates are given in arcseconds relative to component A. The $\pm 1\sigma$ error bars are also indicated.

The primary lens, a single galaxy, was detected in 1998 by Kneib et al. After a PSF subtraction of the four lensed images, they obtained the following position for the lensing galaxy relative to source A:

$$\mathrm{RA} = 0.112'' \ \pm \ 0.02''$$

and

$$\mathrm{DEC} = 0.503'' \ \pm \ 0.02''.$$

Considering their error bars, this result is compatible with ours in right ascension as the difference amounts to $\Delta\mathrm{RA} = -0.025''$. But this is not true for the declination: $\Delta\mathrm{DEC} = -0.086''$. Possible systematic errors, in particular on the lens position, are investigated in the next section.

Finally, as already mentioned, the intensity distribution along the partial Einstein ring is significantly different in the two filters: it is more regular in the wide band

filter, F160W, than in the narrower one, F180M. As the latter was chosen to emphasize the [OIII] emission lines (499 - 501 nm) and thus to obtain a mapping of the narrow emission line region in the quasar host galaxy, such a difference is not unexpected. The partial ring observed in the broad-band filter is a distorted image of the full host galaxy, while the narrow emission-line region is more prominent in the F180M filter. In particular, two bright knots are seen close to images A and C (see Fig. 8.5). These knots cannot correspond to deconvolution artifacts, which might be caused, e.g., by an imperfect modeling of the PSF. Indeed, such artifacts would be expected around all point sources and at the same position relative to these point sources, which is not the case. Moreover, the observed positions are in agreement with the inverted parity expected between two neighbouring images in such a lensed system. These bright knots must therefore correspond to the emission line region in the quasar host galaxy, which is thus probably brighter on one side than on the other. A detailed modeling of the system, including an inversion of the lens equation, should allow the reconstruction of an image of the host galaxy and of the narrow line region. This would be the first time one could map the host and narrow line region of a BAL QSO at such a high redshift.

8.5 Synthetic image

The accuracy of our results is further tested by carrying the same procedure on a synthetic image having characteristics similar to those of the HST/NIC2 F160W images of the Cloverleaf: four point sources, a faint lensing object and a partial Einstein ring (see left frame of Fig. 8.6). This synthetic image was convolved with a PSF similar to the actual one, but unknown to the test performer. Random noise was then added to reach a S/N comparable to that of the real combined HST image (see right frame of Fig. 8.6).

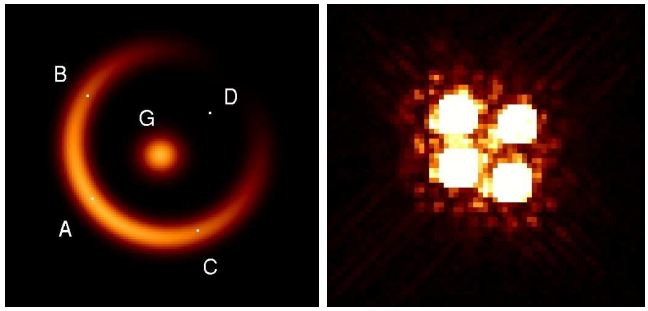

Figure 8.6: *Left*: synthetic image of a gravitationally lensed quasar with a configuration similar to the Cloverleaf: four point sources, a faint lens and a partial Einstein ring. The orientation is the same as in the original F160W Cloverleaf images. *Right*: the same image convolved with a HST-type PSF unknown to the test performer.

The results obtained after three iterations ($\chi^2_r = 1.206$) are presented on Fig. 8.7, which displays the background, the point sources plus background and the residual

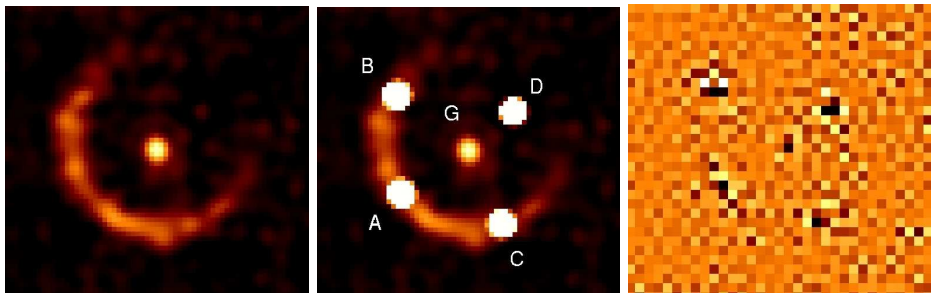

Figure 8.7: Results of the last iteration for the artificial Cloverleaf. *L*eft: diffuse background. *M*iddle: diffuse background plus point sources. *Right*: residual map of the deconvolution, the scale ranging from -3σ in black to $+3\sigma$ in white.

maps. Some remnant structures can be seen under the point sources on the residual map, but much fainter than on the one of the actual frames: only one PSF, constant throughout the field, was used to create the convolved synthetic image, which made it easier to recover it with ISMCS.

In general, the flux in the background (ring + lens) is recovered within 4%, which can be considered as excellent since this diffuse background is very weak compared to the point sources. However, because of the smoothing constraint, the deconvolved ring and lens appear slightly flatter than the original ones. The largest differences are found under the brightest point source (A), where the deconvolved ring is about 43% below the original one.

Table 8.3 summarizes the astrometry of this artificial Cloverleaf: the first pair of columns present the measurements made on the final deconvolved image resulting from ISMCS, the second pair of columns present the results when using a deconvolved Tiny Tim PSF in a unique deconvolution, and the last one the measurements made on the original image. The differences between the positions obtained for a particular source reach a maximum of about 0.3 mas with a mean value around 0.1 mas, which is slightly better than the internal precision estimated in Table 8.1 and significantly more accurate than the ones obtained from the deconvolution with the Tiny Tim PSF. On the other hand, the lens galaxy position is not as accurate as the ones of the point sources: the

	ISMCS		Tiny Tim		Original image	
ID	ΔRA (″)	ΔDEC (″)	ΔRA (″)	ΔDEC (″)	ΔRA (″)	ΔDEC (″)
A	0.	0.	0.	0.	0.	0.
B	0.7719	0.1770	0.7726	0.1755	0.7718	0.1767
C	-0.4538	0.7140	-0.4538	0.7129	-0.4538	0.7138
D	0.3913	1.0480	0.3921	1.0483	0.3913	1.0479
G	0.1826	0.6151	0.1787	0.5877	0.1819	0.5940

Table 8.3: Relative astrometry of the artificial Cloverleaf. The two coordinates are given in arcseconds relative to component A. See text for details.

maximum difference amounts to 20 milliarcseconds (i.e. a quarter of a pixel). Indeed, the position of such very faint and angularly small diffuse objects is rather sensitive to inaccuracies in the PSF: any error in the wings of a bright point source PSF may have impacts on the faint neighbouring objects. In the case of the real Cloverleaf, given these possible sources of errors and the results of the simulations, we estimate the accuracy on the lens galaxy position to amount to some 20 mas.

Part III

Light curves for two gravitational lenses from the COSMOGRAIL sample

The important thing is not to stop questioning.
Albert Einstein (1879 - 1955)

9 The quadruply lensed quasar HE 0435-1223

Contents

9.1 Introduction

This chapter will be part of a paper entitled "*COSMOGRAIL: the COSmological MOnitoring of GRAvItational Lenses IX. New time delays for the gravitational lens HE 0435-1223*" and currently in preparation.

The object of interest in this chapter is HE 0435-1223 (RA = 04:38:14.8999 and DEC = -12:17:14.3988, J2000) discovered by Wisotzki et al. (2000) during the Hamburg/ESO (*European Southern Observatory*) Survey (HES) for bright quasars in the southern hemisphere. Two years later, it was identified as a quadruply imaged quasar by Wisotzki et al. (2002). The redshift of the source is $z_s = 1.689$ (Wisotzki et al., 2000) and the one of the lens is $z_l = 0.4546 \pm 0.0002$ (Morgan et al., 2005). The quasar shows evidence for intrinsic variability which makes it a good candidate for determining the time delays between the different images. The local environment of the lensing galaxy has been studied in detail by Morgan et al. (2005) using HST/ACS (*Advanced Camera*

for Surveys) images and is thus well known: the lens of HE 0435-1223 lies in a spiral-rich group composed of at least 10 galaxies within 40″.

The symmetry of the image configuration implies short time delays, around a few weeks at most. That is an advantage to disentangle the intrinsic variability of the source from long-term microlensing effects. But it is also a limitation: we need very accurate and well-sampled light curves to be able to determine such short delays.

The study of HE 0435-1223 as a lensed system has already been carried out by Kochanek et al. (2006). They measured the following time delays over two years of optical monitoring: $\Delta t_{AD} = -14.37^{+0.75}_{-0.85}$, $\Delta t_{AB} = -8.00^{+0.73}_{-0.82}$ and $\Delta t_{AC} = -2.10^{+0.78}_{-0.71}$ days. They fixed H_0 to a value of 72 ± 7 km s^{-1}Mpc^{-1} (Freedman et al., 2001) and derived constraints on the lens galaxy. They found that the latter must have a rising rotation curve at the radius of the lensed images and a non-constant mass-to-light ratio. Moreover high dark matter surface densities are required in the halo.

In this chapter we apply the revised semi-automated reduction pipeline to the COSMOGRAIL data and ISMCS to HST/NIC2 images of HE 0435-1223.

9.2 Monitoring

9.2.1 Observational material

HE 0435-1223 was monitored during four years, from January 2004 to February 2008, through the R-band filter[1], using three different telescopes: the Swiss 1.2m Euler telescope located on the ESO La Silla site (Chile), the Belgian-Swiss 1.2m Mercator telescope located at the Roque de Los Muchachos Observatory, La Palma, Canary Island (Spain), and finally the 1.5m telescope located at the Maidanak Observatory (Uzbekistan).

At the Euler telescope, HE 0435-1225 was followed from January 2004 to February 2008. The 2048×2048 CCD camera of this telescope has a field of view of $11' \times 11'$, the pixel size being 0.″344. An epoch of observation is composed of 5 dithered frames with an exposure time of 360s each. The mean frequency of observation (when the object is visible) is one epoch every 6 days, for a total of 160 different epochs. The mean seeing per epoch varies from 0.″88 to 2.″55 with an average value of 1.″37.

At the Cassegrain focal station of the Mercator telescope is mounted MEROPE, a 2048×2048 CCD camera with a field of view of $6.5' \times 6.5'$ and a resolution of 0.″19 per pixel. The Mercator frames of HE 0435-1223 were obtained from September 2004 to January 2008 and consist of 82 epochs, the mean temporal sampling step being one night of observation every 11 days. Usually one epoch is composed of five dithered frames, each of them having an exposure time of 360s. The mean seeing per epoch varies from 0.″98 to 2.″40 with an average value of 1.″59.

The frames obtained with the 1.5m telescope of the Maidanak Observatory were acquired from October 2004 to January 2007. Two CCD cameras were used during this period. Until July 2006 the 2000×800 pixels SITE camera was mounted on the telescope. Then it was changed to the 4096×4096 pixels SI camera. Both have a pixel

[1]The central wavelength of the R-Gunn filter is 662.91 nm for a width of 31.38 nm.

size of 0.″266, which involves a field of view of $8.9' \times 3.5'$ for SITE and of $18.1' \times 18.1'$ for SI. When HE 0435-1223 was observed, a set of 10 dithered frames of 180s or of 6 dithered 300s exposures was acquired with a mean frequency of one set every 16 days for a total of 34 epochs. More rarely the set was composed of 3 dithered frames of 600s exposure time each. The mean seeing per epoch ranges from 0.″97 to 2.″37 with an average value of 1.″31.

In addition we also include 136 epochs from the two years monitoring of Kochanek et al. (2006). It started in August 2003 and ended in April 2005, one epoch consisting in 3 R-band exposures of 5 minutes each, the mean frequency of observation being one epoch every 4 days. These frames were obtained with the ANDICAM camera mounted on the 1.3m Small and Moderate Aperture Research Telescope System (SMARTS) located at the Cerro Tololo Inter-American Observatory (CTIO) in Chile. They selected the images with a seeing below or equal to 1.″8. See Kochanek et al. (2006) for details about the acquisition of the data and the processing of the images.

The main information about these data sets is summarized in Table 9.1 on p. 113.

9.2.2 Image processing

To obtain the light curves of the lensed images of HE 0435-1223, we apply the revised semi-automated reduction pipeline as described in Chapter 6. As already stated, the

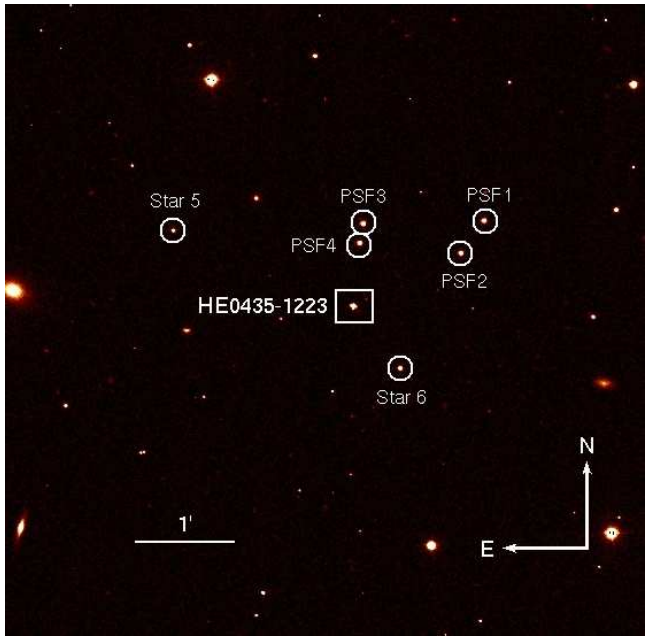

Figure 9.1: Partial field of view of the Euler reference frame of HE 0435-1223. The reference stars are encircled and labeled from 1 to 6. Those labeled *PSF* are also used to determine the PSF.

main difficulty in the image processing comes from the fact that we have to assemble data coming from different telescopes: each camera has a different size, resolution and orientation on the sky.

Euler is chosen as the reference telescope to avoid dividing the pixels of its detector into smaller ones as it has the lowest resolution. The reference frame, thus chosen amongst Euler data, was acquired on the night of the 11th of November 2005 and has a seeing of 0.″82. The reference stars used for the alignment and the flux calibration are encircled in the field of view of HE 0435-1223 shown on Fig. 9.1. The preliminary light curves are shown in Chapter 6 on Fig. 6.4 (p. 76). Let us note that this graph includes 172 epochs, while we only use 160 epochs. Indeed, for various reasons (not enough frames acquired during a night, cosmic rays located on the lensed system, ...), 12 epochs of observation were ruled out between the elaboration of the preliminary light curves and of the final ones.

The next step is the deconvolution with the MCS algorithm. At this stage four sources amongst the reference stars are chosen to determine a PSF for each frame. They are labeled *PSF1* to *PSF4* on Fig. 9.1. Here again, the deconvolved frames have half the pixel size of the original one, i.e. 0.″172, and the final PSF is a Gaussian with a FWHM of 2 pixels. The intensity of each source is allowed to vary from one frame to the other while the smooth background, which includes the lens galaxy, is held constant in all the frames. The deconvolved image is shown in Fig. 9.2. The point sources are labeled as in Wisotzki et al. (2002), G being the lens galaxy. To gain in precision, the relative positions of the point sources are fixed at the values extracted from deeper images acquired with the HST (see Sect. 9.3).

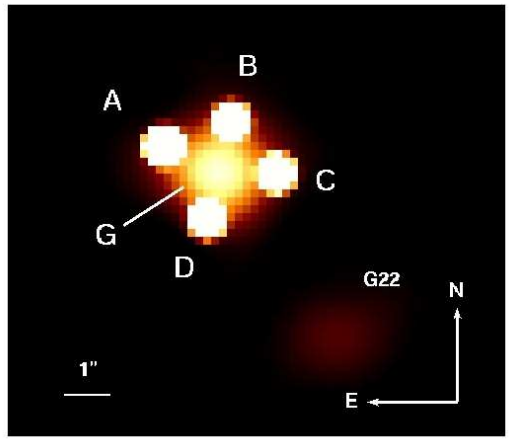

Figure 9.2: Result from the simultaneous deconvolution of the ground-based frames of HE 0435-1223. G is the lens galaxy and G22 its closest neighbour.

Fig. 9.3 shows the light curves obtained for each lensed image. For clarity, each season is displayed separately in Fig. 9.4. They are extracted from the simultaneous

deconvolution of all the frames. Euler was arbitrarily chosen as the reference telescope also in terms of flux. Each point in those figures is the mean of the consecutive observations made during one night, i.e. of an epoch. The total uncertainty for each point of each light curve of the quasar is estimated as explained in Sect. 6.6.2 (p. 80).

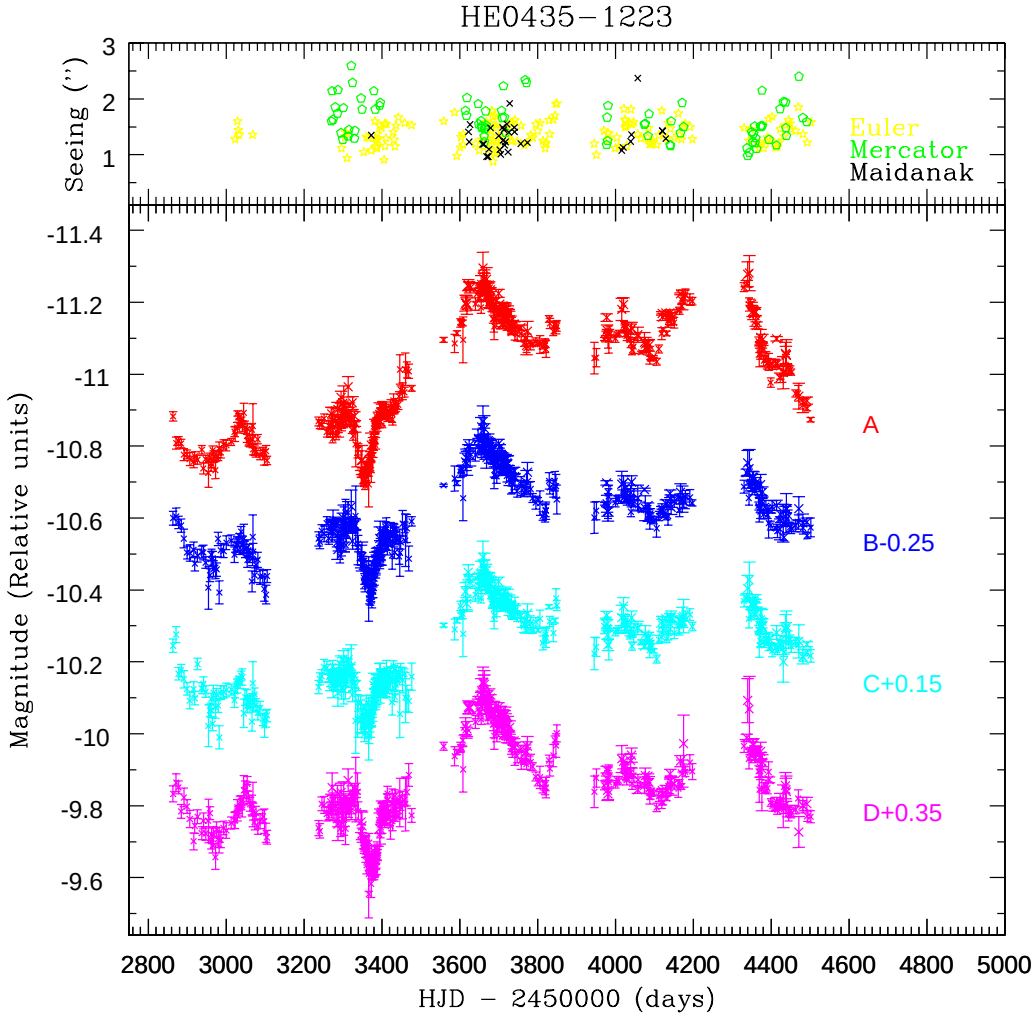

Figure 9.3: Light curves of the four lensed images of HE 0435-1223 from December 2003 to February 2008. The magnitude is given in arbitrary units as a function of the Heliocentric Julian Day (HJD). Each color corresponds to a lensed image: red for A, blue for B, cyan for C and magenta for D, as labeled on Fig 9.2. The $\pm 1\sigma$ error bars are also represented. On the top part of the graph, the mean seeing of each epoch is plotted against HJD.

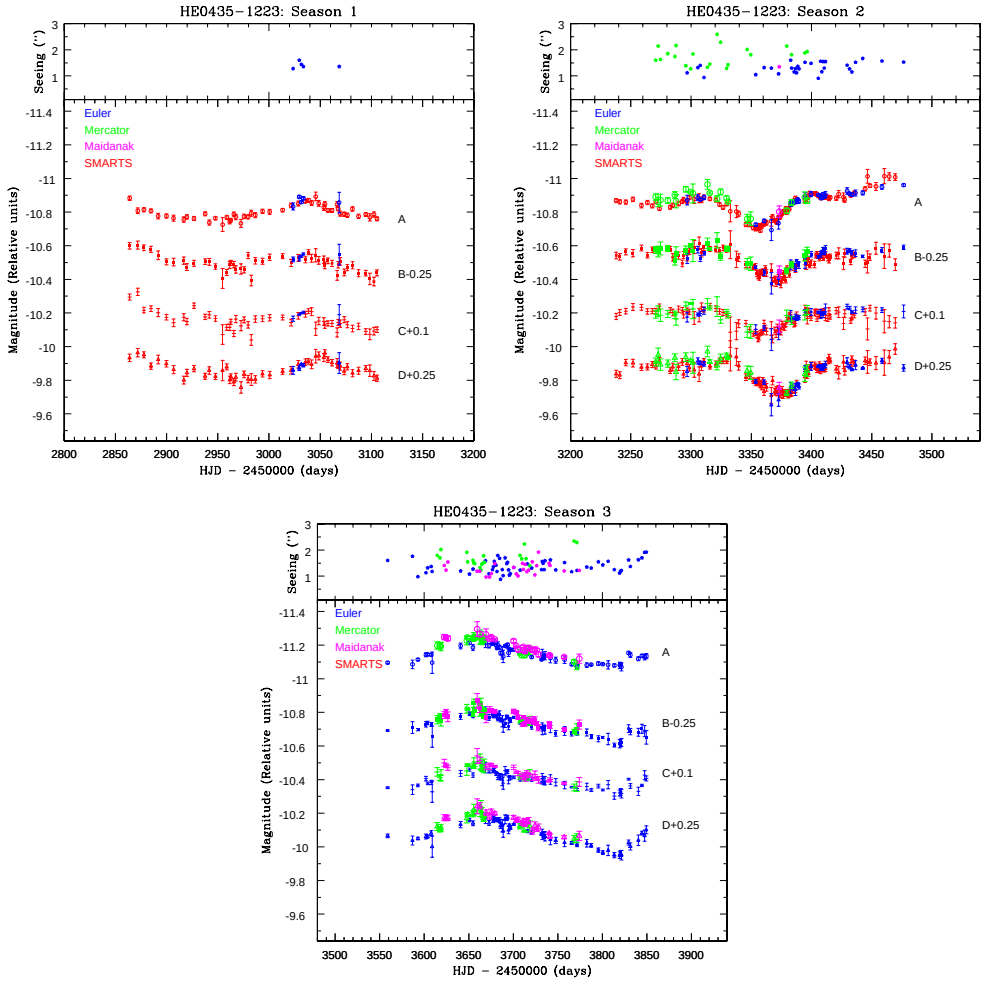

Figure 9.4: Light curves per season of the four lensed images of HE 0435-1223 from December 2003 to February 2008. The magnitude is given in arbitrary units as a function of the Heliocentric Julian Day. Each color corresponds to a telescope: blue for Euler, green for Mercator, magenta for Maidanak and red for SMARTS. The empty circles correspond to image A, the full squares to image B, the vertical lines to image C and the empty triangles to image D. The $\pm 1\sigma$ error bars are also represented. This figure continues on the next page.

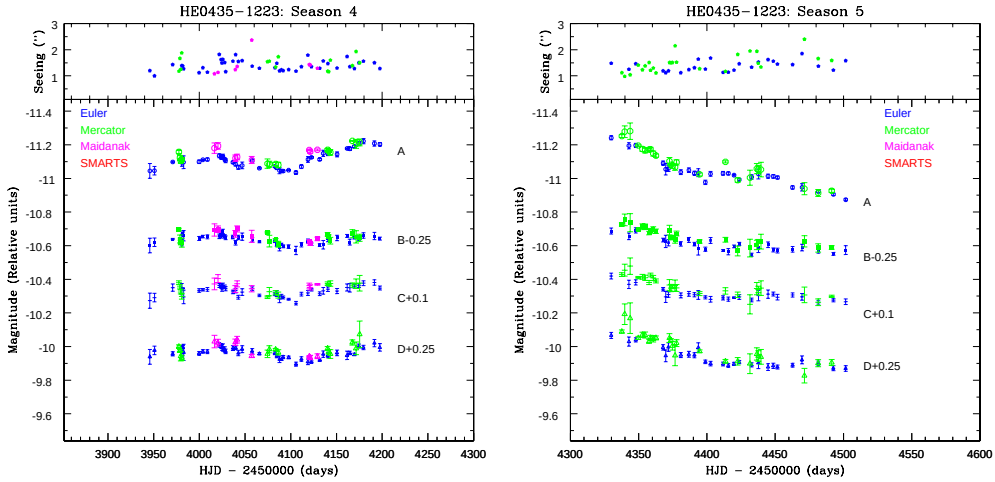

Figure 9.4: continued.

To find the flux scale to apply to SMARTS data, we compare the flux obtained during several common nights of observation with Euler (at least 10 so that the sample is representative). As the images have been treated with different processing techniques, we apply one magnitude shift per light curve to account for any discrepancy caused, e.g., by a different astrometry or lens galaxy. The statistical noise is given in Kochanek et al. (2006). As we want the total error, we need an estimation of the systematic one. We obtain it with the same method as explained in Sect. 6.6.2 thanks to the flux of a nearby star, also given with its statistical noise in Kochanek et al. (2006).

9.3 HST/NIC2 images

In this section, our aim is to obtain accurate relative astrometry for the four components of HE 0435-1223 and its lensing galaxy in applying ISMCS (see Chapter 7). The results will be used, in the paper, as constraints for the modeling of the lensing system. It is mandatory to obtain as much precision and constraints as possible. For this purpose, we analyse some HST images available in the archives of the Space Telescope Science Institute. They were acquired in the framework of the CASTLES project[2] in October 2004 (PI: C.S. Kochanek) with the camera 2 of NICMOS (NIC2). The data consist in four dithered frames calibrated by CALNICA[3] and acquired through the F160W filter (H-band) in the MULTIACCUM mode, each image being a combination of 19 samples. The total exposure time amounts to approximately 44 minutes and the mean pixel scale is $0''.075652$ (STScI NICMOS Group, 2007).

[2]Let us recall that CASTLES stands for *Cfa-Arizona Space Telescope LEns Survey*.
[3]Let us recall that CALNICA is the HST image reduction pipeline.

Three iterations of ISMCS are necessary to obtain a reduced χ^2 of 1.66. The final pixel size is half the original one and the final PSF of the deconvolved image is chosen to be a Gaussian with a FWHM of 2 pixels. Fig. 9.5 shows, from left to right, a combination of the four initial frames, the deconvolved image and the mean residual map from the last deconvolution. A nearly complete ring, i.e. a stretched and distorted version of the quasar host galaxy, is obvious.

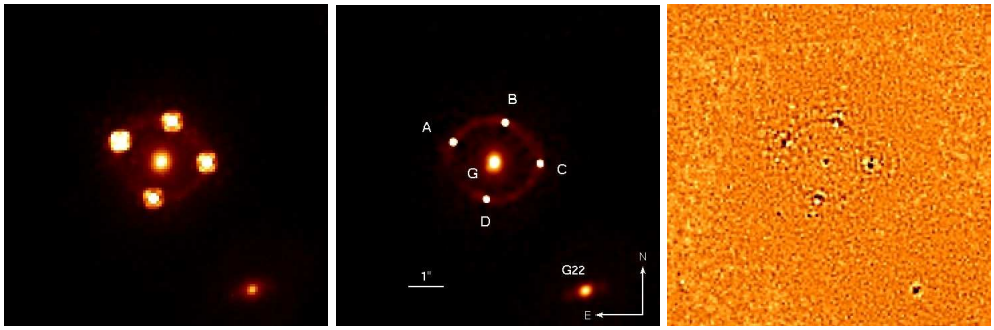

Figure 9.5: *Left*: combination of the four original HST/NIC2 F160W frames of HE 0435-1223. The field of view is $9''\times9''$. *Middle*: deconvolved image obtained from the last iteration of ISMCS with a de Vaucouleurs profile for the lens. See text for details. *Right*: mean residual map in units of sigma, the color scale ranging from -4 in white to +4 in black.

The astrometry and photometry of the four components and the lens are listed in Table 9.2. The relative positions are corrected from the known distortions of the NIC2 camera, as well as from the difference of pixel scale between the x and y directions. Every measurement is accompanied by its $\pm1\sigma$ error bars which are calculated in measuring the dispersion of the values around the mean of the individually deconvolved frames. Based on the work of Chantry & Magain (2007) on the Cloverleaf gravitational lens, we estimate that the total error, coming amongst others from an incomplete correction of the distortion, amounts to 2 milliarcseconds, as HE 0435-1223 is twice as extended as the Cloverleaf on NIC2. The results obtained by Morgan et al. (2005) and by Kochanek et al. (2006) are shown in Table 9.3. The first ones are based on HST/ACS images, while those from the second paper come from the same NIC2 images as the ones we use. Concerning the point sources the agreement is good with both sets of results: within their error bars, we obtain the same values. But for the lens, our result is slightly closer to Morgan et al. (2005) than to Kochanek et al. (2006). Let us note that, in order to determine the center of the lens galaxy with the highest accuracy, we make a special run of the MCS algorithm, where the numerical background is set to zero and the lens galaxy modeled by a de Vaucouleurs profile[4] (de Vaucouleurs, 1948). The center of this analytical profile is taken as the best estimate of the lens position. This procedure allows to force the de Vaucouleurs profile to adjust to the full lens galaxy light distribution. Letting the MCS algorithm represent the lens as the sum of an analytic profile and a numerical component would allow the center of the analytic profile to depart from the

[4]See Sect. 5.3.2 on p. 58 for details.

center of the total light distribution.

ID	ΔRA (″)	ΔDEC (″)	Magnitude
A	0.	0.	17.20 ± 0.01
B	-1.4743 ± 0.0004	+0.5518 ± 0.0006	17.69 ± 0.01
C	-2.4664 ± 0.0003	-0.6022 ± 0.0013	17.69 ± 0.02
D	-0.9378 ± 0.0005	-1.6160 ± 0.0006	17.95 ± 0.01
G	-1.1700 ± 0.0030	-0.5646 ± 0.0004	16.20 ± 0.12

Table 9.2: Relative astrometry and photometry of the four components and the lensing galaxy of HE 0435-1223. These results are extracted from the simultaneous deconvolution of the HST/NIC2 images. The right ascension and declination are given in arcseconds relative to component A. The apparent magnitude is given in the Vega system. The $\pm 1\sigma$ error bars internal to the deconvolution process are indicated.

	Morgan et al. (2005)		Kochanek et al. (2006)	
ID	ΔRA (″)	ΔDEC (″)	ΔRA (″)	ΔDEC (″)
A	0.	0.	0.	0.
B	-1.4772 ± 0.002	+0.5532 ± 0.002	-1.476 ± 0.003	+0.553 ± 0.001
C	-2.4687 ± 0.002	-0.6033 ± 0.002	-2.467 ± 0.002	-0.603 ± 0.004
D	-0.9377 ± 0.002	-1.6147 ± 0.002	-0.939 ± 0.002	-1.614 ± 0.001
G	-1.1687 ± 0.002	-0.5723 ± 0.002	-1.165 ± 0.002	-0.573 ± 0.002

Table 9.3: Relative astrometry of HE 0435-1223 from Morgan et al. (2005) on HST/ACS images and from Kochanek et al. (2006) on HST/NIC2 images. The right ascension and declination are given in arcseconds relative to component A. The $\pm 1\sigma$ error bars are also indicated.

The shape parameters of the main lens galaxy can also be derived from this adjustment of a de Vaucouleurs profile. They are presented in Table 9.4: the PA[5] in degrees positive East of North, the ellipticity, the effective semi-major and semi-minor axes and the effective radius. A de Vaucouleurs profile with a small ellipticity works well, which is in complete agreement with Eigenbrod et al. (2006b) who found that a S0 profile redshifted to z=0.454 is well adapted to represent the spectrum of the lens of HE 0435-1223. Its elongation l, i.e. the semi-major to semi-minor axes ratio, amounts to 1.10 ± 0.09, which is in agreement with the value found by Morgan et al. (2005), i.e. $1.20^{+0.23}_{-0.28}$, within the error bars. For the PA they obtained 172.6, which is very close to our result, and for the effective radius, they obtained $1.20^{+0.5}_{-0.35}$ arcseconds, which is also in agreement, within their error bars, with what we obtain.

[5]Let us recall that PA stands for *Position Angle* and is the angle that folds back the direction of the major axis over the direction of the North.

ID	PA (°)	Ellipticity	a_{eff} ($''$)	b_{eff} ($''$)	R_{eff} ($''$)
G	174.8 ± 1.7	0.09 ± 0.01	1.57 ± 0.09	1.43 ± 0.08	1.50 ± 0.08

Table 9.4: Measured shape parameters for the lensing galaxy of HE 0435-1223. The second column gives the position angle, or PA, in degrees positive East of North. The ellipticity is given in the third column and the two next columns present respectively the effective semi-major and semi-minor axes of the elliptical isophotes, in arcseconds. The effective radius is shown in the last column. Each measurement is accompanied by its $\pm 1\sigma$ internal error bars.

9.4 Time delays from a numerical fit of the light curves

This part of the work has been realized by E. Eulaers. The aim is of course to obtain the time delays between the different lensed images of HE 0435-1223.

We use a revised numerical method that will be explained in detail in Eulaers & et al. (in preparation) and which is based on Burud et al. (2001). For a series of given time delays, the method minimizes the difference between the data and a numerically modeled light curve with equally spaced sampling points while adjusting two parameters: the flux ratio between two light curves and a slope that models slow linear microlensing variations. The model is smoothed on the scale of the typical sampling of the observations, and this smoothing term is weighted by a Lagrange multiplier. The best time delay is the one that minimizes the χ^2 between the model and the data points. This basic version has been considerably modified, in particular for lens systems with more than two images. In the case of HE 0435-1223, the new version takes the light curves of the four images into account and seeks for the combination of time delays and flux ratios that minimizes the global χ^2 while imposing consistency between the time delays of all the images (e.g. $\Delta t_{AB} + \Delta t_{BC} = \Delta t_{AC}$).

We test different data sets: Euler for seasons 2 and 3, SMARTS for seasons 1 and 2 and all the COSMOGRAIL data for seasons 2 and 3. We do not take into account seasons 4 and 5 in these tests as microlensing effects are obviously stronger than intrinsic quasar variations during these seasons, especially for image A. Including them without further correction would lower the quality of the time delay measurements. Another test is then performed on the whole data set, including seasons 4 and 5, after correction of all observing seasons for slow microlensing by a method implemented by M. Tewes (Tewes & et al., in preparation).

The results are displayed in Table 9.5. The complete data set with all the seasons gives a range of time delays that appear equally likely. When we look carefully, these results seem to be some kind of average of the results from the different data sets, knowing that Euler dominates as it contains the larger number of data points.

Let us compare our results with what Kochanek et al. (2006, hereafter K06) obtained over two years of optical monitoring. The SMARTS data set, i.e. the one used by K06, with our method gives $\Delta t_{AC} < 0$. That result is in agreement, within the error bars, with the result of K06: $\Delta t_{AC} = -2.10^{+0.78}_{-0.71}$ days. However, the two other delays we obtain with this data set are significantly different from the original results of K06 using the same data: $\Delta t_{AB} = -8.00^{+0.73}_{-0.82}$ days and $\Delta t_{AD} = -14.37^{+0.75}_{-0.85}$ days. This is partic-

Telescope	Seasons	Δt_{AC} (days)	Δt_{AB} (days)	Δt_{AD} (days)
SMARTS	1-2	-2.8 ± 0.75	-11.7 ± 0.9	-15.9 ± 0.88
Euler	2-3	$+1.5 \pm 0.6$	-6.97 ± 0.85	-14.9 ± 0.9
Eul.+Merc.+Maid.	2-3	$+0.39 \pm 0.88$	-5.5 ± 0.79	-12.6 ± 0.86
All	All	$-0.9/+1.4$	$-5.8/-5.0$	$-16.0/-14.0$

Table 9.5: Time delays obtained with the numerical fit of the light curves of HE 0435-1223. For the last line, all the range of delays between the two quoted values appear equally likely.

ularly striking for Δt_{AB}, the difference amounting to nearly 4 days. These discrepancies likely come from the different time delay fitting methods used in both cases, and maybe, to some extent, to the different error bars used on each point of the curves: indeed, we corrected the ones obtained by K06 which appear unrealistically small and enlarged them whenever possible to account for the systematic errors (see Sect. 9.2). The other data set compatible with $\Delta t_{AC} < 0$, though not as much as the SMARTS data set, is the complete one with all the seasons. However, for Δt_{AB}, the range of possible delays is far from the value obtained by K06. The results from Euler+Mercator+Maidanak are not in agreement with SMARTS results, whether obtained by our method or taken from K06.

To conclude this section, we stress the fact that a highly symmetric lensed system such as HE 0435-1223 with very small time delays (going from about 0 to less than 20 days) is not well suited for a precise determination of H_0. Indeed, the shortness of the time delays requires very small error bars (significantly smaller than one day) to get an accurate value of the Hubble constant. While the internal error bars, derived from a given data set analysed by a given method, are smaller than 1 day, the comparison between the different data sets shows discrepancies which can reach several days. While this would not be very harmful in the case of a lens with time delays of the order of several months, this is too large in the present case. Indeed, a lensed quasar such as the present one is much better suited for determining the masse distribution in the lensing galaxy, adopting H_0 as given by other methods (see Sect 2.2 on p. 10), than for determining H_0 itself.

9.5 Complementary studies

The following complementary studies for HE 0435-1223 will appear in the paper which is currently in preparation:

- the measurement of the time delays with a different method (in charge: M. Tewes, in progress) and the comparison with the results from the numerical fit of the light curves,

- the acquisition of the stellar population parameters (age and metallicity) and the kinematics (velocity, velocity dispersion) for the lensing galaxy (in charge: M. Koleva, done),

- the acquisition of constraints on the total mass density slope of the lensing galaxy with N-body simulations (in charge: Y. Revaz and C. Faure, done),
- the reconstruction of the source thanks to the extra constraints provided by the extended ring image, using the semi-linear inversion method of Warren & Dye (2003, in charge: S. Dye, done),
- the acquisition of parametric models with LENSMODEL (Keeton (2001b), see Sect. 4.8.2, in charge: D. Sluse, in progress),
- the acquisition of non-parametric models with PIXELENS (Saha (2004), see Sect. 4.8.3, in charge: J. Coles and P. Saha, in progress).

Let us note that the additional constraints on the lensing galaxy will allow to break the mass-sheet-degeneracy in putting constraints on the mass distribution during the parametric modeling.

Telescope	Period of observation	Number of epochs	Mean seeing	Mean temporal sampling
Euler	January 2004 - February 2008	160	$1\farcs37$	1 epoch every 6 days
Mercator	September 2004 - January 2008	82	$1\farcs59$	1 epoch every 11 days
Maidanak	October 2004 - January 2007	34	$1\farcs31$	1 epoch every 16 days
SMARTS	August 2003 - April 2005	136	$\leq 1\farcs8$	1 epoch every 4 days
TOTAL	August 2003 - February 2008	415	-	-

Table 9.1: Summary of the optical data obtained with the four telescopes.

Appendix: photometry table

Table 9.6: Photometry of HE 0435-1223. "Epoch" is actually equal to HJD − 2450000 and $\bar{s}$ is the mean seeing per epoch of observation.

Telescope	Epoch	$\bar{s}$ ($''$)	m_A	σ_A	m_B	σ_B	m_C	σ_C	m_D	σ_D
SMARTS	2863.883	/	-10.883	0.013	-10.350	0.019	-10.395	0.018	-10.183	0.022
SMARTS	2871.829	/	-10.808	0.017	-10.354	0.024	-10.426	0.022	-10.214	0.025
SMARTS	2877.843	/	-10.814	0.012	-10.338	0.017	-10.317	0.017	-10.201	0.018
SMARTS	2884.784	/	-10.807	0.012	-10.329	0.018	-10.326	0.017	-10.134	0.019
SMARTS	2891.827	/	-10.776	0.017	-10.293	0.026	-10.302	0.024	-10.173	0.026
SMARTS	2899.843	/	-10.777	0.012	-10.254	0.018	-10.275	0.017	-10.148	0.019
SMARTS	2906.848	/	-10.764	0.018	-10.253	0.022	-10.242	0.023	-10.113	0.024
SMARTS	2916.803	/	-10.756	0.016	-10.262	0.022	-10.274	0.021	-10.051	0.024
SMARTS	2919.828	/	-10.771	0.013	-10.223	0.020	-10.249	0.019	-10.094	0.021
SMARTS	2926.780	/	-10.762	0.012	-10.246	0.018	-10.344	0.016	-10.119	0.019
SMARTS	2937.672	/	-10.790	0.012	-10.255	0.017	-10.277	0.016	-10.074	0.018
SMARTS	2941.689	/	-10.738	0.016	-10.254	0.020	-10.289	0.020	-10.108	0.022
SMARTS	2947.698	/	-10.764	0.011	-10.226	0.016	-10.267	0.016	-10.073	0.018
SMARTS	2954.711	/	-10.726	0.041	-10.156	0.060	-10.172	0.058	-10.108	0.061
SMARTS	2958.742	/	-10.769	0.012	-10.191	0.018	-10.215	0.017	-10.129	0.018
SMARTS	2961.682	/	-10.744	0.014	-10.236	0.021	-10.215	0.020	-10.052	0.022
SMARTS	2962.680	/	-10.752	0.012	-10.248	0.016	-10.247	0.016	-10.070	0.018
SMARTS	2965.630	/	-10.788	0.012	-10.238	0.019	-10.178	0.019	-10.039	0.021
SMARTS	2967.637	/	-10.771	0.016	-10.209	0.023	-10.264	0.021	-10.068	0.024
SMARTS	2972.619	/	-10.733	0.023	-10.212	0.031	-10.224	0.030	-10.007	0.034
SMARTS	2975.669	/	-10.774	0.014	-10.207	0.018	-10.259	0.018	-10.085	0.020
SMARTS	2979.632	/	-10.772	0.012	-10.292	0.019	-10.229	0.019	-10.057	0.022
SMARTS	2982.682	/	-10.794	0.018	-10.143	0.032	-10.140	0.032	-10.054	0.035
SMARTS	2986.634	/	-10.782	0.015	-10.260	0.019	-10.264	0.019	-10.055	0.022
SMARTS	2993.664	/	-10.805	0.013	-10.258	0.017	-10.266	0.017	-10.088	0.019
SMARTS	3000.684	/	-10.802	0.015	-10.281	0.019	-10.272	0.019	-10.081	0.022
SMARTS	3013.317	/	-10.812	0.010	-10.288	0.015	-10.273	0.015	-10.102	0.017
SMARTS	3021.612	/	-10.840	0.014	-10.248	0.021	-10.243	0.020	-10.109	0.022
Euler	3023.583	1.28	-10.834	0.021	-10.269	0.014	-10.267	0.016	-10.110	0.023
SMARTS	3028.619	/	-10.851	0.015	-10.278	0.020	-10.283	0.020	-10.145	0.022
Euler	3029.594	1.60	-10.891	0.007	-10.275	0.015	-10.290	0.004	-10.122	0.014
Euler	3031.587	1.44	-10.859	0.007	-10.287	0.007	-10.299	0.004	-10.145	0.002
Euler	3033.577	1.36	-10.882	0.009	-10.301	0.006	-10.304	0.007	-10.140	0.010
SMARTS	3035.614	/	-10.866	0.011	-10.267	0.018	-10.293	0.017	-10.158	0.019
SMARTS	3038.592	/	-10.871	0.010	-10.312	0.015	-10.311	0.014	-10.162	0.016
SMARTS	3041.618	/	-10.855	0.015	-10.276	0.024	-10.308	0.023	-10.145	0.026
SMARTS	3045.653	/	-10.893	0.026	-10.293	0.040	-10.207	0.040	-10.193	0.041
SMARTS	3048.616	/	-10.852	0.017	-10.263	0.023	-10.252	0.022	-10.195	0.024
SMARTS	3053.581	/	-10.828	0.017	-10.267	0.022	-10.250	0.022	-10.185	0.024
SMARTS	3054.576	/	-10.848	0.015	-10.233	0.020	-10.229	0.021	-10.211	0.021
SMARTS	3057.528	/	-10.811	0.011	-10.260	0.017	-10.238	0.016	-10.173	0.017
SMARTS	3061.539	/	-10.810	0.012	-10.245	0.019	-10.238	0.018	-10.154	0.019
SMARTS	3066.577	/	-10.846	0.017	-10.174	0.029	-10.184	0.027	-10.152	0.027
SMARTS	3067.597	/	-10.820	0.012	-10.237	0.019	-10.244	0.018	-10.141	0.020
Euler	3068.556	1.36	-10.856	0.061	-10.297	0.062	-10.291	0.059	-10.153	0.062
SMARTS	3069.533	/	-10.791	0.015	-10.257	0.022	-10.237	0.021	-10.134	0.023
SMARTS	3073.533	/	-10.788	0.013	-10.191	0.020	-10.260	0.018	-10.104	0.021
SMARTS	3076.505	/	-10.782	0.012	-10.220	0.018	-10.230	0.018	-10.130	0.019
SMARTS	3081.553	/	-10.819	0.013	-10.234	0.021	-10.208	0.020	-10.092	0.021
SMARTS	3087.494	/	-10.775	0.013	-10.187	0.021	-10.221	0.019	-10.107	0.021
SMARTS	3094.500	/	-10.786	0.011	-10.187	0.017	-10.190	0.017	-10.120	0.018
SMARTS	3098.511	/	-10.769	0.021	-10.153	0.034	-10.173	0.032	-10.107	0.034
SMARTS	3102.479	/	-10.786	0.016	-10.137	0.026	-10.192	0.023	-10.075	0.026
SMARTS	3105.485	/	-10.760	0.012	-10.189	0.018	-10.201	0.017	-10.062	0.019
SMARTS	3237.884	/	-10.869	0.012	-10.292	0.019	-10.280	0.018	-10.088	0.021
SMARTS	3240.859	/	-10.861	0.012	-10.284	0.019	-10.303	0.017	-10.080	0.020
SMARTS	3245.860	/	-10.860	0.012	-10.314	0.018	-10.311	0.017	-10.155	0.019
SMARTS	3251.810	/	-10.876	0.013	-10.306	0.022	-10.336	0.020	-10.152	0.023

Telescope	Epoch	$\bar{s}$ ($''$)	m_A	σ_A	m_B	σ_B	m_C	σ_C	m_D	σ_D
SMARTS	3258.833	/	-10.839	0.013	-10.336	0.017	-10.334	0.017	-10.127	0.020
SMARTS	3263.793	/	-10.857	0.013	-10.294	0.017	-10.309	0.016	-10.129	0.018
SMARTS	3267.836	/	-10.837	0.012	-10.326	0.017	-10.311	0.016	-10.143	0.018
Mercator	3270.672	1.60	-10.890	0.019	-10.325	0.021	-10.293	0.023	-10.159	0.023
SMARTS	3270.816	/	-10.863	0.013	-10.321	0.017	-10.311	0.017	-10.135	0.019
Mercator	3272.687	2.14	-10.861	0.028	-10.315	0.032	-10.312	0.031	-10.200	0.041
SMARTS	3273.787	/	-10.821	0.012	-10.323	0.017	-10.338	0.016	-10.167	0.019
Mercator	3274.661	1.63	-10.872	0.035	-10.334	0.038	-10.287	0.037	-10.143	0.034
Mercator	3280.671	1.85	-10.869	0.017	-10.334	0.018	-10.294	0.021	-10.150	0.022
SMARTS	3282.705	/	-10.829	0.011	-10.330	0.015	-10.317	0.015	-10.109	0.018
SMARTS	3284.804	/	-10.841	0.013	-10.281	0.022	-10.303	0.020	-10.128	0.023
Mercator	3286.616	1.74	-10.902	0.020	-10.262	0.027	-10.289	0.022	-10.184	0.023
Mercator	3287.630	2.16	-10.865	0.039	-10.307	0.037	-10.264	0.037	-10.099	0.046
SMARTS	3289.712	/	-10.851	0.013	-10.291	0.021	-10.323	0.018	-10.131	0.021
SMARTS	3292.776	/	-10.863	0.012	-10.245	0.020	-10.316	0.017	-10.159	0.020
SMARTS	3293.773	/	-10.874	0.014	-10.295	0.021	-10.289	0.020	-10.086	0.022
Mercator	3295.657	1.39	-10.936	0.017	-10.324	0.025	-10.343	0.024	-10.187	0.026
Euler	3296.775	1.12	-10.872	0.029	-10.274	0.029	-10.275	0.029	-10.102	0.030
SMARTS	3296.777	/	-10.863	0.013	-10.277	0.017	-10.313	0.017	-10.150	0.019
SMARTS	3298.703	/	-10.887	0.011	-10.316	0.017	-10.306	0.016	-10.123	0.019
Mercator	3299.675	1.27	-10.920	0.005	-10.352	0.012	-10.356	0.006	-10.168	0.006
Mercator	3301.622	1.84	-10.911	0.056	-10.321	0.066	-10.323	0.058	-10.155	0.062
SMARTS	3302.659	/	-10.877	0.025	-10.342	0.039	-10.271	0.038	-10.111	0.043
Euler	3305.662	1.32	-10.886	0.017	-10.326	0.020	-10.291	0.009	-10.165	0.019
SMARTS	3306.684	/	-10.883	0.027	-10.365	0.037	-10.286	0.039	-10.086	0.044
Euler	3307.684	1.40	-10.875	0.007	-10.274	0.018	-10.297	0.015	-10.153	0.012
SMARTS	3308.711	/	-10.873	0.017	-10.308	0.024	-10.335	0.024	-10.135	0.028
SMARTS	3310.673	/	-10.891	0.010	-10.337	0.015	-10.320	0.015	-10.161	0.017
Euler	3310.795	0.94	-10.887	0.013	-10.305	0.010	-10.314	0.021	-10.147	0.013
Mercator	3313.677	1.33	-10.965	0.028	-10.365	0.031	-10.356	0.030	-10.220	0.032
Mercator	3315.624	1.45	-10.914	0.006	-10.330	0.007	-10.330	0.012	-10.161	0.011
SMARTS	3315.652	/	-10.879	0.010	-10.332	0.015	-10.343	0.015	-10.134	0.017
SMARTS	3320.696	/	-10.872	0.013	-10.330	0.017	-10.326	0.017	-10.146	0.019
Mercator	3321.663	2.59	-10.880	0.018	-10.382	0.046	-10.338	0.059	-10.137	0.026
SMARTS	3323.637	/	-10.846	0.011	-10.324	0.016	-10.309	0.016	-10.165	0.017
Mercator	3324.589	2.29	-10.920	0.018	-10.285	0.022	-10.259	0.020	-10.180	0.026
SMARTS	3326.603	/	-10.828	0.012	-10.337	0.017	-10.303	0.017	-10.167	0.018
Mercator	3329.601	1.29	-10.883	0.013	-10.333	0.017	-10.309	0.012	-10.198	0.014
SMARTS	3329.682	/	-10.848	0.011	-10.326	0.015	-10.292	0.015	-10.165	0.016
Mercator	3330.668	1.43	-10.863	0.008	-10.330	0.014	-10.284	0.014	-10.183	0.010
SMARTS	3332.594	/	-10.805	0.063	-10.356	0.083	-10.186	0.090	-10.195	0.090
SMARTS	3337.677	/	-10.803	0.036	-10.269	0.049	-10.192	0.051	-10.189	0.052
SMARTS	3339.622	/	-10.791	0.016	-10.279	0.023	-10.236	0.023	-10.136	0.025
SMARTS	3345.555	/	-10.727	0.013	-10.238	0.019	-10.238	0.018	-10.068	0.020
Mercator	3346.567	2.01	-10.760	0.027	-10.243	0.031	-10.187	0.033	-10.106	0.030
SMARTS	3348.651	/	-10.726	0.014	-10.237	0.018	-10.201	0.018	-10.078	0.020
Mercator	3349.583	1.81	-10.761	0.040	-10.243	0.040	-10.191	0.041	-10.094	0.038
SMARTS	3351.639	/	-10.706	0.011	-10.223	0.015	-10.177	0.015	-10.047	0.017
SMARTS	3353.584	/	-10.702	0.014	-10.226	0.018	-10.185	0.018	-10.037	0.019
Euler	3353.723	1.05	-10.725	0.009	-10.223	0.007	-10.203	0.027	-10.043	0.012
SMARTS	3354.670	/	-10.709	0.014	-10.184	0.019	-10.172	0.019	-10.043	0.020
SMARTS	3355.660	/	-10.706	0.015	-10.174	0.021	-10.149	0.020	-10.039	0.022
SMARTS	3356.647	/	-10.719	0.014	-10.164	0.019	-10.158	0.019	-10.048	0.020
SMARTS	3357.582	/	-10.690	0.011	-10.194	0.015	-10.183	0.014	-10.022	0.016
SMARTS	3358.630	/	-10.715	0.012	-10.190	0.016	-10.184	0.015	-10.010	0.017
SMARTS	3359.624	/	-10.729	0.010	-10.198	0.015	-10.189	0.014	-10.050	0.016
SMARTS	3360.595	/	-10.730	0.014	-10.188	0.021	-10.237	0.020	-9.984	0.024
Euler	3360.663	1.32	-10.748	0.011	-10.190	0.016	-10.210	0.014	-10.039	0.014
SMARTS	3361.625	/	-10.742	0.011	-10.215	0.016	-10.212	0.016	-10.026	0.018
SMARTS	3362.605	/	-10.736	0.013	-10.188	0.020	-10.190	0.020	-10.008	0.023
SMARTS	3366.603	/	-10.745	0.029	-10.201	0.041	-10.208	0.041	-9.960	0.048
Euler	3366.730	1.30	-10.694	0.063	-10.127	0.063	-10.142	0.065	-9.904	0.066
SMARTS	3367.669	/	-10.770	0.015	-10.136	0.024	-10.146	0.023	-10.048	0.025
SMARTS	3369.662	/	-10.751	0.011	-10.151	0.018	-10.199	0.017	-9.982	0.020
SMARTS	3370.637	/	-10.744	0.013	-10.125	0.018	-10.172	0.017	-9.993	0.019
SMARTS	3371.592	/	-10.740	0.014	-10.143	0.019	-10.215	0.018	-9.978	0.021

Telescope	Epoch	$\bar{s}$ ($''$)	m_A	σ_A	m_B	σ_B	m_C	σ_C	m_D	σ_D
SMARTS	3372.609	/	-10.769	0.010	-10.163	0.015	-10.186	0.014	-10.003	0.016
Euler	3372.672	1.08	-10.734	0.036	-10.155	0.037	-10.176	0.035	-9.933	0.038
Maidanak	3373.240	1.35	-10.803	0.034	-10.194	0.036	-10.222	0.036	-10.003	0.035
SMARTS	3373.634	/	-10.768	0.012	-10.159	0.020	-10.190	0.018	-9.968	0.021
SMARTS	3374.591	/	-10.781	0.012	-10.121	0.021	-10.187	0.018	-9.968	0.022
SMARTS	3375.586	/	-10.795	0.013	-10.148	0.019	-10.233	0.018	-9.992	0.021
SMARTS	3376.612	/	-10.803	0.013	-10.183	0.019	-10.221	0.018	-9.963	0.020
SMARTS	3377.603	/	-10.803	0.013	-10.167	0.019	-10.214	0.018	-9.974	0.021
SMARTS	3378.636	/	-10.821	0.012	-10.145	0.017	-10.235	0.016	-9.972	0.018
Mercator	3379.465	2.14	-10.808	0.016	-10.200	0.018	-10.285	0.033	-9.974	0.016
SMARTS	3379.620	/	-10.799	0.012	-10.213	0.018	-10.258	0.016	-9.976	0.019
SMARTS	3380.602	/	-10.815	0.012	-10.202	0.017	-10.273	0.015	-9.963	0.019
SMARTS	3381.588	/	-10.820	0.013	-10.181	0.018	-10.284	0.017	-9.971	0.020
SMARTS	3382.583	/	-10.845	0.011	-10.226	0.016	-10.290	0.015	-9.973	0.019
Euler	3382.693	1.60	-10.853	0.019	-10.236	0.030	-10.282	0.033	-10.005	0.031
Mercator	3383.439	1.81	-10.858	0.016	-10.236	0.018	-10.254	0.023	-10.020	0.020
SMARTS	3383.611	/	-10.850	0.013	-10.241	0.017	-10.259	0.017	-9.977	0.019
Euler	3383.620	1.30	-10.862	0.007	-10.234	0.006	-10.274	0.004	-10.016	0.012
SMARTS	3385.591	/	-10.867	0.012	-10.223	0.019	-10.235	0.018	-9.994	0.021
Euler	3385.620	1.15	-10.858	0.006	-10.235	0.010	-10.269	0.007	-9.996	0.007
SMARTS	3386.601	/	-10.884	0.010	-10.208	0.016	-10.239	0.015	-9.995	0.018
Euler	3386.677	1.28	-10.863	0.014	-10.213	0.016	-10.281	0.012	-9.994	0.035
SMARTS	3387.592	/	-10.867	0.010	-10.232	0.014	-10.292	0.014	-10.034	0.016
Euler	3387.621	1.12	-10.863	0.007	-10.262	0.006	-10.264	0.008	-10.019	0.008
Euler	3388.668	1.37	-10.877	0.003	-10.250	0.004	-10.274	0.011	-10.028	0.009
Euler	3389.595	1.27	-10.864	0.010	-10.235	0.019	-10.272	0.012	-10.013	0.016
Mercator	3394.452	1.88	-10.888	0.032	-10.293	0.033	-10.287	0.028	-10.087	0.043
SMARTS	3394.604	/	-10.871	0.020	-10.265	0.029	-10.319	0.028	-10.070	0.033
Euler	3394.621	1.52	-10.897	0.020	-10.245	0.029	-10.305	0.017	-10.120	0.018
SMARTS	3395.603	/	-10.880	0.017	-10.236	0.026	-10.306	0.024	-10.136	0.028
Mercator	3396.396	1.93	-10.867	0.016	-10.314	0.027	-10.318	0.027	-10.107	0.034
SMARTS	3396.540	/	-10.884	0.022	-10.270	0.034	-10.268	0.033	-10.097	0.036
SMARTS	3397.559	/	-10.895	0.010	-10.271	0.016	-10.314	0.015	-10.090	0.018
SMARTS	3398.553	/	-10.914	0.010	-10.234	0.015	-10.292	0.014	-10.126	0.016
SMARTS	3399.577	/	-10.908	0.010	-10.250	0.016	-10.270	0.015	-10.143	0.016
Euler	3399.623	1.48	-10.907	0.015	-10.300	0.016	-10.307	0.020	-10.133	0.024
SMARTS	3402.527	/	-10.909	0.011	-10.238	0.019	-10.301	0.018	-10.138	0.020
SMARTS	3403.559	/	-10.911	0.010	-10.292	0.015	-10.309	0.015	-10.131	0.016
SMARTS	3404.573	/	-10.905	0.011	-10.299	0.016	-10.265	0.015	-10.113	0.017
SMARTS	3405.560	/	-10.897	0.010	-10.290	0.014	-10.308	0.014	-10.111	0.016
Euler	3405.617	0.91	-10.902	0.005	-10.285	0.008	-10.304	0.008	-10.134	0.005
SMARTS	3406.563	/	-10.897	0.011	-10.275	0.016	-10.287	0.016	-10.143	0.017
SMARTS	3407.560	/	-10.884	0.011	-10.291	0.016	-10.292	0.015	-10.106	0.017
Euler	3407.615	1.56	-10.892	0.016	-10.299	0.017	-10.294	0.027	-10.127	0.017
Euler	3408.566	1.16	-10.883	0.007	-10.311	0.013	-10.294	0.008	-10.116	0.006
SMARTS	3408.573	/	-10.891	0.011	-10.298	0.016	-10.308	0.016	-10.133	0.017
SMARTS	3409.559	/	-10.888	0.010	-10.277	0.015	-10.304	0.014	-10.117	0.016
Euler	3409.575	1.55	-10.904	0.012	-10.325	0.015	-10.290	0.017	-10.125	0.015
SMARTS	3410.557	/	-10.889	0.013	-10.320	0.017	-10.309	0.017	-10.117	0.018
Euler	3410.562	1.30	-10.891	0.003	-10.304	0.007	-10.295	0.005	-10.138	0.011
SMARTS	3411.560	/	-10.891	0.011	-10.299	0.017	-10.271	0.017	-10.119	0.018
Euler	3411.577	1.55	-10.904	0.019	-10.332	0.019	-10.330	0.024	-10.144	0.020
SMARTS	3413.559	/	-10.890	0.011	-10.278	0.018	-10.267	0.017	-10.165	0.018
SMARTS	3414.548	/	-10.881	0.013	-10.268	0.021	-10.313	0.018	-10.184	0.020
SMARTS	3415.546	/	-10.888	0.010	-10.287	0.014	-10.276	0.013	-10.167	0.015
SMARTS	3420.566	/	-10.883	0.013	-10.292	0.020	-10.314	0.019	-10.116	0.022
SMARTS	3422.590	/	-10.907	0.022	-10.305	0.033	-10.305	0.032	-10.094	0.037
SMARTS	3426.545	/	-10.890	0.024	-10.246	0.038	-10.238	0.036	-10.158	0.039
SMARTS	3427.548	/	-10.874	0.015	-10.306	0.024	-10.296	0.023	-10.107	0.026
Euler	3429.588	1.41	-10.926	0.019	-10.318	0.017	-10.338	0.014	-10.157	0.027
Euler	3431.609	1.27	-10.909	0.007	-10.321	0.012	-10.329	0.011	-10.131	0.013
SMARTS	3432.535	/	-10.899	0.010	-10.254	0.016	-10.254	0.015	-10.139	0.016
SMARTS	3433.538	/	-10.904	0.011	-10.293	0.017	-10.276	0.016	-10.177	0.017
Euler	3433.554	1.15	-10.904	0.009	-10.309	0.013	-10.305	0.008	-10.113	0.006
SMARTS	3435.535	/	-10.915	0.011	-10.296	0.017	-10.287	0.016	-10.151	0.018
Euler	3436.558	1.52	-10.914	0.018	-10.306	0.020	-10.316	0.020	-10.139	0.026

Telescope	Epoch	$\bar{s}$ ($''$)	m_A	σ_A	m_B	σ_B	m_C	σ_C	m_D	σ_D
Euler	3442.538	1.67	-10.915	0.012	-10.287	0.007	-10.322	0.014	-10.122	0.005
SMARTS	3444.512	/	-10.938	0.013	-10.243	0.022	-10.306	0.020	-10.166	0.022
SMARTS	3446.492	/	-11.013	0.041	-10.253	0.065	-10.205	0.065	-10.159	0.068
SMARTS	3448.503	/	-10.957	0.011	-10.283	0.019	-10.329	0.017	-10.157	0.020
SMARTS	3453.506	/	-10.953	0.023	-10.335	0.036	-10.299	0.035	-10.152	0.039
Euler	3458.511	1.57	-10.950	0.014	-10.324	0.014	-10.317	0.014	-10.166	0.015
SMARTS	3460.480	/	-11.014	0.045	-10.288	0.073	-10.251	0.070	-10.155	0.075
SMARTS	3464.483	/	-11.012	0.022	-10.321	0.039	-10.248	0.037	-10.188	0.039
SMARTS	3469.479	/	-11.008	0.020	-10.237	0.034	-10.241	0.031	-10.236	0.031
Euler	3476.491	1.53	-10.961	0.008	-10.341	0.013	-10.309	0.038	-10.123	0.019
Euler	3558.922	1.60	-11.095	0.007	-10.441	0.003	-10.452	0.005	-10.315	0.011
Euler	3586.855	1.76	-11.085	0.025	-10.460	0.035	-10.440	0.029	-10.288	0.027
Euler	3592.907	0.98	-11.114	0.007	-10.447	0.007	-10.466	0.007	-10.299	0.008
Euler	3601.884	1.13	-11.143	0.012	-10.479	0.016	-10.506	0.013	-10.312	0.014
Euler	3603.891	1.32	-11.144	0.006	-10.487	0.010	-10.478	0.008	-10.311	0.009
Euler	3607.893	1.37	-11.142	0.008	-10.478	0.012	-10.483	0.013	-10.332	0.014
Euler	3608.890	1.18	-11.096	0.064	-10.405	0.063	-10.428	0.063	-10.251	0.063
Mercator	3614.699	1.79	-11.198	0.022	-10.506	0.024	-10.546	0.025	-10.371	0.023
Mercator	3617.704	1.70	-11.197	0.016	-10.517	0.025	-10.512	0.017	-10.353	0.015
Mercator	3618.715	2.02	-11.192	0.025	-10.502	0.033	-10.525	0.034	-10.364	0.021
Maidanak	3622.495	1.41	-11.248	0.015	-10.534	0.021	-10.599	0.021	-10.424	0.018
Maidanak	3624.495	1.23	-11.246	0.011	-10.552	0.016	-10.583	0.011	-10.421	0.016
Maidanak	3626.499	1.54	-11.240	0.014	-10.524	0.029	-10.571	0.016	-10.423	0.016
Euler	3640.880	1.20	-11.195	0.017	-10.526	0.017	-10.537	0.017	-10.383	0.018
Mercator	3647.727	1.91	-11.227	0.026	-10.572	0.026	-10.552	0.027	-10.420	0.027
Mercator	3648.704	1.55	-11.246	0.006	-10.568	0.004	-10.588	0.007	-10.443	0.011
Euler	3650.807	1.08	-11.214	0.009	-10.542	0.011	-10.559	0.009	-10.410	0.010
Mercator	3654.700	1.61	-11.239	0.007	-10.540	0.014	-10.577	0.008	-10.447	0.018
Euler	3654.759	1.27	-11.186	0.016	-10.535	0.017	-10.527	0.013	-10.391	0.015
Mercator	3655.715	1.51	-11.250	0.025	-10.604	0.026	-10.599	0.031	-10.470	0.034
Mercator	3656.712	1.48	-11.241	0.013	-10.565	0.016	-10.592	0.014	-10.458	0.011
Maidanak	3659.468	1.19	-11.296	0.043	-10.619	0.043	-10.641	0.044	-10.491	0.045
Maidanak	3662.414	1.19	-11.265	0.016	-10.574	0.025	-10.615	0.017	-10.494	0.019
Mercator	3662.707	1.33	-11.248	0.042	-10.570	0.042	-10.608	0.045	-10.472	0.042
Mercator	3663.702	1.23	-11.243	0.037	-10.599	0.036	-10.596	0.038	-10.488	0.038
Mercator	3664.679	1.46	-11.226	0.023	-10.558	0.024	-10.583	0.031	-10.457	0.027
Mercator	3665.674	1.49	-11.243	0.016	-10.559	0.018	-10.565	0.017	-10.433	0.019
Mercator	3666.705	1.78	-11.228	0.006	-10.527	0.013	-10.558	0.018	-10.410	0.005
Mercator	3667.653	1.53	-11.245	0.012	-10.556	0.017	-10.606	0.016	-10.438	0.015
Euler	3668.810	1.59	-11.215	0.031	-10.552	0.031	-10.571	0.030	-10.421	0.033
Maidanak	3669.417	0.97	-11.264	0.033	-10.518	0.030	-10.576	0.016	-10.454	0.016
Euler	3672.800	1.09	-11.197	0.014	-10.521	0.018	-10.552	0.012	-10.392	0.015
Maidanak	3673.405	0.97	-11.237	0.015	-10.566	0.018	-10.580	0.019	-10.432	0.017
Maidanak	3675.430	1.10	-11.248	0.009	-10.561	0.010	-10.587	0.009	-10.461	0.015
Euler	3676.659	1.25	-11.210	0.009	-10.543	0.015	-10.559	0.018	-10.427	0.014
Euler	3677.687	1.36	-11.211	0.007	-10.526	0.006	-10.554	0.008	-10.401	0.007
Euler	3678.693	1.57	-11.224	0.014	-10.534	0.017	-10.568	0.014	-10.425	0.013
Maidanak	3679.337	1.48	-11.235	0.005	-10.558	0.007	-10.579	0.006	-10.449	0.010
Euler	3680.649	1.42	-11.200	0.007	-10.533	0.008	-10.536	0.010	-10.412	0.007
Euler	3681.724	1.18	-11.182	0.008	-10.543	0.009	-10.538	0.004	-10.408	0.007
Euler	3682.650	1.79	-11.200	0.019	-10.511	0.012	-10.512	0.013	-10.411	0.013
Euler	3684.655	1.68	-11.186	0.012	-10.537	0.022	-10.516	0.016	-10.408	0.015
Euler	3685.695	0.88	-11.153	0.011	-10.505	0.012	-10.521	0.015	-10.375	0.016
Euler	3687.628	1.25	-11.154	0.036	-10.497	0.034	-10.496	0.033	-10.376	0.037
Euler	3688.702	1.02	-11.133	0.037	-10.469	0.037	-10.479	0.037	-10.344	0.038
Euler	3690.841	1.70	-11.195	0.005	-10.486	0.025	-10.553	0.026	-10.414	0.026
Euler	3692.717	1.48	-11.192	0.005	-10.524	0.010	-10.546	0.010	-10.416	0.007
Euler	3693.588	1.53	-11.203	0.007	-10.520	0.008	-10.548	0.012	-10.426	0.012
Euler	3694.748	1.24	-11.153	0.021	-10.466	0.020	-10.496	0.021	-10.350	0.023
Euler	3695.718	1.04	-11.177	0.005	-10.509	0.010	-10.519	0.005	-10.379	0.007
Euler	3696.733	1.10	-11.171	0.008	-10.502	0.013	-10.509	0.009	-10.365	0.011
Maidanak	3700.329	1.34	-11.225	0.011	-10.557	0.013	-10.573	0.013	-10.425	0.011
Euler	3700.675	1.33	-11.174	0.008	-10.522	0.006	-10.514	0.008	-10.384	0.006
Maidanak	3703.338	1.09	-11.195	0.004	-10.546	0.008	-10.544	0.007	-10.407	0.010
Maidanak	3705.337	1.01	-11.174	0.013	-10.522	0.012	-10.536	0.013	-10.412	0.014
Mercator	3707.550	1.79	-11.158	0.017	-10.502	0.016	-10.516	0.013	-10.372	0.015

Telescope	Epoch	$\bar{s}$ ($''$)	m_A	σ_A	m_B	σ_B	m_C	σ_C	m_D	σ_D
Euler	3707.709	1.23	-11.152	0.009	-10.488	0.008	-10.500	0.008	-10.372	0.008
Mercator	3709.534	1.66	-11.140	0.013	-10.505	0.013	-10.515	0.006	-10.378	0.008
Maidanak	3710.303	1.49	-11.169	0.006	-10.478	0.009	-10.511	0.009	-10.390	0.011
Maidanak	3711.274	1.26	-11.191	0.007	-10.521	0.009	-10.532	0.009	-10.405	0.012
Mercator	3712.541	2.23	-11.138	0.012	-10.485	0.008	-10.516	0.024	-10.346	0.003
Maidanak	3713.291	1.45	-11.163	0.010	-10.481	0.013	-10.505	0.013	-10.383	0.012
Mercator	3714.448	1.67	-11.153	0.010	-10.486	0.011	-10.509	0.012	-10.381	0.012
Maidanak	3715.292	1.17	-11.180	0.009	-10.509	0.012	-10.543	0.010	-10.402	0.012
Euler	3715.700	1.47	-11.147	0.007	-10.482	0.011	-10.500	0.008	-10.343	0.009
Maidanak	3717.273	1.23	-11.184	0.014	-10.497	0.012	-10.527	0.012	-10.405	0.019
Mercator	3718.463	1.40	-11.170	0.025	-10.499	0.027	-10.528	0.031	-10.373	0.033
Euler	3720.673	1.31	-11.129	0.007	-10.466	0.016	-10.503	0.013	-10.337	0.013
Maidanak	3721.299	1.55	-11.171	0.010	-10.503	0.019	-10.514	0.019	-10.344	0.019
Maidanak	3724.279	1.05	-11.168	0.022	-10.501	0.022	-10.529	0.023	-10.377	0.022
Maidanak	3726.287	1.40	-11.171	0.008	-10.486	0.009	-10.505	0.009	-10.350	0.009
Maidanak	3728.264	1.92	-11.144	0.013	-10.458	0.018	-10.499	0.020	-10.368	0.018
Euler	3731.732	1.25	-11.114	0.004	-10.459	0.007	-10.481	0.006	-10.326	0.006
Euler	3732.607	1.56	-11.145	0.030	-10.452	0.035	-10.506	0.030	-10.324	0.031
Euler	3733.609	1.49	-11.131	0.010	-10.450	0.012	-10.503	0.016	-10.324	0.016
Euler	3734.716	1.25	-11.134	0.009	-10.465	0.010	-10.478	0.008	-10.311	0.011
Euler	3735.585	1.59	-11.137	0.024	-10.445	0.024	-10.493	0.024	-10.312	0.028
Maidanak	3740.208	1.49	-11.140	0.005	-10.481	0.010	-10.489	0.003	-10.331	0.006
Maidanak	3741.216	1.41	-11.138	0.009	-10.465	0.009	-10.500	0.011	-10.313	0.013
Euler	3741.722	1.62	-11.122	0.027	-10.459	0.031	-10.501	0.028	-10.295	0.032
Euler	3747.663	1.24	-11.110	0.018	-10.425	0.017	-10.484	0.022	-10.288	0.018
Maidanak	3757.179	1.20	-11.130	0.007	-10.445	0.009	-10.478	0.007	-10.307	0.009
Euler	3757.632	1.52	-11.112	0.022	-10.439	0.026	-10.468	0.022	-10.276	0.025
Euler	3765.596	1.17	-11.086	0.009	-10.422	0.013	-10.455	0.005	-10.273	0.009
Mercator	3768.365	2.34	-11.101	0.010	-10.436	0.013	-10.453	0.021	-10.297	0.022
Mercator	3771.394	2.29	-11.079	0.025	-10.450	0.033	-10.460	0.030	-10.301	0.027
Euler	3771.629	1.22	-11.072	0.012	-10.426	0.012	-10.447	0.013	-10.265	0.014
Maidanak	3774.113	1.22	-11.119	0.027	-10.477	0.027	-10.486	0.026	-10.316	0.027
Euler	3782.583	1.35	-11.081	0.014	-10.430	0.021	-10.458	0.020	-10.271	0.022
Euler	3787.555	1.31	-11.084	0.005	-10.405	0.013	-10.438	0.009	-10.259	0.011
Euler	3795.545	1.55	-11.090	0.011	-10.393	0.018	-10.461	0.012	-10.231	0.012
Euler	3800.544	1.43	-11.087	0.006	-10.401	0.006	-10.438	0.005	-10.216	0.010
Euler	3806.538	1.57	-11.083	0.025	-10.392	0.034	-10.470	0.025	-10.229	0.031
Euler	3813.507	1.25	-11.079	0.009	-10.356	0.012	-10.402	0.019	-10.201	0.016
Euler	3819.517	1.12	-11.079	0.019	-10.363	0.024	-10.420	0.018	-10.200	0.020
Euler	3820.502	1.19	-11.084	0.011	-10.372	0.018	-10.426	0.021	-10.210	0.018
Euler	3821.503	1.22	-11.070	0.023	-10.370	0.024	-10.417	0.026	-10.201	0.028
Euler	3829.488	1.62	-11.154	0.009	-10.453	0.023	-10.503	0.006	-10.276	0.015
Euler	3831.495	1.37	-11.141	0.014	-10.435	0.018	-10.462	0.014	-10.252	0.020
Euler	3840.483	1.63	-11.119	0.012	-10.432	0.024	-10.430	0.024	-10.289	0.031
Euler	3844.486	1.70	-11.136	0.009	-10.453	0.027	-10.465	0.007	-10.332	0.012
Euler	3847.474	1.91	-11.129	0.017	-10.439	0.032	-10.527	0.027	-10.317	0.033
Euler	3849.469	1.92	-11.134	0.015	-10.402	0.040	-10.507	0.014	-10.351	0.023
Euler	3945.903	1.20	-11.044	0.044	-10.351	0.044	-10.373	0.045	-10.189	0.044
Euler	3950.920	1.00	-11.046	0.025	-10.370	0.025	-10.391	0.026	-10.227	0.025
Euler	3970.855	1.43	-11.098	0.004	-10.390	0.003	-10.450	0.022	-10.207	0.013
Mercator	3977.708	1.18	-11.157	0.010	-10.447	0.006	-10.480	0.011	-10.250	0.009
Mercator	3978.700	1.67	-11.122	0.015	-10.390	0.024	-10.455	0.012	-10.226	0.007
Mercator	3979.715	1.25	-11.105	0.015	-10.368	0.013	-10.425	0.012	-10.193	0.028
Mercator	3980.713	1.88	-11.113	0.012	-10.368	0.026	-10.398	0.016	-10.183	0.016
Euler	3980.796	1.39	-11.096	0.024	-10.384	0.035	-10.441	0.033	-10.222	0.025
Euler	3981.836	1.38	-11.120	0.002	-10.422	0.010	-10.447	0.003	-10.247	0.009
Euler	3982.802	1.27	-11.096	0.038	-10.409	0.031	-10.395	0.040	-10.216	0.049
Euler	3999.749	1.12	-11.099	0.011	-10.393	0.012	-10.433	0.011	-10.209	0.011
Euler	4003.883	1.31	-11.111	0.004	-10.404	0.008	-10.438	0.007	-10.221	0.011
Euler	4008.810	1.14	-11.113	0.009	-10.402	0.012	-10.440	0.011	-10.220	0.012
Maidanak	4016.477	1.08	-11.180	0.030	-10.443	0.036	-10.472	0.035	-10.280	0.037
Maidanak	4020.454	1.13	-11.194	0.019	-10.448	0.019	-10.505	0.023	-10.273	0.021
Euler	4021.787	1.82	-11.135	0.011	-10.406	0.014	-10.464	0.012	-10.260	0.014
Euler	4023.840	1.62	-11.125	0.011	-10.410	0.014	-10.459	0.013	-10.253	0.013
Euler	4024.775	1.49	-11.130	0.013	-10.421	0.009	-10.443	0.013	-10.245	0.017
Euler	4025.738	1.63	-11.131	0.013	-10.435	0.013	-10.464	0.013	-10.245	0.021

Telescope	Epoch	$\bar{s}$ ($''$)	m_A	σ_A	m_B	σ_B	m_C	σ_C	m_D	σ_D
Euler	4027.784	1.51	-11.114	0.008	-10.405	0.011	-10.456	0.010	-10.234	0.015
Euler	4028.773	1.16	-11.106	0.012	-10.397	0.011	-10.444	0.013	-10.221	0.014
Euler	4036.693	1.56	-11.096	0.007	-10.401	0.010	-10.425	0.011	-10.241	0.014
Maidanak	4039.413	1.24	-11.120	0.019	-10.421	0.020	-10.442	0.020	-10.275	0.019
Euler	4039.670	1.81	-11.085	0.011	-10.367	0.013	-10.433	0.014	-10.243	0.011
Maidanak	4041.408	1.36	-11.128	0.017	-10.450	0.018	-10.473	0.018	-10.291	0.020
Euler	4042.638	1.55	-11.067	0.012	-10.399	0.013	-10.394	0.011	-10.212	0.016
Euler	4046.837	1.58	-11.077	0.020	-10.404	0.022	-10.424	0.020	-10.234	0.021
Maidanak	4057.376	2.37	-11.110	0.022	-10.406	0.036	-10.444	0.018	-10.194	0.009
Euler	4057.814	1.37	-11.105	0.011	-10.385	0.013	-10.444	0.011	-10.222	0.015
Euler	4065.692	1.29	-11.060	0.004	-10.372	0.005	-10.404	0.007	-10.207	0.007
Mercator	4074.534	1.54	-11.088	0.028	-10.429	0.004	-10.394	0.008	-10.207	0.023
Mercator	4076.542	1.56	-11.084	0.018	-10.377	0.034	-10.427	0.024	-10.234	0.021
Euler	4082.644	1.31	-11.072	0.006	-10.377	0.008	-10.413	0.010	-10.213	0.011
Mercator	4083.533	1.34	-11.086	0.009	-10.384	0.008	-10.420	0.012	-10.232	0.006
Euler	4084.710	1.48	-11.063	0.010	-10.360	0.014	-10.415	0.017	-10.195	0.012
Mercator	4086.433	1.73	-11.080	0.016	-10.358	0.017	-10.406	0.018	-10.215	0.016
Euler	4087.679	1.19	-11.047	0.019	-10.340	0.021	-10.382	0.021	-10.174	0.019
Euler	4089.735	1.23	-11.045	0.004	-10.358	0.007	-10.399	0.011	-10.174	0.005
Euler	4091.700	1.20	-11.044	0.007	-10.346	0.008	-10.392	0.009	-10.188	0.009
Euler	4097.678	1.24	-11.049	0.003	-10.345	0.011	-10.381	0.006	-10.185	0.008
Euler	4105.692	1.18	-11.035	0.010	-10.322	0.025	-10.358	0.011	-10.145	0.012
Euler	4111.634	1.35	-11.070	0.011	-10.355	0.013	-10.412	0.011	-10.176	0.013
Euler	4118.727	1.79	-11.113	0.017	-10.377	0.012	-10.419	0.015	-10.159	0.017
Maidanak	4120.221	1.43	-11.169	0.004	-10.372	0.010	-10.462	0.015	-10.192	0.003
Maidanak	4121.201	1.42	-11.159	0.010	-10.364	0.012	-10.452	0.016	-10.185	0.013
Euler	4122.646	1.35	-11.125	0.004	-10.359	0.007	-10.438	0.008	-10.159	0.006
Maidanak	4129.172	1.29	-11.170	0.005	-10.391	0.010	-10.470	0.005	-10.193	0.015
Euler	4131.653	1.29	-11.113	0.007	-10.353	0.009	-10.414	0.011	-10.170	0.006
Euler	4135.545	1.57	-11.149	0.018	-10.356	0.026	-10.431	0.020	-10.205	0.019
Mercator	4140.375	1.18	-11.170	0.009	-10.418	0.010	-10.474	0.010	-10.239	0.012
Euler	4140.614	1.47	-11.148	0.013	-10.391	0.017	-10.442	0.014	-10.198	0.015
Mercator	4141.422	1.16	-11.162	0.006	-10.403	0.010	-10.469	0.007	-10.219	0.014
Mercator	4143.357	1.60	-11.155	0.017	-10.380	0.020	-10.475	0.016	-10.205	0.026
Euler	4150.617	1.30	-11.143	0.015	-10.396	0.016	-10.430	0.015	-10.212	0.016
Euler	4161.574	1.74	-11.178	0.003	-10.408	0.008	-10.451	0.021	-10.198	0.025
Euler	4164.550	1.35	-11.177	0.010	-10.371	0.018	-10.450	0.025	-10.212	0.010
Mercator	4167.343	1.39	-11.223	0.002	-10.422	0.024	-10.466	0.013	-10.274	0.016
Euler	4169.563	1.28	-11.190	0.008	-10.398	0.009	-10.458	0.011	-10.203	0.008
Mercator	4171.376	1.93	-11.205	0.026	-10.402	0.036	-10.474	0.028	-10.239	0.037
Euler	4174.525	1.50	-11.207	0.012	-10.395	0.016	-10.463	0.012	-10.254	0.012
Mercator	4175.363	1.50	-11.214	0.020	-10.397	0.021	-10.477	0.047	-10.323	0.079
Euler	4179.509	1.56	-11.222	0.015	-10.410	0.016	-10.477	0.014	-10.245	0.013
Euler	4191.490	1.50	-11.208	0.016	-10.408	0.021	-10.481	0.016	-10.270	0.022
Euler	4197.482	1.28	-11.203	0.011	-10.392	0.008	-10.448	0.012	-10.245	0.022
Euler	4329.922	1.48	-11.242	0.012	-10.437	0.018	-10.519	0.017	-10.316	0.018
Mercator	4337.720	1.12	-11.252	0.009	-10.476	0.010	-10.528	0.011	-10.339	0.010
Mercator	4339.734	0.98	-11.278	0.035	-10.503	0.035	-10.554	0.036	-10.442	0.061
Euler	4342.870	1.25	-11.194	0.018	-10.406	0.020	-10.470	0.025	-10.280	0.027
Mercator	4343.740	1.04	-11.281	0.049	-10.487	0.054	-10.578	0.049	-10.419	0.091
Euler	4347.890	1.46	-11.196	0.012	-10.441	0.016	-10.482	0.015	-10.289	0.012
Mercator	4349.712	1.41	-11.196	0.004	-10.446	0.005	-10.510	0.007	-10.301	0.009
Mercator	4352.719	1.23	-11.175	0.014	-10.464	0.016	-10.515	0.014	-10.320	0.015
Mercator	4354.722	1.38	-11.167	0.015	-10.462	0.016	-10.509	0.016	-10.319	0.017
Mercator	4357.670	1.51	-11.172	0.009	-10.425	0.010	-10.481	0.012	-10.281	0.012
Mercator	4358.698	1.21	-11.174	0.012	-10.438	0.014	-10.526	0.011	-10.302	0.014
Mercator	4360.736	1.30	-11.148	0.015	-10.448	0.015	-10.508	0.015	-10.295	0.018
Mercator	4362.727	1.11	-11.136	0.010	-10.436	0.013	-10.490	0.012	-10.302	0.012
Euler	4367.885	1.19	-11.091	0.013	-10.384	0.011	-10.441	0.010	-10.245	0.016
Euler	4369.813	1.12	-11.055	0.034	-10.375	0.036	-10.396	0.033	-10.195	0.035
Euler	4371.862	1.19	-11.060	0.019	-10.367	0.018	-10.409	0.016	-10.247	0.025
Mercator	4372.615	1.51	-11.102	0.022	-10.443	0.028	-10.466	0.032	-10.301	0.026
Mercator	4373.661	1.50	-11.081	0.008	-10.396	0.011	-10.448	0.022	-10.288	0.009
Mercator	4374.682	1.51	-11.075	0.015	-10.396	0.009	-10.453	0.009	-10.254	0.025
Mercator	4376.713	2.15	-11.067	0.019	-10.388	0.023	-10.462	0.033	-10.197	0.061
Mercator	4377.726	1.52	-11.096	0.015	-10.422	0.014	-10.448	0.021	-10.271	0.020

Telescope	Epoch	$\bar{s}$ ($''$)	m_A	σ_A	m_B	σ_B	m_C	σ_C	m_D	σ_D
Euler	4380.860	1.12	-11.037	0.014	-10.361	0.013	-10.405	0.015	-10.199	0.015
Euler	4386.767	1.24	-11.049	0.014	-10.384	0.015	-10.414	0.014	-10.204	0.017
Euler	4390.834	1.31	-11.031	0.012	-10.359	0.010	-10.408	0.012	-10.199	0.015
Euler	4393.656	1.64	-11.034	0.023	-10.336	0.041	-10.407	0.025	-10.244	0.029
Mercator	4394.657	1.27	-11.024	0.009	-10.375	0.010	-10.415	0.012	-10.222	0.008
Euler	4398.862	1.26	-10.977	0.013	-10.329	0.012	-10.393	0.009	-10.159	0.010
Euler	4402.647	1.68	-11.027	0.014	-10.381	0.017	-10.381	0.017	-10.149	0.013
Euler	4411.801	1.13	-11.030	0.011	-10.321	0.005	-10.389	0.012	-10.147	0.011
Mercator	4413.600	1.17	-11.099	0.006	-10.385	0.014	-10.431	0.019	-10.162	0.011
Euler	4415.686	1.14	-11.030	0.009	-10.314	0.019	-10.382	0.012	-10.137	0.011
Euler	4419.827	1.22	-11.019	0.005	-10.346	0.008	-10.391	0.004	-10.147	0.009
Mercator	4422.574	1.82	-10.990	0.013	-10.319	0.029	-10.408	0.016	-10.162	0.022
Euler	4423.663	1.46	-10.992	0.007	-10.361	0.009	-10.396	0.014	-10.158	0.009
Mercator	4431.579	1.95	-11.004	0.045	-10.336	0.052	-10.351	0.057	-10.148	0.059
Euler	4432.722	1.33	-11.008	0.013	-10.296	0.010	-10.377	0.011	-10.141	0.013
Mercator	4436.585	1.94	-11.058	0.030	-10.354	0.028	-10.445	0.036	-10.206	0.037
Mercator	4437.562	1.48	-11.054	0.024	-10.376	0.011	-10.439	0.019	-10.194	0.032
Euler	4437.685	1.53	-11.026	0.029	-10.339	0.030	-10.403	0.031	-10.153	0.034
Mercator	4439.543	1.34	-11.053	0.043	-10.374	0.044	-10.448	0.043	-10.189	0.044
Euler	4444.788	1.62	-11.014	0.012	-10.356	0.017	-10.412	0.024	-10.128	0.020
Euler	4448.615	1.56	-11.012	0.011	-10.324	0.012	-10.412	0.012	-10.136	0.015
Euler	4451.662	1.45	-11.005	0.009	-10.321	0.014	-10.394	0.017	-10.129	0.012
Euler	4462.719	1.43	-10.946	0.010	-10.329	0.017	-10.407	0.012	-10.139	0.011
Euler	4469.665	1.85	-10.947	0.022	-10.339	0.020	-10.396	0.020	-10.170	0.023
Mercator	4471.408	2.40	-10.939	0.035	-10.376	0.034	-10.407	0.046	-10.077	0.043
Mercator	4481.462	1.66	-10.914	0.020	-10.336	0.025	-10.364	0.020	-10.151	0.021
Euler	4481.639	1.37	-10.922	0.008	-10.323	0.017	-10.364	0.012	-10.150	0.014
Mercator	4491.404	1.59	-10.926	0.010	-10.339	0.011	-10.399	0.007	-10.155	0.017
Euler	4492.638	1.22	-10.905	0.007	-10.301	0.009	-10.376	0.009	-10.121	0.015
Euler	4501.646	1.58	-10.873	0.006	-10.324	0.026	-10.367	0.017	-10.119	0.016

The beginning of knowledge is the discovery of something we do not understand.

Frank Herbert (1920 - 1986)

10 The quadruply lensed quasar WFI J2026-4536

Contents

10.1 Introduction

Let us start with reminding that the light curves for this object have been obtained in collaboration with Gilles Orban de Xivry in the framework of his master thesis (Orban de Xivry, 2009). As I co-supervised his work (supervisor: P. Magain), I am in charge of the study of this object.

We owe the discovery of WFI J2026-453 to Morgan et al. (2004): this quadruply lensed quasar (RA = $20^{\rm h}26^{\rm m}10^{\rm s}.43$ and DEC = $-45°36'27''.10$, J2000) was first observed during an optical survey using the WFI camera mounted on the MPG/ESO 2.2m telescope. To date, not much is known about this gravitational mirage: the redshift of the source is z_s=2.23, the one of the lens has never been measured, no time delay has ever been obtained and no modeling has ever been done. Still, Morgan et al. (2004) gave a few more considerations that might be helpful for us: they found that the longest delay might be around one week or two, that the environment of the lens is quite simple and that the image fluxes are likely to be corrupted by microlensing.

10.2 Observational material

The monitoring of WFI J2026-453 started at the end of April 2004. The object was followed, through the R-band filter, until October 2008 with the Swiss 1.2m Euler telescope located in Chile, on the ESO La Silla site. The 2048×2048 CCD camera of Euler has a resolution of $0\farcs344$ and a field of view of $11' \times 11'$. During each night of observation, 5 dithered frames of 360s each were acquired. In total, that object have been observed during 218 different nights with a mean sampling step (when the object is visible) of one epoch every 6 days. The mean seeing per epoch varies from $0\farcs99$ to $2\farcs24$ with an average value of $1\farcs47$.

10.3 Image processing

To reduce all the frames at our disposal, we use the revised semi-automated reduction pipeline described in Chapter 6.

The image with the best seeing is chosen as the reference frame. It was acquired on the night of the 18^{th} August 2005 and has a seeing of $0\farcs90$. This frame is displayed on Fig. 10.1. The reference stars chosen in the field of WFI J2026-453 are highlighted with circles. We then check if these stars are non-variable in plotting their mean magnitude per night, obtained with SExtractor, against the Heliocentric Julian Day: Fig. 10.2 shows that the curves of all the chosen stars are flat. All these stars are averaged per night in what we call a "mean star". This curve is shown in green on Fig. 10.2. The precision of this mean is estimated by its standard deviation and reaches 3×10^{-4} mag, which represents the photometric precision. The red light curve labeled "QSO" is drawn from the flux measured in a box containing the four lensed images and the main lens galaxy, again averaged over an epoch of observation. As already mentioned, it does not represent the real intrisic variability of the source. The complete system varies on a maximum scale of around 0.35 magnitude in nearly three years.

Amongst the reference stars, four stars, labeled as S1, S3, S7 and S9 on Fig. 10.1, are chosen so that we can use them to create one PSF per image with the *PSFsimult* algorithm. We can then apply MCS to the whole set of frames. Let us remind that at this stage of the reduction, some frames, unnoticed until then, have been rejected for diverse reasons, such as a bad flat field correction or a loss of the guiding star during observation. That is why the preliminary light curves present 224 epochs, while the final light curves are drawn from 218 nights, as announced above. As usual we adopt an analytical Gaussian with a FWHM of 2 pixels as the resolution of the deconvolved frame. Thanks to the dithering technique used during observation, we can adopt a sampling step twice smaller than the original one: the pixel size is $0\farcs172$ in the final deconvolved frame. Let us remind that during deconvolution, the intensity of each source is allowed to vary from image to image. However, the smooth background is constant in the whole set.

The original reference image of the quasar is shown in Fig. 10.3 along with the deconvolved frame. The point sources are labeled as in Morgan et al. (2004). It is clear that the lensing galaxy remains undetected. This is due to the resolution of the

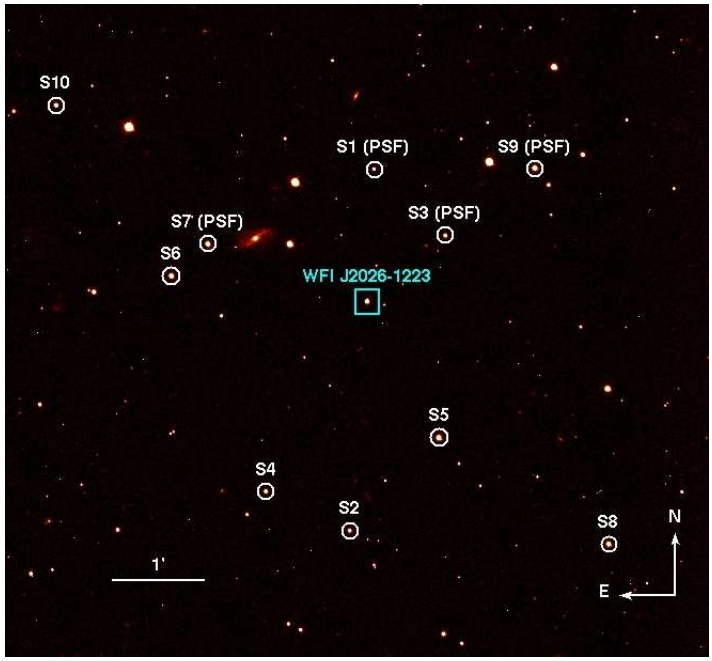

Figure 10.1: Partial field of view of the reference frame of WFI J2026-453. The reference stars are encircled and labeled from S1 to S10. Amongst them, S1, S3, S7 and S9 were used to determine the PSF, as marked in parentheses next to their label.

camera and to the signal-to-noise ratio. Moreover, we can see that A_1 and A_2 are highly blended, as already obvious on the original frame. That is why, having in mind the final aim, i.e. the time delay measurement, it is better to sum their contributions into one component that we call A. Indeed, the individual curves of A_1 and A_2 are very noisy as shown on Fig. 10.4 and the delay between A_1 and A_2 is supposed to be very short, probably around 2 or 3 days. The final light curves are displayed in Fig. 10.5. Let us recall that, to estimate the $\pm 1\sigma$ error bars, the statistical noise and the systematic errors have to be considered. The first one is quite easy to obtain: the dispersion around the mean of the fluxes during a night is a good estimate. The second one, the systematic contribution, is estimated thanks to the deconvolution of a star in the field. To avoid any bias in that process, the star should not be one of the PSF stars, nor should it be located too far from the lensed quasar or the PSF stars themselves. We choose S4 for that purpose (see Fig. 10.1). The light curve of S4 is shown in black on Fig. 10.4 and Fig. 10.5: the curve is nearly flat, as it should be for a non-variable star.

A few remarks can be made about the light curves of the three lensed images. First, not much structure is observable: there is no sharp peak or deep hole. Then, source C being the faintest source amongst the four, its curve is quite noisy and some points seem to be affected by large errors. Finally, it is unlikely that such light curves will provide reliable time delays, as confirmed by some first tests run by M. Tewes using a

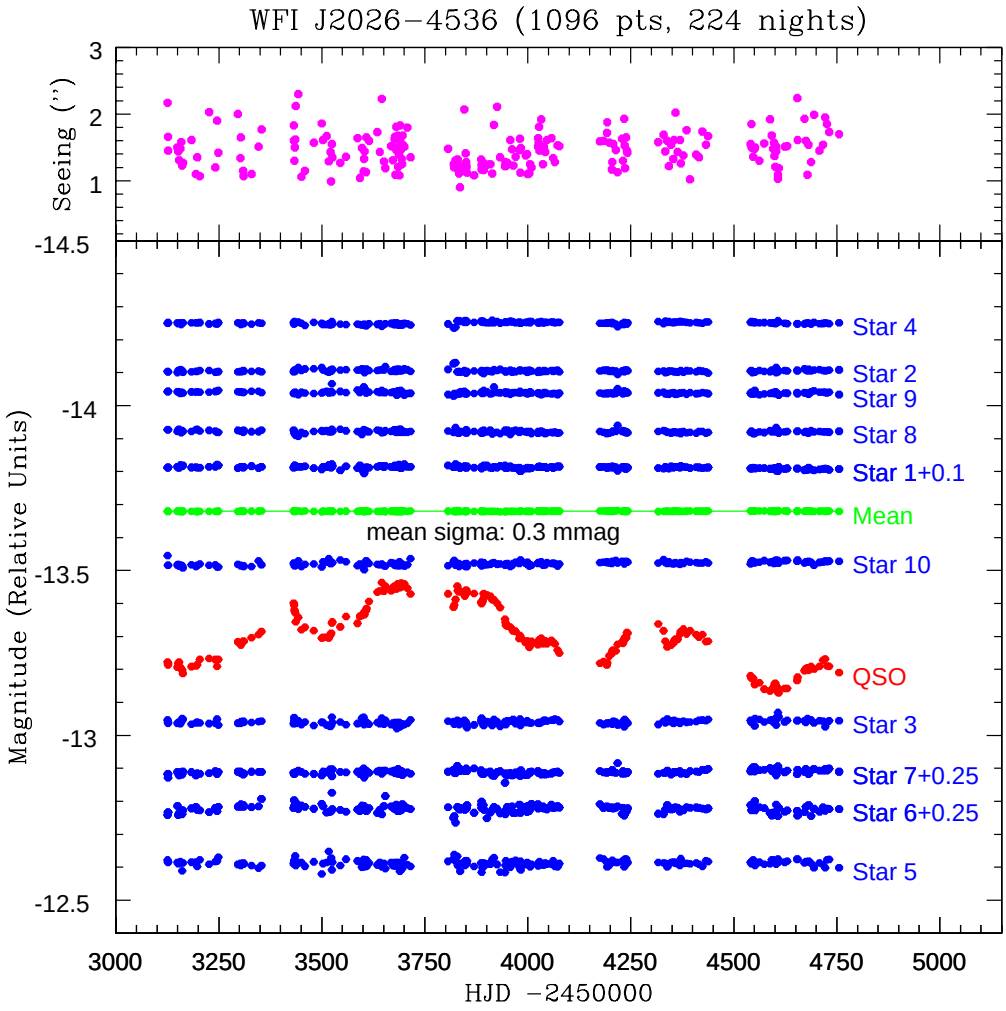

Figure 10.2: Preliminary light curves of WFI J2026-453 from April 2004 to October 2008. The magnitude is given in arbitrary units as a function of the Heliocentric Julian Day (HJD). The blue light curves are related to the reference stars in the field of WFI J2026-453 while the red one is drawn from the flux measured in a box containing the four lensed images and the main lens galaxy.

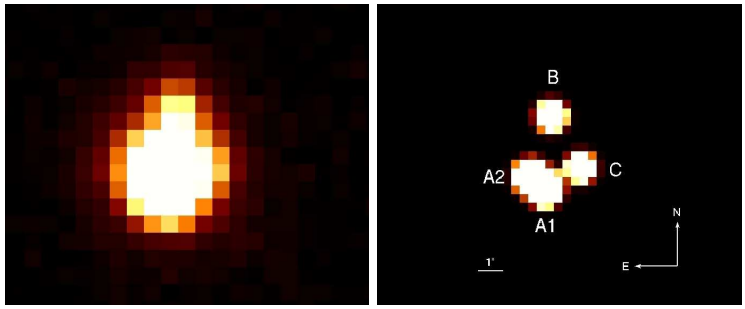

Figure 10.3: *Left*: original reference image of the quasar. The four lensed images are not clearly distinguishable. *Right*: result from the simultaneous deconvolution of the ground-based frames.

revised version (Tewes & et al., in preparation) of the minimum dispersion method of Pelt et al. (1998).

10.4 Conclusions

Given the light curves we obtain, WFI J2026-453 does not seem to be an ideal candidate to obtain H_0. Maybe a monitoring with a higher resolution camera and longer exposure times could allow for the measurement of the time delays. We should also hope for sharper variations of the quasar intrinsic luminosity.

Even if the time delays were known, that object could not be used to determine the Hubble constant or the mass distribution in the lensing galaxy in the present circumstances. Indeed, the redshift of the lens has never been measured. A. Eigenbrod and G. Letawe attempted to obtain a redshift from spectra acquired with the FOcal Reducer and low dispersion Spectrograph (FORS1) mounted on the ESO Very Large Telescope (VLT) at the Observatory of Paranal in Chile. They applied a version of the MCS deconvolution algorithm adapted for spectra (Courbin et al., 2000). However, the system is so compact that it is really a challenge to disentangle the lens spectrum from the much stronger overlapping quasar spectra. The best result so far is a very noisy spectrum, without any obvious emission line, so that no redshift could be measured until now.

Let us note that the geometry of this system is studied in Chapter 12 with the application of ISMCS. Indeed, WFI J2026-453 is part of a sample of seven lensed quasars, chosen amongst the COSMOGRAIL objects, with no measured time delay.

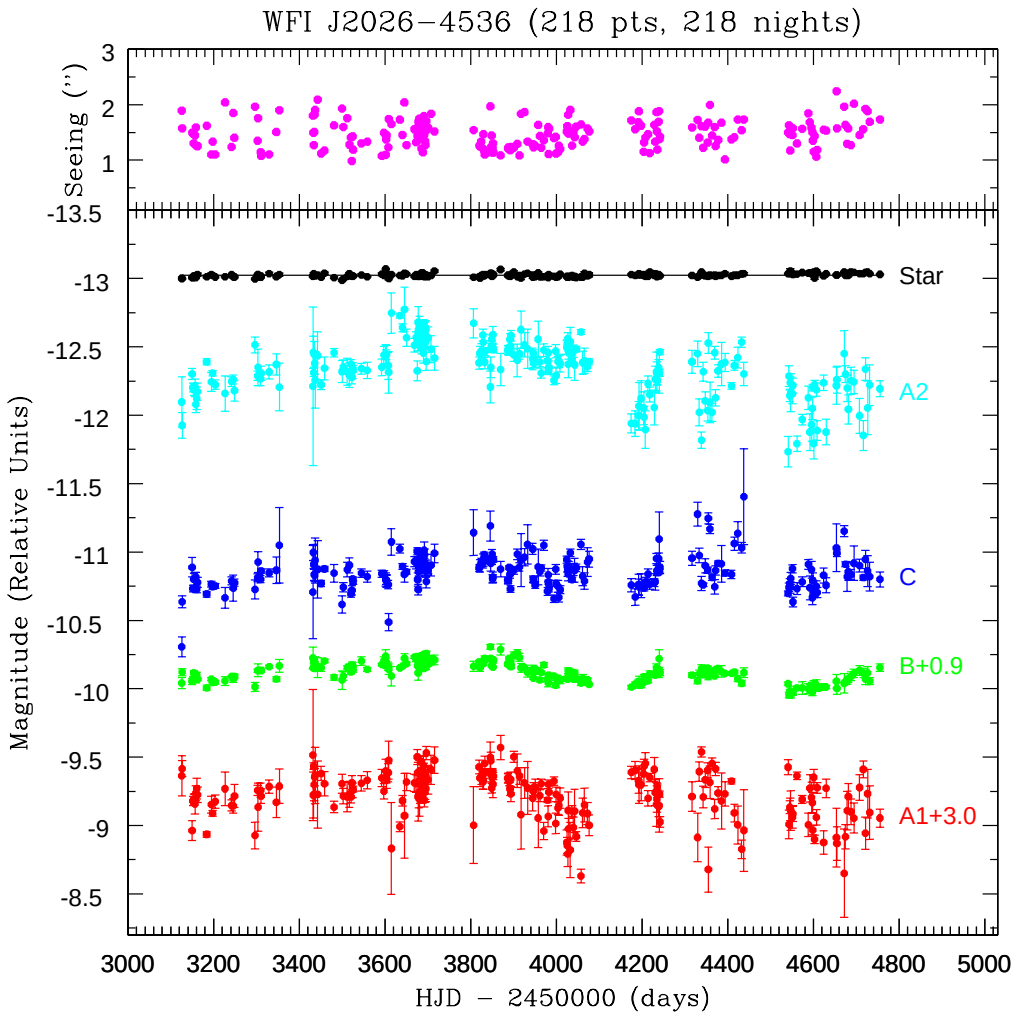

Figure 10.4: Light curves of the four lensed images of WFI J2026-453 from April 2004 to October 2008. The magnitude is given in arbitrary units as a function of the Heliocentric Julian Day (HJD). Each color corresponds to a lensed image: red for A1, cyan for A2, green for B and blue for C. The black points correspond to the curve of the star S4 used to estimate the error bars of the quasar (see text for details). Each point is plotted with the $\pm 1\sigma$ error bars. On the top part of the graph, the mean seeing of each epoch is plotted in magenta against HJD.

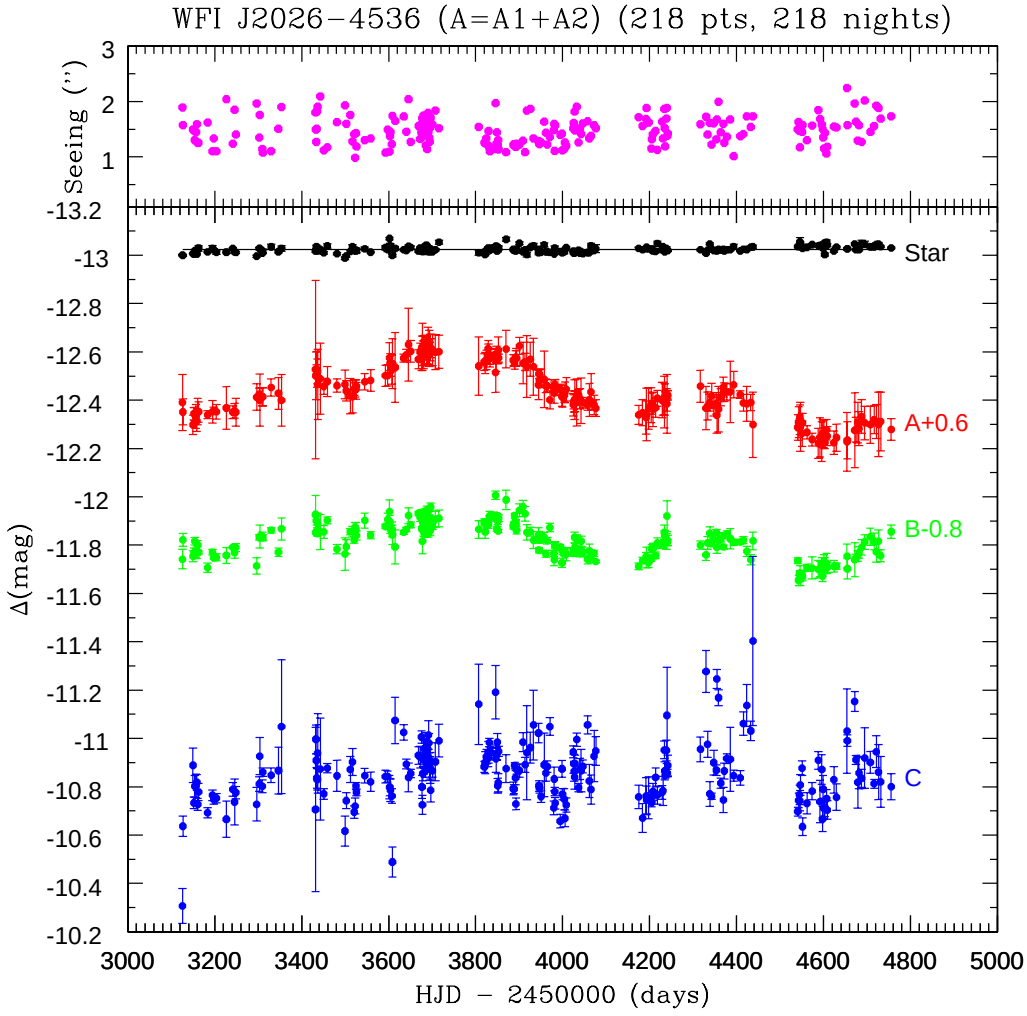

Figure 10.5: Light curves of the three (A=A_1+A_2, B, C) lensed images of WFI J2026-453 from April 2004 to October 2008. The curve of A is drawn in red. The comments made in the caption of Fig. 10.4 remain valid.

Appendix: photometry table

Table 10.1: Photometry of WFI J2026-453. "Epoch" is actually equal to HJD − 2450000 and $\bar{s}$ is the mean seeing per epoch of observation.

Epoch	$\bar{s}$ ($''$)	m_B	σ_B	m_C	σ_C	m_A	σ_A
3125.902	1.89	-10.942	0.040	-10.306	0.072	-12.991	0.117
3126.894	1.58	-11.021	0.027	-10.636	0.042	-12.951	0.054
3149.878	1.49	-10.954	0.023	-10.889	0.071	-12.898	0.040
3151.815	1.48	-10.968	0.020	-10.733	0.024	-12.944	0.026
3153.848	1.30	-11.017	0.015	-10.801	0.045	-12.942	0.028
3156.797	1.45	-10.968	0.018	-10.804	0.049	-12.932	0.049
3158.785	1.59	-10.971	0.027	-10.818	0.032	-12.913	0.043
3160.844	1.25	-11.001	0.019	-10.728	0.025	-12.953	0.055
3162.782	1.26	-10.969	0.007	-10.778	0.036	-12.951	0.042
3183.833	1.62	-10.907	0.019	-10.692	0.021	-12.940	0.017
3194.865	1.10	-10.971	0.011	-10.765	0.022	-12.952	0.047
3197.845	1.33	-10.946	0.004	-10.747	0.019	-12.956	0.015
3203.857	1.10	-10.949	0.015	-10.752	0.019	-12.952	0.031
3226.760	2.04	-10.957	0.033	-10.666	0.076	-12.968	0.089
3241.776	1.24	-10.991	0.005	-10.789	0.029	-12.950	0.027
3245.770	1.85	-10.970	0.024	-10.737	0.095	-12.956	0.031
3248.700	1.40	-10.990	0.017	-10.776	0.026	-12.950	0.057
3296.611	1.96	-10.914	0.034	-10.727	0.070	-13.013	0.055
3302.555	1.35	-11.032	0.012	-10.812	0.030	-13.025	0.025
3303.593	1.76	-11.036	0.048	-10.927	0.077	-13.000	0.108
3309.545	1.15	-11.036	0.019	-10.802	0.027	-13.015	0.038
3310.602	1.08	-11.031	0.011	-10.861	0.017	-13.015	0.037
3329.546	1.11	-11.062	0.010	-10.848	0.030	-13.053	0.036
3346.579	1.50	-10.971	0.017	-10.867	0.097	-13.028	0.066
3353.571	1.90	-11.067	0.046	-11.049	0.277	-13.000	0.107
3431.855	1.80	-11.127	0.078	-10.706	0.341	-13.127	0.369
3432.865	1.50	-11.052	0.005	-10.996	0.060	-13.101	0.099
3433.894	1.27	-11.100	0.017	-10.909	0.029	-13.128	0.020
3434.872	1.51	-11.059	0.013	-10.836	0.042	-13.128	0.075
3435.872	1.82	-11.047	0.010	-10.830	0.044	-13.120	0.051
3436.869	1.91	-11.090	0.042	-10.939	0.165	-13.066	0.146
3442.844	2.09	-11.054	0.073	-10.873	0.211	-13.089	0.147
3450.866	1.12	-11.055	0.026	-10.770	0.022	-13.057	0.034
3458.875	1.17	-11.102	0.015	-10.877	0.020	-13.077	0.062
3480.851	1.63	-10.983	0.019	-10.845	0.065	-13.061	0.028
3499.766	1.93	-10.963	0.067	-10.616	0.063	-13.065	0.059
3502.805	1.60	-10.994	0.029	-10.742	0.033	-13.039	0.042
3511.808	1.76	-11.056	0.012	-10.872	0.054	-13.018	0.073
3516.805	1.28	-11.056	0.022	-10.903	0.055	-13.014	0.066
3520.878	1.41	-11.022	0.013	-10.695	0.025	-13.046	0.027
3522.881	0.99	-11.075	0.019	-10.720	0.033	-13.048	0.036
3524.901	1.43	-11.065	0.028	-10.804	0.014	-13.045	0.040
3525.885	1.19	-11.040	0.019	-10.777	0.014	-13.058	0.016
3544.782	1.30	-11.102	0.031	-10.846	0.030	-13.077	0.034
3558.669	1.33	-11.041	0.014	-10.820	0.040	-13.082	0.044
3592.505	1.08	-11.078	0.008	-10.842	0.026	-13.101	0.044
3597.562	1.49	-11.106	0.027	-10.842	0.023	-13.103	0.044
3601.643	1.10	-11.139	0.048	-10.799	0.048	-13.175	0.063
3602.675	1.38	-11.097	0.026	-10.798	0.035	-13.152	0.030
3603.738	1.45	-11.065	0.016	-10.786	0.046	-13.146	0.047
3607.550	1.23	-11.065	0.031	-10.762	0.029	-13.127	0.061
3608.620	1.74	-11.043	0.040	-10.488	0.063	-13.151	0.104
3614.795	1.65	-10.993	0.071	-11.074	0.096	-13.136	0.144
3634.708	1.73	-11.053	0.008	-11.025	0.032	-13.174	0.016
3640.710	1.46	-11.065	0.009	-10.894	0.021	-13.188	0.024
3645.610	2.04	-11.122	0.033	-10.838	0.059	-13.231	0.151
3650.577	1.27	-11.084	0.013	-10.855	0.018	-13.203	0.045
3668.529	1.56	-11.131	0.009	-10.930	0.036	-13.169	0.040

Epoch	$\bar{s}$ ($''$)	m_A	σ_A	m_B	σ_B	m_C	σ_C
3672.542	1.32	-11.116	0.017	-10.923	0.045	-13.200	0.036
3675.527	1.44	-11.135	0.013	-11.006	0.026	-13.169	0.045
3676.545	1.60	-11.069	0.009	-10.799	0.047	-13.217	0.049
3677.573	1.70	-11.016	0.052	-10.725	0.039	-13.221	0.098
3678.544	1.37	-11.095	0.037	-10.854	0.029	-13.195	0.051
3680.542	1.75	-11.060	0.021	-10.930	0.079	-13.198	0.067
3681.571	1.69	-11.051	0.015	-10.958	0.057	-13.195	0.049
3682.586	1.50	-11.089	0.019	-10.909	0.032	-13.224	0.025
3684.547	1.68	-11.072	0.026	-10.865	0.025	-13.223	0.047
3685.572	1.21	-11.135	0.018	-10.911	0.036	-13.231	0.033
3686.548	1.59	-11.105	0.005	-10.986	0.039	-13.191	0.040
3687.546	1.42	-11.077	0.014	-10.978	0.010	-13.213	0.046
3688.573	1.14	-11.146	0.016	-10.944	0.036	-13.216	0.031
3689.533	1.62	-11.134	0.016	-10.956	0.025	-13.200	0.051
3690.547	1.79	-11.100	0.036	-10.924	0.033	-13.226	0.077
3691.575	1.46	-11.049	0.016	-11.014	0.059	-13.207	0.025
3692.559	1.56	-11.083	0.027	-10.981	0.040	-13.192	0.046
3693.532	1.34	-11.090	0.027	-10.875	0.049	-13.214	0.074
3694.531	1.27	-11.115	0.011	-10.909	0.015	-13.215	0.025
3695.531	1.53	-11.060	0.019	-10.878	0.064	-13.218	0.055
3696.543	1.71	-11.158	0.017	-10.785	0.048	-13.216	0.040
3700.544	1.59	-11.078	0.012	-10.866	0.027	-13.209	0.065
3707.546	1.84	-11.108	0.033	-10.903	0.079	-13.199	0.072
3715.538	1.52	-11.111	0.035	-10.991	0.068	-13.201	0.068
3806.868	1.54	-11.065	0.037	-11.142	0.167	-13.141	0.121
3819.855	1.26	-11.096	0.013	-10.882	0.023	-13.158	0.034
3821.852	1.25	-11.054	0.025	-10.900	0.046	-13.154	0.044
3824.860	1.34	-11.079	0.008	-10.924	0.030	-13.167	0.040
3828.904	1.21	-11.099	0.007	-10.917	0.034	-13.214	0.034
3829.850	1.47	-11.084	0.014	-10.942	0.045	-13.190	0.042
3831.860	1.17	-11.113	0.008	-10.982	0.018	-13.172	0.024
3832.875	1.10	-11.122	0.018	-10.948	0.018	-13.174	0.036
3835.905	1.13	-11.115	0.007	-10.941	0.021	-13.186	0.007
3845.901	1.97	-11.207	0.017	-11.191	0.110	-13.115	0.082
3846.892	1.14	-11.123	0.011	-10.916	0.056	-13.167	0.048
3847.870	1.24	-11.117	0.014	-10.935	0.024	-13.190	0.034
3848.856	1.44	-11.068	0.010	-10.936	0.026	-13.178	0.024
3849.860	1.19	-11.114	0.015	-10.984	0.035	-13.181	0.030
3850.894	1.22	-11.099	0.014	-10.804	0.031	-13.197	0.017
3851.862	1.30	-11.059	0.006	-10.816	0.038	-13.208	0.055
3852.878	1.14	-11.111	0.014	-10.947	0.021	-13.175	0.016
3869.832	1.09	-11.187	0.041	-10.876	0.058	-13.212	0.078
3886.889	1.21	-11.077	0.010	-10.793	0.027	-13.165	0.024
3887.892	1.23	-11.088	0.009	-10.790	0.019	-13.165	0.023
3889.848	1.23	-11.122	0.011	-10.888	0.013	-13.152	0.023
3891.888	1.18	-11.090	0.013	-10.837	0.029	-13.174	0.032
3892.872	1.18	-11.094	0.011	-10.729	0.024	-13.178	0.036
3893.930	1.24	-11.061	0.015	-10.872	0.020	-13.173	0.032
3900.809	1.22	-11.145	0.026	-10.867	0.028	-13.225	0.035
3908.758	1.29	-11.160	0.027	-10.984	0.039	-13.153	0.086
3913.755	1.09	-11.130	0.029	-10.891	0.031	-13.159	0.036
3917.606	1.83	-11.053	0.032	-10.941	0.194	-13.140	0.128
3925.695	1.86	-11.055	0.018	-10.962	0.064	-13.170	0.070
3932.856	1.34	-11.021	0.035	-11.056	0.145	-13.139	0.118
3944.677	1.28	-11.042	0.030	-11.022	0.040	-13.063	0.060
3945.821	1.29	-10.979	0.011	-10.803	0.022	-13.109	0.019
3946.773	1.23	-11.021	0.013	-10.795	0.021	-13.083	0.024
3950.680	1.26	-11.043	0.011	-10.759	0.024	-13.089	0.038
3957.589	1.63	-11.033	0.019	-10.891	0.131	-13.086	0.117
3961.782	1.44	-10.964	0.015	-10.857	0.033	-13.060	0.029
3964.561	1.22	-11.018	0.013	-10.883	0.024	-13.059	0.026
3970.689	1.36	-11.074	0.017	-11.049	0.036	-13.001	0.038
3979.609	1.48	-10.966	0.012	-10.713	0.028	-13.050	0.014
3980.739	1.59	-10.941	0.026	-10.832	0.049	-13.031	0.044
3981.722	1.11	-10.999	0.013	-10.780	0.017	-13.066	0.020
3982.718	1.57	-10.995	0.018	-10.732	0.024	-13.051	0.033

Epoch	$\bar{s}$ ($''$)	m_A	σ_A	m_B	σ_B	m_C	σ_C
3994.583	1.40	-10.993	0.010	-10.658	0.028	-13.043	0.023
3998.596	1.42	-10.927	0.019	-10.874	0.035	-13.018	0.043
3999.574	1.12	-10.977	0.015	-10.770	0.023	-13.012	0.040
4003.574	1.14	-10.963	0.008	-10.749	0.044	-13.020	0.029
4005.569	1.26	-10.976	0.012	-10.669	0.035	-13.032	0.043
4008.643	1.20	-10.963	0.027	-10.724	0.029	-13.045	0.048
4024.626	1.51	-10.975	0.014	-10.945	0.025	-12.982	0.047
4025.573	1.61	-10.973	0.018	-10.895	0.040	-12.993	0.029
4026.567	1.56	-10.971	0.017	-10.864	0.041	-12.995	0.044
4027.560	1.82	-11.032	0.021	-10.840	0.051	-13.003	0.082
4028.557	1.48	-10.992	0.014	-10.895	0.036	-12.995	0.043
4032.533	1.90	-11.025	0.018	-10.995	0.028	-12.991	0.097
4036.531	1.26	-10.984	0.007	-10.796	0.017	-13.021	0.025
4039.529	1.51	-10.971	0.019	-10.873	0.044	-13.006	0.042
4042.520	1.41	-11.016	0.020	-10.867	0.087	-12.998	0.094
4046.515	1.61	-10.972	0.020	-10.884	0.027	-12.990	0.022
4057.523	1.64	-10.941	0.018	-11.056	0.037	-12.979	0.021
4061.539	1.33	-10.976	0.028	-10.823	0.069	-13.001	0.068
4065.529	1.38	-10.951	0.023	-10.788	0.060	-13.034	0.076
4072.540	1.57	-10.967	0.013	-10.926	0.106	-12.981	0.040
4076.538	1.52	-10.933	0.005	-10.948	0.059	-12.967	0.034
4174.875	1.72	-10.913	0.013	-10.758	0.049	-12.940	0.039
4183.872	1.56	-10.936	0.013	-10.671	0.060	-12.949	0.054
4191.876	1.68	-10.953	0.017	-10.761	0.077	-12.928	0.069
4192.866	1.88	-10.949	0.043	-10.745	0.058	-12.941	0.109
4197.833	1.62	-10.929	0.022	-10.755	0.087	-12.966	0.086
4203.858	1.16	-10.944	0.011	-10.757	0.018	-12.980	0.072
4204.866	1.32	-10.986	0.017	-10.735	0.019	-12.986	0.044
4207.851	1.41	-10.986	0.023	-10.780	0.035	-12.962	0.071
4213.876	1.47	-10.957	0.014	-10.838	0.039	-12.968	0.040
4217.854	1.13	-11.008	0.022	-10.765	0.038	-13.008	0.033
4228.814	1.64	-11.003	0.010	-10.776	0.028	-13.000	0.073
4230.781	1.33	-11.001	0.015	-10.783	0.060	-13.006	0.068
4233.869	1.87	-11.053	0.030	-10.952	0.037	-12.992	0.107
4234.897	1.52	-11.042	0.020	-10.866	0.037	-13.003	0.065
4235.881	1.19	-11.032	0.007	-10.848	0.013	-13.019	0.015
4238.872	1.69	-11.016	0.033	-10.951	0.043	-13.001	0.047
4239.924	1.88	-11.120	0.064	-11.095	0.199	-12.985	0.121
4240.877	1.38	-11.012	0.013	-10.856	0.016	-13.023	0.017
4241.918	1.42	-11.019	0.023	-10.887	0.043	-13.019	0.020
4316.652	1.59	-11.000	0.017	-10.955	0.051	-13.058	0.067
4329.811	1.73	-10.960	0.023	-11.277	0.087	-12.967	0.090
4333.528	1.40	-11.009	0.027	-10.976	0.054	-12.976	0.058
4338.534	1.61	-11.049	0.027	-10.770	0.051	-12.989	0.035
4342.642	1.23	-11.005	0.008	-10.761	0.012	-13.018	0.052
4347.531	1.60	-11.024	0.022	-10.900	0.051	-12.979	0.044
4353.528	1.32	-11.052	0.013	-10.869	0.022	-12.987	0.045
4354.716	1.67	-10.991	0.025	-11.247	0.039	-12.937	0.074
4358.483	1.99	-11.019	0.033	-11.168	0.033	-12.963	0.093
4363.497	1.44	-11.025	0.012	-10.815	0.021	-13.012	0.036
4369.597	1.60	-10.993	0.008	-10.746	0.052	-13.055	0.040
4371.493	1.26	-11.041	0.007	-10.865	0.033	-13.033	0.038
4377.512	1.36	-11.046	0.014	-10.916	0.020	-13.034	0.033
4385.549	1.67	-11.027	0.042	-10.914	0.133	-13.034	0.127
4393.504	1.01	-11.012	0.013	-10.846	0.022	-13.064	0.054
4408.528	1.38	-11.013	0.008	-10.836	0.030	-13.024	0.016
4415.513	1.41	-11.021	0.014	-11.062	0.048	-12.989	0.035
4423.541	1.73	-10.974	0.021	-11.137	0.087	-12.985	0.072
4432.530	1.54	-10.940	0.021	-11.031	0.040	-12.990	0.034
4437.533	1.73	-11.018	0.036	-11.404	0.350	-12.899	0.136
4540.878	1.50	-10.936	0.012	-10.697	0.019	-12.887	0.053
4542.902	1.63	-10.855	0.021	-10.743	0.030	-12.909	0.064
4544.885	1.47	-10.881	0.013	-10.767	0.040	-12.892	0.033
4545.910	1.17	-10.881	0.033	-10.742	0.042	-12.932	0.049
4546.878	1.48	-10.864	0.030	-10.808	0.043	-12.890	0.102
4550.905	1.45	-10.878	0.018	-10.877	0.030	-12.862	0.053

Epoch	$\bar{s}$ ($''$)	m_A	σ_A	m_B	σ_B	m_C	σ_C
4551.884	1.57	-10.871	0.018	-10.635	0.037	-12.906	0.040
4561.881	1.30	-10.906	0.015	-10.732	0.044	-12.867	0.027
4573.888	1.57	-10.905	0.046	-10.782	0.035	-12.838	0.027
4587.917	1.84	-10.900	0.037	-10.910	0.037	-12.822	0.062
4591.833	1.68	-10.901	0.032	-10.738	0.088	-12.845	0.081
4595.857	1.58	-10.921	0.027	-10.871	0.061	-12.829	0.083
4597.841	1.50	-10.873	0.025	-10.666	0.052	-12.863	0.057
4598.913	1.35	-10.906	0.009	-10.790	0.057	-12.843	0.021
4600.832	1.15	-10.929	0.032	-10.710	0.042	-12.861	0.058
4602.895	1.44	-10.920	0.028	-10.715	0.038	-12.827	0.027
4606.904	1.06	-10.924	0.042	-10.750	0.038	-12.878	0.043
4608.796	1.19	-10.907	0.021	-10.704	0.038	-12.852	0.039
4623.881	1.55	-10.912	0.024	-10.829	0.055	-12.825	0.048
4629.696	1.53	-10.913	0.012	-10.757	0.055	-12.845	0.056
4653.832	2.24	-10.955	0.050	-11.031	0.174	-12.828	0.121
4654.778	1.58	-10.902	0.043	-10.991	0.024	-12.835	0.077
4671.822	1.96	-10.940	0.071	-11.153	0.041	-12.876	0.155
4674.799	1.63	-10.947	0.015	-10.911	0.019	-12.879	0.051
4678.805	1.30	-10.955	0.021	-10.819	0.107	-12.907	0.085
4681.571	1.57	-10.970	0.024	-10.856	0.064	-12.883	0.071
4687.681	1.27	-10.991	0.032	-10.834	0.037	-12.932	0.070
4694.681	2.02	-11.013	0.030	-10.919	0.126	-12.906	0.069
4707.569	1.45	-11.035	0.035	-10.901	0.045	-12.899	0.077
4716.482	1.56	-11.016	0.035	-10.812	0.018	-12.919	0.057
4721.546	1.92	-10.972	0.042	-10.945	0.066	-12.912	0.070
4726.523	1.88	-11.017	0.047	-10.861	0.114	-12.900	0.133
4731.504	1.69	-10.956	0.025	-10.821	0.105	-12.912	0.121
4755.552	1.73	-11.056	0.028	-10.800	0.054	-12.879	0.045

Part IV

Observational constraints and modeling

Whatever you are by nature, keep to it; never desert your line of talent. Be what nature intended you for and you will succeed.

Sydney Smith (1771 - 1845)

11

Contribution to WFI J2033-4723 with ISMCS

Contents

11.1 Introduction

WFI J2033-4723 (RA = $20^{\rm h}33^{\rm m}42^{\rm s}.08$ and DEC = $-47°23'43''.00$, J2000), a quadruply imaged quasar, was discovered in La Silla, Chile, during an optical survey using the MPG/ESO 2.2m telescope operated by the European Southern Observatory, MPG standing for *Max Planck Gesellschaft*. This discovery is related by Morgan et al. (2004). The source redshift is $z_s = 1.66$ while, according to Eigenbrod et al. (2006b), the galaxy has a redshift of $z_l = 0.661$. The magnitude of the entire system is estimated at ~ 17.9 in the g filter[1]. The maximum separation between two lensed images amounts to $2''.5$. This gravitational mirage is surrounded by at least six galaxies within a radius of 20 arcseconds, which makes it a difficult system to model.

That object has been studied in detail by the COSMOGRAIL collaboration. C. Vuissoz was the lead author of the paper and her work consisted in obtaining the light curves from ground-based data, the final aim being of course the measurement of H_0. As already mentioned, the time delays extracted from the light curves are not enough

[1]The passband of the g filter is $458\ nm \leq \lambda \leq 528\ nm$.

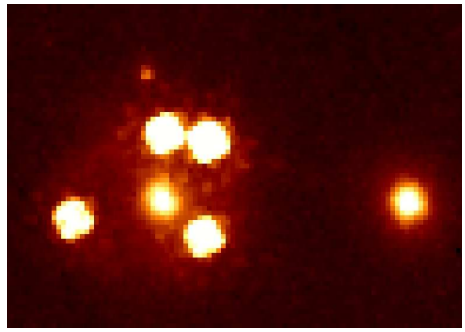

Figure 11.1: Combination of the four calibrated and reduced images of WFI J2033-4723 obtained with HST/NIC2 through the F160W filter. North is to the top and East to the left.

to get to the Hubble constant. Also needed are the redshifts of the lens and source which are already known, and a good knowledge of the geometry of the system. That is why we apply ISMCS to HST/NIC2 images of WFI J2033-4723: in order to have at our disposal accurate constraints on the positions of the lens and on the lensed images. These constraints can then be used to model the potential of the lens and, in including the delays, to finally obtain the Hubble constant.

All these details can be found in the related paper at the end of this chapter. We will only relate here our contribution to this study.

11.2 HST/NIC2 images

Our set of images was acquired with the camera 2 of NICMOS through the F160W filter on the 14^{th} of April 2004. The set is composed of four images obtained in the MULTIACCUM mode: the first frame is a combination of 19 samples while the other three frames are a combination of 20 samples. As a consequence, the first image has an exposure time of 640s while the others have an exposure time of 704s. According to the version 6.3 of the Tiny Tim software (Krist & Hook, 2004), the mean pixel size of these frames is $0\farcs07568$. As for the Cloverleaf, we use the images calibrated by CALNICA[2]. A combination of these four frames is shown on Fig. 11.1. Let us notice that the lensing galaxy is already obvious in between the four point sources. Moreover, two other objects are present on the frame: the first one, which turns out to be a nearby galaxy (Morgan et al., 2004), to the West of the system, and the other one, whose nature is unknown, to the North of the galaxy.

11.3 Deconvolution with ISMCS

Here again, no star is available in the field or in extra images acquired in the same conditions as WFI J2033-4723. We thus use the iterative strategy, ISMCS, which allows

[2]Let us recall that CALNICA is the HST image reduction pipeline.

to improve the Tiny Tim PSF step by step and to separate possible significant extended structures from the point sources. As in the case of H1413+117 and HE 0435-1223, we use a sampling step 2 times smaller than the original pixel size and a Gaussian with a FWHM of 2 pixels for $\mathcal{R}(\vec{x})$, i.e. the PSF of the deconvolved frame. These choices lead to an improvement of the resolution of the deconvolved frame compared to the original images as well as a good sampling of the resulting light distribution.

Convergence is reached after three iterations and the reduced χ^2 amounts to 3.59. The results are shown on Fig. 11.2. The mean residual map shown on the right panel indicates that there is no systematic structure under the lensed images. That means that the instrumental profile is well adapted. The irregular remnant structures differ from one lensed image to the other and show that no single PSF can perfectly reproduce the four images, which is probably due to small variations of the PSF in the field.

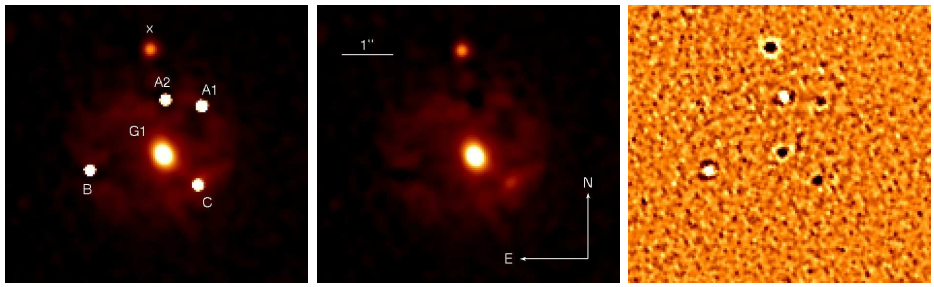

Figure 11.2: Results of the simultaneous deconvolution for WFI J2033-4723 (last iteration of ISMCS). North is to the top and East to the left. *L*eft: deconvolved frame, i.e. point sources plus smooth background; the point sources are labeled as in Morgan et al. (2004), G_1 being the main lensing galaxy and X the unknown object. *Middle*: smooth background common to all images. *R*ight: mean residual map, in units of sigma, of the simultaneous deconvolution; the colour scale ranges from -4σ in black to $+4\sigma$ in white.

On Fig. 11.2, the resulting deconvolved frame was obtained with a larger smoothing parameter than the one leading to the best reduced χ^2: the aim is simply to highlight the presence of a diffuse and faint structure surrounding the four lensed images (see middle panel). Several questions come straight to mind. First, at which distance is this structure located? Then could it be a kind of halo associated to the lens galaxy? In that case, why is it encircling the lensed images? This first hypothesis does not seem very likely. Another possibility is that this structure is located between us and the lensed system, along the line of sight: it could be a dust cloud and the perspective could make it seemingly encircling the four images. But again, we would be in special conditions. Or, it could simply be a distorted version of the host galaxy of the lensed quasar. To define the real nature of this structure, a very deep and highly resolved spectrum could allow the measurement of its redshift and tell us where it is located compared to the lensing galaxy. Such data are not available yet.

Here again, it is worth using a special feature of MCS, which allows to introduce, in the deconvolution, an analytical model[3] to represent the light distribution of a galaxy.

[3]See Sect. 5.3.2 on p. 58 for details.

Let us recall that, as a part of the image background, this model is constrained by all the frames of the set. According to Eigenbrod et al. (2006b), the main lens of WFI J2033-4723 is an early-type galaxy. A de Vaucouleurs (de Vaucouleurs, 1948) profile is thus used in MCS to model it. The case of G_2, the companion galaxy located on the western side of our lensed quasar, is slightly different. Indeed, that galaxy is likely to be an elliptical (Vuissoz et al., 2008) but it has not been shown yet. We thus test both light profiles available with MCS, i.e. the de Vaucouleurs and exponential (Freeman, 1970) models, and conclude that a de Vaucouleurs profile is better adapted to model it. Let us note that G_2 is not visible on Fig. 11.2. The results are summarized in Table 11.1. The columns show the following usual parameters: the PA in degrees positive East of North, the ellipticity, the effective semi-major and semi-minor axes and the effective radius. For each parameter, we list the standard deviation of the mean extracted from the individual deconvolutions of each frame. Let us insist on the fact that the listed value of the parameter itself is not the mean of the individual values, but the result coming from the simultaneous deconvolution. Moreover, as in the case of HE 0435-1223, the center of these galaxies along with the shape parameters are determined with an analytical profile only, i.e. the numerical background is set to zero during the deconvolution.

Label	PA (°)	Ellipticity	a_{eff} ($''$)	b_{eff} ($''$)	R_{eff} ($''$)
G_1	27.8 ± 4.3	0.18 ± 0.03	0.665 ± 0.036	0.556 ± 0.025	0.61 ± 0.03
G_2	6.4 ± 3.1	0.15 ± 0.02	0.389 ± 0.004	0.334 ± 0.005	0.36 ± 0.005

Table 11.1: Measured shape parameters for the lensing galaxy G_1 of WFI J2033-4723 and its companion galaxy G_2. They are derived from a fit of a de Vaucouleurs profile, included in the MCS algorithm. See text for details.

11.4 Astrometry and photometry

The astrometric and photometric results extracted from the last iteration are listed in Table 11.2. They are derived the same way as for the Cloverleaf and HE 0435-1223: we deconvolve each image individually except for the results concerning the galaxy which are better constrained on the simultaneous deconvolution. For each measurement, the standard deviation of the mean obtained from the individual deconvolutions is provided. Of course, these are internal error bars. And as we have no image acquired in different conditions with the same or a similar quality instrument, we cannot compare the results and thus cannot obtain reliable estimation of the total error bars. But this has been done for the Cloverleaf in Chantry & Magain (2007) in comparing the results obtained in two filters and two telescope orientations (see Chapter 8). If we suppose that the main source of error is an uncorrected distortion, then the total error will essentially depend on the spatial extension of the object on the CCD. In comparing WFI J2033-4723 to the Cloverleaf, we estimate that the total errors are of the order of 2 mas.

Let us compare our astrometric results with those obtained by Morgan et al. (2004) in treating the very same images. The latter are listed in Table 11.3. Our results are

ID	ΔRA (″)	ΔDEC (″)	Magnitude
B	0.	0.	17.77 ± 0.02
A1	-2.1946 ± 0.0004	1.2601 ± 0.0003	17.16 ± 0.02
A2	-1.4809 ± 0.0004	1.3756 ± 0.0005	17.52 ± 0.02
C	-2.1128 ± 0.0003	-0.2778 ± 0.0003	17.88 ± 0.02
G_1	-1.4388 ± 0.0020	0.3113 ± 0.0008	18.59 ± 0.03
G_2	-5.4100 ± 0.0006	0.2850 ± 0.0003	18.14 ± 0.02

Table 11.2: Relative astrometry and photometry for the four components of WFI J2033-4733, its primary lens and G_2. These results come from the application of ISMCS to HST/NIC2 frames of the object. The two coordinates are given in arcseconds relative to component B along the two usual directions: the right ascension and the declination. The photometry is given in apparent magnitude in the Vega system. For each measurement, we present the $\pm 1\sigma$ internal error bars.

compatible with theirs within their error bars which are the dominating ones. The largest difference is observed for the position of the lens galaxy. This is not unexpected as a blended diffuse object is more sensitive to the image processing.

We notice that the error bars of the magnitudes shown in the last column of Table 11.2 are larger by a factor of 3 to 10 than those obtained for the Cloverleaf in the same filter (see Table 8.1). There is no obvious explanation based on the deconvolution process itself: the results are quite satisfying when we look at the χ^2 and the mean residual map. One aspect of WFI J2033-4723 comes then to mind: the presence of the diffuse background surrounding the four lensed images. Let us compare it to source C (see on the left panel of Fig. 11.2) which is the less-magnified image: their total fluxes are of the same order, the approximate magnitude of the halo in the Vega system being of 17.7. The latter value is estimated on the simultaneously deconvolved frame in subtracting the contribution of the galaxy itself from the total flux of the background (halo plus galaxy). Even if this method is quite coarse, it is enough for us to give the following conclusion: the halo can be partly responsible for the loss of accuracy in our photometry compared to what we obtain when we apply ISMCS to the Cloverleaf. Indeed, as the PSF is improved step by step in subtracting an approximate background,

ID	ΔRA (″)	ΔDEC (″)
B	0.	0.
A1	-2.193 ± 0.03	1.258 ± 0.02
A2	-1.477 ± 0.03	1.368 ± 0.02
C	-2.108 ± 0.03	-0.282 ± 0.03
G_1	-1.412 ± 0.33	0.277 ± 0.20
G_2	-5.397 ± 0.10	0.247 ± 0.20

Table 11.3: Relative astrometry of WFI J2033-4723 obtained by Morgan et al. (2004). The two coordinates are given in arcseconds relative to component B along the two usual directions: the right ascension and the declination. The $\pm 1\sigma$ error bars are also given.

our process is very sensitive to any structure under the sources. The worst situation that can occur to us is an object with a flat and nearly constant background under each point source. And this is exactly the case for WFI J2033-4723.

The previous discussion can lead to another one, related to the algorithm itself: the MCS version that we used when we treated the Cloverleaf and WFI J2033-4723 did not allow to impose non-varying source intensities from one frame to the other[4]. In other words that means that the background in each frame is the same except for a multiplicative factor and an additive term but the intensity of the point sources is free to vary from one image to the other (see Eq. 5.25 on p. 60): the ratio between the intensity of the sources and the background is not the same in each frame. And in certain cases, it seems to be more advantageous, in terms of χ^2, to have a slightly different ratio in the images. That will, of course, degrade the accuracy of the photometry. This nasty effect can be avoided with the new version of the algorithm in constraining the point sources and the background to have the same relative intensity in all images.

[4]The reason of this choice is simple: the algorithm was first used to obtain light curves of varying gravitationally lensed systems.

11.5 Related paper

The paper related to WFI J2033-4723 is shown on the following pages.

COSMOGRAIL: the COSmological MOnitoring of GRAvItational Lenses

VII. Time delays and the Hubble constant from WFI J2033-4723

C. Vuissoz, F. Courbin, D. Sluse, G.Meylan, V. Chantry, E. Eulaers, C. Morgan, M. E. Eyler, C. S. Kochanek, J. Coles, P. Saha, P. Magain, and E. E. Falco

Astronomy & Astrophysics, 2008, 488, 481-490

A&A 488, 481–490 (2008)
DOI: 10.1051/0004-6361:200809866

Astronomy & Astrophysics

COSMOGRAIL: the COSmological MOnitoring of GRAvItational Lenses⋆,⋆⋆

VII. Time delays and the Hubble constant from WFI J2033–4723

C. Vuissoz[1], F. Courbin[1], D. Sluse[1], G. Meylan[1], V. Chantry[2,⋆⋆⋆], E. Eulaers[2], C. Morgan[3,4], M. E. Eyler[4], C. S. Kochanek[3], J. Coles[5], P. Saha[5], P. Magain[2], and E. E. Falco[6]

[1] Laboratoire d'Astrophysique, École Polytechnique Fédérale de Lausanne (EPFL), Observatoire de Sauverny, 1290 Versoix, Switzerland
e-mail: christel.vuissoz@epfl.ch
[2] Institut d'Astrophysique et de Géophysique, Université de Liège, Allée du 6 août 17, Sart-Tilman, Bât. B5C, 4000 Liège, Belgium
[3] Department of Astronomy and the Center for Cosmology and Astroparticle Physics, The Ohio State University, Columbus, OH 43210, USA
[4] Department of Physics, United States Naval Academy, 572C Holloway Road, Annapolis MD 21402, USA
[5] Institute of Theoretical Physics, University of Zürich, Winterthurerstrasse 190, 8057 Zürich, Switzerland
[6] Harvard-Smithsonian Center for Astrophysics, 60 Garden Street, Cambridge MA 02138, USA

Received 28 March 2008 / Accepted 2 July 2008

ABSTRACT

Gravitationally lensed quasars can be used to map the mass distribution in lensing galaxies and to estimate the Hubble constant H_0 by measuring the time delays between the quasar images. Here we report the measurement of two independent time delays in the quadruply imaged quasar WFI J2033−4723 ($z = 1.66$). Our data consist of R-band images obtained with the Swiss 1.2 m EULER telescope located at La Silla and with the 1.3 m SMARTS telescope located at Cerro Tololo. The light curves have 218 independent epochs spanning 3 full years of monitoring between March 2004 and May 2007, with a mean temporal sampling of one observation every 4th day. We measure the time delays using three different techniques, and we obtain $\Delta t_{B-A} = 35.5 \pm 1.4$ days (3.8%) and $\Delta t_{B-C} = 62.6^{+4.1}_{-2.3}$ days ($^{+6.5\%}_{-3.7\%}$), where A is a composite of the close, merging image pair. After correcting for the time delays, we find R-band flux ratios of $F_A/F_B = 2.88 \pm 0.04$, $F_A/F_C = 3.38 \pm 0.06$, and $F_{A1}/F_{A2} = 1.37 \pm 0.05$ with no evidence for microlensing variability over a time scale of three years. However, these flux ratios do not agree with those measured in the quasar emission lines, suggesting that longer term microlensing is present. Our estimate of H_0 agrees with the concordance value: non-parametric modeling of the lensing galaxy predicts $H_0 = 67^{+13}_{-10}$ km s^{-1} Mpc^{-1}, while the Single Isothermal Sphere model yields $H_0 = 63^{+7}_{-3}$ km s^{-1} Mpc^{-1} (68% confidence level). More complex lens models using a composite de Vaucouleurs plus NFW galaxy mass profile show twisting of the mass isocontours in the lensing galaxy, as do the non-parametric models. As all models also require a significant external shear, this suggests that the lens is a member of the group of galaxies seen in field of view of WFI J2033−4723.

Key words. gravitational lensing – cosmology: cosmological parameters – quasars: individual: WFI J2033−4723

1. Introduction

When a quasar is gravitationally lensed and we observe multiple images of the source there are light travel time differences between the images. Any intrinsic variation of the quasar is observed at different times in each image with a measurable "time delay" between them. Refsdal (1964) first showed that time delays provide a means of determining the Hubble constant H_0 independent of any local distance calibrator, provided a mass model can be inferred for the lensing galaxy. Conversely, one can also assume H_0 in order to study the distribution of the total mass in the lensing galaxy.

During the past 25 years, time delays have been measured in only 17 systems, at various accuracy levels (see Oguri 2007, for a review). As the error in the time delay propagates directly into H_0, it is important to make it as small as possible. Unfortunately, most existing time delays have uncertainties of the order of 10% that are comparable to the current uncertainties in H_0. This uncertainty can be reduced by increasing the sample of lenses with known time delays, and by simultaneously fitting all lenses in the sample with a common value for H_0 (Saha et al. 2006b,a; Coles 2008).

COSMOGRAIL is an optical monitoring campaign that aims at measuring time delays for a large number of gravitationally lensed quasars to accuracies of a few percent using a network of 1- and 2-m class telescopes. The first result of this campaign was the measurement of the time delay in the doubly imaged quasar SDSS J1650+4251 to an accuracy of 3.8% based on two

⋆ Based on observations obtained with the 1.2 m EULER Swiss Telescope, the 1.3 m Small and Moderate Aperture Research Telescope System (SMARTS) which is operated by the SMARTS Consortium, and the NASA/ESA *Hubble Space Telescope* as part of program HST-GO-9744 of the Space Telescope Science Institute, which is operated by the Association of Universities for Research in Astronomy, Inc., under NASA contract NAS 5-26555.
⋆⋆ Table 4 is only available in electronic form at the CDS via anonymous ftp to cdsarc.u-strasbg.fr (130.79.128.5) or via http://cdsweb.u-strasbg.fr/cgi-bin/qcat?J/A+A/488/481
⋆⋆⋆ Research Fellow, Belgian National Fund for Scientific Research (FNRS).

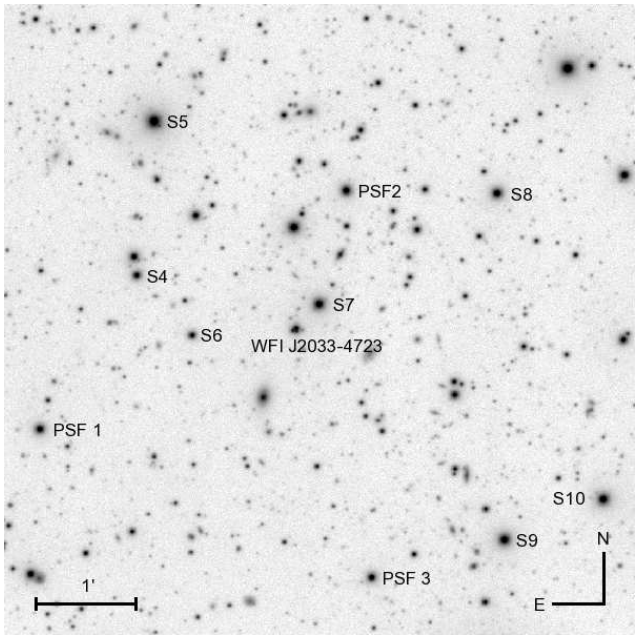

Fig. 1. The 6.3′ × 6.3′ field of view around WFI J2033−4723. This image is the central part of a combination of 418 *R*-band frames obtained with the 1.2 m EULER Telescope with a total exposure time of 48 h and a mean seeing of 1.3″. The three stars PSF1−3 used to model the Point Spread Function (PSF) and the 7 reference stars S4−10 used for frame alignment and flux calibration are indicated.

observing seasons of data (Vuissoz et al. 2007). COSMOGRAIL complements a second monitoring group whose most recent results are a delay for HE 1104-1805 (Poindexter et al. 2007). In this paper we present time-delay measurements for the quadruply imaged quasar WFI J2033−4723 based on merging 3 years of optical monitoring data from the two groups. In a companion effort, Morgan et al. (2008) analyzed the merged data for the two-image lens QJ0158−4325, succeeding in measuring the size of the source accretion disk but failing to measure a time delay due to the high amplitude of the microlensing variability in this system.

WFI J2033−4723 ($20^h33^m42\overset{s}{.}08$, −47°23′43″.0; J2000.0) was discovered by Morgan et al. (2004) and consists of 4 images of a $z = 1.66$ quasar with a maximum separation of 2.5″. The lens galaxy was identified by Morgan et al. (2004) and has a spectroscopic redshift of $z_{\rm lens} = 0.661 \pm 0.001$ (Eigenbrod et al. 2006). The lens appears to be the member of a group, with at least 6 galaxies within 20″ of the lens (Morgan et al. 2004), and we will have to account for this environment in any lens model.

We describe the monitoring data and its analysis in Sect. 2. In Sect. 3 we present the near-IR *Hubble Space Telescope* (HST) observations that we used to obtain accurate differential astrometry of the lens components and surface photometry of the lens galaxy. We estimate the time delays in Sect. 4 and model them using parametric (Sect. 5) and non-parametric (Sect. 6) models for the mass distribution of the lens galaxy. We summarize our results in Sect. 7.

2. Photometric monitoring

Our 3-year photometric monitoring of WFI J2033−4723 was carried out from March 2004 to May 2007 with the 1.2 m EULER telescope and the 1.3 m SMARTS telescope located in Chile at La Silla and the Cerro Tololo Interamerican Observatory (CTIO), respectively. WFI J2033−4723 was monitored from both sites for three years during its visibility window from early March to mid-December.

The 1.2 m EULER telescope is equipped with a 2048 × 2048 CCD camera which has 0.344″ pixels and produces an image with an 11′ field of view. The mean sampling of the EULER data is one epoch every five days, where each epoch consists of five dithered 360 s images taken with an *R*-band filter. The worst gaps due to weather or technical problems are 2–3 weeks. The EULER data set consists of 141 epochs of data obtained between May 2004 and May 2007. The image quality varies between 0.9″ and 2.0″ *FWHM* over 3 years, with a median of 1.4″.

The 1.3 m SMARTS telescope is equipped with the dual-beam ANDICAM (DePoy et al. 2003) camera. Here we use only the optical channel which has 0.369″ pixels and a 6.5′ × 6.3′ field of view. The mean sampling of the SMARTS data is one epoch every eight days, with three 300 s exposures at each epoch. The SMARTS data set consists of 77 epochs of data obtained between March 2004 and December 2006. The seeing on the images varies between 0.5″ and 2.0″, with a median of 1.4″.

The combined data set consists of 218 observing epochs comprising 956 images covering the common field of view shown in Fig. 1. The average temporal sampling when

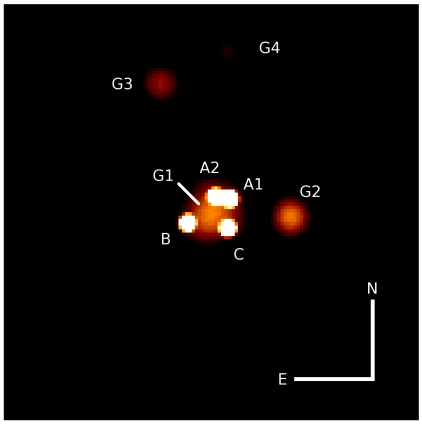

Fig. 2. Result of the simultaneous deconvolution of the 956 *R*-band images (EULER+SMARTS) of WFI J2033−4723. The pixel size of this image is half the pixel size of the EULER detector, i.e., 0.172″, and the resolution is 2 pixels Full-Width-Half-Maximum, i.e., 0.344″. The field of view is 22″ on a side. Two galaxies G2 and G3 are seen to the West and North of the main lensing galaxy G1. G3 is part of a group included in the lens modeling, while G1 and G2 are modeled individually (see Sect. 5).

WFI J2033−4723 was visible is one observation every 4 days over a period of three years, one of the best sets of monitoring data available for a lensed quasar.

The EULER data are reduced using the automated pipeline described in Vuissoz et al. (2007) and the SMARTS data with the SMARTS pipeline, using standard methods. The reduced frames are then aligned and interpolated to a common reference frame, one of the best-seeing (1″) EULER images, taken on the night of 5 April 2006. The 10 stars (PSF1−3 and S4−10) shown in Fig. 1 are used to determine the geometric transformation needed for each EULER and SMARTS image to match the reference frame. The transformation includes image parity, rotation, shifting and rescaling. These 10 stars are also used to determine the photometric zero point of each image relative to the reference image. After interpolation, cosmic rays are removed using the L.A.Cosmic algorithm (van Dokkum 2001). We check that no data pixels are mistakenly removed by this process.

The light curves of the quasars are measured by simultaneously deconvolving all the images using the MCS algorithm (Magain et al. 1998). This method has already been successfully applied to the monitoring data of several lensed quasars (e.g. Vuissoz et al. 2007; Hjorth et al. 2002; Burud et al. 2002a,b). The deconvolved images have a pixel scale of 0.172″ (one-half the pixel scale of the EULER data) and are constructed to have a Gaussian PSF with a 2 pixel (0.344″) *FWHM*. The Point Spread Function (PSF) for each of the 956 images is constructed from the three stars PSF1−3 (see Fig. 1). During the deconvolution process, the relative positions of the quasar images are held fixed to the values derived from fitting the HST images in Sect. 3, while their fluxes are allowed to vary from frame to frame. The flux, position and shape of the lensing galaxy are the same for all frames, but the values vary freely as part of the fit.

Figure 2 shows an example of a deconvolved image. It is clear that we will have no difficulty estimating the fluxes of components *B* and *C* separately. Components A_1 and A_2, however, are separated by only 0.724″, which is only twice the resolution of our deconvolved images, and remain partially blended after deconvolution. Since the delay between these images should be very small, we will sum the fluxes of the two images and consider only the light curve of the total flux $A = A_1 + A_2$. The resulting *R*-band light curves are displayed in Fig. 3.

We also display in Fig. 3 the deconvolved light curve of the isolated star *S*6, which has roughly the same color as WFI J2033−4723. Each point is the mean of the images taken at a given epoch and the error bar is the 1σ standard error of the mean. The light curve is flat, with a standard deviation over the 3 years of monitoring of $\sigma_{\rm tot} = 0.010$ mag about its average, which is roughly consistent with the mean error bar of $\sigma_{\rm mean} = 0.006$ mag of the individual epochs.

The dispersion of the points in the star's light curve reflects both statistical errors and systematic errors from the photometric calibrations and the construction of the PSF. To the extent that all the light curves suffer from the same systematic errors, we can correct the quasar's light curves by subtracting the residuals of the star's light curve from each of them. We then define the uncertainty in a quasar's light curve as the quadrature sum of the uncertainties in the two light curves. This procedure will increase the photon noise but should minimize the systematic errors.

3. HST near-IR imaging

We determine the relative positions of the lens components and the light profile for the main lens galaxy G1 and its closest neighbor G2 (see Fig. 2) by analyzing our HST images of the system. These data were obtained in the framework of the CASTLES program (Cfa-Arizona Space Telescope LEns Survey), which provides HST images for all known gravitationally lensed quasars. We deconvolve these images using a modified version of the MCS deconvolution algorithm for images with poor knowledge of the PSF (Magain et al. 2007). We previously used this approach to unveil the faint Einstein ring and the lensing galaxy hidden in the glare of the quasar images of the so-called "cloverleaf" HE1413+117 (Chantry & Magain 2007). We analyze the Near Infrared Camera and Multi-Object Spectrometer (NICMOS) *F160W* (*H*-band) images obtained with the NIC2 camera. The data consist of four dithered MULTIACCUM images with a total exposure time of 2752 s and a mean pixel scale of 0.07568″ (Krist & Hook 2004). We calibrate the images using CALNICA, the HST image reduction pipeline, subtract constants for each quadrant of NIC2 to give each image a mean background of zero, and create a noise map for each frame.

The images are simultaneously deconvolved in a manner similar to that used for the EULER and SMARTS data. The NICMOS frames lack any PSF stars, so we construct the PSF using the quasar images themselves in the iterative method of Chantry & Magain (2007). We first estimate the PSF of each frame using Tiny Tim (Krist & Hook 2004) and then we deconvolve them to have the final Gaussian PSF. During the deconvolution, each image is decomposed into a set of point sources and any extended flux. The latter is then reconvolved to the resolution of the original data and subtracted from the four initial frames, leading to images with far less contamination by extended structures. Four new PSFs are estimated from these new images, and we carry out a new deconvolution. The process is repeated until the residual maps are close to being consistent with the estimated noise (e.g. Courbin et al. 1998). In this case,

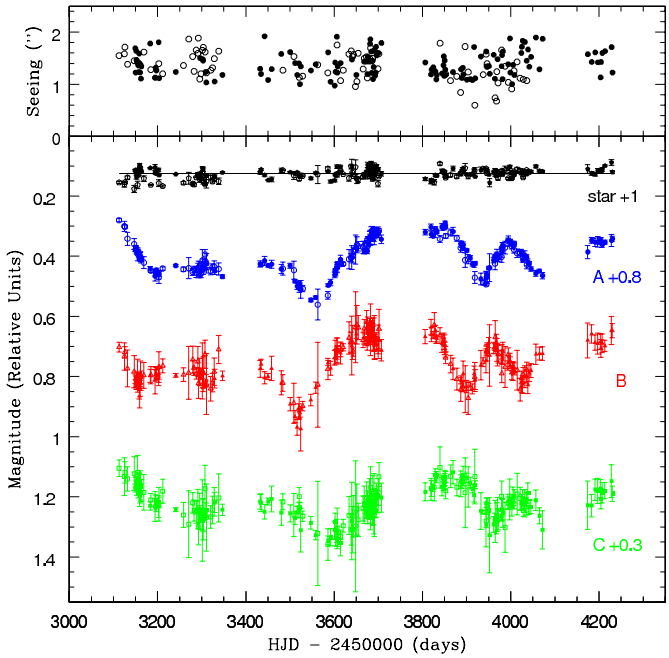

Fig. 3. Our *R*-band light curves obtained for WFI J2033−4723 as well as for the reference star S6 (see Fig. 1). The magnitudes are given in relative units. The filled symbols correspond to the EULER observations while the SMARTS data points are marked by open symbols. Components A_1 and A_2 were summed into one single component *A*. The curves have been shifted in magnitude for visibility, as indicated in the figure.

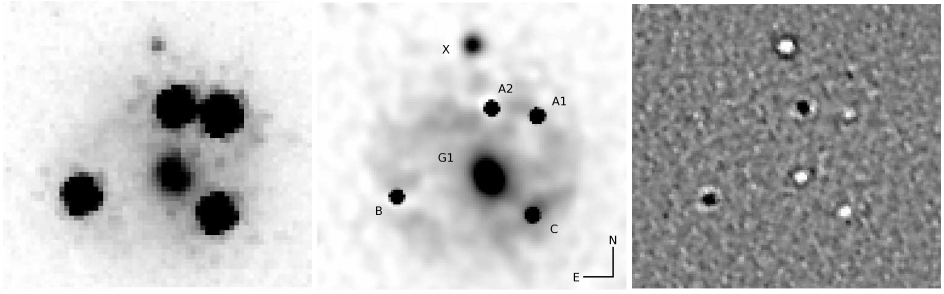

Fig. 4. *Left*: deep NICMOS2 image, taken in the *F*160*W*-band. This image is a combination of 4 frames, for a total exposure time of 46 min. North is up and East to the left. The field of view is 4″ on a side. *Middle*: simultaneous deconvolution of the individual NICMOS images (see text), using the MCS deconvolution algorithm. The PSF in this image is an analytical Gaussian with 2 pixels Full-Width-at-Half-Maximum (*FWHM*), i.e., the resolution is 0.075″. The pixel size is 0.035″, i.e., oversampled by a factor of two compared to the original pixel size. *Right*: residual map of the deconvolution, with the cut levels set to ±5σ. Only minor structures are seen in the center of the sharpest objects, which is acceptable given the quality of the NICMOS PSF.

convergence is reached after three iterations and the final reduced χ^2 is 3.59. The final deconvolved image shown in Fig. 4 has half the pixel scale of the initial images and a Gaussian PSF with a *FWHM* of 0.075″.

As part of the MCS deconvolution we also fit analytical models to the main lens galaxy (G1) and its nearby companion G2. The main lens is an early-type galaxy (Eigenbrod et al. 2006), as its companion is likely to be, so we use elliptical de Vaucouleurs profiles for both. The uncertainties are estimated by the scatter of the measurements from a separate set of fits to each independent image. We also estimate that there are systematic errors in the astrometry from the NICMOS pixel scale and focal plane distortions of order 2 milli-arcsec based on our earlier fits to the NICMOS data of H1413+117 (Chantry & Magain 2007). These

Table 1. Relative astrometry and photometry for the four components of WFI J2033−4723 and for the lensing galaxies G1 and G2.

ID	$\Delta\alpha$ (″)	$\Delta\delta$ (″)	Magnitude
B	0.	0.	17.77 ± 0.02
*A*1	−2.1946 ± 0.0004	1.2601 ± 0.0003	17.16 ± 0.02
*A*2	−1.4809 ± 0.0004	1.3756 ± 0.0005	17.52 ± 0.02
C	−2.1128 ± 0.0003	−0.2778 ± 0.0003	17.88 ± 0.02
G1	−1.4388 ± 0.0019	0.3113 ± 0.0008	18.59 ± 0.03
G2	−5.4100 ± 0.0006	0.2850 ± 0.0003	18.14 ± 0.02

Table 2. Shape parameters for the main and secondary lensing galaxies.

Obj.	PA (°)	Ellipticity	a_0 (″)	b_0 (″)
G1	27.8 ± 4.3	0.18 ± 0.03	0.665 ± 0.036	0.556 ± 0.025
G2	6.4 ± 3.1	0.15 ± 0.02	0.389 ± 0.004	0.334 ± 0.005

systematic errors are compatible with the Lehár et al. (2000) comparison of NICMOS and VLBI astrometry for radio lenses.

The relative astrometry and photometry of the lens components and of the lensing galaxies G1 and G2 are given in Table 1. Coordinates are relative to image *B*, in the same orientation as Fig. 4. The photometry is in the Vega system. For each measurement, we give the 1σ internal error bars, to which a systematic error of 2 milli-arcsec should be added. The models for G1 and G2 are presented in Table 2, with the effective semi-major and semi-minor axes of the light distribution a_0 and b_0. Each measurement is accompanied by its 1σ error bar.

4. Time delay measurement

We measure the time delays between the blended light curve of A_1/A_2 and images *B* and *C* using three different techniques: *i* the minimum dispersion method of Pelt et al. (1996); *ii* the polynomial method of Kochanek et al. (2006); and *iii* the method of Burud et al. (2001). Since WFI J2033−4723 shows well-defined variations (see Fig. 3), it is already clear by visual inspection that $\Delta t_{B-A} \sim 35$ days and $\Delta t_{B-C} \sim 65$ days.

4.1. Minimum dispersion method

In the minimum dispersion method, time delays are computed for pairs of light curves using a cross-correlation technique that takes into account irregular sampling. The two light curves are first normalized to have zero mean. Then, one of the light curves is used as a reference and the second curve is shifted relative to it by a range of time delays. For each delay, we calculate the mean dispersion between the shifted points and their nearest temporal neighbors in the reference light curve. The best time-delay estimate is the one that minimizes this dispersion function. Since the mean sampling of our curves is one epoch every four days and since there is a limit to the number of time delays that can be tested independently, we test time delays in steps of 2 days. Figure 5 shows an example of a dispersion curve where we have then fit a parabola and set the best time delay to be the one corresponding to the minimum of the parabola.

There is, however, a complication in the step of normalizing the light curves, arising from sampling the light curve of each lensed image over a different time period of the intrinsic source variability (Vuissoz et al. 2007). We solve this problem by computing the dispersions as a function of a small magnitude shift Δm in the normalization, measuring both the minimum dispersion $D_{\min}(\Delta m)$ and the best fitting time delay $\Delta t(\Delta m)$ as shown in Fig. 6. Our final value for the delay is the one corresponding to the shift Δm that minimizes the overall dispersion.

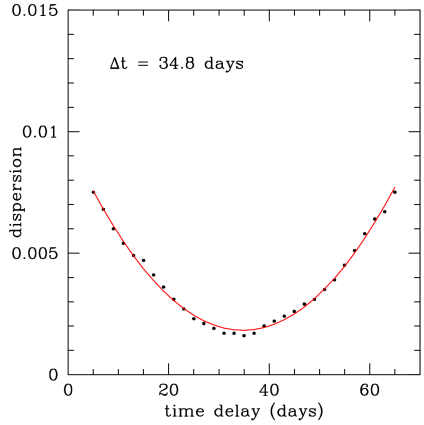

Fig. 5. Example of a dispersion curve as obtained from the minimum dispersion method, for components *B* and *A*. The position of the parabola minimum gives the time delay. Each point is separated by 2 days, i.e. about half the data mean sampling. The time delay indicated here is for only one realization of the boot-strap procedure (see text).

We then estimate the uncertainties by randomly perturbing the data points, based on a Gaussian distribution with the width of the measurement errors, and computing the dispersions and time delays again. We define the uncertainties by the 1σ dispersion in the results for 100 000 trials (Vuissoz et al. 2007). The resulting uncertainty estimates are symmetric about the mean, so our final estimates based on this method are

$$\Delta t_{B-A} = 35.6 \pm 1.3 \text{ days } (3.6\%)$$
$$\Delta t_{B-C} = 64.6 \pm 3.4 \text{ days } (5.3\%). \quad (1)$$

While we have not taken microlensing effects into account for this analysis, it should matter little, as the method is not very sensitive (Eigenbrod et al. 2005) to the very low amplitude microlensing variability observed for this system (see Sect. 4.2).

4.2. Polynomial fit of the light curves

In the polynomial method (Kochanek et al. 2006), the intrinsic light curve of the source is modeled as a polynomial that is simultaneously fit to all three light curves. Each quasar image has an additional low order polynomial to model slow, uncorrelated variability due to microlensing. We increase the source polynomial order for each season until the improvement in the χ^2 statistics of the fits cease to be significant. This results in using polynomial orders of 11, 10, 17 and 4 for the four seasons of data. The low amplitude microlensing variations are modeled with a simple linear function for the four seasons. Figure 7 shows the best fits to the data and the residuals from the model. The effects of microlensing in this system are very small, with variations of only ∼0.01 mag over three years. As with the minimum dispersion method, we estimate the uncertainties by randomly

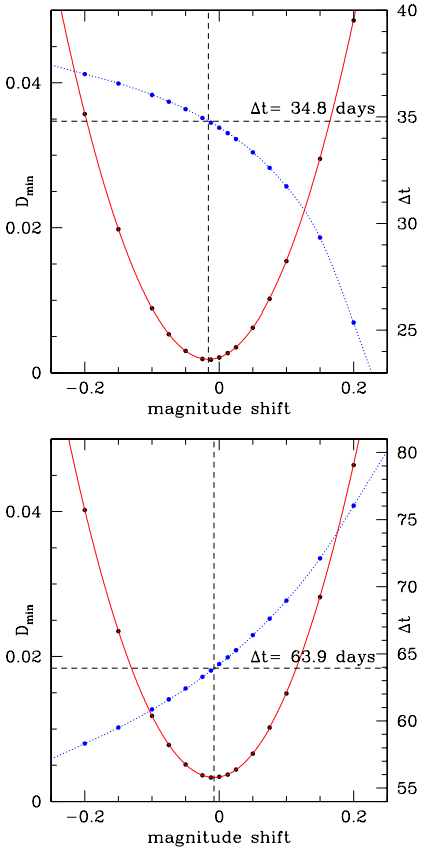

Fig. 6. Variation of the dispersion function minimum $D_{\rm min}$ (red solid curves), as a function of the magnitude shift used for the normalization (see Sect. 4.1). Each $D_{\rm min}$ corresponds to a different estimate of the time delay, indicated on the blue dotted curves. The final time delay is the one with the lowest $D_{\rm min}$. *The top panel* is for the *B*-*A* time delay, *the bottom* one for *B*-*C*. Time delays indicated here are for only one realization of the boot-strap procedure (see text).

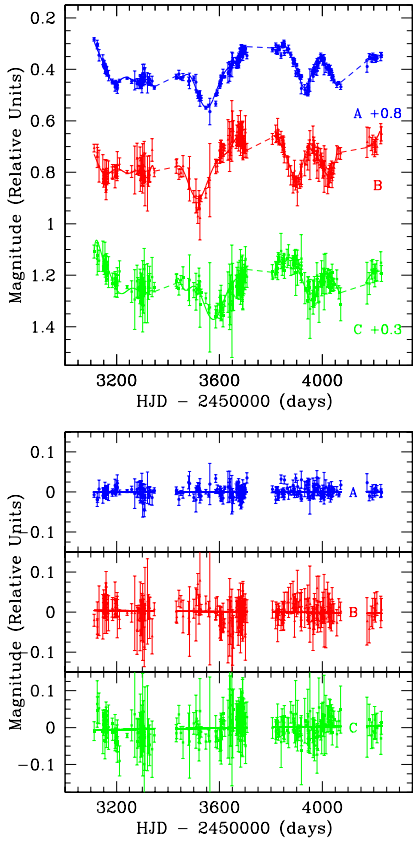

Fig. 7. *Top*: best polynomial fit to the light curves, which are shifted vertically for display purpose. *Bottom*: the residuals of the fit.

perturbing the light curves 100 000 times and using the standard deviation of the trials as the error estimates to find that

$$\Delta t_{B-A} = 35.0 \pm 1.1 \text{ days } (3.0\%)$$
$$\Delta t_{B-C} = 61.2 \pm 1.5 \text{ days } (2.4\%). \quad (2)$$

4.3. Numerical modeling of the light curves

Our last approach is based on the method described in Burud et al. (2001), which determines the time delay between a pair of light curves using a gridded numerical model for the source light curve. For a series of time delays, we fit the data with a flux ratio between the two curves, and a linear trend for microlensing on each full light curve. The numerical source model is smoothed on the scale of the temporal sampling, based on a smoothing function weighted by a Lagrange multiplier. The best time delay is the one that minimizes the χ^2 between the model and data points.

This method has several advantages: first, none of the data light curves is taken as a reference: they are all treated on an equal basis. Furthermore, as the model is purely numerical, no assumption is made on the shape of the quasar's intrinsic light curve (except that it is sufficiently smooth). Finally, a model light curve is obtained for the intrinsic variations of the quasar, as for the polynomial fit method (see Sect. 4.2).

We have applied this method to the two pairs of light curves of WFI J2033−4723. The resulting fits to the light curves and their residuals are shown in Fig. 8. Using a Monte Carlo method to estimate the uncertainties, we find from 7000 trials (adding normally distributed random errors with the appropriate standard deviation on each data point):

$$\Delta t_{B-A} = 36.0 \pm 1.5 \text{ days } (4.2\%)$$
$$\Delta t_{B-C} = 61.9 \,^{+6.7}_{-0.5} \text{ days } (^{+11\%}_{-1\%}). \quad (3)$$

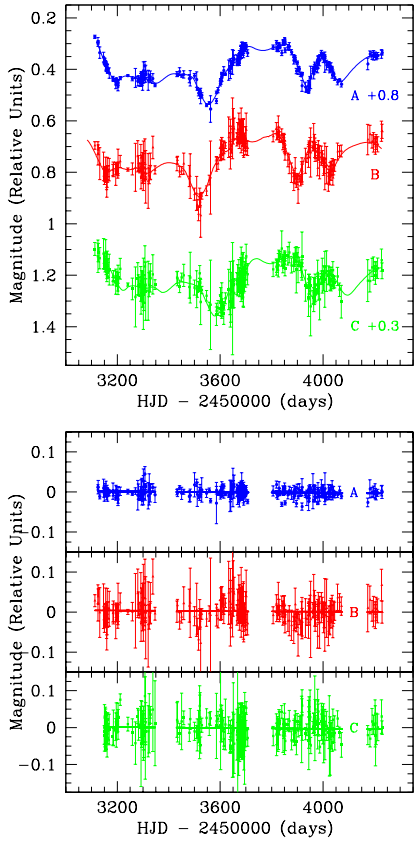

Fig. 8. *Top*: the light curves of the quasar images shown along with the best numerical model. *Bottom*: the residuals of the fit.

We note a secondary peak in the Δt_{B-C} Monte Carlo distribution, around 69 days, in addition to the main peak at 61.9 days. There is, however, no evidence of such a secondary peak in the results of the minimum dispersion method and the polynomial fitting technique. This translates into an asymmetrical error bar on the result obtained with the numerical fitting of the light curves, and is taken into account in our final estimate of the time delay between quasar images B and C.

4.4. Final time delays

For the final delay estimate we adopt the unweighted mean of the three methods, and we take as uncertainties the quadrature sum of the average statistical error and the dispersion of the results from the individual methods about their mean. Our final estimate of the time delays is

$$\Delta t_{B-A} = 35.5 \pm 1.4 \text{ days } (3.8\%)$$
$$\Delta t_{B-C} = 62.6\,^{+4.1}_{-2.3} \text{ days } (^{+6.5\%}_{-3.7\%}). \quad (4)$$

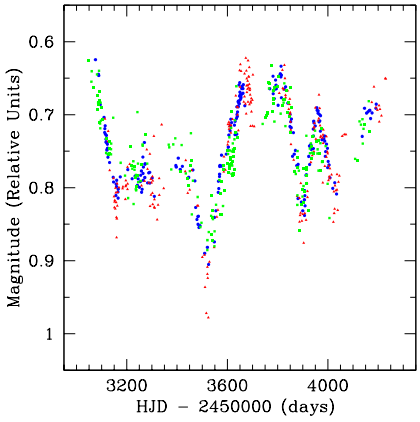

Fig. 9. Light curves of the three quasar images, shifted by their respective time delay and flux ratio. The blue circles correspond to image A, the red triangles to B and the green squares to C.

We cannot measure the time delay between the individual A_1 and A_2 light curves, but values larger than $\Delta t_{A1-A2} = 2$ days are incompatible with any of the models we consider in the following section. We can nevertheless estimate the flux ratio between A_1 and A_2. After correcting for the time delays, we find that the R-band flux ratios between the images are

$$\frac{F_A}{F_B} = 2.88 \pm 0.04, \quad \frac{F_A}{F_C} = 3.38 \pm 0.06, \quad \frac{F_{A1}}{F_{A2}} = 1.37 \pm 0.05. \quad (5)$$

Figure 9 displays the light curves obtained for the three quasar images, after shifting by the time delays and flux ratios. Note that these flux ratios differ from those measured by Morgan et al. (2004) from the MgII broad emission lines, probably due to long-term microlensing (on a longer scale than our monitoring 3-year baseline), as discussed in the next section.

5. Parametric modeling

5.1. Observational constraints

We constrain the mass models of WFI J2033−4723 using the positions of the four lensed images, the position of the lens galaxy G1 and the two delay measurements, for a total of 12 constrains. Except when indicated, we do not use the image flux ratios because they can be affected by extinction (Falco et al. 1999; Jean & Surdej 1998) and milli-lensing by substructures (Mao & Schneider 1998). We can also constrain the structure of G1 given its ellipticity e, position angle θ_e and effective radius R_e to the extent that these properties are correlated with those of its dark matter halo. Although a possible mismatch between the light and mass distributions is not impossible, we adopt the formal errors of 0.002″ on the position of the lens G1 (Table 2). This is motivated by the small offset between the centers of mass and light found by Yoo et al. (2006) in a sample of four lensing galaxies.

Finally, WFI J2033−4723 is located in a group of galaxies, labeled G2–G6 in Fig. 10. We include G2 as a singular isothermal sphere (SIS) in all our models since it is close (4″) and of similar luminosity to G1. As Morgan et al. (2004), we are unable to successfully model the system without including G2.

Table 3. Result of the parametric lens modeling.

Name	Comp.	Mass	e, θ_e	γ, θ_γ	#d.o.f.	χ^2	h	Comments
SIE+γ		$b = 0.96$	0.21, (20.8)	0.187, 7.4	1	15.3	–	Time delays not used
SIE+γ		$b = 0.94$	0.13, (30.5)	0.063, 24.6	2	3.6	$0.79^{+0.04}_{-0.02}$	$G_{\rm group}$ included
SIE+γ		$b = 0.97$	0.16, 84.4	0.059, 46.9	1	0.30	$0.63^{+0.07}_{-0.03}$	$G_{\rm group}$ included
dVC+γ		$b = 2.71$	0.20, (20.1)	0.305, 9.7	1	34.4	–	Time delays not used
dVC+γ		$b = 2.83$	0.18, 83.1	0.116, 64.5	1	0.01	$0.92^{+0.06}_{-0.03}$	$G_{\rm group}$ included
NFW+γ		$\kappa_s = 0.20$	0.16, (27.4)	0.070, –3.6	1	0.38	–	$r_s = 10''$ (fixed); time delays not used
NFW+γ		$\kappa_s = 0.21$	0.15, 85.7	0.079, 9.5	1	0.06	$0.29^{+0.03}_{-0.03}$	$r_s = 10''$ (fixed); $G_{\rm group}$ included
NFW+γ		$\kappa_s = 0.09$	0.15, 85.4	0.076, 30.6	1	0.01	$0.63^{+0.10}_{-0.08}$	$r_s = 1''$ (fixed); $G_{\rm group}$ included
dVC+NFW+γ	Light	$b = 1.56$	(0.17), (29.3)	0.057, 37.0	–	–	–	$R_e = 0.608''$(fixed)
	Halo	$\kappa_s = 0.082$	0.065, (29.3)		1	6.33	$0.78^{+0.12}_{-0.10}$	$r_s = 10''$ (fixed); $G_{\rm group}$ included
dVC+NFW+γ	Light	$b = 1.53$	(0.16), (26.4)	0.075, 27.5	–	–	–	same model as above, with
	Halo	$\kappa_s = 0.10$	0.43, 89.8		3	3.2	$0.69^{+0.20}_{-0.10}$	flux ratios included

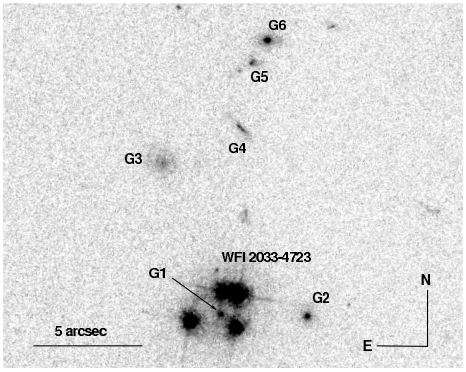

Fig. 10. Environment of WFI J2033−4723 as seen in an HST/ACS F814 (I-band) image. The main lens galaxy G1 and the close companion G2 were included in our analysis of the NICMOS image, and here we have labeled additional group members as G3−G6.

When enough observational constraints are available we further add galaxies G3−G6 as a SIS mass distribution located at the barycenter $G_{\rm group}$ of the group. In all models we include an external shear of amplitude γ and position angle θ_γ that represents the gravitational perturbations due to mass unaccounted for explicitly. We also experiment with including mass at the position of object X (Fig. 4, 2″ North of G1) and find that doing so does not improve the models.

We consider a sequence of standard mass models for G1, including a singular isothermal ellipsoid (SIE), a de Vaucouleurs (dVC) model and a NFW model (Navarro et al. 1997), and we fit the data using `LENSMODEL` (v1.99g) (Keeton 2001). The results are summarized in Table 3, where Cols. #1 and #2 describe the model family, and #3 the mass parameter (either the Einstein radius b in arcseconds or the mean mass surface density κ_s, as defined in Keeton 2001). Column #4 is for the ellipticity e and PA θ_e of the lens G1. Note that the measured PA of G1 is $\theta = 27.8°$ (Table 2). Column #5 gives the external shear amplitude γ and PA θ_γ, #6 the number of degrees of freedom for each model, and #7 the resulting reduced χ^2. Column #8 finally shows the best estimate for $h = H_0/100$. A minus sign in this column means that time delays are not used as constraints. All angles are given positive East of North, and values given in parentheses are fitted to the observations. All models assume $\Delta t_{A1-A2} = 2$ days and include the companion galaxy G2, with a resulting mass $0.1\, m_{\rm G1} < m_{\rm G2} < m_{\rm G1}$.

5.2. SIE models

Our first model consists of an SIE for G1, an SIS for G2 and an external shear. When we fit only the image positions but include a prior on the position angle θ_e (from Table 1) we do not find a good fit unless the constraint on the position of the lensing galaxy is relaxed. The prior on the position angle is justified by statistical studies finding correlations between the position angles but not the axis ratios of the visible and total mass distributions (Ferreras et al. 2008; Keeton et al. 1997). With the inclusion of the time delays we have enough constraints to add the group halo to the model. With the position angle of G1 constrained, we obtain poor fits to the data with reduced $\chi^2 = 3.6$ for $N_{\rm d.o.f.} = 2$. When we leave the position angle free, we find good fits but the model PA is 55° from the observed. These models have Hubble parameters of $h \simeq 0.63^{+0.07}_{-0.03}$ with the spread dominated by the degeneracies between the ellipticity and the shear.

5.3. De Vaucouleurs models

Next we consider a constant mass-to-light ratio model of the lens galaxy based on a De Vaucouleurs model. The position angle and the effective radius $R_e = 0.608''$ (the geometric mean of the semi-axes in Table 1, corresponding to 4 kpc for $h = 0.72$) are constrained by the values measured for the galaxy. This model does not fit well the lens configuration ($\chi^2 \sim 34.4$), mainly due to the small uncertainty on the lens galaxy position. When we include the time delays we find a good fit ($\chi^2 \simeq 0.01$) as long as we allow G1 to be misaligned with respect to the observed galaxy. As expected from the reduced surface density compared to the SIE model (Kochanek 2002), we find a much higher value for the Hubble parameter, $h = 0.92$.

5.4. NFW models

We use an NFW model with a fixed break radius of $r_s = 10''$ (40 kpc), where the break radius is related to the virial radius through the concentration $c = R_{\rm vir}/r_s$. Since r_s lies well outside the Einstein radius of the lens, its particular value is not important. This model is not realistic by itself because the shallow $\rho \propto 1/r$ central density cusp of the model will lead to a visible central image. We again find that we can fit the astrometry well

even when the position angle of the lens is constrained, but we cannot do so after including the time delays unless we allow the model of G1 to be misaligned relative to the light. In any case, this model leads to a fifth image about 3 mag fainter than *A* that should be visible on our NICMOS data. This NFW model has a higher surface density near the Einstein ring than the SIE model, so we find a lower value for the Hubble parameter of $h \simeq 0.29$. Using an unphysically small break radius of $r_s = 1''$ raises the density and hence the Hubble parameter to $h \simeq 0.63$.

5.5. De Vaucouleurs plus NFW models

As our final, and most realistic, parametrized model we combine a dVC model constrained by the visible galaxy with an NFW model for the halo. The two components are first constrained to have the same position and position angle, the parameters of the dVC model are constrained by the observations, and the NFW model has a fixed $r_s = 10''$ break radius. This model leads to a poor fit, with $\chi^2 = 6.33$ for $N_{\rm d.o.f.} = 1$. When we free the PA of the NFW model, we find an acceptable fit for $N_{\rm d.o.f.} = 0$, but the misalignment of the NFW model relative to the optical is 40°.

We can further constrain the model by including the three MgII emission line flux ratios from Morgan et al. (2004). We use the line flux ratios instead of those obtained from the light curves, because they should be insensitive to microlensing. With these three additional constraints we still find that the 89.8° position angle of the NFW model is strongly misaligned from the 26.4° position angle of the dVC model, indicating a twisting of the mass isocontours. The model has a reduced χ^2 of 3.2 for $N_{\rm d.o.f.} = 3$. The model flux ratios are significantly different from the constraints. We find $F_A/F_B = 2.81$, $F_A/F_C = 5.01$, and $F_{A1}F_{A2} = 1.26$ while Morgan et al. (2004) report $F_A/F_B = 2.55 \pm 0.60$, $F_A/F_C = 2.02 \pm 0.35$, and $F_{A1}/F_{A2} = 1.61 \pm 0.35$. The match of the flux ratios is better if we do not include the constraints from the time delays. In all cases, F_B/F_C is the most "anomalous" flux ratio, as also found by Morgan et al. (2004). While the differences between the line and continuum flux ratios suggests the presence of long-term microlensing, we see no evidence for the time variability in the flux ratios expected from microlensing. We also note that the broad line flux ratios vary with wavelength (Morgan et al. 2004), which suggests that dust extinction may as well be affecting the flux ratios.

6. Non-parametric modeling

We use the non-parametric `PixeLens` (Saha & Williams 2004) method as our second probe of the mass distribution. This approach has the advantage that it makes fewer assumptions about the shape of the G1 than the ellipsoidal parametric models. The models include priors on the steepness of the radial mass profile, imposes smoothness criteria on the profile and we restrict to models symmetric about the lens center. We include two point masses to represent G2 and the group. We run 1000 trial models at a resolution of ∼0.23″/pixel which are constrained to fit the image positions and the time delays exactly. For each model we vary the Einstein radii of G2 and the group over the ranges $0.03'' < R_{\rm E}({\rm G2}) < 3''$ and $0.3'' < R_{\rm E}({\rm group}) < 5''$, respectively. Apart from the inclusion of these additional point masses, the method and priors are as explained in detail in Coles (2008). A test, where the technique is used to infer H_0 from a *N*-body and hydro simulated lens, and an additional discussion of the priors are described in Read et al. (2007). Figure 11 shows the resulting probability distribution for H_0 from the 1000 models. The median value of the distribution is

$$H_0 = 67.1\,^{+13.0}_{-9.9}\ {\rm km\,s^{-1}\ Mpc^{-1}} \qquad (6)$$

where the error bars are at 68% confidence. As already illustrated by our parametric modeling, the predicted H_0 value depends on the density gradient of the models. Figure 12 shows the mean surface density contours of the models, and we see a twisting of the contours away from that of the visible galaxy in the outer regions.

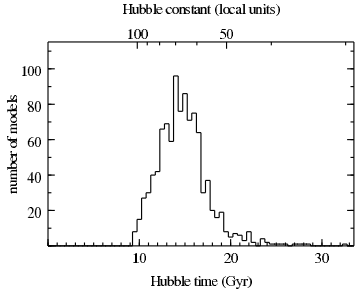

Fig. 11. Distribution of H_0 from 1000 non-parametric models. The bottom-axis gives the Hubble time, the top-axis H_0 in km s^{-1} Mpc^{-1}.

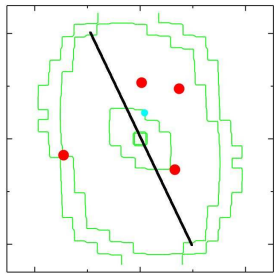

Fig. 12. Mean mass distribution from 1000 pixellated lens models. The red dots are the quasar images and the blue dot the source position. The thick solid line indicates the observed major axis of the lensing galaxy. Each tick-mark measures 1″. The third contour from the outside traces the critical mass density $\Sigma_{\rm crit} = 1.19 \times 10^{11}\ M_\odot$ arcsec^{-2}, and the others are drawn logarithmically from the critical one (each contour is 2.5 larger/smaller than the previous one). North is to the top and East to the left.

7. Conclusions

By combining data from COSMOGRAIL and the SMARTS 1.3 m telescope we measure two independent time delays in the quadruply imaged quasar WFI J2033−4723 (Morgan et al. 2004). The fractional uncertainties of ∼4% are among the best obtained so far from an optical monitoring. We obtain the light curves of the quasar images using the MCS deconvolution photometry algorithm (Magain et al. 1998) and then measure time delays using three different approaches with a final estimate of

$$\Delta t_{B-A} = 35.5 \pm 1.4 \ \text{days} \ (3.8\%)$$
$$\Delta t_{B-C} = 62.6\,^{+4.1}_{-2.3} \ \text{days} \ (^{+6.5\%}_{-3.7\%}) \qquad (7)$$

where A is the mean light curve of the blended of quasar images A_1 and A_2. We find little evidence of microlensing in this system, which makes WFI J2033−4723 a very good system for measuring clean time delays.

The parametric models are consistent with concordance value of H_0 when the lens galaxy has an isothermal mass profile out to the radius of the Einstein ring. As expected, the models allow higher (lower) values as the mass distribution is more centrally concentrated (extended) using de Vaucouleurs (NFW) mass distribution. The non-parametric models predict $H_0 = 67.1\,^{+13.0}_{-9.9}$ km s^{-1} Mpc^{-1}.

The addition of the time delays as a constraint on the lens models does not alter the mismatch between the observed and predicted image flux ratios. The largest flux ratio anomaly is the 45% difference between the MgII flux ratios found for images B/C. Morgan et al. (2004) also noted that the F_B/F_C flux ratio varies with wavelength, suggesting the presence of chromatic microlensing. The lack of significant variability in the flux ratio over our three year monitoring period suggests either that the effective source velocities in this lens are very low or that the affected images lie in one of the broad demagnified valleys typical of microlensing magnification patterns for low stellar surface densities.

Several galaxies close to the line of sight have a significant impact on the mass modeling. We generally model the potential as the sum of a main lensing galaxy G1, a companion galaxy G2 (∼4″ West of G1), and a nearby group (∼9″ North of G1). Both the parametric and non-parametric models suggest that the isodensity contours of G1 itself must be twisted, with some evidence that the outer regions are aligned with the tidal field of the group rather than the luminous galaxy. This could indicate that G1 is a satellite rather than the central galaxy of the group (e.g. Kuhlen et al. 2007). The twisting seems to be required even though the angular structure of the potential can be adjusted through the companion galaxy G2, an external tidal shear, and in some cases a group halo. Clarifying this issue requires more constraints such as detailed imaging of the Einstein ring image of the quasar host, measuring the redshifts of the nearby galaxies, and measuring the velocity dispersion of G1.

Acknowledgements. We would like to thank all the observers at the EULER telescope for the acquisition of these monitoring data. We also thank Profs. G. Burki and M. Mayor for their help in the flexible scheduling of the observing runs, improving the necessary regular temporal sampling. We are very grateful to Prof. A. Blecha and the technical team of the Geneva Observatory for their efficient help with the electronics of the CCD camera. Many thanks also to Sandrine Sohy for her commitment in the programming part of the deconvolution techniques. Finally, we would like to thank Chuck Keeton for his advice on the use of LENSMODEL. This work is supported by ESA and the Belgian Federal Science Policy Office under contract PRODEX 90195. C.S.K. is funded by National Science Foundation grant AST-0708082. COSMOGRAIL is financially supported by the Swiss National Science Foundation (SNSF).

References

Burud, I., Magain, P., Sohy, S., & Hjorth, J. 2001, A&A, 380, 805
Burud, I., Courbin, F., Magain, P., et al. 2002a, A&A, 383, 71
Burud, I., Hjorth, J., Courbin, F., et al. 2002b, A&A, 391, 481
Chantry, V., & Magain, P. 2007, A&A, 470, 467
Coles, J. 2008, ApJ, 679, 17
Courbin, F., Lidman, C., Frye, B. L., et al. 1998, ApJ, 499, L119
DePoy, D. L., Atwood, B., Belville, S. R., et al. 2003, in Presented at the Society of Photo-Optical Instrumentation Engineers (SPIE) Conference, Instrument Design and Performance for Optical/Infrared Ground-based Telescopes, ed. M. Iye, & A. F. M. Moorwood, Proc. SPIE, 4841, 827
Eigenbrod, A., Courbin, F., Vuissoz, C., et al. 2005, A&A, 436, 25
Eigenbrod, A., Courbin, F., Meylan, G., Vuissoz, C., & Magain, P. 2006, A&A, 451, 759
Falco, E. E., Impey, C. D., Kochanek, C. S., et al. 1999, ApJ, 523, 617
Ferreras, I., Saha, P., & Burles, S. 2008, MNRAS, 383, 857
Hjorth, J., Burud, I., Jaunsen, A. O., et al. 2002, ApJ, 572, L11
Jean, C., & Surdej, J. 1998, A&A, 339, 729
Keeton, C. R. 2001, ArXiv Astrophysics e-prints
Keeton, C. R., Kochanek, C. S., & Seljak, U. 1997, ApJ, 482, 604
Kochanek, C. S. 2002, ApJ, 578, 25
Kochanek, C. S., Morgan, N. D., Falco, E. E., et al. 2006, ApJ, 640, 47
Krist, J., & Hook, R. 2004, The Tiny Tim's user Guide v.6.3
Kuhlen, M., Diemand, J., & Madau, P. 2007, ApJ, 671, 1135
Lehár, J., Falco, E. E., Kochanek, C. S., et al. 2000, ApJ, 536, 584
Magain, P., Courbin, F., & Sohy, S. 1998, ApJ, 494, 472
Magain, P., Courbin, F., Gillon, M., et al. 2007, A&A, 461, 373
Mao, S., & Schneider, P. 1998, MNRAS, 295, 587
Morgan, C. W., Eyler, M. E., Kochanek, C. S., et al. 2008, ApJ, 676, 80
Morgan, N. D., Caldwell, J. A. R., Schechter, P. L., et al. 2004, AJ, 127, 2617
Navarro, J. F., Frenk, C. S., & White, S. D. M. 1997, ApJ, 490, 493
Oguri, M. 2007, ApJ, 660, 1
Pelt, J., Kayser, R., Refsdal, S., & Schramm, T. 1996, A&A, 305, 97
Poindexter, S., Morgan, N., Kochanek, C. S., & Falco, E. E. 2007, ApJ, 660, 146
Read, J. I., Saha, P., & Macciò, A. V. 2007, ApJ, 667, 645
Refsdal, S. 1964, MNRAS, 128, 307
Saha, P., & Williams, L. L. R. 2004, AJ, 127, 2604
Saha, P., Coles, J., Macciò, A. V., & Williams, L. L. R. 2006a, ApJ, 650, L17
Saha, P., Courbin, F., Sluse, D., Dye, S., & Meylan, G. 2006b, A&A, 450, 461
van Dokkum, P. G. 2001, PASP, 113, 1420
Vuissoz, C., Courbin, F., Sluse, D., et al. 2007, A&A, 464, 845
Yoo, J., Kochanek, C. S., Falco, E. E., & McLeod, B. A. 2006, ApJ, 642, 22

Not only is the Universe stranger than we imagine, it is stranger than we can imagine.

Arthur Eddington (1882 - 1944)

12

Application of ISMCS to a sample of seven lensed quasars and simple models

Contents

V. Chantry , D. Sluse, P. Magain

Submitted to *Astronomy & Astrophysics* under the following title:

COSMOGRAIL: the COSmological MOnitoring of GRAvItational Lenses[1] *VIII. Deconvolution of high resolution near-IR images and simple mass models for seven gravitationally lensed quasars*

Aims: **For a sample of seven gravitationally lensed quasars, we aim at obtaining very accurate positional constraints for gravitationally lensed quasars and shape parameters for the light distribution of the lensing galaxy. We**

[1]Based on observations made with the NASA/ESA HST Hubble Space Telescope, obtained from the data archive at the Space Science Institute, which is operated by AURA, the Association of Universities for Research in Astronomy, Inc., under NASA contract NAS-5-26555.

also want to find simple mass models that reproduce the observed configuration and predict time delays. Finally we want to test, for the quads, whether there are clues of astrometric perturbations coming from substructures in the lensing galaxy, preventing from finding a good fit of the simple models.

Methods: **We apply the iterative MCS deconvolution method to near-IR HST archives data of seven gravitationally lensed quasars. This deconvolution method allows to separate the contribution from the point sources to the one from extended structures such as Einstein rings. That method leads to an accuracy of 1-2 mas on the relative positions of the sources and lens. The limiting factor of the method is the uncertainty on the instrumental geometric distortions. We then compute mass models of the lensing galaxy using state-of-the-art modeling techniques.**

Results: **We obtain relative positions for the lensed images and lens shape parameters for seven lensed quasars: HE 0047-1756, RX J1131-1231, SDSS J1138+0314, SDSS J1155+6346, SDSS J1226-0006, WFI J2026-4536 and HS 2209+1914. The lensed image positions are derived with 1-2 mas accuracy. Isothermal and de Vaucouleurs mass models are calculated for the whole sample. The effect of the lens environment on the lens mass models is taken into account with a shear term. Doubly imaged quasars are equally well fitted by each of these models. A large amount of shear is necessary to reproduce SDSS J1155+6346 and SDSS J1226-006. In the latter case, we identify a nearby galaxy as the dominant source of shear. The quadruply imaged quasar SDSS J1138+0314 is well reproduced by simple lens models, which is not the case for the two other quads, RX J1131-1231 and WFI J2026-4536. This might be the signature of astrometric perturbations due to massive substructures in the galaxy unaccounted for by the models. Other possible explanations are also presented.**

12.1 Introduction

Refsdal (1964) was the first to state that gravitationally lensed quasars can be very useful for determining parameters of our Universe: combined with a model of the mass distribution in the lensing galaxy, the time delay between different lensed images can lead to the determination of the *Hubble constant*, H_0. This motivated many of the early lensed quasars studies and time delay measurements campaigns. Unfortunately it quickly became clear that systematic errors propagate in the final estimation of H_0. One way to reduce these systematic errors is to derive accurate relative astrometry of gravitationally lensed images and lens galaxy light profiles based on high resolution frames.

Strong lensing is also a promising tool to estimate the amount (possibly as a function of redshift) of dark matter clumps (hereafter, following other authors, we will call them "substructures") in distant galaxies and compare it to predictions of numerical simulations (see e.g. Zackrisson & Riehm, 2009; Koopmans et al., 2009a). The first

evidence that strongly lensed quasars are sensitive to substructures in galaxies comes from the so-called "anomalous flux ratios": for many systems, the flux ratios between the lensed images deviate from those predicted by simple lens models (Kochanek, 1991; Mao & Schneider, 1998; Dalal & Kochanek, 2002; Keeton, Gaudi & Petters, 2003). It has long been thought that substructures only act on the image flux ratios because of the dependence of these latter on the second derivative of the gravitational potential. However, recent works explore two new routes to detect substructures in lensed quasars. A method suggests to use time delay measurements, as shown by Keeton & Moustakas (2009) who have highlighted small changes in time delays because of substructures. Even if these delays are likely to be modified only by a few tenth of a percent, future large monitoring campaigns should allow the detection of the signature of substructures (Moustakas et al., 2009). Another method proposes to detect substructures in the lensing galaxy through their effects on the position of lensed images. The amplitude and probability we should expect for this phenomenon is still debated. On one hand, observable astrometric perturbations should be due to the most massive substructures. But because of the scarcity of high mass dark matter clumps, Metcalf & Madau (2001) derived a low probability and, on average, low astrometric perturbations. On the other hand, Chen et al. (2007) showed that lower mass substructures also play a role. Including a large range of sub-halo masses, they find that substructures could induce astrometric perturbations as large as 10 mas (see Zackrisson & Riehm, 2009, for a more complete review). Observationaly, astrometric perturbations caused by substructures were detected in a few systems. The most remarkable ones being B0216+112 (Koopmans et al., 2002; More et al., 2009) and B0128+437 (Biggs et al., 2004). In both cases, the anomalies have been unveiled thanks to high resolution radio images.

Although we cannot yet reach the spatial resolution of the *Very Large Baseline Array* (VLBA) in the optical range, it has been shown by some of us (Chantry & Magain, 2007) that a sophisticated deconvolution technique (ISMCS[2]) applied to *Hubble Space Telescope* (HST) images could lead to relative positions of lensed quasar images with milliarcsecond (mas) accuracy, reducing the error bars by a factor > 2 compared to other techniques. In the present paper, we apply this technique to a sample of seven gravitational lenses without measured time delays. All these systems are photometrically monitored by the COSMOGRAIL[3] collaboration and should get a time delay measurement in the near future. The goals of this paper are twofold. First we want to provide shape parameters of the lensing galaxy and accurate relative astrometry for these systems together with simple lens models. From the latter, prospective time delays are also calculated, complementing time delays predicted with non-parametric modeling (Saha et al., 2006). Second, we systematically investigate, for quadruply imaged quasars, the ability of simple smooth models to reproduce the image configuration within a few milliarcseconds. From this systematic and uniform approach, we want to test whether the actual data show evidence for astrometric perturbations due to substructures.

The lens sample studied in this paper is composed of seven different systems without time delay measurements: four doubly imaged quasars for which no detailed modeling and/or relative astrometry has ever been published and three quadruply imaged quasars.

[2]Iterative Strategy combined with the MCS deconvolution algorithm.

[3]*COSmological MOnitoring of GRAvItational Lenses*; `http://www.cosmograil.org`

The ISMCS deconvolution of the gravitational lenses having already measured time delays will be presented in another paper, together with new lens models (Chantry, Sluse & et al., in preparation).

The studied sample is detailed in Sect. 12.2 and the data in Sect. 12.3, while the image processing technique is explained in Sect. 12.4 along with the results. The modeling strategy is explained in Sect. 12.5. A discussion of the models is presented in Sect. 12.6. We then conclude in Sect. 12.7.

12.2 An overview of our sample

Here are the seven gravitationally lensed quasars of our sample :

- **HE 0047-1756 (a)**

  This object (RA = $00^{\mathrm{h}}50^{\mathrm{m}}27^{\mathrm{s}}.82$ and DEC = $-17°40'08''.79$, J2000) was discovered by Wisotzki et al. (2000) in the framework of the Hamburg/ESO Survey (HES) for bright quasars, covering the Southern sky. It was later identified by Wisotzki et al. (2004) as a doubly imaged quasar at a redshift of $z_s = 1.68$. The lens is an elliptical galaxy with a spectroscopic redshift of $z_l = 0.407 \pm 0.001$ (Eigenbrod et al., 2006b; Ofek et al., 2006).

- **RX J1131-1231 (b)**

  This quadruply imaged quasar (RA = $11^{\mathrm{h}}31^{\mathrm{m}}55^{\mathrm{s}}.39$ and DEC = $-12°31'54''.99$, J2000) was discovered serendipitously in 2003 by Sluse et al. They found a redshift of $z_l = 0.295 \pm 0.002$ for the lens while the source lies at $z_s = 0.657 \pm 0.001$. Preliminary time delays have been proposed by Morgan et al. (2006) and revised estimates will be published in Kozłovski et al. (in preparation). The system was characterized in details in terms of astrometry and photometry by Sluse et al. (2006). Claeskens et al. (2006) modeled it and also reconstructed the source which appears to be a Type 1 Seyfert spiral galaxy. A similar work was perfomed by Brewer & Lewis (2008) using a Bayesian approach. Substructures in the main lens were studied by Sugai et al. (2007), Sluse et al. (2007) and Dai, Kochanek, Chartas, Kozłowski, Morgan, Garmire & Agol (2010), while the two latter also investigated the microlensing effects.

- **SDSS J1138+0314 (c)**

  This quadruply imaged object (RA = $11^{\mathrm{h}}38^{\mathrm{m}}03^{\mathrm{s}}.70$ and DEC = $+03°14'57''.99$, J2000) was discovered in 2008 during the Sloan Digital Sky Survey (SDSS) by Inada et al.. The redshifts of the quasar and the lens were measured by Eigenbrod et al. (2006b) and are respectively equal to $z_s = 2.438$ and $z_l = 0.445 \pm 0.001$. No detailed modeling has ever been published for this system and no time delay is available.

- **SDSS J1155+6346 (d)**

  This doubly imaged quasar (RA = $11^{h}55^{m}17^{s}.35$ and DEC = $+63°46'22''.00$, J2000) was discovered by Pindor et al. (2004) in the SDSS data set. They measured the redshifts of the quasar and the lens: $z_s = 2.888$ and $z_l = 0.176$. They also found that one of the two images of the quasar is very close to the lensing galaxy (at around 10% in effective radius off the center of the lens) and is the brightest. That configuration cannot be reproduced by a simple model of mass distribution.

- **SDSS J1226-0006 (e)**

  This system (RA = $12^{h}26^{m}08^{s}.02$ and DEC = $-00°06'02''.19$, J2000) is a doubly imaged quasar discovered in the framework of the SDSS by Inada et al. (2008). The quasar is located at a redshift of $z_s = 1.125$. According to Eigenbrod et al. (2006b), the lens is likely to be an early-type galaxy, with a spectroscopic redshift of $z_l = 0.516 \pm 0.001$. This system has no measured time delay, no published relative astrometry and no detailed modeling study.

- **WFI J2026-4536 (f)**

  Morgan et al. (2004) discovered this quadruply imaged quasar (RA = $20^{h}26^{m}10^{s}.43$ and DEC = $-45°36'27''.10$, J2000) during an optical survey using the WFI camera mounted on the MPG/ESO 2.2m telescope operated by the European Southern Observatory (ESO). The redshift of the source is $z_s = 2.23$. The one of the lens is unknown, although it is clearly visually detected on high resolution images. No time delay has ever been measured but according to Morgan et al. (2004), the longest one might be of the order of at most a week or two. They also found out that the lensed images are likely affected by microlensing.

- **HS 2209+1914 (g)**

  This system (RA = $22^{h}11^{m}30^{s}.30$ and DEC = $+19°29'12''.00$, J2000) is a doubly imaged quasar, with $z_s = 1.07$, discovered during the Hamburg-Cfa Bright Quasar Survey (HS) by Hagen, Engels & Reimers (1999). They clearly detected the lensing galaxy. Nothing else is available for this system: no time delay, no lens redshift and no modeling.

12.3 Observational material

The images we analyse were acquired with the camera 2 of the *Near-Infrared Camera and Multi-Object Spectrometer* (NICMOS) mounted on the HST (hereafter NIC2). They were all obtained in the framework of the CASTLES project (*Cfa-Arizona Space*

Object	Obs. date (y-m-d)	NF	t_{exp}	NI	$\chi^2_{r,f}$	$\chi^2_{r,l}$
(a) HE 0047-1756	2003-12-10	4	44'	3	60.49	1.39
(b) RX J1131-1231	2003-11-17	8	89'	4	74.56	2.58
(c) SDSS J1138+0314	2003-11-06	4	44'	3	18.50	1.69
(d) SDSS J1155+6346	2003-12-12	5	84'	4	86.66	2.93
(e) SDSS J1226-0006	2003-11-21	4	44'	3	16.78	1.01
(f) WFI J2026-4536	2003-10-21	4	46'	4	36.62	4.35
(g) HS 2209+1914	2003-10-14	4	44'	4	40.36	4.2

Table 12.1: General information about the acquisition of HST/NIC2 images and about the application of ISMCS for (a) HE 0047-1756, (b) RX J1131-1231, (c) SDSS J1138+0314, (d) SDSS J1155+6346, (e) SDSS J1226-0006, (f) WFI J2026-4536 and (g) HS 2209+1914. *NF* stands for the number of frames, t_{exp} for the total exposure time, *NI* for the number of iterations, $\chi^2_{r,f}$ and $\chi^2_{r,l}$ for the reduced χ^2 respectively at the first and last iteration.

Telescope LEns Survey[4]), the PI being C. S. Kochanek, and are available in the HST archives. The filter used is the F160W which is very close to the H-Band. Some details about the image acquisition are summarized in the first columns of Table 12.1: the name of the object, the date of observation, the number of frames and the total exposure time. All the frames were obtained after the installation of the *NICMOS Cooling System*, or NCS, in 2002. Every image was acquired with dithering and in the MULTIACCUM mode, each one of them being a combination of about twenty subframes. As these objects were all observed between october and december 2003, the pixel size of the detector on the sky does not change from one target to the other, also because the plate scale of NICMOS has become very stable since the installation of the NCS. The values we use were measured during part b of the third Servicing Mission Observatory Verification, SMOV3b, and are the following: x=0.075948″and y=0.075355″(STScI NICMOS Group, 2007).

12.4 ISMCS on HST/NIC2 images

To extract accurate spatial and shape parameters from our data, we need a method capable of separating the contributions of the lensed point sources from the ones of the more diffuse components (galaxies, halos, arcs, rings, ...). This is exactly what the MCS deconvolution algorithm (Magain, Courbin & Sohy, 1998) provides. One of the advantages of this deconvolution method with respect to other techniques is that it does not violate the sampling theorem. In practice that means that we do not try to fully deconvolve an image in order to obtain an infinite resolution. Instead, we choose a resolution for the final deconvolved image, in our case a Gaussian with 2 pixels of *Full-Width-at-Half-Maximum* (FWHM), and we deconvolve our images with a partial *Point Spread Function* or PSF (which gives the total PSF when reconvolved with our 2 pixels FWHM Gaussian). To do that, we need to know very well the shape of the PSF.

[4] `http://www.cfa.harvard.edu/castles`

As the NIC2 field is only $19\farcs2 \times 19\farcs2$, we do not have the possibility to use field stars (with a *Spectral Energy Distribution*, or SED, similar to that of the lensed quasar) to determine the PSF. Moreover, since the lensed quasar images are contaminated by the lensing galaxy or partial Einstein rings underneath them, we cannot use these images directly to improve our PSF. Instead, we use ISMCS (see Chantry & Magain, 2007, for further details), a special iterative strategy coupled with the MCS algorithm. The HST PSF being quite complex (it includes spike-like features and an intense first Airy ring), we start the deconvolution process using a PSF created by the Tiny Tim software (Krist & Hook, 2004) as a first guess of the true PSF. We improve the Tiny Tim function in adjusting it at the same time on all the point sources of a frame using a technique described in Magain et al. (2007) which allows to add a numerical component to the input PSF so that it is better adapted to the actual frame. We then obtain a set of modified PSFs which we use to simultaneously deconvolve all the frames at our disposal, with a sampling step two times smaller than the original one. In doing so, we obtain a first approximation of the diffuse background and after reconvolving it to the inital resolution, we subtract it from the original frames and we obtain new ones, partially cleaned from the extended structures. On these modified frames which contain point sources less contaminated by smooth structures, we improve once again our PSFs. This iterative process has to be repeated until the reduced chi square, χ^2_r (see here below Eq. 12.1), reaches a value close to unity in an area determined by the maximum extension of the lensed system, and until the residuals are sufficiently flat, i.e. around the level of the noise in the image. The reduced chi square of an image with N pixels is mathematically defined as follows:

$$\chi^2_r = \frac{1}{N} \sum_{\vec{x}} \left(\frac{\mathcal{M}(\vec{x}) - \mathcal{D}(\vec{x})}{\sigma(\vec{x})} \right)^2 \tag{12.1}$$

where $\mathcal{M}(\vec{x})$ is the model reconvolved by the partial PSF, $\mathcal{D}(\vec{x})$ the observed signal and $\sigma(\vec{x})$ the standard deviation associated to that signal.

The original frame (combination of all observations), the deconvolved image and the mean residual maps[5] at the first and last iterations are displayed for each system in Fig. 12.1. When we examine the residual maps, the improvement brought by ISMCS is undeniable. Moreover, we notice that the remnant structures underneath the point sources, on the residual map from the last iteration, are in disagreement with each other, which is the sign of a variable PSF throughout the detector, even on small spatial scales. The number of iterations necessary to reach a reasonably flat residual map is shown in the last columns of Table 12.1 along with the values of the χ^2_r at the first iteration and at the last iteration. Let us note that the iterative process is stopped when the PSF is no longer improved significantly.

The astrometry, corrected from the x/y scale difference and the distortions of NIC2, and the photometry (magnitudes in the Vega system and flux ratios) are shown in Table 12.2 on p. 171. The 1σ error bars were calculated in deconvolving each frame individually and in determining the dispersion around the mean. They are very small

[5]The residual map is the map of the difference between the model and the original frame in units of sigma.

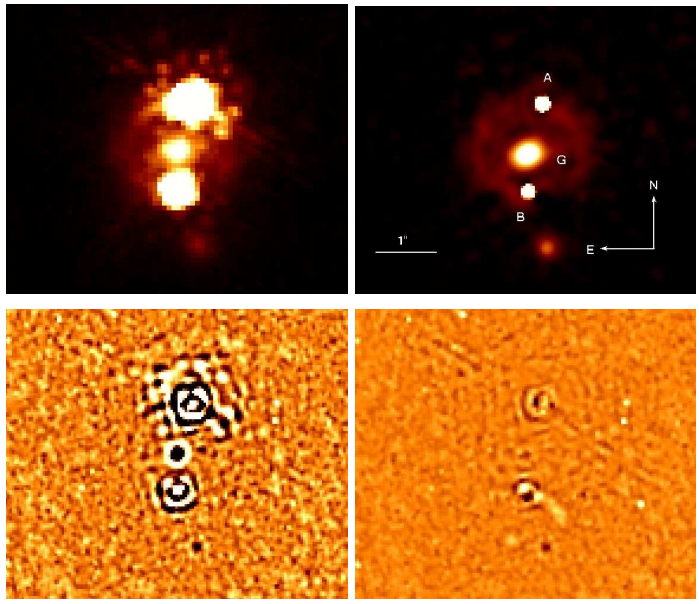

(a) HE 0047-1756

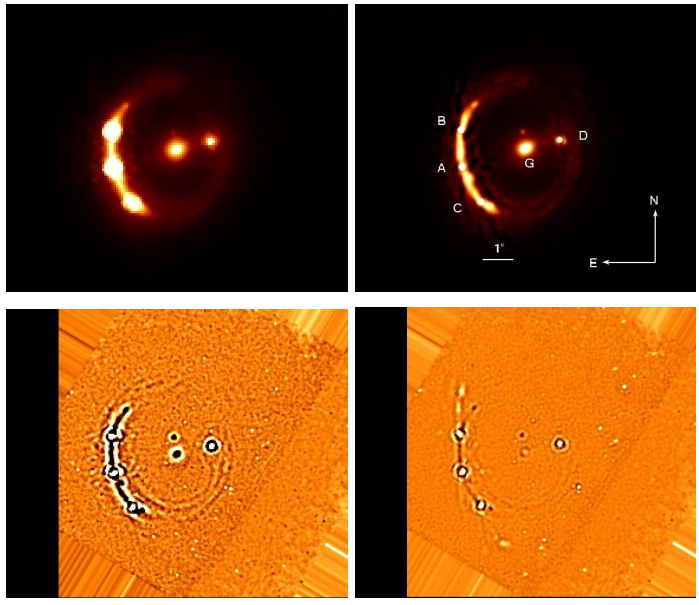

(b) RX J1131-1231

Figure 12.1: HST/NIC2 results respectively for (a) HE 0047-1756, (b) RX J1131-1231, (c) SDSS J1138+0314, (d) SDSS J1155+6346, (e) SDSS J1226-0006, (f) WFI J2026-4536 and (g) HS 2209+1914. *Top Left*: combination of the original F160W frames. *Top Right*: deconvolved image obtained from the last iteration of ISMCS. *Bottom Left*: mean residual map from the first iteration of ISMCS. *Bottom Right*: mean residual map from the last iteration of ISMCS. Both residual maps are expressed in units of σ and their color scale ranges from -5 in black to +5 in white. The labels are the same as in previous studies if any. This figure continues on the next pages.

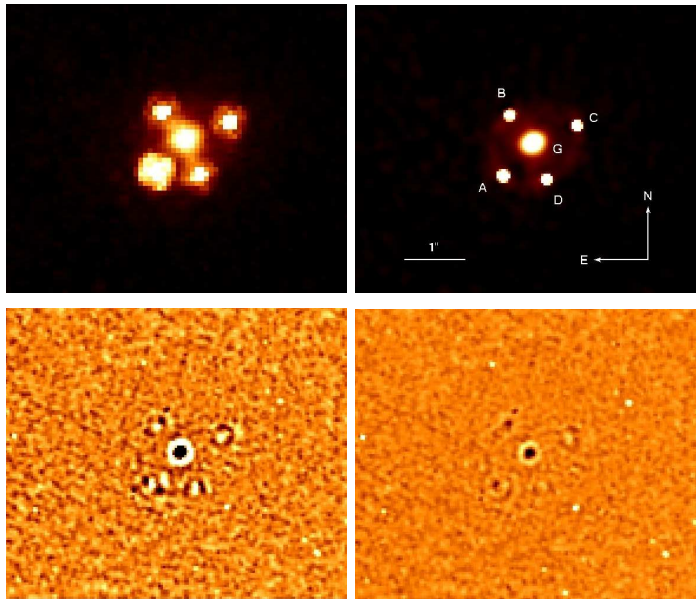

(c) SDSS J1138+0314

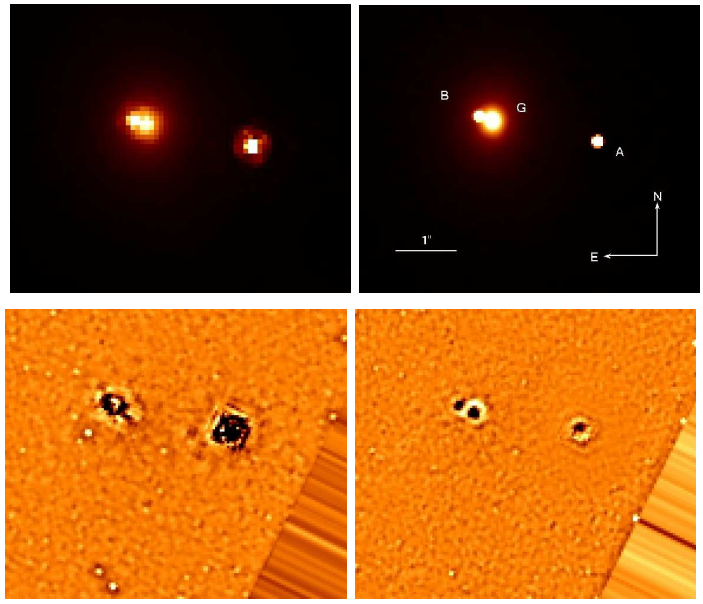

(d) SDSS J1155+6346

Figure 12.1: continued.

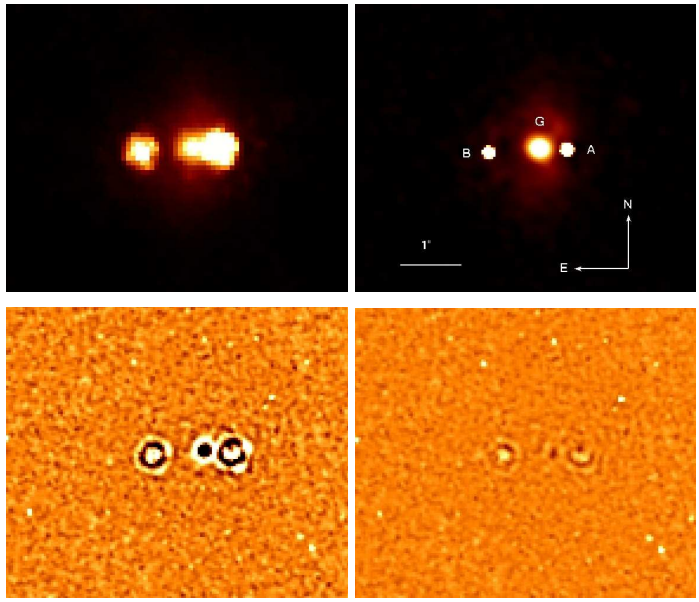

(e) SDSS J1226-0006

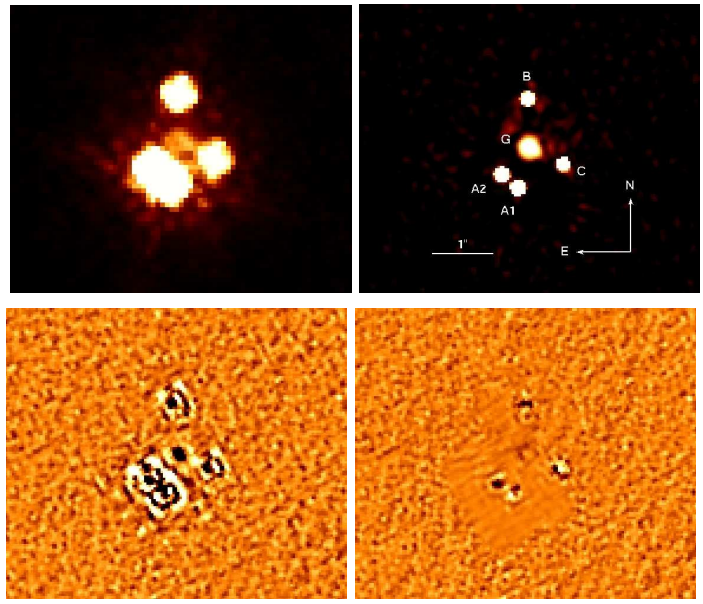

(f) WFI J2026-4536

Figure 12.1: continued.

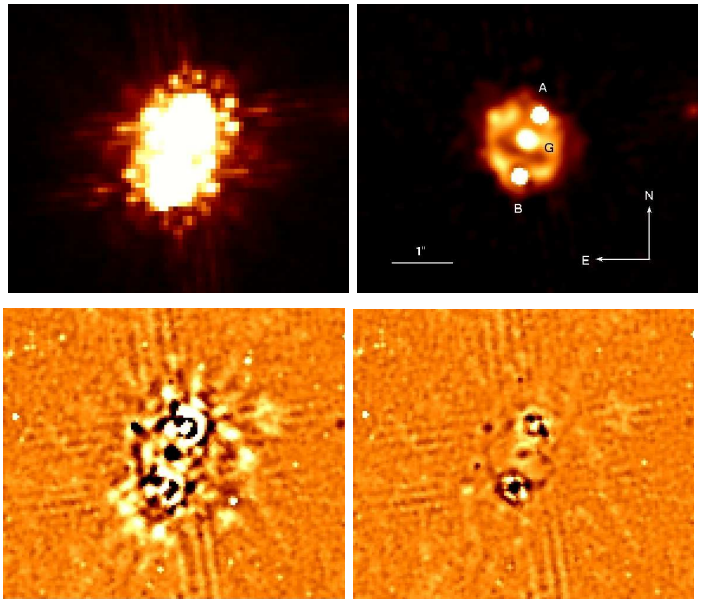

(g) HS 2209+1914

Figure 12.1: continued.

because they are inherent to the deconvolution technique: no external systematic error is included in these error bars. To estimate the total error, we compare the spatial extension of each object on the detector to the one of the Cloverleaf (H1413+117). The latter was used as a test of ISMCS in Chantry & Magain (2007): in comparing the astrometry of the point sources obtained in two different filters and with two different orientations on the sky, they could estimate the total error, i.e. 1 mas, accounting e.g. for a possible remnant distortion in the images. The estimated total errors based on the Cloverleaf are displayed in the fifth column of Table 12.2. Of course, as they are based on the maximum extension of the object no matter the direction, they should be considered as upper limits.

Since the total error derived in Chantry & Magain (2007) for H1413+117 was based on a comparison of the relative positions of the lensed images obtained at different wavelengths with the same instrument, we want to probe the accuracy in a more independent way. In a future paper treating the lenses with already measured time delays (Chantry et al., in preparation), we will present a comparison between our astrometry and the one obtained by Patnaik et al. (1999) from radio data for the quad JVAS B1422+231 (Patnaik et al., 1992). To estimate the error affecting our results, we choose one lensed image as the reference source and we calculate the distance between it and every other lensed image. We then measure the difference between the distances obtained with our positions and the ones calculated with the radio astrometry. The scatter of these differences of distance around the mean is about 2.6 mas. Assuming the uncertainty is

identical in right ascension and in declination, we derive an error on the relative astrometry of 1.8 mas in RA and in DEC. Of course this estimation is valid only if the radio lobes of the unlensed quasar are co-centered with the optical emission and if the errors on the radio data are negligible. This estimate is well compatible with the 1.5 mas error derived from the analysis of the Cloverleaf for this quad. The level of accuracy of our positional constraints can thus be trusted.

Together with the point-source deconvolution, we use an analytical model to characterize the lensing galaxy light distribution. To ensure in this case that the maximum amount of light of the galaxy is included in the profile, the deconvolution is performed with no numerical component. Since most of the lensing galaxies are ellipticals, we use a de Vaucouleurs light profile (de Vaucouleurs, 1948). This procedure allows us to extract the galaxy shape parameters summarized in Table 12.3: the position angle (orientation) of the galaxy, its ellipticity, the effective semi-major and semi-minor axis. The effective radius R_{eff} is further calculated as being the geometrical mean between the two effective semi-axes (Kochanek, 2002). The 1σ error bars were also calculated in deconvolving each frame individually and in determining the dispersion around the mean.

A few remarks can be made about the results from the deconvolution:

- HE 0047-1756: a faint Einstein ring, stretched image of the quasar host galaxy, is revealed by the deconvolution.

- RX J1131-1231: Sluse et al. (2006) reports astrometric measurements on the same frames with the MCS deconvolution algorithm but with no iterative strategy. Their results agree within the error bars with those presented here. An offset of up to 3 mas between both results is observed. This difference is probably due to the large brightness of the Einstein ring. Indeed, the different amount of recovered background under the PSF can lead to a small shift in position. The absolute photometry is also affected by the ring brightness.

- SDSS J1138+0314: a faint Einstein ring is revealed by the deconvolution process.

- SDSS J1155+6346: our astrometry is not in agreement with Pindor et al. (2004) especially concerning the lens. The difference for source B amounts to $0\farcs1$ in RA and $0\farcs04$ in DEC while for the lens the offset is much larger and amounts to $1\farcs55$ in RA and $0\farcs28$ in DEC. However, our astrometry is in agreement with the one listed in the CASTLES database.

- WFI J2026-4536: the astrometry we obtain, except for the right ascension of the lens ($\Delta RA = 0\farcs03$), is in agreement, within the error bars, with the results of Morgan et al. (2004) in using the same frames but a different image processing technique.

- HS 2209+1914: a bulge is clearly observable but an additional extended structure is also visible. It could either be a dust halo, some spiral arms, in which case the lens would be a late-type galaxy, or even a distorted Einstein ring. A spectrum of the lens and higher resolution imaging would help to disentangle between these

hypotheses. As we do not know what this structure is related to, we fit a de Vaucouleurs model on the bulge only, in using a special feature of the MCS algorithm: a mask encircling the lens galaxy to avoid the model to fit this extended structure. Moreover, the residual map contains many intense structures. However, as these structures do not have the same shape under both point sources, we cannot recover the residuals with another iteration of ISMCS. According to the NICMOS Data Handbook (STScI NICMOS Group, 2007), the response of NIC2 becomes highly non-linear at 22 500 ADU. For HS 2209+1914, the maximum level in the central pixels of the brightest lensed image reaches 90 000 to 110 000 counts depending on the considered frame. Saturation is thus likely responsible for the intense remnant structures on the residual map. As a consequence, the obtained constraints for HS 2209+1914 with ISMCS should be considered with precaution.

Let us note that all our results are in agreement with what can be found in the CASTLES database, within their error bars, ours being smaller.

12.5 Parametric modeling

Our goals are twofold. First, we aim at providing simple models and prospective time delays for the lensed quasars monitored by COSMOGRAIL. Second, we aim to test whether simple smooth lens models are able to reproduce the mas relative astrometry of quadruply imaged quasars in three systems without measured time delays. Our strategy consists in using the LENSMODEL software package v1.99g and v1.99m (Keeton, 2001b) to model the mass distribution of our seven systems. For a chosen model of the mass distribution, the code minimizes a χ^2 defined as the square of the difference between observable quantities and their "model counterparts", weighted by the observational errors on these quantities. Two different lens models are considered. First, an isothermal profile, which is the standard mass distribution to model gravitational lenses (Kassiola & Kovner, 1993), and second, a de Vaucouleurs profile, for which we assume that the light perfectly traces the mass in the inner regions of lensing galaxies. These two models should provide a good approximation of the extreme slopes of the mass distribution at the location of the lensed images and of the expected time delays (Kochanek, 2002). In addition, the study of the galaxy-galaxy lensing sample from the *Sloan Lens ACS*[6] *Survey* (SLACS, Bolton et al., 2006) has revealed that the massive elliptical lensing galaxies are nearly kinematically undistinguishable from isothermal ellipsoids (see e.g. Koopmans et al., 2009b). This supports the use of an isothermal gravitational potential as a fiducial model to test the ability of smooth lens models to reproduce quadruply imaged quasars with mas accuracy. Since lensing galaxies are never isolated, we model the effect of the environment with an external shear term characterized by an amplitude γ and a position angle θ_γ (pointing towards the mass at the origin of the shear). All the models are computed for a flat universe with the following cosmological parameters: $H_0 = 70$ km/s/Mpc, $\Omega_m = 0.3$ and $\Omega_\lambda = 0.7$.

[6] ACS stands for *Advanced Camera for Surveys*.

To model our systems, we use every constraint at our disposal: the relative astrometry of the lensed images, with the uncertainties displayed in the fifth column of Table 12.2 (p. 171), the position of the main lens, with the error inherent to the deconvolution when it is larger than the MTE, and, in the case of doubly imaged quasars, the flux ratio between the two point sources, which accounts for two additional constraints while the source flux provides one free parameter. In principle, fluxes can be contaminated by different effects such as microlensing by stars in the galaxy, dust extinction and also by the time delay itself. As the flux ratios are measured in the near-infrared, all these effects should be small (Yonehara, Hirashita & Richter, 2008). We thus assume a 1σ error of 10% on the flux ratios. In summary, we have 10 constraints for the quads, while we have 8 for the doubles. For the de Vaucouleurs model, we assume that the total mass profile follows the light profile. We thus add three constraints (with their error bars) to the model: the PA of the galaxy, its ellipticity e and effective radius R_{eff} (see Table 12.3 on p. 172). Due to the limited number of observational constraints, isothermal mass profiles are assumed to be spherically symmetric (SIS, i.e. *Singular Isothermal Sphere*) when modeling doubles. This is not a strong asumption as the quadrupole term of the potential modifies only slightly the time delays of doubly imaged quasars (Kochanek, 2002; Wucknitz, 2002). For quads, we allow the ellipticity of the isothermal mass distribution (SIE, i.e. *Singular Isothermal Ellipsoid*) to deviate from the ellipticity of the light profile. This enables to account for dark matter halos that would be rounder/flatter then the light distribution (Ferreras, Saha & Burles, 2008). The position angle of the total mass distribution can be constrained as the one of the light profile as these two distributions might only be slightly misaligned (Keeton, Kochanek & Seljak, 1997; Ferreras et al., 2008). Finally, we also assume that the center of the total mass distribution and the one of the light profile are identical within the error bars. This is supported by the work of Yoo et al. (2006) who found, for four lensed quasars with an Einstein ring, that the offset between the light and the total mass distribution is limited to a few mas. Calculating the number of degree(s) of freedom (d.o.f.), which is the difference between the number of model parameters and observable quantities, we find 0 d.o.f. when modeling doubly imaged quasars and 2 (resp. 3) d.o.f. when modeling quads with SIE (resp. de Vaucouleurs) + external shear.

The results are displayed in Table 12.4 on p. 173. The first column gives the name of the object, the second gives the type of mass distribution used ("DV" stands for *de Vaucouleurs profile*), the third gives the mass scale parameter (the angular Einstein radius R_{Ein} in arcseconds), the fourth gives the mass distribution ellipticity e and its orientation θ_e in degrees positive East of North, the fifth column shows the value of the effective radius R_{eff} in the case of a de Vaucouleurs model, column #6 gives the intensity of the shear γ and its orientation θ_γ in degrees positive East of North, the column entitled "d.o.f." gives the number of degree(s) of freedom, the χ^2 of the fit is given in column #8 while the last column gives the predicted time delays in days when the lens redshift is known. Let us note that $\Delta t_{AB} > 0$ means that A varies before B.

12.6 Discussion

For the doubles, both SIS+shear and DV+shear models can reproduce the image configuration as well as the flux ratio, even with our constraints on the shape of the galaxy in the case of a de Vaucouleurs profile. Two systems require a large amount of shear (i.e. $\gamma > 0.1$ for both mass models) to reproduce the lens configuration: SDSS J1226-0006 and SDSS J1155+6346. For SDSS J1226-006, the HST/NIC2 images actually reveal a galaxy G_2 at RA $= 1\farcs7153$ and DEC $= 3\farcs1710$ from image A ($4\farcs3$ from the main deflector), nearly in the direction of θ_γ. This galaxy, which type is unknown, is likely not the only source of shear. Indeed, the luminosity ratio between G_2 and the lens is $L_{lens}/L_{G_2} = 4.8$. Assuming we can use the Faber-Jackson relation ($L \propto \sigma^4$, Faber & Jackson, 1976), this ratio leads to $\sigma_{lens}/\sigma_{G_2} = 1.5$, σ_{lens} and σ_{G_2} being respectively the velocity dispersion in the lens and in G_2. The isothermal model allows us to translate R_{Ein} of the lens to σ_{lens}. We find $\sigma_{lens} = 212$ km/s and thus $\sigma_{G_2} = 141$ km/s. Using formula A.20 of Momcheva, Williams, Keeton & Zabludoff (2006) and supposing G_2 is at the same redshift as the lens, this induces a shear of $\gamma = 0.039$, nearly 3 times smaller then the one predicted by the SIS model. Other galaxies in the field are probably responsible for the remaining shear.

A more dramatic case is SDSS J1155+6346, for which models predict a shear as large as 0.4 to reproduce the observed configuration. This is one of the largest shears needed to reproduce a lensed quasar system. On some larger field images of this object (obtained with the ACS/WFC, i.e. the *Wide Field Camera* mounted on the *Advanced Camera for Surveys*, PI: C. S. Kochanek), we see that there is no massive galaxy in its vicinity. We thus suspect that a massive galaxy cluster lies outside the ACS field, though nothing is clearly visible on the SDSS data[7]. Deeper images would be necessary to infirm or confirm the existence of this cluster.

In the case of HE 0047-175, a diffuse component lies at RA $= -0\farcs0434$ and DEC $= -2\farcs3393$ from image A ($1\farcs56$ from the lens), in the direction of the shear (see Fig. 12.1) unregarding the employed model. Although very faint (about 2 mag fainter than the lens), this galaxy is likely the major contribution to the shear in this system. Indeed, a SIS with $\sigma = 88$ km/s would produce the observed amount of shear, if located at the position of this faint companion (assuming $z_{comp} = z_{lens} = 0.407$).

The quadruply imaged quasars allow to test the ability of simple smooth models to reproduce a relative astrometry with mas accuracy. Only the relative astrometry of SDSS J1138+0314 is easily reproduced with our models.

Conversely, for WFI J2026-4536 and RX J1131-1231, we find that a very large χ^2 is associated to our models. In the first case, the main contribution in the χ^2 comes from the difference between the PA of the model and the PA of the light distribution. In the second case, the large χ^2 is mainly due to the impossibility of the model to recover the image positions. In any case, an underestimation of the error bars on the quasar lensed images is unlikely. For RX J1131-1231, a reduced $\chi^2 \sim 1$ can only be obtained if we increase the error bars on the positions of the lensed images by a factor 10. Alternatively, we also get a good fit if we allow more freedom to the position of the lensing galaxy

[7] `http://cas.sdss.org/dr7/en/`

(i.e. error = 0.02). Following this procedure we find that the offset between the light and mass distribution centroid amounts to 88 pc. This value is marginaly consistent with the upper limit of 70 pc derived for B1938+666 by Yoo et al. (2006). It is however inconsistent with the maximum offset value of $\sim$ 20 pc found for the three other systems they analysed, suggesting that the offset between light and mass distribution is not the cause of the astrometric perturbation we observe. Claeskens et al. (2006) also found that models (simple or more complex) fitting simultaneously the Einstein ring of RX J1131-1231 and the quasar lensed images lead to a poor χ^2. Brewer & Lewis (2008) were also unable to reproduce the lensed quasar relative positions to mas accuracy using the lens model based on the Einstein ring. For WFI J2026-4536, an acceptable χ^2 cannot be obtained in enlarging the error bars on the positions of the sources or the lens but only in relaxing the constraint on the position angle of the galaxy. This could be due to the presence of a galaxy located at RA = $-7\farcs398$ and DEC = $-1\farcs940$ (Morgan et al., 2004) from image B, that we ignored in the modeling.

Concerning the flux ratios of the quads, which are considered as free parameters, we notice that they do not change significantly from one model to the other. However, there is a mismatch between these predicted ratios and the ones measured on the HST/NIC2 frames, which is probably the signature of ,e.g., microlensing effects and/or extinction by the lens galaxy.

The previous results suggest that it is common for simple lens models to fail in reproducing mas astrometry of quadruply imaged quasars. To further investigate the question, we have searched the literature for lensed quasars having images with mas astrometric error bars (i.e. up to $0\farcs002$ on the lensed image positions) and published simple models. We found nine systems gathering these conditions[8]: MG0414+0534 (Ros et al., 2000), HE0435-1223 (Morgan et al., 2005; Kochanek et al., 2006), SDSS0924+0219 (Keeton et al., 2006; Eigenbrod et al., 2006a), H1413+117 (Chantry & Magain, 2007; MacLeod, Kochanek & Agol, 2009), B1422+231 (Bradač et al., 2002), B1608+656 (Koopmans et al., 2003), B1933+503 (Cohn et al., 2001), WFI2033-4723 (Vuissoz et al., 2008), B2045+265 (McKean et al., 2007). Two of these systems (H1413+117, B1933+503) are easily reproduced by simple models because of the large uncertainty affecting the position of the lensing galaxy ($\sigma_{gal} > 0\farcs01$). Out of the four systems for which VLA[9] data are available[10] (MG0414+0534, B1422+231, B1608-656, B2045+265), only B1422+231 shows convincing evidence that smooth models allow to reproduce the relative astrometry, although substructures are needed to reproduce the flux ratios (Bradač et al., 2002). For MG0414+0534, B1608+656 and B2045+265, complex models including a bright susbtructure (MG0414+0534) or a companion galaxy (B1608+656, B2045+265) are needed to get to acceptable fits. Out of the last three systems (HE0435-1223, SDSS0924+0219, WFI2033-4723), constrained by relative astrometric positions derived from HST images, a good fit is obtained only for HE0435-1223. A SIE+γ

[8]Although B0712+472 has accurate astrometry, the model published by Jackson et al. (1998) is provided without information about the χ^2 thus not allowing to estimate the quality of the fit.

[9]VLA stands for *Very Large Array*. This radio observatory is located in New Mexico. It is composed of 27 radio antennas of 25 meters in diameter.

[10]B1933+503 also has VLA data but has already been ruled out, its configuration being easily reproduced with simple models.

model leads to $\chi^2_r \sim 33$ for SDSS0924-0219 (Keeton et al., 2006) and to $\chi^2_r \sim 15$ for WFI2033-4723. In both cases, relaxing the constraint on the lens galaxy centroid allows to get a perfect fit of the astrometry. For WFI2033-4723 more complex models including a nearby group allow to reproduce the astrometry but these models are not fully satisfactory (Vuissoz et al., 2008). Kochanek & Dalal (2004) compile seven quads (some of them also compiled here) for which they fitted SIE+γ models. Unfortunately, there is only sparse information on the astrometric error used and we cannot infer any trend from this study.

To conclude, out of the seven usable systems amongst the nine quads, at least three show astrometric perturbations with respect to predictions of simple lens models (MG0414+0534, SDSS0924+0219, WFI2033-4723). For two of the remaining systems (B1608+656, B2045+265), conclusions are difficult to draw because the need to include a companion galaxy comes naturally from deep near-IR imaging. The last two systems (HE0435-1223, B1422+231) are well reproduced by simple smooth models.

Although the considered sample of quads gathers heterogeneous data sets and analyses, it indicates that relative astrometry of quads often deviates from simple models expectation when trying to reproduce it to the mas precision. The considered sample suggests that the situation is less critical for "central quads" (i.e. with the source lying close to the center of the central astroid caustic) than for fold systems (i.e. source lying close to a fold caustic). This might be a normal geometrical effect (image positions vary more slowly when moving the source in the central region of the astroid) but it might also be due to substructures leading to severe deformations of the caustics (Bradač et al., 2002). It remains to be seen how significant this effect is with respect to the relative astrometric uncertainty on the image positions or the amount of shear.

Substructures are not the only explanation for the frequent inability of simple lens models to fit the configuration of quads. Other possible explanations are astrometric perturbations due to the lens environment, asymmetries in the mass distribution, disky/boxy projected mass profiles, offsets between the galaxy light centroid and mass centroid. The last two solutions seem however to be ruled out by Kochanek & Dalal (2004) and Yoo et al. (2006). The evidence that bright substructures/nearby satellite galaxies explain astrometric perturbations of some systems suggest that substructures may be one of the major contributor to the astrometric perturbations of quads.

All this motivates a systematic study of the ability of simple models to reproduce the configuration of quads, with good control on the error estimates and uniform modeling. Such a work is beyond the scope of this paper and is delayed to a forthcoming paper, when the iterative deconvolution method will have been applied to a larger number of quadruply imaged quasars.

12.7 Conclusions

In applying ISMCS, i.e. the MCS deconvolution algorithm combined with an iterative strategy, to HST/NIC2 images of seven lensed quasars, we have obtained accurate relative positional constraints on the lensed images, lensing galaxy as well as shape parameters for this galaxy. We reach an accuracy of around 1 mas on the lensed image

positions. We also detect a partial Einstein ring in two cases, the double HE 0047-1756 and the quadruple SDSS J1138+0314. Deeper images are needed to perform clear source reconstruction. In the case of HS 2209+1914, the deconvolved frame reveals a structure around the bulge of the lens galaxy which cannot be clearly identified. This structure could be either an Einstein ring or some not well-resolved spiral arms of a big late-type galaxy. This question probably deserves further study: a spectrum of the surrounding structures could give extra information about its true nature.

We also obtain simple mass models for every system. In the case of doubles, both the isothermal and de Vaucouleurs profiles can reproduce the observed configuration. For SDSS J1155+6346, a good fit can only be reached with an extremely and anomalously high external shear, 0.392 for a SIS and 0.453 for a DV, indicating the presence of a galaxy group or cluster probably located outside the field of view of the ACS. For SDSS J1226-006, the large shear (γ=0.1) is probably partially due to a nearby galaxy located $4\farcs3$ from the main deflector. In the case of quads, a good χ^2 can only be obtained for one object: SDSS J1138+0314. The two other quads of our sample, RX J1131-1231 and WFI J2026-4536, need more complicated models to account for their observed configuration. For RX J1131-1231, the offset between the light and mass distribution cannot account for the astrometric perturbation we observe. The study of the literature allows us to conclude that most of the quads cannot be modeled with simple profiles when the astrometic accuracy reaches around 1 mas: some need the presence of companion galaxies, some others need substructures. This finding motivates the acquisition of mas astrometry for all the quads together with simple modeling.

In the framework of the COSMOGRAIL collaboration, the next step for these seven systems is the acquisition of well-sampled light curves to extract time delays. Then, if the redshift of the lens is known, our astrometric constraints will help in reducing the systematic errors on the Hubble constant.

Acknowledgements

COSMOGRAIL is financially supported by the Swiss National Science Foundation (SNSF). This work is also supported by the Belgian Federal Science Policy (BELSPO) in the framework of the PRODEX Experiment Arrangement C-90312. VC thanks the Belgian National Fund for Scientific Research (FNRS). A fellowship from the Alexander von Humboldt Foundation to DS is gratefully acknowledged.

Object	Label	ΔRA (″)	ΔDEC (″)	MTE (mas)	Magnitude	Flux ratio
(a) HE 0047-1756	A	0.	0.	1.0	15.19 ± 0.01	1.
	B	0.2328 ± 0.0008	-1.4094 ± 0.0002	1.0	16.69 ± 0.01	0.253 ± 0.002
	G	0.2390 ± 0.0022	-0.8098 ± 0.0056	1.0	17.17 ± 0.02	/
(b) RX J1131-1231	A	0.	0.	2.0	15.36 ± 0.01	1.
	B	0.0347 ± 0.0005	1.1870 ± 0.0005	2.0	15.58 ± 0.01	0.816 ± 0.003
	C	-0.5920 ± 0.0007	-1.1146 ± 0.0004	2.0	16.42 ± 0.01	0.374 ± 0.003
	D	-3.1154 ± 0.0012	0.8801 ± 0.0013	2.0	17.76 ± 0.01	0.110 ± 0.001
	G	-2.0269 ± 0.0016	0.6095 ± 0.0015	2.0	15.55 ± 0.03	/
(c) SDSS J1138+0314	A	0.	0.	1.0	17.89 ± 0.01	1.
	B	-0.1003 ± 0.0006	0.9777 ± 0.0007	1.0	19.07 ± 0.01	0.346 ± 0.004
	C	-1.1791 ± 0.0003	0.8119 ± 0.0007	1.0	18.89 ± 0.01	0.400 ± 0.002
	D	-0.6959 ± 0.0003	-0.0551 ± 0.0003	1.0	19.02 ± 0.01	0.354 ± 0.003
	G	-0.4633 ± 0.0071	0.5340 ± 0.0036	1.0	17.77 ± 0.01	/
(d) SDSS J1155+6346	A	0.	0.	1.5	16.83 ± 0.02	1.
	B	1.8983 ± 0.0005	0.4052 ± 0.0005	1.5	17.87 ± 0.01	0.710 ± 0.017
	G	1.6982 ± 0.0024	0.3438 ± 0.0009	1.5	15.71 ± 0.01	/

Table 12.2: Relative positions, maximum total error ("MTE"), magnitudes and flux ratios of the lensed images and lensing galaxy respectively for (a) HE 0047-1756, (b) RX J1131-1231, (c) SDSS J1138+0314, (d) SDSS J1155+6346, (e) SDSS J1226-0006, (g) WFI J2026-4536 and (f) HS 2209+1914. See Fig. 12.1 for the labels. The luminosity of the galaxies is measured in an aperture equal to the effective radius, R_{eff}, given in Table 12.3 on p. 172. The $\pm 1\sigma$ error bars shown along with the results are inherent to the deconvolution technique. This table continues on the next page.

Object	Label	ΔRA (″)	ΔDEC (″)	MTE (mas)	Magnitude	Flux ratio
(e) SDSS J1226-0006	A	0.	0.	1.0	17.05 ± 0.01	1.
	B	1.2563 ± 0.0002	-0.0550 ± 0.0007	1.0	17.80 ± 0.01	0.499 ± 0.006
	G	0.4386 ± 0.0029	0.0209 ± 0.0034	1.0	17.71 ± 0.03	/
(f) WFI J2026-4536	B	0.	0.	1.0	17.08 ± 0.01	1.
	A_1	0.1613 ± 0.0007	-1.4290 ± 0.0005	1.0	15.58 ± 0.01	3.988 ± 0.018
	A_2	0.4140 ± 0.0007	-1.2146 ± 0.0006	1.0	16.03 ± 0.01	2.634 ± 0.017
	C	-0.5721 ± 0.0006	-1.0437 ± 0.0003	1.0	17.26 ± 0.01	0.851 ± 0.07
	G	-0.0479 ± 0.0015	-0.7916 ± 0.0015	1.0	18.94 ± 0.04	/
(g) HS 2209+1914	A	0.	0.	1.0	14.37 ± 0.02	1.
	B	0.3307 ± 0.0004	-0.9863 ± 0.0010	1.0	14.63 ± 0.01	0.790 ± 0.027
	G	0.2155 ± 0.0037	-0.3947 ± 0.0054	1.0	21.58 ± 0.2	/

Table 12.2: continued.

Object	PA (°)	e	a_{eff} (″)	b_{eff} (″)	R_{eff} (″)
(a) HE 0047-1756	113.8 ± 5.5	0.22 ± 0.02	1.02 ± 0.03	0.81 ± 0.02	0.91 ± 0.02
(b) RX J1131-1231	108.6 ± 2.4	0.25 ± 0.04	1.25 ± 0.06	0.97 ± 0.01	1.11 ± 0.03
(c) SDSS J1138+0314	122.7 ± 6.5	0.16 ± 0.02	0.93 ± 0.04	0.79 ± 0.03	0.86 ± 0.03
(d) SDSS J1155+6346	0.7 ± 3.4	0.15 ± 0.02	1.23 ± 0.02	1.06 ± 0.01	1.14 ± 0.01
(e) SDSS J1226-0006	45.2 ± 6.1	0.07 ± 0.02	0.72 ± 0.04	0.67 ± 0.02	0.69 ± 0.03
(f) WFI J2026-4536	60.8 ± 5.4	0.24 ± 0.03	0.72 ± 0.03	0.57 ± 0.02	0.64 ± 0.02
(g) HS 2209+1914	63.1 ± 3.25	0.05 ± 0.02	0.55 ± 0.01	0.52 ± 0.01	0.53 ± 0.01

Table 12.3: Measured shape parameters for the lensing galaxy respectively in the following systems: (a) HE 0047-1756, (b) RX J1131-1231, (c) SDSS J1138+0314, (d) SDSS J1155+6346, (e) SDSS J1226-0006, (f) WFI J2026-4536 and (g) HS 2209+1914. The columns present, from left to right, the name of the object, the position angle (PA), in degrees East of North, the ellipticity e ($e = 1 - b/a$), the effective semi-major axis (a_{eff}), the effective semi-minor axis (b_{eff}) and finally, the effective radius (R_{eff}), the three of them being expressed in arcseconds. Each parameter is given with the $\pm 1\sigma$ error.

Object	Model	R_{Ein}	e, θ_e	R_{eff}	γ, θ_γ	Flux ratios	d.o.f.	χ^2	Time delays
(a)	SIS + γ	0.75	/	/	0.048, 7.37	$f_B/f_A = 0.253$	0	0.0	$\Delta t_{AB} = 11.9$
HE 0047-1756	DV + γ	0.75	0.22, 113.8	0.91	0.120, 15.99	$f_B/f_A = 0.253$	0	0.0	$\Delta t_{AB} = 16.5$
(b)	SIE + γ	1.84	0.19, 118.21	/	0.101, 96.49	$f_B/f_A = 0.641$	2	338.4	$\Delta t_{AB} = -1$
RX J1131-1231						$f_C/f_A = 0.548$			$\Delta t_{AC} = -1.3$
						$f_D/f_A = 0.057$			$\Delta t_{AD} = 116.3$
	DV + γ	1.79	0.32, 114.71	1.09	0.213, 101.61	$f_B/f_A = 0.682$	3	314.3	$\Delta t_{AB} = -1.9$
						$f_B/f_A = 0.584$			$\Delta t_{AC} = -2.4$
						$f_B/f_A = 0.042$			$\Delta t_{AD} = 198.6$
(c)	SIE + γ	0.66	0.05, 118.54	/	0.108, 32.07	$f_B/f_A = 0.506$	2	2.6	$\Delta t_{AB} = 3.4$
SDSS J1138+0314						$f_C/f_A = 0.714$			$\Delta t_{AC} = -1.7$
						$f_D/f_A = 0.945$			$\Delta t_{AD} = 0.9$
	DV + γ	0.66	0.15, 121.32	0.86	0.145, 32.27	$f_B/f_A = 0.505$	3	4.9	$\Delta t_{AB} = 3.8$
						$f_C/f_A = 0.712$			$\Delta t_{AC} = -1.9$
						$f_D/f_A = 0.925$			$\Delta t_{AD} = 1.0$
(d)	SIS + γ	0.59	/	/	0.392, 169.66	$f_B/f_A = 0.710$	0	0.0	$\Delta t_{AB} = 20.6$
SDSS J1155+6346	DV + γ	0.58	0.15, 0.70	1.14	0.453, 168.99	$f_B/f_A = 0.710$	0	0.0	$\Delta t_{AB} = 25.0$

Table 12.4: Results of the parametric modeling respectively for: (a) HE 0047-1756, (b) RX J1131-1231, (c) SDSS J1138+0314, (d) SDSS J1155+6346, (e) SDSS J1226-0006, (f) WFI J2026-4536 and (g) HS 2209+1914. See Sect. 12.5 for details. This table continues on the next page.

Object	Model	R_{Ein}	e, θ_e	R_{eff}	γ, θ_γ	Flux ratios	d.o.f.	χ^2	Time delays
(e)	SIS + γ	0.57	/	/	0.100, 8.01	$f_B/f_A = 0.499$	0	0.0	$\Delta t_{AB} = -25.5$
SDSS J1226-0006	DV + γ	0.57	0.07, 45.22	0.69	0.145, 4.55	$f_B/f_A = 0.499$	0	0.0	$\Delta t_{AB} = -34.3$
(f)	SIE + γ	0.66	0.13, 124.70	/	0.101, 77.51	$f_{A_1}/f_B = 3.578$	2	264.8	z_l unknown
WFI J2026-4536						$f_{A_2}/f_B = 2.937$			
						$f_C/f_B = 1.125$			
	DV + γ	0.65	0.16, 126.82	0.64	0.149, 82.95	$f_{A1}/f_B = 3.286$	3	287.1	z_l unknown
						$f_{A_2}/f_B = 2.651$			
						$f_C/f_B = 1.013$			
(g)	SIS + γ	0.52	/	/	0.031, 94.28	$f_B/f_A = 0.790$	0	0.0	z_l unknown
HS 2209+1914	DV + γ	0.52	0.05, 63.08	0.53	0.041, 99.57	$f_B/f_A = 0.790$	0	0.0	z_l unknown

Table 12.4: continued.

The important thing in science is not so much to obtain new facts as to discover new ways of thinking about them.

William Bragg (1862 - 1942)

13

ISMCS applied to a sample of eleven lensed quasars with measured time delays

Contents

13.1 Introduction

Our aim is to apply ISMCS to a sample of lensed quasars with measured time delays. Indeed, it is composed of eleven systems which have already been monitored and studied by other teams: JVAS B0218+357, SBS 0909+532, RX J0911.4+0551, FBQS J0951+2635, HE 1104-1805, PG 1115+080, JVAS B1422+231, SBS 1520+53, CLASS B1600+434, CLASS B1608+656 and HE 2149-2745. In this chapter we present the positional constraints we obtain thanks to the iterative strategy.

As for the sample of seven lensed quasars, we want to model these systems with simple profiles to see how positions with mas accuracy can be reproduced. Moreover,

these systems have already been monitored: their time delays are supposedely known. In including them in the modeling, we can obtain an estimation of H_0, which is our final objective. In a concern of homogeneity, i.e. to avoid any bias that could be brought by the variety of techniques used to measure the delays, we prefer to apply, to the light curves published in previous papers, a method inspired by the one explained in Burud et al. (2001). This task is entrusted to E. Eulaers, in the framework of her PhD thesis. The first results concerning the time delay measurement and modeling are given hereafter. The complete study will appear in the paper which is currently in preparation.

However, this is not our unique goal. As explained in Chantry, Sluse & Magain (2010) and Chapter 12, and considering the accuracy we reach on the positions, a study of the substructures in the main lensing galaxy might be possible. Indeed, as discussed in Zackrisson & Riehm (2009), substructures can be responsible for astrometric perturbations as large as 10 mas. That means that the configuration of some of our lensed quasars might not be well reproduced by smooth models. A more sophisticated analysis of astrometric perturbations than the one presented in Chantry et al. (2010, submitted to A&A), should be performed in collaboration with C. R. Keeton, using a new verion of the LENSMODEL software (Keeton, 2001b) which is currently being developed.

13.2 Our sample under the magnifying glass

Here are the eleven gravitationally lensed quasars under investigation in this chapter :

- **JVAS B0218+357 (a)**

  This system (RA = $02^{\mathrm{h}}21^{\mathrm{m}}05^{\mathrm{s}}.48$ and DEC = $+35°56'13''.78$, J2000) is a doubly imaged blazar (BL Lac type). It was first considered as such in 1993 by Patnaik et al. in the context of the Jodrell Bank/VLA Astrometric Survey (JVAS). It has the smallest image separation found so far in lensed quasar systems, which implies a time delay of only a few days, which has already been measured, amongst others, by Biggs et al. (1999) and Cohen et al. (2000). The lens is probably a gas-rich late-type galaxy (Keeton, Kochanek & Falco, 1998). Its redshift is $z_l = 0.6847$ (Browne et al., 1993; Stickel & Kuehr, 1993; Carilli, Rupen & Yanny, 1993) and the redshift of the source is $z_s = 0.944 \pm 0.002$ (Cohen, Lawrence & Blandford, 2003). The lensing galaxy seems to be isolated and the potential not to be disturbed by any other nearby galaxies (Lehár et al., 2000). Some models for this system have been presented in Wucknitz et al. (2004) and York et al. (2005).

- **SBS 0909+532 (b)**

  Discovered as a quasar (RA = $09^{\mathrm{h}}13^{\mathrm{m}}01^{\mathrm{s}}.05$ and DEC = $+52°59'28''.83$, J2000) by Stepanyan et al. (1991) in the framework of the Second Byurakan Survey (SBS), the hypothesis of its lensed nature was first emitted by Kochanek et al. (1997) who found a redshift of $z_s = 1.377$ for the source, and then supported by Oscoz et al. (1997). In 1998, Bade et al. resolved the system into a pair of sources

during the Hamburg-Cfa Bright Quasar Survey. According to Lehár et al. (2000), the tidal environment of this system is non-negligible. The two lensed images are bright and close to each other ($\sim 1''$) which made it difficult for them to detect the lensing galaxy even on high resolution near-IR images: they concluded that the lens is probably an early-type galaxy with a large effective radius and a low surface brightness. Despite of this, Lubin et al. (2000) managed to measure its redshift: $z_l = 0.830$. Dust extinction in the lensing galaxy has been studied several times: Motta et al. (2002); Mediavilla et al. (2005); Jean & Surdej (2007). The time delay was measured by Ullán et al. (2006) and revised by Goicoechea et al. (2008) in the first robotic monitoring of a lensed quasar with the Liverpool Robotic Telescope located in La Palma, Spain. Recently, the differential X-ray absorption and dust-to-gas ratio of the lens were studied by Dai & Kochanek (2009).

- **RX J0911.4+0551 (c)**

  This lensed quasar (RA = $09^h11^m27^s.50$ and DEC = $+05°50'52''.00$, J2000) was discovered in 1997 by Bade et al. amongst the AGN candidates of the ROSAT All-Sky Survey (RASS). Its lensed nature was confirmed by Burud et al. (1998) who first obtained high resolution optical and near-IR images of this quadruply imaged system. Its configuration requires an external shear: three of the four images are very close to each other, implying a short time delay (probably less than a week) while the fourth one is isolated. Burud et al. (1998) also observed a reddening of some of the four images, requiring differential extinction from the lens. Hjorth et al. (2002) measured the delay between the three closest components and the fourth one. The quasar is located at a redshift of $z_s = 2.8$ (Bade et al., 1997) while the nearly circular early-type lens galaxy lies at a redshift of $z_l = 0.769$, which has been measured by Kneib, Cohen & Hjorth (2000). These authors also discovered that the lens belongs to a massive cluster, located $38''$ South-West of the lensed system, and responsible for the shear required in the modeling. Chartas et al. (2001) noticed that the lensed quasar is a "mini-BAL" or *mini-Broad Absorption Line*. Recently, Anguita et al. (2008) studied the environment of the lens and the microlensing effects in this system. One of their conclusions is that images A_1 and A_3 (see hereafter frame (c) in Fig. 13.1) are likely demagnified by microlensing from the stars in the lensing galaxy while Burud et al. (1998) found that A_2 and A_3 are demagnified. As the flux ratios increase continuously with wavelength, they emitted the hypothesis of extinction by dust in the lensing galaxy. The main lens is also known to have a small satellite galaxy in the North-West direction.

- **FBQS J0951+2635 (d)**

  This system (RA = $09^h51^m22^s.57$ and DEC = $+26°35'14''.10$, J2000), discovered during the FIRST Bright QSO Survey (FBQS), is a doubly imaged quasar located at a redshift of $z_s = 1.24$ according to Schechter et al. (1998) who first identified the two observed objects as lensed images of the same source. The time delay was measured by Jakobsson et al. (2005) who also found $z_s = 1.246 \pm 0.001$, in

agreement with previous results. The redshift of the lens was measured several times, the latest by Eigenbrod, Courbin & Meylan (2007), who obtained a higher result than in previous studies: $z_l = 0.260 \pm 0.002$.

- **HE 1104-1805 (e)**

  First considered as a good lens candidate by Wisotzki et al. (1993) in the framework of the Hamburg/ESO Survey (HES) for bright quasars, the nature of this doubly lensed quasar (RA = $11^h06^m33^s.45$ and DEC = $-18°21'24''.20$, J2000) was confirmed in 1998 by Courbin et al. and Remy et al. (1998), when the lensing galaxy was finally detected. Its colours are consistent with an early-type galaxy. The redshift of the source is the following: $z_s = 2.319$ (Smette et al., 1995). Lidman et al. (2000) measured a lens redshift of $z_l = 0.729 \pm 0.001$, in agreement with the previous estimates based on the position of the lens in the fundamental plane. As it is a particular system, the lens being closer to the bright image than the faint one, Lehár et al. (2000) included it in their study of ten two-image gravitational lenses. They found that the image configuration could only be matched by models having a large misalignment between the light and the total mass or with a large external shear suggested by the relatively high separation of the images. In relaxing the constraint on the flux ratios they could find more usual models. The time delay between the two images of HE 1104-1805, sometimes called the "Double Hamburger", has been controversial for several years. First measured by Wisotzki et al. (1998), it was disconfirmed by Gil-Merino et al. (2002). But the latter publication was directly followed by a criticism of Pelt, Refsdal & Stabell (2002) on the arguments used to discredit the first value of the time delay. It was remeasured by Ofek & Maoz (2003), confirmed the same year by Wyrzykowski et al. and lately improved by Poindexter et al. (2007). One of the difficulties is the non-negligeable influence of microlensing on the measured fluxes (see e.g. Schechter et al., 2003). The environment has been studied in detail by Faure et al. (2004) but they did not find any evidence of a galaxy group in the surroundings of HE 1104-1805 justifying the external shear needed in the models.

- **PG 1115+080 (f)**

  Weymann et al. (1980) first identified PG 1115+080 (RA = $11^h18^m17^s.00$ and DEC = $+07°45'57''.70$, J2000) as a gravitationally lensed quasar in the framework of the Palomar-Green survey (PG). At that time they only detected three point sources, while this system is indeed a quad (Hege et al., 1981) with two very close-by images. The source is a BAL (*Broad Absorption Line*) quasar lying at a redshift of $z_s = 1.722$. According to Tonry (1998), the lens is part of a group located at a redshift of 0.311 ± 0.001, while $z_l = 0.3098 \pm 0.0002$. Schechter et al. and Barkana both measured the time delays of PG 1115+080 in 1997, two of the four sources being considered as one as they are too close to properly separate their flux contribution. Historically this is the second object for which the time delays were ever measured. This system was then modeled in detail by Keeton &

Kochanek (1997), whose results were improved by Courbin et al. (1997): the latter put stronger constraints on the position of the lens and the multiple images. Let us note that an external shear is required to obtain a decent model. A new method of non-parametric modeling was also tested on this system by Saha & Williams (1997). An IR Einstein ring, distorted image of the quasar host galaxy, was detected for the first time by Impey et al. (1998). Treu & Koopmans (2002) broke the mass-sheet degeneracy of the lens using additional dynamical constraints. According to Yoo et al. (2005), the lens is elliptical. Its dark matter fraction has been studied by Chiba et al. (2005) while Yoo et al. (2006) investigated its halo. They found a low upper limit of the order of 1 mas on the possible offset between the center of the light distribution and the one of the total halo. Moreover Chiba et al. (2005) and Pooley et al. (2009) studied the substructures in this lens galaxy. Morgan et al. (2008) recently used the microlensing effect in the lensed images to constrain the size of the quasar accretion disk.

- **JVAS B1422+231 (g)**

  This quadruple system (RA = $14^{\mathrm{h}}24^{\mathrm{m}}38^{\mathrm{s}}.09$ and DEC = $+22°56'00''.60$, J2000) was discovered in 1992 by Patnaik et al. during the Jodrell/VLA Astrometric Survey. The same authors measured the redshift of the quasar: $z_s = 3.62$. The lensed nature of B1422+231 was first noticed by Lawrence et al. (1992) and then supported by Remy et al. (1993). Impey et al. (1996) determined a first estimate of the lens redshift: $z_l \simeq 0.4$. According to Tonry (1998), as first published by Kundic et al. (1997), the lens is part of a group at a redshift of $z_g = 0.339 \pm 0.002$, while $z_l = 0.3366 \pm 0.0004$. Patnaik & Narasimha (2001) were the first to measure the time delays, but only between the three brightest images amongst the four ones. The models were investigated in detail by Mao & Schneider (1998) and substructures in the lensing galaxy seem to play an important role as stated by Bradač et al. (2002). However, Chiba et al. (2005) put an upper limit on the contribution of substructure lensing. Meanwhile non-parametric modeling of these systems has also been proposed by Raychaudhury, Saha & Williams (2003).

- **SBS 1520+53 (h)**

  The Second Byurakan Survey allowed Chavushyan et al. (1997) to discover this doubly imaged BAL quasar (RA = $15^{\mathrm{h}}21^{\mathrm{m}}44^{\mathrm{s}}.83$ and DEC = $+52°54'48''.60$, J2000) of redshift $z_s = 1.855 \pm 0.002$. The lensing galaxy was identified by Crampton, Schechter & Beuzit in 1998. The time delay as well as the redshift of the lens, $z_l = 0.717$, were measured by Burud et al. (2002b). The same year, Faure et al. (2002) published a detailed study of this system including a modeling: an external shear is mandatory to obtain a reasonable fit. That is explained by the presence of a neighbouring galaxy and by the fact that the lens lies in a cluster. In a recent publication, Auger et al. (2008) pointed out that the previous measurement of the lens redshift might be wrong, suggesting a new value of $z_l = 0.761$, though not conclusively. Khamitov et al. published a delay in 2006, in agreement with the

previous result. Microlensing was also studied for this object e.g. by Gaynullina et al. (2005) and Paraficz et al. (2006).

- **CLASS B1600+434 (i)**

  This system (RA = $16^{\rm h}01^{\rm m}40^{\rm s}.45$ and DEC = $+43°16'47''.80$, J2000) is a two-image lensed quasar first identified as such by Jackson et al. (1995) in the context of the Cosmic Lens All-Sky Survey (CLASS). The source lies at a redshift of $z_s = 1.59$ (Fassnacht & Cohen, 1998). The primary lensing object is an edge-on spiral galaxy with redshift $z_l = 0.41$ (Jaunsen & Hjorth, 1997; Fassnacht & Cohen, 1998) modeled in detail by Koopmans, de Bruyn & Jackson (1998). The galactic environment was studied by Auger et al. (2007): it is composed of at least seven galaxies which lead to around 10% change in the estimation of H_0 when taken into account. The time delay was measured by Burud et al. and Koopmans et al. in 2000.

- **CLASS B1608+656 (j)**

  This lensed quasar (RA = $16^{\rm h}09^{\rm m}13^{\rm s}.96$ and DEC = $+65°32'29''.00$, J2000), which is indeed the core of a post-starburst radio galaxy of redshift $z_s = 1.394$ (Fassnacht et al., 1996), was discovered by Myers et al. in 1995 as part of the Cosmic Lens All-Sky Survey. This object is quadruply lensed by two galaxies located at the same redshift: $z_l = 0.6304$. The time delays were first measured by Fassnacht et al. (1999) and then improved by Fassnacht et al. (2002). The modeling of this system was carried out several times, amongst others by Koopmans & Fassnacht (1999) and Koopmans et al. (2003). The lens potential seems to require a relatively large external shear. This led Fassnacht et al. (2006) to study the mass along the line of sight to this system. They drew several conclusions: the main lens appears to be located in a low mass group of redshift $z_g = 0.631$ and composed of eight confirmed members, three other groups are located in the foreground of the pimary lens, they contain 10 confirmed members each and are respectively located at $z_{g_1} = 0.265$, $z_{g_2} = 0.426$ and $z_{g_3} = 0.52$. More recently Suyu et al. (2009) made use of the Einstein ring of B1608+656 to extract more constraints on the lens potential and Suyu et al. (2010) derived the Hubble constant from a very complete study of this system.

- **HE 2149-2745 (k)**

  Burud et al. (2002a) were the first to publish a time delay for this doubly lensed BAL quasar (RA = $21^{\rm h}52^{\rm m}07^{\rm s}.44$ and DEC = $-27°31'50''.20$, J2000). It was discovered in 1996 by Wisotzki et al. in the context of the Hamburg/ESO Survey for bright quasars. According to them the redshift of the source is $z_s = 2.033$ while the lensing galaxy remained undetected until Lopez, Wucknitz & Wisotzki (1998) who also constrained its redshift, i.e. $0.3 < z_l < 0.5$. In that publication, the authors also modeled the system and realized that an external shear was

necessary. Therefore, Faure et al. (2004) studied the galactic environment of HE 2149-2745 and concluded that a galaxy group is present along the line of sight of this system. The redshift of the lens, an early-type galaxy, was recently remeasured by Eigenbrod et al. (2007): $z_l = 0.603 \pm 0.001$. This value is slightly higher than the previous estimates.

Some gravitationally lensed systems with known time delays have been put aside for different reasons. The following system is very famous and has been studied many times: PKS 1830-211. But as this object is very complicated and lies in a very crowded field, we do not include it in our sample. Another interesting system with a known delay is SDSS J1004+4112 (Fohlmeister et al., 2007, 2008). But the lensing component is a cluster of galaxies rather than a single galaxy with a possible shear and its image separation is very large. For these reasons, we also exclude it from our sample. Finally QSO 0957+561, the first object with a measured time delay, has also been rejected from the sample: this doubly imaged quasar is still at the center of the debate regarding the time delay. It has also been modeled many times and the lensing galaxy is located at the center of a cluster, which makes it a more complicated object.

13.3 ISMCS on HST/NIC2 images

In this section, we apply ISMCS to high resolution images acquired with the Camera 2 of NICMOS on board the HST. They were obtained in the framework of the CASTLES project, with E. Falco as PI. We have at our disposal 4 (8 in the case of JVAS B1422+231) dithered frames taken through the F160W filter (H-band) in MULTIACCUM mode, each of them being a combination of 18 to 20 samples. The first four columns of Table 13.1 display information about the image acquisition such as the date of observation of every object and the total exposure time t_{exp}. The original pixel size of NIC2 depends on the observation date and ranges between $0\farcs075$ and $0\farcs076$ (STScI NICMOS Group, 2007).

As usual, we choose a Gaussian with a FWHM of two pixels as the shape of a point source in the final deconvolved frame. The number of iterations and the values of the χ^2_r at the first iteration and at the last iteration are presented in the last three columns of Table 13.1. The original frame, i.e. the combination of all observations, as well as the deconvolved frame are displayed in Fig. 13.1 for each system studied. These results were obtained with a combination of a smoothed numerical background and a galactic profile. This allows to obtain complementary constraints on the shape of the light distribution in the lensing galaxies. As all the results, these shape parameters, i.e. position angle, ellipticity and effective semi-major and semi-minor axes, come from the last iteration of ISMCS. But to ensure in this case that the maximum amount of light of the galaxy is included in the profile, the deconvolution is performed with no numerical component. These parameters are listed in Table 13.2 on p. 197. Also shown is the effective radius, which is the geometric mean between the effective major and minor axes of the ellipse (Kochanek, 2002). Let us note that for early-type galaxies, we fit a de Vaucouleurs model (de Vaucouleurs, 1948) and for late-type galaxies, we fit an exponential luminosity profile (Freeman, 1970).

Object	Obs. date (y-m-d)	NF	t_{exp}	NI	$\chi^2_{r,f}$	$\chi^2_{r,l}$
(a) JVAS B0218+357	1997-08-19	4	43'	4	23.11	1.64
(b) SBS 0909+532	1997-11-07	4	47'	3	12.70	1.43
(c) RX J0911.4+0551	1998-10-18	4	43'	3	9.47	1.47
(d) FBQS J0951+2635	1998-03-19	4	43'	4	60.37	0.92
(e) HE 1104-1805	1997-11-22	4	43'	4	31.15	1.73
(f) PG 1115+080	1997-11-17	4	43'	4	16.40	2.68
(g) JVAS B1422+231	1998-02-27	8	85'	4	118.3	1.76
(h) SBS 1520+530	1998-07-20	4	47'	3	11.62	1.74
(i) CLASS B1600+434	1997-10-10	4	43'	3	6.213	1.26
(j) CLASS B1608+656	1997-09-29	4	47'	4	28.50	2.09
(k) HE 2149-2745	1998-09-04	4	43'	3	18.47	1.37

Table 13.1: General information about the acquisition of HST/NIC2 images and the application of ISMCS for (a) JVAS B0218+357, (b) SBS 0909+532, (c) RX J0911.4+0551, (d) FBQS J0951+2635, (e) HE 1104-1805, (f) PG 1115+080, (g) JVAS B1422+231, (h) SBS 1520+530, (i) CLASS B1600+434, (j) CLASS B1608+656 and (k) HE 2149-2745. *NF* stands for the number of frames, t_{exp} for the total exposure time, *NI* for the number of iterations, $\chi^2_{r,f}$ and $\chi^2_{r,l}$ for the reduced χ^2 respectively at the first and last iteration.

Also displayed in Fig. 13.1 is the mean residual maps (difference between the model and the initial signal in units of sigma) from the first and last iterations of ISMCS. While the improvement brought by the application of ISMCS is clearly visible, there are remnant structures on the location of the point sources of most systems. However, there is no systematic trend within each image, meaning that it could not have been recovered by improving the PSF: it is probably the signature of PSF variations through the detector.

The astrometry and photometry of the point sources and lensing galaxy from the last iteration are listed in Table 13.3 on p. 198. The relative positions are corrected from the known distortions of the NIC2 camera, as well as from the difference of pixel scale between the x and y directions. The $\pm 1\sigma$ error bars shown in this table are calculated in deconvolving each frame individually and in measuring the dispersion of the values around their mean. These are internal error bars inherent to the image processing. We estimate from the conclusions of Chantry & Magain (2007) concerning the Cloverleaf that the maximum total error (MTE) affecting the point source positions in our systems varies from 0.5 to 2 milliarcseconds (see fifth column of Table 13.3), depending on the size of the system on the detector. We reach that conclusion in assuming that the main source of error is an incomplete correction of the distortions and then in comparing the maximum spatial extension on the detector of the considered object with the one of the Cloverleaf.

A few remarks can be made about the results:

- JVAS B0218+357: Lehár et al. (2000) derived a position for the lens in averaging the results they obtained with the same frames as ours and with archival

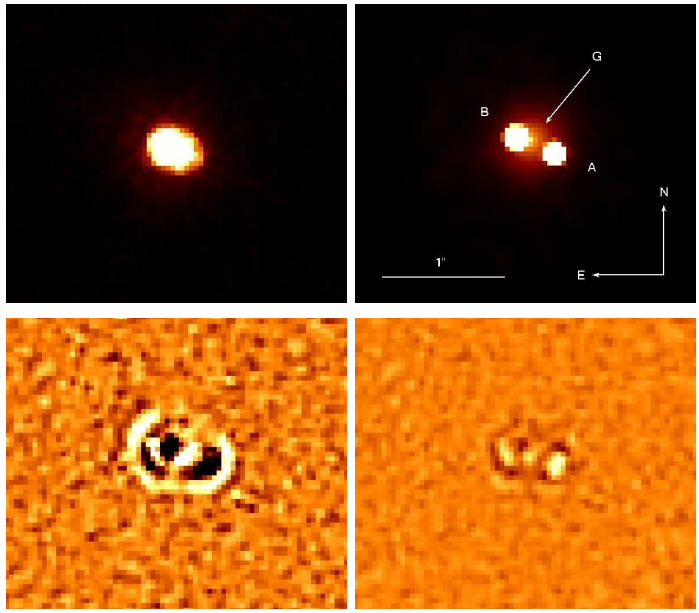

(a) JVAS B0218+357

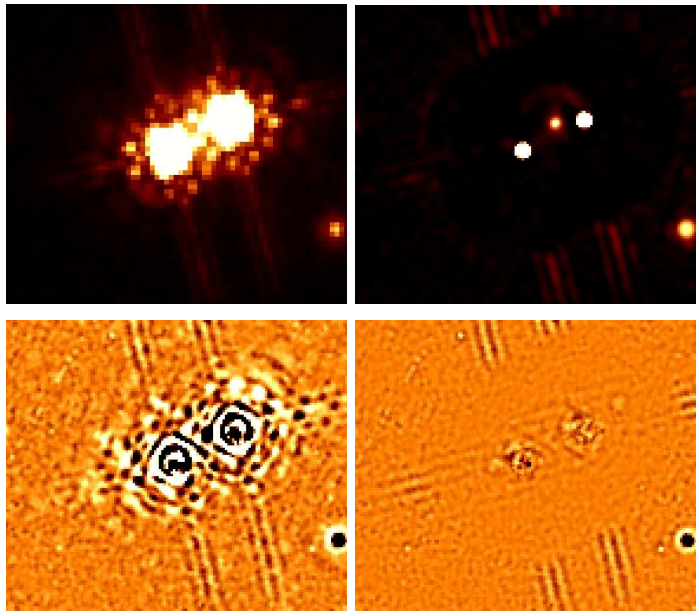

(b) SBS 0909+532

Figure 13.1: HST/NIC2 results for (a) JVAS B0218+357, (b) SBS 0909+532, (c) RX J0911.4+0551, (d) FBQS J0951+2635, (e) HE 1104-1805, (f) PG 1115+080, (g) JVAS B1422+231, (h) SBS 1520+530, (i) CLASS B1600+434, (j) CLASS B1608+656 and (k) HE 2149-2745. *Top Left*: combination of the original F160W frames. *Top Right*: image deconvolved with ISMCS. *Bottom Left*: mean residual map from the first iteration of ISMCS. *Bottom Right*: mean residual map from the last iteration of ISMCS. Both residual maps are expressed in units of σ and their color scale ranges from -5 in black to +5 in white. This figure continues on the next pages.

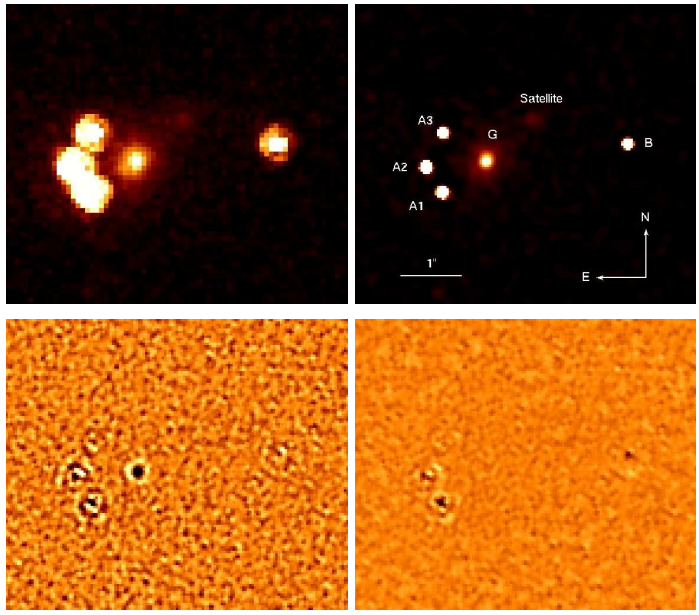

(c) RX J0911.4+0551

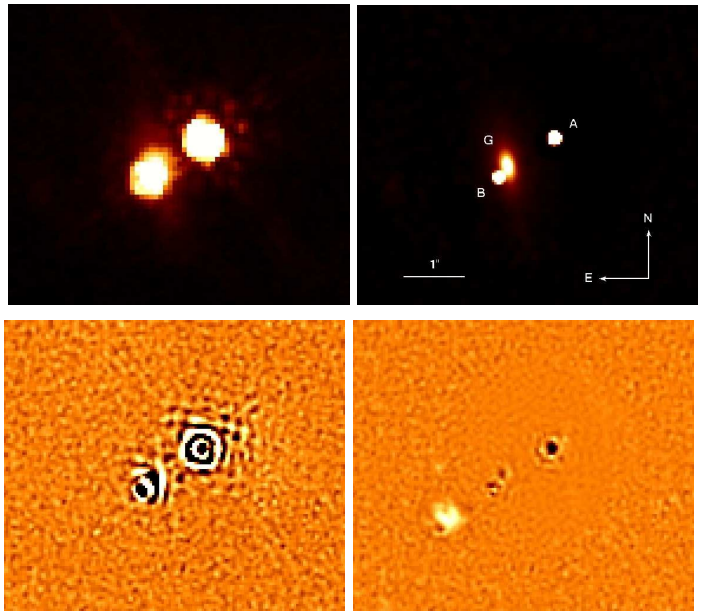

(d) FBQS J0951+2635

Figure 13.1: continued.

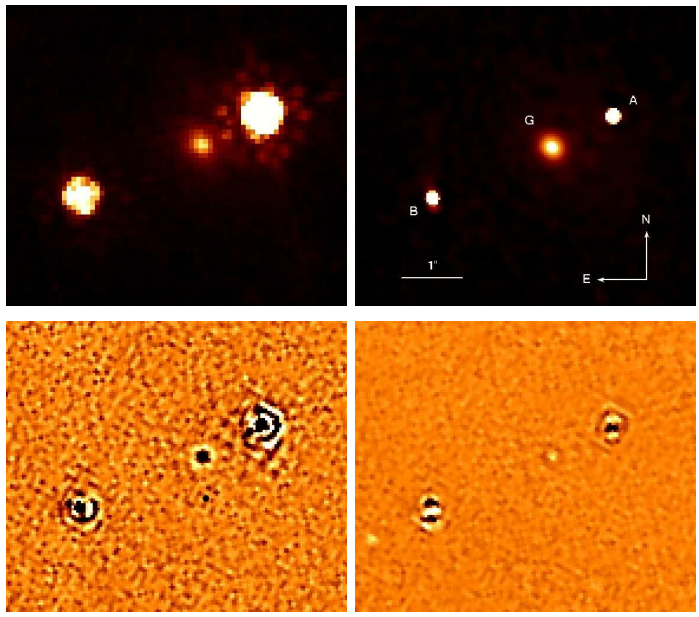

(e) HE 1104-1805

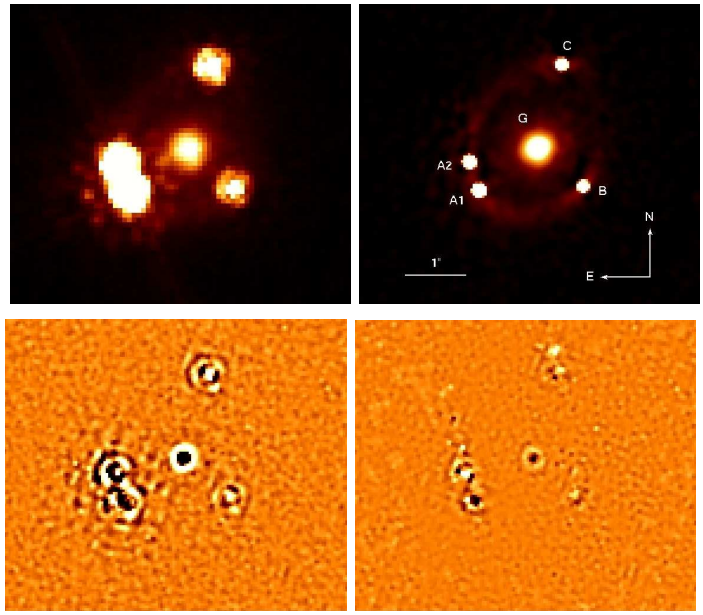

(f) PG 1115+080

Figure 13.1: continued.

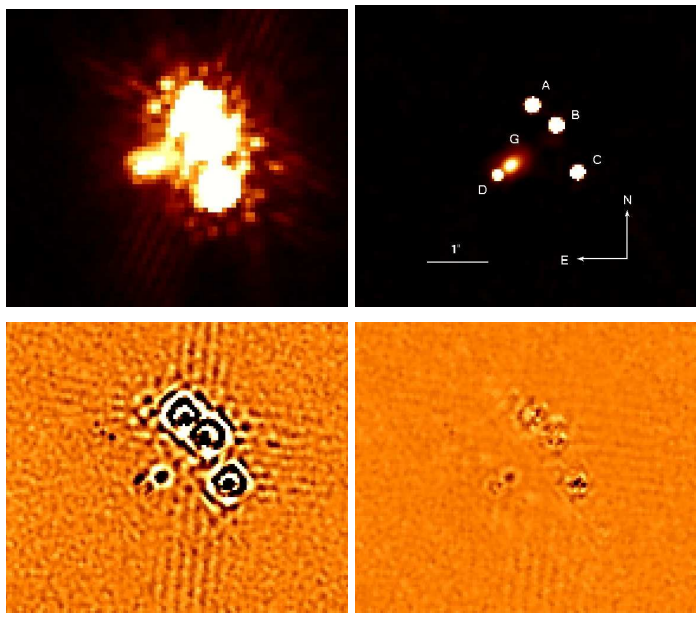

(g) JVAS B1422+231

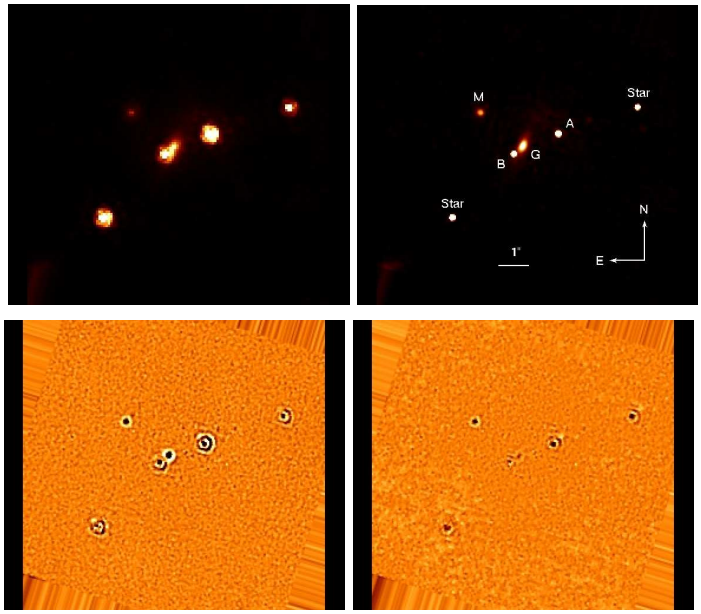

(h) SBS 1520+530

Figure 13.1: continued.

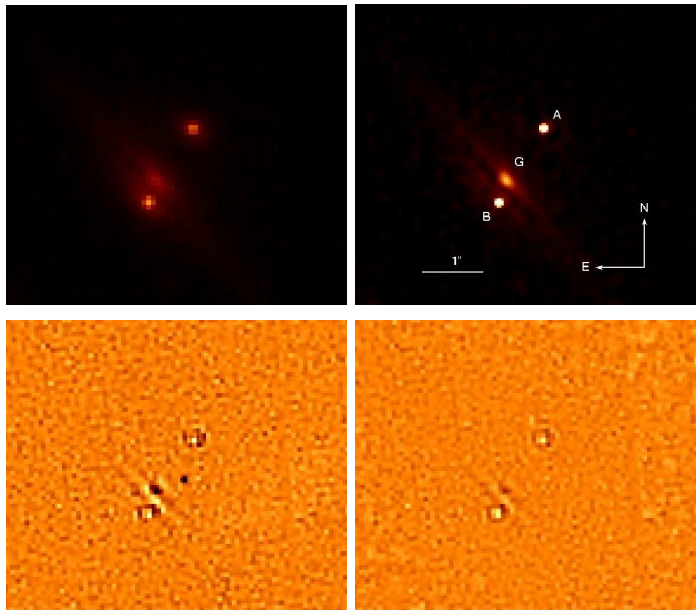

(i) CLASS B1600+434

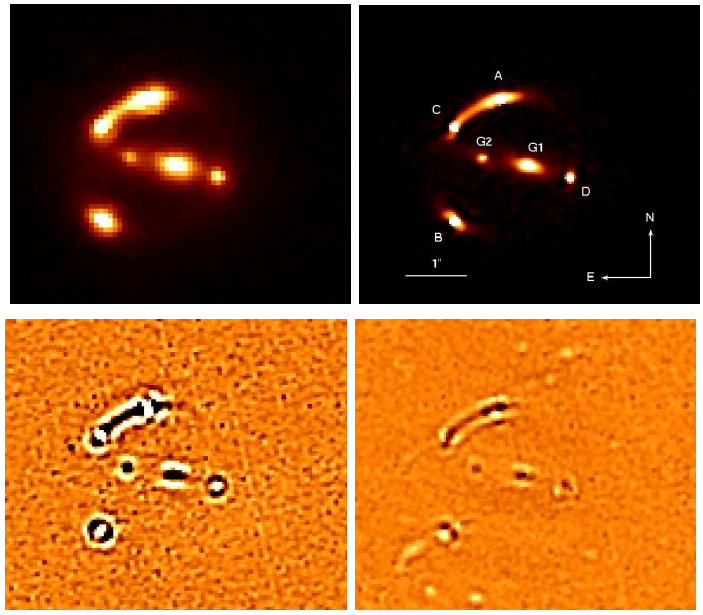

(j) CLASS B1608+656

Figure 13.1: continued.

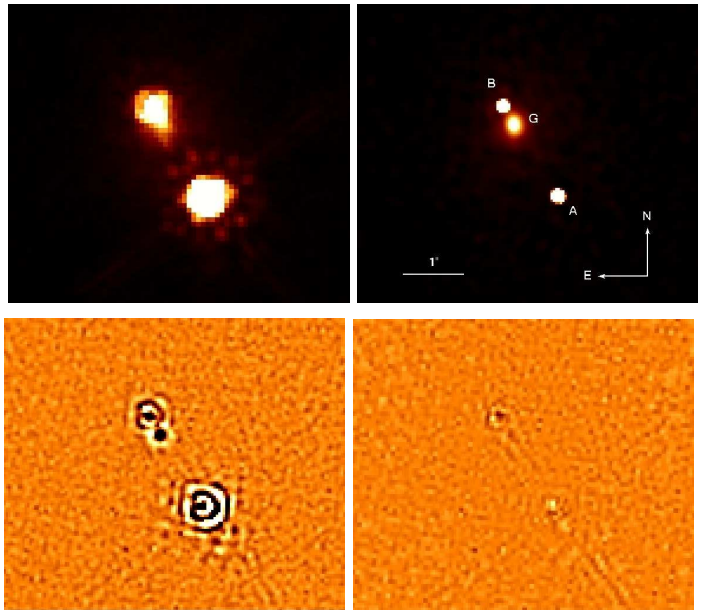

(k) HE 2149-274

Figure 13.1: continued.

HST/NIC1[1] images. The position we find is different from theirs by the following amount: ΔRA = 0.″02 and ΔDEC = 0.″03, though in agreement within their 0.″03 error bar. When only compared to their NIC2 results, the difference is the same in RA but larger in DEC (ΔDEC = 0.″05). It is also different from the centroid of the radio ring found by Patnaik et al. (1993): ΔRA = 0.″07 and ΔDEC = 0.″01. According to Lehár et al. (2000), both these positions are affected by systematics and are thus not reliable. The ellipticity we find for the bulge is in agreement with the one extracted from HST/ACS images by York et al. (2005). However, the spiral arms are not visible on our original images nor on the final deconvolved frame, while they appear on the ACS data.

- SBS 0909+532: We clearly detect the lensing galaxy, which is a first. But we are not in agreement with Lehár et al. (2000) who stated that this galaxy is likely to have a large effective radius and a low surface brightness. The lens we detect in the deconvolved frame has a small angular radius and is well fitted by a de Vaucouleurs model which favours the early-type nature of this galaxy. Moreover, we notice that, at a large distance from the core, the spikes of the PSF of the bright point sources, which not very well sampled (they have a FWHM of less than two pixels), appear in the background and on the residual map. This is because: (1) they are not accurately modeled by the Tiny Tim software, (2) we

[1] *NIC1* is the camera 1 of NICMOS.

did not attempt to correct the PSF at such distances, much larger than the extent of the whole lensed system.

- FBQS 0951+2635: The ellipticity we find with ISMCS is larger than the one found by Jakobsson et al. (2005). The latter is likely underestimated probably due to a too large smoothing parameter or an oversimplified PSF as they used the MCS deconvolution algorithm but not combined with an iterative strategy.
- CLASS B1600+434: The high blending between the lens and source B prevents from reaching the desired level of accuracy and the internal error is higher than the estimated total error for the right ascension of source B.

13.4 JVAS B1422+231 as a tool to test the level of accuracy reached by ISMCS

The maximum total errors presented in Table 13.3 (p. 198) are derived, as already mentioned, from a comparison between each object and the Cloverleaf. The total error on the point source positions of the latter was estimated through a comparison of relative positions obtained from two data sets, both acquired with HST/NIC2 but through two different filters and with two different orientations of the instrument. Here we test the accuracy in a completely independent way using JVAS B1422+231. Indeed, the latter was observed at radio wavelengths by Patnaik et al. (1999), which is expected to give more accurate results on positions as the sources are resolved. Table 13.4 gives the positions obtained from HST/NIC2 images treated with ISMCS and the positions obtained from radio data. Let us note that, compared to Table 13.3 or to the original paper of Patnaik et al. (1999), the reference image has been changed from B to C. Indeed, C is the least blended of the four images, B being blended with A and D with the lens. That way, we try to avoid any inaccuracy coming from a less than optimal reference position.

To estimate the error affecting our results, we calculate the distance between image C and every other lensed image for both sets of results. This is shown in the fourth column of Table 13.4. We then measure the difference between the same distances in both data sets. This is displayed in the top part of the last column in the same table. The mean of these differences is -0.72 mas while the scatter σ_{dist} around the mean is 2.6 mas. The latter represents the error affecting our results. It can be approximated as follows:

$$\sigma_{dist} \approx \sqrt{\sigma_{\mathrm{RA}}^2 + \sigma_{\mathrm{DEC}}^2}\,. \tag{13.1}$$

Assuming the uncertainty is identical in RA and DEC, we derive an error on the relative astrometry of:

$$\sigma_{\mathrm{RA}} \approx \sigma_{\mathrm{DEC}} \approx \frac{\sigma_{dist}}{\sqrt{2}} = 1.8 \text{ mas}. \tag{13.2}$$

This error of 1.8 mas is compatible with the 1.5 mas error derived from the comparison between JVAS B1422+231 and the Cloverleaf. Of course this estimation relies on certain hypotheses. First, the radio lobes of the unlensed quasars must be co-centered with the

	HST/NIC2			
Label	ΔRA (″)	ΔDEC (″)	Distance to C	≠ in distance
A	-0.7220 ± 0.0005	1.0685 ± 0.0004	1.28956	-0.00005
B	-0.3360 ± 0.0003	0.7516 ± 0.0005	0.82329	-0.00442
C	0.	0.	0.	0.
D	-1.2831 ± 0.0006	-0.0496 ± 0.0008	1.28406	0.00159
	Radio data (Patnaik et al., 1999)			
Label	ΔRA (″)	ΔDEC (″)	Distance to C	/
A	-0.72313 ± 0.00005	1.06769 ± 0.00005	1.28952	/
B	-0.33388 ± 0.00005	0.74771 ± 0.00005	0.81887	/
C	0.	0.	0.	/
D	-1.28453 ± 0.00005	-0.05444 ± 0.00005	1.28565	/

Table 13.4: Astrometry of the lensed images of JVAS B1422+231. *Top table:* results obtained with ISMCS applied to HST/NIC2 data. *Bottom table:* results obtained from radio data by Patnaik et al. (1999). *Left part*: astrometry of the point sources. *Right part*: calculations for the estimate of the error (see text for details). All of these values are expressed in arcseconds.

optical emission, which is not always true, even at such a distance. Then, the errors on the radio data must be negligible. They are indeed small, i.e. of the order of 0.05 mas, but not null. Thus, we can conclude that the estimation of the level of accuracy reached on the positional constraints by ISMCS from the analysis of the Cloverleaf is realistic.

13.5 Remeasured time delays

For our analysis we do not use the original time delays, which have been measured in a heterogeneous way. Instead, we use the delays remeasured by E. Eulaers. The method used to obtain them is a numerical one which bases are explained in Burud et al. (2001). In brief, the algorithm minimizes the difference between the data and a numerical light curve which is modeled with equally spaced points. This is done for a set of given time delays. Two parameters are adjusted during the process: the flux ratio between two light curves and a slope that accounts for slow linear microlensing variations. The best time delay is the one that minimizes the χ^2 between the model and the data points. The original version has been strongly improved regarding many different technical aspects. That will be detailed in Eulaers & et al. (in preparation) along with the different tests carried out on the already published light curves of our eleven lenses. Here we report some results obtained for four of the eleven lensed quasars in our sample, without any further explanation on the method. The resulting time delays as well as the reference of the light curves and the flux ratios are displayed in Table 13.5 on p. 200 and will be used in the next section to obtain H_0. The flux ratios were also extracted from the numerical method and are thus corrected from the effect of the time delay.

A few remarks can be made. First of all, the light curves of RX J0911.4+0551,

SBS 1520+530 and CLASS B1600+434 were made available online by Paraficz et al. (2006) in a numerical version. Then concerning RX J0911.4+0551, which is actually a quad, source A is the sum of sources A_1, A_2 and A_3. Indeed, those three lensed images are too close to allow a good separation of their flux contribution with ground-based data. But still we have to keep in mind that there is a short time delay between them. Moreover, the adopted convention is the following: $\Delta t_{AB} = t_A - t_B$, i.e. a negative time delay means that the flux of A varies before the one of B, i.e. A is the leading lensed image.

With this new method, we obtain time delays in agreement with previously obtained ones, within the published error bars as ours are smaller, as shown in Table 13.5.

The re-analysis of the light curve of two more systems, FBQS J0951+2635 and HE 2149-2745, reveals that the published time delays are not very robust. First, when we apply the numerical method to the light curves of FBQS J0951+2635 published by Jakobsson et al. (2005), we notice that in removing some suspicious points from the curves, the delay changes significantly depending on the removed points. As the results are not stable, we prefer not to draw any conclusion on this object. The case of HE 2149-2745 is a bit different. Indeed, when the time delay is applied to the light curves of Burud et al. (2002a), the overlapping part contains only a few points, with no sharp structure. As a consequence, we also prefer not to rely on these curves.

All of these statements will be detailed and illustrated in Eulaers & et al. (in preparation) along with the study of the already published light curves of the five remaining lensed quasars in the sample, i.e. JVAS B0218+357, SBS 0909+532, PG 1115+080, JVAS B1422+231 and CLASS B1608+656.

13.6 The Hubble constant

The aim is to derive H_0 from all the lenses of our sample with reliable time delay. However, this section concerns only the four lensed quasars of the sample for which the time delay has already been remeasured: RX J0911.4+0551, HE 1104-1805, SBS 1520+530 and CLASS B1600+434.

13.6.1 Parametric modeling

We model the gravitational potential creating the observed configuration with the version 1.99m of the LENSMODEL software (Keeton, 2001b). Our approach is exactly the same as the one described in Sect. 12.5 (p. 165). We first model our systems with a singular isothermal model, i.e. a SIS for the doubles as we do not have enough constraints to introduce an ellipticity, and a SIE for the quads. Then we model our systems with a constant mass-to-light ratio profile, i.e. a de Vaucouleurs model in the case of an early-type lens galaxy or an exponential disk for a late-type lens galaxy. We also include an external shear in both cases as a galaxy is rarely isolated. Finally, we introduce the remeasured time delay in the modeling to obtain an estimate of the Hubble constant. Let us note that all the models are computed for a flat universe with the following cosmological parameters: $\Omega_m = 0.3$ and $\Omega_\lambda = 0.7$.

The constraints we use are the following: the astrometry of the sources (with the MTE, i.e. the maximum total error displayed in the fifth column of Table 13.3) and main lens (with, in the case of a diffuse object, the error inherent to the deconvolution as it is larger than the MTE) and finally the time delay(s) of Table 13.5 to derive H_0, each delay accounting for one constraint and H_0 for one parameter. In the case of RX J0911.4+0551, we increase the error bar on the time delay to 5% of the delay itself, i.e. ≈ 7 days. Indeed, it was measured from the sum of the flux of three blended images. So this value is a weighted mean of three delays that could differ from each other by a few days. And for SBS 1520+530, we use the redshift of the lens measured by Auger et al. (2008).

For quads, we thus have enough constraints with the positions of the point sources (8) and the lens (2), plus the time delays (1 to 3 additional constraints) when trying to get H_0. As a consequence we do not use the flux ratios: they are likely contaminated e.g. by differential extinction by the lens galaxy. As doubles are underconstrained (4 constraints from the image positions, 2 from the lens position and 1 from the time delay when H_0 is set free, for a total of 7), it is necessary to use the flux ratios (2 more constraints for a total of 9). We thus use the ones measured by the numerical method applied to obtain the time delays. Indeed, these flux ratios are corrected from the effect of the intrinsic variability of the quasar which, combined with the time delay, introduces an error in the estimation of the flux ratio. To some extent, they are also corrected from long-term microlensing thanks to a linear variation (one per season) with a slope adjusted by the program when minimizing the χ^2. However, these ratios are not corrected from the differential extinction produced by dust in the lensing galaxy or the total extinction from the host galaxy of the quasar itself. As a consequence, we increase the error bars up to 5% of the measured ratio.

The results are listed in Table 13.6 on p. 200. The first column gives the name of the object, the second gives the type of mass distribution used in LENSMODEL, the third gives the mass scale parameter (Einstein radius R_{Ein} in arcseconds), the fourth gives the ellipticity e and the position angle θ_e in degrees positive East of North, the fifth column shows the value of the effective radius R_{eff} in the case of a de Vaucouleurs model and the scale length R_d in the case of an exponential light profile, column number 6 gives the intensity of the shear γ and its position angle θ_γ in degrees positive East of North, the next column gives the number of degree(s) of freedom (d.o.f.), the χ^2 of the fit is given in column number 8 while the last one gives $h = H_0/100$ km/s/Mpc. "DV" stands for *de Vaucouleurs light profile* and "EXP" for *exponential light profile*.

13.6.2 Discussion

The two mass distributions at stake here, i.e. the isothermal profile and the distribution with a constant mass-to-light ratio, are profiles with the most extreme slopes at the location of the lensed images (Kochanek, 2002; Kochanek & Schechter, 2004). They thus lead to extreme values of the Hubble constant, which allows to set a lower limit and an upper limit on it and draw conclusions about the most likely distribution when comparing the results to one of the most popular values: $H_0 = 72 \pm 8$ km/s/Mpc (HST Key Project, Freedman et al., 2001). However, let us note that the isothermal profile is

favoured by many results obtained, e.g., by the *Sloan Lens ACS Survey* (SLACS, Bolton et al., 2006) team on galaxy-galaxy lensing as shown per example by Barnabè et al. (2009): they studied a sample of six galaxies and showed that they are all well described by a power-law profile with a logarithmic slope close to isothermal, i.e. $\gamma = 1.98 \pm 0.05$ with an intrinsic scatter of around 5%.

As in the previous chapter (see Sect. 12.6, p. 167), we cannot reproduce the configuration of a quadruply imaged quasar with such simple models. Indeed, for the object RX J0911.4+0551, the χ^2 is too high to rely on the result. Apparently there are different reasons: the positions of the lensed images are not very well reproduced, nor are the constraints from the light distribution in the case of a de Vaucouleurs profile. To obtain a reliable result we have to relax the constraints on the positions of the lensed images and increase the error bar by a factor 10, i.e. the error becomes $0\farcs02$. That could be the sign of the presence of substructures in the lensing galaxy. For the position of the lens galaxy we have to increase the error by a factor 7 to reach a reduced χ^2 of around 1. In that case the error is thus equal to $0\farcs028$, which corresponds to a mismatch between the light distribution and the mass distribution of around $285 \times h$ pc, i.e. 200 pc with $h = 0.70$. This offset is not in agreement with the values found by Yoo et al. (2006) for four quads, not even with the upper limit of 70 pc derived for B1938+666. As a consequence, this anomaly we observe can probably not be explained by an offset between the centroids of the light and mass distributions or, at least, not completely explained by that phenomenon.

The three doubles can be reproduced with both mass distributions. But two amongst the three systems, HE 1104-1805 and SBS 1520+530, require a high shear ($\gamma > 0.1$). According to Lehár et al. (2000), the configuration of HE 1104-1805 is not possible to reproduce unless a large external shear, which is suggested by the large separation of the images ($3\farcs20$ according to our astrometry), or a high misalignment between mass and light is included. In the case of SBS 1520+530, the lensing galaxy lies in a cluster (Faure et al., 2002) and is surrounded by at least two nearby galaxies. One of them is labeled M on our deconvolved image (see Fig 13.1), and the other one is not observable on this frame but is located South-East of the system, in the direction defined by images A and B. According to Faure et al. (2002), they are located at the same redshift as the lens and play a significant role in the modeling. That explains the need of a large external shear when not taking these galaxies directly into account in the modeling.

If we do not take the case of RX J0911.4+0551 into account in our attempt to estimate the Hubble constant, we have a sample of three doubly lensed quasars to try and derive some statistics on H_0. It is clearly not enough but hopefully, more results will come as we are still at the beginning of this study. In the isothermal case we obtain a mean value of $H_0 = 59.1 \pm 11.7$ km/s/Mpc and with the constant M/L profile we obtain a mean value of $H_0 = 85.9 \pm 15.5$ km/s/Mpc. The quoted error is the standard deviation of the mean. The dispersion of the measurements is large and both measures stand on each side of the value of $H_0 = 72 \pm 8$ km/s/Mpc (Freedman et al., 2001). This high dispersion could be explained in investigating several hypotheses: the mass-sheet degeneracy (Falco et al., 1985, see Sect. 4.8 on p. 44) through the influence of the environment not well accounted for (under or overestimated) or the difference between the real mass slope of the lens and the slope used in the profile. Let us note that

HE 1104-1805 leads to the highest estimates of H_0, as already noticed e.g. by Kochanek & Schechter (2004). The reasons are quite obscure and are worth being investigated in a future study. It could come from an anomalously high tidal shear field suggested by the fact that the brightest image is the inner one. Concerning the two other systems, we notice that the isothermal profile leads to a low value of H_0, i.e. 51.1 km/s/Mpc and 43.9 km/s/Mpc respectively for SBS 1520+530 and CLASS B1600+434, while the profile with a constant mass-to-light ratio leads to values closer to the one obtained by Freedman et al. (2001), i.e. 65.0 km/s/Mpc for SBS 1520+530 and 76.6 km/s/Mpc in the case of CLASS B1600+434. That behaviour has already been observed several times in doubly lensed quasars, e.g. by Kochanek & Schechter (2004). It suggests that the mass distribution of galaxies is more likely to have a constant-mass-to-light ratio, which is not in agreement with results obtained, e.g., by the SLACS team on the isothermality of galaxies, as already explained above.

To model the doubly imaged quasars, we use flux ratios corrected from the time delay combined with the intrinsic variability and from long-term microlensing effects. Falco et al. (1999) measured the flux ratios of our three systems amongst others (see Table 13.7) and corrected them from the differential extinction produced by dust in the lensing galaxy and the total extinction from the host galaxy of the quasar itself but not from microlensing effects and intrinsic variabilities. To study the effect of the choice of one type of correction instead of the other, we also model the three doubly imaged quasars with the extinction-corrected flux ratios. That allows to estimate the error on H_0 introduced because of the non-correction from the extinction: less than 5% for SBS 1520+530 and HE 1104-1805. However, for CLASS B1600+434, it could reach 10% which is not surprising given that the lensing galaxy of this system is a spiral, thus likely to strongly affect the lensed images of the quasar in terms of extinction, as shown by the difference between our flux ratio and the one from Falco et al. (1999).

Object	Label	Flux ratios
(e) HE 1104-1805	A	1.
	B	0.29 ± 0.01
(h) SBS 1520+530	A	1.
	B	0.42 ± 0.01
(i) CLASS B1600+434	A	1.
	B	0.92 ± 0.07

Table 13.7: Extinction-corrected flux ratios for the three doubly lensed quasars of our subsample (Falco et al., 1999): (e) HE 1104-1805, (h) SBS 1520+530 and (i) CLASS B1600+434. They are corrected from the differential extinction produced by dust in the lensing galaxy and from extintion by the host galaxy of the lensed quasar. Flux of image A is the reference flux which induces a ratio of 1.

We can also take the case of RX J0911.4+0551 into account in the estimation of the Hubble constant. Indeed, if the high χ^2 is mostly due to substructure lensing not accounted for, the value of H_0 will not be very affected by its inclusion in the modeling, the time delay being perturbed by only some fraction of a day (Keeton & Moustakas,

2009). On the contrary if the high χ^2 is due to a mismatch between the centroid of mass and light distributions, the values of H_0 derived from RX J0911.4+0551 with the two simple mass models are not reliable. Taking the four systems into account, we obtain a mean value of $H_0 = 66.95 \pm 11.4$ km/s/Mpc in the isothermal case and of $H_0 = 93.3 \pm 13.2$ km/s/Mpc with the constant M/L. The quoted error is the standard deviation of the mean: the scatter of the values is large. It suggests that we are facing a variety of lens galaxies which can differ from each other e.g. by the slope of their mass distribution, by their environment (more or less complicated, presence of close neighbours, ...). At this stage, it is not possible to derive definite conclusions: more lenses should be included.

13.7 Prospective application to substructure studies

Sects. 12.6 and 13.6.2 show that substructure lensing might play a role in certain systems, particularly in the quadruply imaged ones as the doubles are underconstrained. We thus briefly introduce this topic in this section. We focus on the work achieved by Keeton (2009). Indeed, it offers an interesting track to study substructures in lensing galaxies through their effect on observables.

The Λ-CDM cosmological model (see Sect. 2.4 on p. 18) is currently the most popular one. It has been successful in describing the Universe on large scales and in explaining many observational results. Still it fails to reproduce observations on small scales. This is especially true when it comes to dark matter distribution in galactic haloes and the predicted number of satellites which is larger than the observed one. That is why the latter issue is called the *Missing Satellite Problem*. In the Λ-CDM paradigm, the dark matter halo of a galaxy is composed of a certain amount of low mass subhalos, also called *substructures* or *clumps*. Whether or not they are traced by luminous components such as stars is not known yet. That is why gravitational lensing constitutes a powerful tool to probe substructures. Indeed, we know that these dark matter clumps can perturb the configuration of, for example, a lensed quasar. There are different signatures of their presence: perturbations in the time delays (see e.g. Morgan et al., 2006; Keeton & Moustakas, 2009), in positions (see e.g. Chen et al., 2007) or anomalous flux ratios in quads (see e.g. Kochanek & Dalal, 2004; Chiba et al., 2005). They can also be detected with radio interferometry as the lensed images are resolved into milli-images (see e.g. Biggs et al., 2004). With these various signatures, it would be possible to obtain constraints about dark matter such as a measurement of the mean density of the clumps, their mass function and spatial distribution.

The aim of Keeton (2009) is to study populations of substructures in terms of mass function and spatial distribution to see how the different observables, i.e. flux ratios, positions and time delays, are affected by these physical properties in terms of probability distributions. The formalism he uses is stochastic lensing with the masses and positions of the clumps as random parameters. These variables are not random at all but the formation scenario is so complicated that this simplification seems reasonable. Moreover, he assumes that all the clumps are independent and identically distributed. He considers them as point masses, which is applicable for all spherical clumps that do

not overlap the line of sight. He also considers two subgroups of clumps, while projected on the image plane: the ones close to the lensed images (local effects) and the ones located far away from the lensed images (long-range effects). As spatial distribution he uses a power law with variable index and as mass function, a fiducial model that we will not detail here. Each clump is represented by a position and a scaled mass. It is then possible to compute statistical properties of lensing observables.

According to him, the shear is dominated by local effects, except when it is small, and is insensitive to the mass function. For the deflection, the local and long-range effects have the same importance. For a uniform spatial distribution, it is essentially dependent on the mass function through m_{eff}, a characteristic clump mass scale that is expressed as follows:

$$m_{eff} = \frac{<m^2>}{<m>}. \tag{13.3}$$

The potential is independent of local effects and depend on long-range effects also through m_{eff}.

To test different spatial distributions, he changes the power law index: the local effects are insensitive while the long-range effects are highly sensitive to it. So the shear is stable regarding the index while the deflection is not. The potential is even more dependent on the index as it is dominated by non-local effects.

Let us now review the directly observable quantities: flux ratios, positions and time delays. The flux ratios are more sensitive to local effects. The positions are mainly dependent on m_{eff}. They also have contributions from local and global populations. Time delays are also mainly sensitive to m_{eff} but influenced by global effects.

A generalization of this theory is needed for spatially extended clumps, arbitrary spatial distributions and mass functions. It is also necessary to join the two different regimes, i.e. clumps far away from the lensed images and clumps close to the lensed images, with a complete theory applicable at intermediate distances. In conclusion there is much work left to do but the study in its actual state already leads to several qualitatively interesting results.

From there, an observational analysis is needed to obtain further constraints on the clump populations. That is why our sample of eleven lensed quasars is very interesting in terms of positional constraints, considering our mas accuracy. A new version of the LENSMODEL software (Keeton, 2001b) is currently being developed by the team of Keeton in order to obtain an algorithm capable of testing various populations of clumps and thus of probing substructures in lensing galaxies, the aim still being to reproduce the observed configuration. Hopefully our sample can be used to try and obtain new constraints about clump populations.

Object	Label	θ_e (°)	e	a_{eff} ($''$)	b_{eff} ($''$)	R_{eff} ($''$)
(a) JVAS B0218+357	G	129.4 ± 13.2	0.05 ± 0.01	0.31 ± 0.01	0.29 ± 0.01	0.30 ± 0.01
(b) SBS 0909+532	G	131.87 ± 16.95	0.11 ± 0.08	0.57 ± 0.06	0.51 ± 0.04	0.54 ± 0.02
(c) RX J0911.4+0551	G	110.0 ± 4.8	0.11 ± 0.01	1.08 ± 0.01	0.97 ± 0.01	1.02 ± 0.01
(d) FBQS J0951+2635	G	11.1 ± 1.6	0.52 ± 0.02	1.10 ± 0.02	0.62 ± 0.01	0.83 ± 0.01
(e) HE 1104-1805	G	49.0 ± 1.9	0.13 ± 0.01	1.38 ± 0.02	1.21 ± 0.01	1.30 ± 0.01
(f) PG 1115+080	G	112.2 ± 0.6	0.04 ± 0.01	0.93 ± 0.01	0.90 ± 0.01	0.91 ± 0.01
(g) JVAS B1422+231	G	121.1 ± 0.8	0.39 ± 0.02	0.51 ± 0.02	0.33 ± 0.02	0.41 ± 0.02
(h) SBS 1520+530	G	153.1 ± 0.9	0.49 ± 0.02	0.99 ± 0.05	0.58 ± 0.01	0.76 ± 0.02
(i) CLASS B1600+434	G	36.9 ± 2.3	0.75 ± 0.08	0.46 ± 0.01	0.18 ± 0.02	0.29 ± 0.01
(j) CLASS B1608+656	G_1	73.5 ± 0.4	0.45 ± 0.01	1.93 ± 0.01	1.18 ± 0.01	1.51 ± 0.01
	G_2	98.9 ± 0.2	0.55 ± 0.01	1.41 ± 0.01	0.76 ± 0.01	1.04 ± 0.01
(k) HE 2149-2745	G	0.9 ± 7.7	0.27 ± 0.01	1.36 ± 0.03	1.03 ± 0.02	1.18 ± 0.02

Table 13.2: Measured shape parameters for the lensing galaxies respectively of (a) JVAS B0218+357, (b) SBS 0909+532, (c) RX J0911.4+0551, (d) FBQS J0951+2635, (e) HE 1104-1805, (f) PG 1115+080, (g) JVAS B1422+231, (h) SBS 1520+530, (i) CLASS B1600+434, (j) CLASS B1608+656 and (k) HE 2149-2745. The columns present the name of the object, the label of the galaxy, the position angle, or PA, of the semi-major axis in degrees positive East of North, the ellipticity e ($e = 1 - b/a$), the effective semi-major axis (a_{eff}), the effective semi-minor axis (b_{eff}) and finally, the effective radius (R_{eff}), the three of them being expressed in arcseconds. Each measurement is accompanied by its $\pm 1\sigma$ internal error bars.

Object	Label	ΔRA (″)	ΔDEC (″)	MTE (mas)	Magnitude	Flux ratio
(a) JVAS B0218+357	A	0.	0.	0.5	17.49 ± 0.04	1.
	B	0.3075 ± 0.0011	0.1264 ± 0.0013	0.5	16.92 ± 0.02	1.646 ± 0.114
	G	0.1975 ± 0.0173	0.0972± 0.0038	0.5	18.11 ± 0.03	/
(b) SBS 0909+532	A	0.	0.	1.0	14.53 ± 0.01	1.
	B	0.9868 ± 0.0004	-0.4973 ± 0.0008	1.0	14.67 ± 0.01	0.885 ± 0.014
	G	0.4640 ± 0.0023	-0.0550 ± 0.0037	1.0	19.44 ± 0.1	/
(c) RX J0911.4+0551	A_1	0.	0.	2.0	17.52 ± 0.01	1.
	A_2	0.2611 ± 0.0009	0.4069 ± 0.0010	2.0	17.58 ± 0.01	0.950 ± 0.008
	A_3	-0.0158 ± 0.0009	0.9575 ± 0.0008	2.0	18.27 ± 0.01	0.513 ± 0.005
	B	-2.9681 ± 0.0013	0.7924 ± 0.0006	2.0	18.60 ± 0.02	0.372 ± 0.004
	G	-0.7019 ± 0.0019	0.5020 ± 0.0039	2.0	18.16 ± 0.06	/
(d) FBQS J0951+2635	A	0.	0.	1.0	15.54 ± 0.01	1.
	B	0.8978 ± 0.0003	-0.6339 ± 0.0007	1.0	16.91 ± 0.02	0.286 ± 0.006
	G	0.7571 ± 0.0052	-0.4512 ± 0.0053	1.0	17.34 ± 0.01	/
(e) HE 1104-1805	A	0.	0.	2.0	15.52 ± 0.01	1.
	B	2.9025 ± 0.0009	-1.3376 ± 0.0028	2.0	16.97 ± 0.03	0.262 ± 0.009
	G	0.9752 ± 0.0030	-0.5071 ± 0.0033	2.0	17.71 ± 0.04	/
(f) PG 1115+080	C	0.	0.	2.0	17.11 ± 0.01	0.255 ± 0.005
	A_1	1.3283 ± 0.0002	-2.0338 ± 0.0015	2.0	15.64 ± 0.02	1.
	A_2	1.4770 ± 0.0032	-1.5759 ± 0.0011	2.0	16.09 ± 0.01	0.659 ± 0.007
	B	-0.3402 ± 0.0007	-1.9596 ± 0.0008	2.0	17.58 ± 0.01	0.165 ± 0.002
	G	0.3799 ± 0.0028	-1.3455 ± 0.0041	2.0	16.96 ± 0.01	/

Table 13.3: Relative position, maximum total error ("MTE"), magnitudes and flux ratios of the lensed images and lensing galaxy respectively for (a) JVAS B0218+357, (b) SBS 0909+532, (c) RX J0911.4+0551, (d) FBQS J0951+2635, (e) HE 1104-1805, (f) PG 1115+080, (g) JVAS B1422+231, (h) SBS 1520+530, (i) CLASS B1600+434, (j) CLASS B1608+656 and (k) HE 2149-2745. See Fig. 13.1 for the labels. The luminosity of the galaxies is measured in an aperture equal to the effective radius, R_{eff}, given in Table 13.2. The $\pm 1\sigma$ error bars shown along the results are internal to the deconvolution process. This table continues on the next page.

Object	Label	ΔRA (″)	ΔDEC (″)	MTE (mas)	Magnitude	Flux ratio
(g) JVAS B1422+231	A	0.3860 ± 0.0004	0.3169 ± 0.0003	1.5	14.35 ± 0.01	1.
	B	0.	0.	1.5	14.23 ± 0.01	1.116 ± 0.003
	C	-0.3360 ± 0.0003	-0.7516 ± 0.0005	1.5	14.92 ± 0.01	0.590 ± 0.002
	D	0.9470 ± 0.0006	-0.8012 ± 0.0005	1.5	18.11 ± 0.02	0.032 ± 0.001
	G	0.7321 ± 0.0037	-0.6390 ± 0.0054	1.5	17.85 ± 0.05	/
(h) SBS 1520+530	A	0.	0.	1.0	17.15 ± 0.01	1.
	B	1.4276 ± 0.0005	-0.6536 ± 0.0004	1.0	17.96 ± 0.01	0.481 ± 0.005
	G	1.1418 ± 0.0015	-0.3874 ± 0.0018	1.0	18.11 ± 0.02	/
(i) CLASS B1600+434	A	0.	0.	1.0	19.98 ± 0.03	1.
	B	0.7300 ± 0.0024	-1.1891± 0.0006	1.0	20.22 ± 0.07	0.897 ± 0.056
	G	0.6044 ± 0.0040	-0.8444 ± 0.0041	1.0	18.97 ± 0.14	/
(j) CLASS B1608+656	A	0.	0.	1.5	18.37 ± 0.07	1.086 ± 0.056
	B	0.7464 ± 0.0026	-1.9578 ± 0.0026	1.5	18.66 ± 0.09	1.
	C	0.7483 ± 0.0038	-0.4465 ± 0.0033	1.5	18.90 ± 0.07	0.855 ± 0.021
	D	-1.1181 ± 0.0025	-1.2527 ± 0.0018	1.5	19.50 ± 0.04	0.418 ± 0.024
	G_1	-0.4561 ± 0.0061	-1.0647 ± 0.0037	1.5	16.85 ± 0.01	/
	G_2	0.2821 ± 0.0015	-0.9359 ± 0.0023	1.5	17.29 ± 0.01	/
(k) HE 2149-2745	A	0.	0.	1.0	15.60 ± 0.01	1.
	B	0.8906 ± 0.0008	1.4459 ± 0.0001	1.0	17.21 ± 0.01	0.233 ± 0.002
	G	0.7188 ± 0.0042	1.1451 ± 0.0058	1.0	17.57 ± 0.03	/

Table 13.3: continued.

Object	Reference of the light curves	Δt_{AB} (days)	New Δt_{AB} (days)	f_B/f_A
RX J0911.4+0551	Hjorth et al. (2002)	146 ± 8	150 ± 3	not used
HE 1104-1805	Wyrzykowski et al. (2003)	157 ± 10	157 ± 1	$0.22 \pm 0.7\ 10^{-3}$
SBS 1520+530	Burud et al. (2002b)	-130 ± 3	-127 ± 2	$0.53 \pm 2.2\ 10^{-3}$
CLASS B1600+434	Burud et al. (2000)	-51 ± 4	-47 ± 1	$0.58 \pm 9.2\ 10^{-3}$

Table 13.5: Time delays for four lensed quasars of our sample. They were obtained with a revised version of the method of Burud et al. (2001) which will be detailed in Eulaers & et al. (in preparation). The convention is the following: $\Delta t_{AB} = t_A - t_B$. *From left to right:* name of the object, publication from which the light curves were retrieved, related published time delay, remeasured time delay and corresponding flux ratio.

Object	Model	R_{Ein}	e,θ_e	R_{eff} or R_d	γ, θ_γ	d.o.f.	χ^2	h
(c) RX J0911.4+0551	SIE+γ	1.11	0.26, 139.07	/	0.33, 12.36	2	182	0.906
	DV+γ	1.06	0.21, 128.33	1.02	0.45, 7.89	3	342	1.154
(e) HE 1104-1805	SIS+γ	1.37	/	/	0.14, 22.79	0	0.0	0.822
	DV+γ	1.36	0.13, 49.07	1.30	0.19, 19.98	0	0.0	1.161
(h) SBS 1520+530	SIS+γ	0.73	/	/	0.14, 2.04	0	0.0	0.511
	DV+γ	0.62	0.49, 153.08	0.76	0.26, 22.27	0	0.0	0.650
(i) CLASS B1600+434	SIS+γ	0.66	/	/	0.10, 38.75	0	0.0	0.439
	EXP+γ	0.63	0.75, 36.93	0.17	0.09, 64.02	0	0.0	0.766

Table 13.6: Results of the parametric modeling respectively for: (c) RX J0911.4+0551, (e) HE 1104-1805, (h) SBS 1520+530 and (i) CLASS B1600+434. See text for details.

Part V

Conclusions and appendices

Little by little, one travels far.
J. R. R. Tolkien (1892 - 1973)

14 Conclusions and perspectives

This thesis has been realized in the framework of the COSMOGRAIL collaboration. Let us recall that COSMOGRAIL stands for *COSmological MOnitoring of GRAvItational Lenses* and gathers astrophysicists from five different countries with a common aim: the measurement of time delays for approximately 30 multiply lensed quasars in order to derive the Hubble constant H_0 and to obtain constraints on the mass distribution in lensing galaxies.

14.1 Data analysis tools

Departing from the semi-automated reduction pipeline developed by Vuissoz (2008), we elaborated a revised version to adapt it to Mercator data, which had never been done before in the COSMOGRAIL collaboration, to update the algorithm of PSF determination and to include a new way of estimating, more realistically, the error bars on the points of the light curves.

Moreover, we developed a new image processing method, which combines an iterative strategy with the MCS deconvolution algorithm. It is called *ISMCS* and it allows to simultaneously determine the PSF of an image and to deconvolve it. It is applicable to images which contain at least two point sources so that the algorithm can separate the contributions of possible diffuse components from the point sources, i.e. the instrumental profile itself.

This technique is particularly well suited to the analysis of multiply imaged quasars: it allows the detection of extended structures such as lensing galaxies, arcs or rings. Moreover it provides accurate astrometry and photometry of the multiple images and of the lensing galaxy, which is very important to model the mass distribution of the lens. This technique was successfully tested on HST/NIC2 images of the quadruply lensed quasar H1413+117 (the Cloverleaf). The internal error on the point source positions, including the random error and the ones inherent to the deconvolution, is of the order

of 0.4 milliarcsecond (mas). When comparing the astrometry coming from two different sets of images, we estimated a total error of the order of 1 mas. It probably finds its origin in an incomplete correction of the geometric distortions. Moreover, we detected the angularly small lensing galaxy and measured its position with an accuracy of 20 mas. We also discovered a partial Einstein ring, which could allow to constrain the deflection model and, through an inversion of the lens equation, to estimate the light distribution in the quasar host galaxy and narrow line region.

14.2 Light curves for two gravitational lenses from the COSMOGRAIL sample

We have applied the modified semi-automated reduction pipeline to HE0435-1223, a quadruply imaged quasar, to obtain its light curves over a period of around four years. The aim was to obtain more reliable time delays than previously done by Kochanek & Schechter (2004), which is very challenging considering the short delays involved. Indeed, a numerical fit of the light curves showed that, according to the chosen data set, the measured delays differ. The final error bars will thus be large relative to the short delays involved, which does not make of HE 0435-1223 a good candidate to obtain the Hubble constant with an accuracy that could compete with standard techniques. We have also applied ISMCS to this object to obtain accurate constraints. The rest of the work, such as the acquisition of additional constraints for the main lens or the mass modeling, is now in the hand of other members of the collaboration. All of these studies, along with the light curves and the application of ISMCS, will figure in the following paper: Chantry & et al. (in preparation).

WFI J2026-1223 is a quadruply imaged quasar that had never been studied before apart in the discovery paper (Morgan et al., 2004). As it was followed by the Euler telescope, we decided to apply the revised semi-automated reduction pipeline to obtain light curves for the four lensed images. This work was carried out by G. Orban de Xivry under my supervision. Two images being highly blended, we summed their flux contribution into one virtual lensed image. However, the quasar does not show sharp variations, which was completely unexpected given the preliminary light curve. Moreover, one lensed image is too faint. As a consequence, WFI J2026-1223 does not seem to be an ideal candidate for H_0, also because we still lack a redshift for the lens. Maybe data with a higher signal-to-noise ratio could allow for the measurement of the time delays.

We can see that obtaining good light curves from a monitoring campaign is far from being easy. We never know if the object is going to show sharp structures to ease the determination of the time delay. Still, it is important to continue that work, in order to increase the number of lensed quasars with measured time delays leading either to a determination of H_0 with higher accuracy or to constraints on the dark matter distribution in lens galaxies.

14.3 Observational constraints and modeling

ISMCS has been applied to WFI J2033-4723 in the framework of a COSMOGRAIL paper as a step towards the measurement of H_0. The maximum internal error on the position of the point sources amounts to 0.5 mas. Thanks to a comparison with the Cloverleaf, we estimated the total error to 2 mas. We also highlighted the main lensing galaxy and introduced a de Vaucouleurs profile in the deconvolution to account for its light distribution, which brought further constraints as the PA and ellipticity that were then used in the modeling. We also detected a faint and relatively flat diffuse structure encircling the four images and the lens. That component remains quite mysterious for the moment: further investigations are necessary to clarify its nature.

A sample of seven lensed quasars chosen amongst the COSMOGRAIL objects has then been studied with ISMCS. As usual, it allowed us to obtain constraints on the point source positions, with an accuracy of around 1 to 2 mas, and lensing galaxies. For two lensed systems, we have detected an Einstein ring: the double HE 0047-1756 and the quadruple SDSS J1138+0314. We then applied the LENSMODEL software (Keeton, 2001b) to these systems to obtain simple mass models using two different profiles, an isothermal and a de Vaucouleurs, and to estimate the time delays. In the case of doubles, both mass profiles can reproduce the observed configuration, even if a high external tidal shear is required in some systems. In the case of quads, a good fit is obtained for SDSS J1138+0314 but not for RX J1131-1231 and WFI J2026-4536. More complicated models, e.g. with substructures or companion galaxies, are probably needed to reproduce their configuration. The next step for these seven lensed quasars is the acquisition of light curves and time delays to allow the measurement of the Hubble constant if the lens redshift is known, which is not yet the case for two of these seven lensed quasars.

The last sample studied is composed of eleven gravitationally lensed quasars with published time delays. Here again we applied ISMCS to these systems and obtained very accurate positional constraints for the lensed images and the main lens as well as shape parameters for the latter. In comparing the radio results for B1422+231 (Patnaik et al., 1999) with ours obtained thanks to ISMCS, we estimated a maximum error of 1.8 mas which is not fr from the 1.05 mas estimated in comparing this object to the Cloverleaf. The estimation of the level of accuracy reached on the positional constraints by ISMCS from the analysis of the Cloverleaf is thus realistic and reliable. For four objects, the delays were remeasured on already published light curves. The LENSMODEL software was then applied to obtain the Hubble constant. Two different simple mass models were used: first an isothermal one and second a profile with a constant mass-to-light ratio (de Vaucouleurs for early-type lens galaxies and exponential for late-type lens galaxies). In the case of doubles, i.e. HE 1104-1805, SBS 1520+530 and CLASS B1600+434, both mass profiles can reproduce the observed configuration, while in the case of the quad RX J0911.4+0551, both mass profiles fail to reproduce the observed configuration with a reasonable χ^2. Without taking RX J0911.4+0551 into account, we obtained a mean of $H_0 = 59.1 \pm 11.7$ km/s/Mpc with the isothermal profile while with the constant M/L profile we obtained a mean of $H_0 = 85.9 \pm 15.5$ km/s/Mpc. Our results thus frame the commonly accepted values of the WMAP team, i.e. $H_0 = 70.5 \pm 1.3$ km/s/Mpc

(Komatsu et al., 2009), and of the Hubble Space Telescope Key Project, i.e. $H_0 = 72 \pm 8$ km/s/Mpc (Freedman et al., 2001). Of course our sample does not contain many objects and we cannot really draw global conclusions from our results. This study is yet to be completed (Chantry et al., in preparation). Given the accuracy reached on the relative positions of the lensed images, the next step with this sample is to study the population of dark matter clumps in the lensing galaxy with a revised version of the LENSMODEL software.

We can thus conclude that doubly lensed quasars can be modeled with simple models even with positions to the mas accuracy. However, quadruply lensed quasars generally show the need for more complicated models. It is thus mandatory to carefully study the environment of every lens and to take into account the possible substructures.

14.4 Outlook

The COSMOGRAIL project has still many years of work ahead. The amount of data still to reduce is quite huge. Moreover, in the present conditions, all the monitored systems could not lead to an estimation of the Hubble constant. Indeed, the redshift of the lens remains unknown for some of the COSMOGRAIL objects. Even if most of the lensing galaxies are not faint, their redshift is far from being trivial to derive. But a technique based on the MCS algorithm allows the spatial deconvolution of spectra (Courbin et al., 2000): it has proved to be very useful and has permitted to obtain many lens redshifts from ground-based data, for example for COSMOGRAIL objects (Eigenbrod et al., 2006b, 2007). If the image separation is larger or if the lens is brighter, the lens spectra can be obtained by traditional techniques such as simple slit spectroscopy.

For some other lensed systems there are no high resolution images available. It will cause a loss of accuracy in the modeling that will propagate into a loss of precision on H_0. But there is a common will of the members of COSMOGRAIL to try and acquire the lacking data, whether spectra or space-based high quality images. Let us note that there remain eight objects from the COSMOGRAIL sample which have already been observed with HST/NIC2: the next planned step is to apply ISMCS to these images.

Moreover, until now the determination of mass distributions has led to the largest contributions in the uncertainties on H_0. We really need to concentrate our efforts on this issue which is at the center of the problem. The study of substructures and how they affect the configuration of a system is also capital for our purpose. Indeed, we are going to reach higher and higher positional accuracies and it is no longer possible to ignore this phenomenon.

To close this work, we can say that the story of lensing is not over yet and that many hopes have been put into that tool, for example to solve the mystery of dark matter.

I like the night. Without the dark, we'd never see the stars.

Edward Cullen in Twilight,
Stephenie Meyer (1973 -)

Bibliography

Adams, T. F. (1974). Variable N galaxies as composite systems. *ApJ* **188**, 463–468.

Anguita, T., Faure, C., Yonehara, A., Wambsganss, J., Kneib, J.-P., Covone, G. & Alloin, D. (2008). Integral field spectroscopy of four lensed quasars: analysis of their neighborhood and evidence for microlensing. *A&A* **481**, 615–627.

Asfandiyarov, I. & et al. (in preparation) .

Auger, M. W., Fassnacht, C. D., Abrahamse, A. L., Lubin, L. M. & Squires, G. K. (2007). The Gravitational Lens-Galaxy Group Connection. II. Groups Associated with B2319+051 and B1600+434. *AJ* **134**, 668–679.

Auger, M. W., Fassnacht, C. D., Wong, K. C., Thompson, D., Matthews, K. & Soifer, B. T. (2008). Lens Galaxy Properties of SBS 1520+530: Insights from Keck Spectroscopy and AO Imaging. *ApJ* **673**, 778–786.

Bade, N., Engels, D., Voges, W., Beckmann, V., Boller, T., Cordis, L., Dahlem, M., Englhauser, J., Molthagen, K., Nass, P., Studt, J. & Reimers, D. (1998). The Hamburg/RASS Catalogue of optical identifications. *A&AS* **127**, 145–152.

Bade, N., Siebert, J., Lopez, S., Voges, W. & Reimers, D. (1997). RX J0911.4+0551: A new multiple QSO selected from the ROSAT All-Sky Survey. *A&A* **317**, L13–L16.

Barkana, R. (1997). Analysis of Time Delays in the Gravitational Lens PG 1115+080. *ApJ* **489**, 21–28.

Barnabè, M., Czoske, O., Koopmans, L. V. E., Treu, T., Bolton, A. S. & Gavazzi, R. (2009). Two-dimensional kinematics of SLACS lenses - II. Combined lensing and dynamics analysis of early-type galaxies at z = 0.08-0.33. *MNRAS* **399**, 21–36.

Barnothy, J. M. (1965). Quasars and the Gravitational Image Intensifier. *AJ* **70**, 666.

Bertin, E. & Arnouts, S. (1996). SExtractor: Software for source extraction. *A&AS* **117**, 393–404.

Biggs, A. D., Browne, I. W. A., Helbig, P., Koopmans, L. V. E., Wilkinson, P. N. & Perley, R. A. (1999). Time delay for the gravitational lens system B0218+357. *MNRAS* **304**, 349–358.

Biggs, A. D., Browne, I. W. A., Jackson, N. J., York, T., Norbury, M. A., McKean, J. P. & Phillips, P. M. (2004). Radio, optical and infrared observations of CLASS B0128+437. *MNRAS* **350**, 949–961.

Binney, J. & Merrifield, M. (1998). *Galactic astronomy*. Princeton University Press (Princeton series in astrophysics).

Blanchet, G. (2006). *Study of the blur, ringing and aliasing artifacts in numerical imaging. Application to restoration*. Ph.D. thesis, Ecole Normale Supérieure de Cachan, France.

Bolton, A. S., Burles, S., Koopmans, L. V. E., Treu, T. & Moustakas, L. A. (2006). The Sloan Lens ACS Survey. I. A Large Spectroscopically Selected Sample of Massive Early-Type Lens Galaxies. *ApJ* **638**, 703–724.

Bradač, M., Schneider, P., Steinmetz, M., Lombardi, M., King, L. J. & Porcas, R. (2002). B1422+231: The influence of mass substructure on strong lensing. *A&A* **388**, 373–382.

Brewer, B. J. & Lewis, G. F. (2008). Unlensing HST observations of the Einstein ring 1RXS J1131-1231: a Bayesian analysis. *MNRAS* **390**, 39–48.

Brotherton, M. S., Tran, H. D., Becker, R. H., Gregg, M. D., Laurent-Muehleisen, S. A. & White, R. L. (2001). Composite Spectra from the FIRST Bright Quasar Survey. *ApJ* **546**, 775–781.

Browne, I. W. A., Patnaik, A. R., Walsh, D. & Wilkinson, P. N. (1993). The Redshift of the Lensing Galaxy in the Gravitationally Lensed System B0218+35.7. *MNRAS* **263**, L32–L36.

Burke, W. L. (1981). Multiple Gravitational Imaging by Distributed Masses. *ApJL* **244**, L1.

Burud, I. (2001). *Gravitational lensing as a tool for determining the age of the Universe*. Ph.D. thesis, Institute of Astrophysics and Geophysics, Université de Liège, Belgium.

Burud, I., Courbin, F., Lidman, C., Jaunsen, A. O., Hjorth, J., Ostensen, R., Andersen, M. I., Clasen, J. W., Wucknitz, O., Meylan, G., Magain, P., Stabell, R. & Refsdal, S. (1998). High-Resolution Optical and Near-Infrared Imaging of the Quadruple Quasar RX J0911.4+0551. *ApJL* **501**, L5–L10.

Burud, I., Courbin, F., Magain, P., Lidman, C., Hutsemékers, D., Kneib, J.-P., Hjorth, J., Brewer, J., Pompei, E., Germany, L., Pritchard, J., Jaunsen, A. O., Letawe, G. & Meylan, G. (2002a). An optical time-delay for the lensed BAL quasar HE 2149-2745. *A&A* **383**, 71–81.

Burud, I., Hjorth, J., Courbin, F., Cohen, J. G., Magain, P., Jaunsen, A. O., Kaas, A. A., Faure, C. & Letawe, G. (2002b). Time delay and lens redshift for the doubly imaged BAL quasar SBS 1520+530. *A&A* **391**, 481–486.

Burud, I., Hjorth, J., Jaunsen, A. O., Andersen, M. I., Korhonen, H., Clasen, J. W., Pelt, J., Pijpers, F. P., Magain, P. & Østensen, R. (2000). An Optical Time Delay Estimate for the Double Gravitational Lens System B1600+434. *ApJ* **544**, 117–122.

Burud, I., Magain, P., Sohy, S. & Hjorth, J. (2001). A novel approach for extracting time-delays from lightcurves of lensed quasar images. *A&A* **380**, 805–810.

Carilli, C. L., Rupen, M. P. & Yanny, B. (1993). Neutral hydrogen 21 centimeter absorption at Z = 0.6847 toward the 'smallest Einstein ring'. *ApJL* **412**, L59–L62.

Chantry, V. & et al. (in preparation). COSMOGRAIL: the COSmological MOnitoring of GRAvItational Lenses. X. New time delays for the gravitational lens HE 0435-1223 .

Chantry, V. & Magain, P. (2007). Deconvolution of HST images of the Cloverleaf gravitational lens. Detection of the lensing galaxy and a partial Einstein ring. *A&A* **470**, 467–473.

Chantry, V., Sluse, D. & et al. (in preparation). COSMOGRAIL: the COSmological MOnitoring of GRAvItational Lenses. XI. Study of 11 gravitationally lensed quasars: deconvolution of high resolution near-IR images, remeasurement of the time delays, simple models and the Hubble constant .

Chantry, V., Sluse, D. & Magain, P. (2010). COSMOGRAIL: the COSmological MOnitoring of GRAvItational Lenses. VIII. Deconvolution of high resolution near-IR images and simple mass models for 7 gravitationally lensed quasars. *submitted to A&A* .

Chartas, G., Dai, X., Gallagher, S. C., Garmire, G. P., Bautz, M. W., Schechter, P. L. & Morgan, N. D. (2001). Chandra Detects a Rapid Flare in the Gravitationally Lensed Mini-Broad Absorption Line QSO RX J0911.4+0551. *ApJ* **558**, 119–126.

Chavushyan, V. H., Vlasyuk, V. V., Stepanian, J. A. & Erastova, L. K. (1997). SBS 1520+530: a new gravitationally lensed system at z=1.855. *A&A* **318**, L67–L70.

Chen, J., Rozo, E., Dalal, N. & Taylor, J. E. (2007). Astrometric Perturbations in Substructure Lensing. *ApJ* **659**, 52–68.

Chiba, M., Minezaki, T., Kashikawa, N., Kataza, H. & Inoue, K. T. (2005). Subaru Mid-Infrared Imaging of the Quadruple Lenses PG 1115+080 and B1422+231: Limits on Substructure Lensing. *ApJ* **627**, 53–61.

Chwolson, O. (1924). Über eine mögliche Form fiktiver Doppelsterne. *Astronomische Nachrichten* **221**, 329.

Claeskens, J.-F., Sluse, D., Riaud, P. & Surdej, J. (2006). Multi wavelength study of the gravitational lens system RXS J1131-1231. II. Lens model and source reconstruction. *A&A* **451**, 865–879.

Cohen, A. S., Hewitt, J. N., Moore, C. B. & Haarsma, D. B. (2000). Further Investigation of the Time Delay, Magnification Ratios, and Variability in the Gravitational Lens 0218+357. *ApJ* **545**, 578–590.

Cohen, J. G., Lawrence, C. R. & Blandford, R. D. (2003). The Redshift of the Lensed Object in the Einstein Ring B0218+357. *ApJ* **583**, 67–69.

Cohn, J. D., Kochanek, C. S., McLeod, B. A. & Keeton, C. R. (2001). Constraints on Galaxy Density Profiles from Strong Gravitational Lensing: The Case of B1933+503. *ApJ* **554**, 1216–1226.

Courbin, F. (1999). *Deconvolution et combinaison optimale d'images astronomiques: application au cas des mirages gravitationnels*. Ph.D. thesis, Institut d'astrophysique et de géophysique, Université de Liège, Belgium; Observatoire de Paris Meudon - DAEC, France.

Courbin, F., Lidman, C. & Magain, P. (1998). Detection of the lensing galaxy in HE 1104-1805. *A&A* **330**, 57–62.

Courbin, F., Magain, P., Keeton, C. R., Kochanek, C. S., Vanderriest, C., Jaunsen, A. O. & Hjorth, J. (1997). The geometry of the quadruply imaged quasar PG 1115+080: implications for H_0. *A&A* **324**, L1–L4.

Courbin, F., Magain, P., Kirkove, M. & Sohy, S. (2000). A Method for Spatial Deconvolution of Spectra. *ApJ* **529**, 1136–1144.

Courbin, F. & Minniti, D., eds. (2002). *Gravitational Lensing: An Astrophysical Tool*, volume 608 of *Lecture Notes in Physics, Berlin Springer Verlag*.

Crampton, D., Schechter, P. L. & Beuzit, J.-L. (1998). Detection of the Galaxy Lensing the Doubly Imaged Quasar SBS 1520+530. *AJ* **115**, 1383–1387.

Dai, X. & Kochanek, C. S. (2009). Differential X-Ray Absorption and Dust-to-Gas Ratios of the Lens Galaxies SBS 0909+523, FBQS 0951+2635, and B 1152+199. *ApJ* **692**, 677–683.

Dai, X., Kochanek, C. S., Chartas, G., Kozłowski, S., Morgan, C. W., Garmire, G. & Agol, E. (2010). The Sizes of the X-ray and Optical Emission Regions of RXJ 1131-1231. *ApJ* **709**, 278–285.

Dalal, N. & Kochanek, C. S. (2002). Direct Detection of Cold Dark Matter Substructure. *ApJ* **572**, 25–33.

de Vaucouleurs, G. (1948). Recherches sur les Nebuleuses Extragalactiques. *Annales d'Astrophysique* **11**, 247.

Djorgovski, S. & Davis, M. (1987). Fundamental properties of elliptical galaxies. *ApJ* **313**, 59–68.

Dyson, F. W., Eddington, A. S. & Davidson, C. (1920). A Determination of the Deflection of Light by the Sun's Gravitational Field, from Observations Made at the Total Eclipse of May 29, 1919. *Royal Society of London Philosophical Transactions Series A* **220**, 291–333.

Eddington, A. S. (1919). The total eclipse of 1919 May 29 and the influence of gravitation on light. *The Observatory* **42**, 119–122.

Eigenbrod, A. (2008). *Astrophysical applications of gravitationally lensed quasars: from dark matter halos to the structure of quasar accretion disks*. Ph.D. thesis, Ecole Polytechnique Fédérale de Lausanne (EPFL), Switzerland.

Eigenbrod, A., Courbin, F., Dye, S., Meylan, G., Sluse, D., Vuissoz, C. & Magain, P. (2006a). COSMOGRAIL: the COSmological MOnitoring of GRAvItational Lenses. II. SDSS J0924+0219: the redshift of the lensing galaxy, the quasar spectral variability and the Einstein rings. *A&A* **451**, 747–757.

Eigenbrod, A., Courbin, F. & Meylan, G. (2007). COSMOGRAIL: the COSmological MOnitoring of GRAvItational Lenses. VI. Redshift of the lensing galaxy in seven gravitationally lensed quasars. *A&A* **465**, 51–56.

Eigenbrod, A., Courbin, F., Meylan, G., Vuissoz, C. & Magain, P. (2006b). COSMOGRAIL: the COSmological MOnitoring of GRAvItational Lenses. III. Redshift of the lensing galaxy in eight gravitationally lensed quasars. *A&A* **451**, 759–766.

Einstein, A. (1911). Über den Einfluß der Schwerkraft auf die Ausbreitung des Lichtes. *Annalen der Physik* **340**, 898–908.

Einstein, A. (1916). Die Grundlage der allgemeinen Relativitätstheorie. *Annalen der Physik* **354**, 769–822.

Einstein, A. (1936). Lens-Like Action of a Star by the Deviation of Light in the Gravitational Field. *Science* **84**, 506–507.

Engels, D., Hagen, H.-J., Cordis, L., Koehler, S., Wisotzki, L. & Reimers, D. (1998). The Hamburg Quasar Survey. II. A first list of 121 quasars. *A&AS* **128**, 507–523.

Eulaers, E. (2008). *Measuring Time Delays in Gravitational Lenses*. Master's thesis, Université de Liège, Belgium.

Eulaers, E. & et al. (in preparation) .

Faber, S. M. & Jackson, R. E. (1976). Velocity dispersions and mass-to-light ratios for elliptical galaxies. *ApJ* **204**, 668–683.

Falco, E. E., Gorenstein, M. V. & Shapiro, I. I. (1985). On model-dependent bounds on H_0 from gravitational images: Application to Q0957 + 561A,B. *ApJL* **289**, L1–L4.

Falco, E. E., Impey, C. D., Kochanek, C. S., Lehár, J., McLeod, B. A., Rix, H.-W., Keeton, C. R., Muñoz, J. A. & Peng, C. Y. (1999). Dust and Extinction Curves in Galaxies with $z > 0$: The Interstellar Medium of Gravitational Lens Galaxies. *ApJ* **523**, 617–632.

Fanaroff, B. L. & Riley, J. M. (1974). The morphology of extragalactic radio sources of high and low luminosity. *MNRAS* **167**, 31–36.

Fassnacht, C. D. & Cohen, J. G. (1998). Keck spectroscopy of three gravitational lens systems discovered in the JVAS and CLASS surveys. *AJ* **115**, 377–382.

Fassnacht, C. D., Gal, R. R., Lubin, L. M., McKean, J. P., Squires, G. K. & Readhead, A. C. S. (2006). Mass along the Line of Sight to the Gravitational Lens B1608+656: Galaxy Groups and Implications for H_0. *ApJ* **642**, 30–38.

Fassnacht, C. D., Pearson, T. J., Readhead, A. C. S., Browne, I. W. A., Koopmans, L. V. E., Myers, S. T. & Wilkinson, P. N. (1999). A Determination of H_0 with the CLASS Gravitational Lens B1608+656. I. Time Delay Measurements with the VLA. *ApJ* **527**, 498–512.

Fassnacht, C. D., Womble, D. S., Neugebauer, G., Browne, I. W. A., Readhead, A. C. S., Matthews, K. & Pearson, T. J. (1996). 1608+656: A Gravitationally Lensed Poststarburst Radio Galaxy. *ApJL* **460**, L103–L106.

Fassnacht, C. D., Xanthopoulos, E., Koopmans, L. V. E. & Rusin, D. (2002). A Determination of H_0 with the CLASS Gravitational Lens B1608+656. III. A Significant Improvement in the Precision of the Time Delay Measurements. *ApJ* **581**, 823–835.

Faure, C., Alloin, D., Kneib, J. P. & Courbin, F. (2004). A search for clusters and groups of galaxies on the line of sight towards 8 lensed quasars. *A&A* **428**, 741–755.

Faure, C., Courbin, F., Kneib, J. P., Alloin, D., Bolzonella, M. & Burud, I. (2002). The lensing system towards the doubly imaged quasar SBS 1520+530. *A&A* **386**, 69–76.

Ferreras, I., Saha, P. & Burles, S. (2008). Unveiling dark haloes in lensing galaxies. *MNRAS* **383**, 857–863.

Fohlmeister, J., Kochanek, C. S., Falco, E. E., Morgan, C. W. & Wambsganss, J. (2008). The Rewards of Patience: An 822 Day Time Delay in the Gravitational Lens SDSS J1004+4112. *ApJ* **676**, 761–766.

Fohlmeister, J., Kochanek, C. S., Falco, E. E., Wambsganss, J., Morgan, N., Morgan, C. W., Ofek, E. O., Maoz, D., Keeton, C. R., Barentine, J. C., Dalton, G., Dembicky, J., Ketzeback, W., McMillan, R. & Peters, C. S. (2007). A Time Delay for the Cluster-Lensed Quasar SDSS J1004+4112. *ApJ* **662**, 62–71.

Freedman, W. L., Madore, B. F., Gibson, B. K., Ferrarese, L., Kelson, D. D., Sakai, S., Mould, J. R., Kennicutt, Jr., R. C., Ford, H. C., Graham, J. A., Huchra, J. P., Hughes, S. M. G., Illingworth, G. D., Macri, L. M. & Stetson, P. B. (2001). Final Results from the Hubble Space Telescope Key Project to Measure the Hubble Constant. *ApJ* **553**, 47–72.

Freeman, K. C. (1970). On the Disks of Spiral and S0 Galaxies. *ApJ* **160**, 811.

Gaynullina, E. R., Schmidt, R. W., Akhunov, T., Burkhonov, O., Gottlöber, S., Mirtadjieva, K., Nuritdinov, S. N., Tadjibaev, I., Wambsganss, J. & Wisotzki, L. (2005). Microlensing in the double quasar SBS 1520+530. *A&A* **440**, 53–58.

Gil-Merino, R., Wisotzki, L. & Wambsganss, J. (2002). The Double Quasar HE 1104-1805: A case study for time delay determination with poorly sampled lightcurves. *A&A* **381**, 428–439.

Goicoechea, L. J., Shalyapin, V. N., Koptelova, E., Gil-Merino, R., Zheleznyak, A. P. & Ullán, A. (2008). First robotic monitoring of a lensed quasar: Intrinsic variability of SBS 0909+532. *New Astronomy* **13**, 182–193.

Guth, A. H. (1981). Inflationary universe: A possible solution to the horizon and flatness problems. *Physical Review D* **23**, 347–356.

Hagen, H.-J., Engels, D. & Reimers, D. (1999). The Hamburg Quasar Survey. III. Further new bright quasars. *A&AS* **134**, 483–487.

Hazard, C., Morton, D. C., Terlevich, R. & McMahon, R. (1984). Nine new quasi-stellar objects with broad absorption lines. *ApJ* **282**, 33–52.

Hege, E. K., Hubbard, E. N., Strittmatter, P. A. & Worden, S. P. (1981). Speckle interferometry observations of the triple QSO PG 1115 + 08. *ApJL* **248**, L1–L3.

Hinshaw, G., Weiland, J. L., Hill, R. S., Odegard, N., Larson, D., Bennett, C. L., Dunkley, J., Gold, B., Greason, M. R., Jarosik, N., Komatsu, E., Nolta, M. R., Page, L., Spergel, D. N., Wollack, E., Halpern, M., Kogut, A., Limon, M., Meyer, S. S., Tucker, G. S. & Wright, E. L. (2009). Five-Year Wilkinson Microwave Anisotropy Probe Observations: Data Processing, Sky Maps, and Basic Results. *ApJS* **180**, 225–245.

Hjorth, J., Burud, I., Jaunsen, A. O., Schechter, P. L., Kneib, J.-P., Andersen, M. I., Korhonen, H., Clasen, J. W., Kaas, A. A., Østensen, R., Pelt, J. & Pijpers, F. P. (2002). The Time Delay of the Quadruple Quasar RX J0911.4+0551. *ApJL* **572**, L11–L14.

Hubble, E. (1929). A Relation between Distance and Radial Velocity among Extra-Galactic Nebulae. *Proceedings of the National Academy of Science* **15**, 168–173.

Impey, C. D., Falco, E. E., Kochanek, C. S., Lehár, J., McLeod, B. A., Rix, H.-W., Peng, C. Y. & Keeton, C. R. (1998). An Infrared Einstein Ring in the Gravitational Lens PG 1115+080. *ApJ* **509**, 551–560.

Impey, C. D., Foltz, C. B., Petry, C. E., Browne, I. W. A. & Patnaik, A. R. (1996). Hubble Space Telescope Observations of the Gravitational Lens System B1422+231. *ApJL* **462**, L53–L57.

Inada, N., Oguri, M., Becker, R. H., Shin, M.-S., Richards, G. T., Hennawi, J. F., White, R. L., Pindor, B., Strauss, M. A., Kochanek, C. S., Johnston, D. E., Gregg, M. D., Kayo, I., Eisenstein, D., Hall, P. B., Castander, F. J., Clocchiatti, A., Anderson, S. F., Schneider, D. P., York, D. G., Lupton, R., Chiu, K., Kawano, Y., Scranton, R., Frieman, J. A., Keeton, C. R., Morokuma, T., Rix, H.-W., Turner, E. L., Burles, S., Brunner, R. J., Sheldon, E. S., Bahcall, N. A. & Masataka, F. (2008). The Sloan Digital Sky Survey Quasar Lens Search. II. Statistical Lens Sample from the Third Data Release. *AJ* **135**, 496–511.

Jackson, N., de Bruyn, A. G., Myers, S., Bremer, M. N., Miley, G. K., Schilizzi, R. T., Browne, I. W. A., Nair, S., Wilkinson, P. N., Blandford, R. D., Pearson, T. J. & Readhead, A. C. S. (1995). 1600+434: a new gravitational lens system. *MNRAS* **274**, L25–L29.

Jackson, N., Nair, S., Browne, I. W. A., Wilkinson, P. N., Muxlow, T. W. B., de Bruyn, A. G., Koopmans, L., Bremer, M., Snellen, I., Miley, G. K., Schilizzi, R. T., Myers, S., Fassnacht, C. D., Womble, D. S., Readhead, A. C. S., Blandford, R. D. & Pearson, T. J. (1998). B0712+472: a new radio four-image gravitational lens. *MNRAS* **296**, 483–490.

Jakobsson, P., Hjorth, J., Burud, I., Letawe, G., Lidman, C. & Courbin, F. (2005). An optical time delay for the double gravitational lens system FBQ 0951+2635. *A&A* **431**, 103–109.

Jaunsen, A. O. & Hjorth, J. (1997). Detection of a spiral lens galaxy and optical variability in the gravitational lens system B1600+434. *A&A* **317**, L39–L42.

Jean, C. & Surdej, J. (2007). Extinction law classification and lens redshift estimate by means of the principal component analysis. *A&A* **471**, 807–812.

Kassiola, A. & Kovner, I. (1993). Elliptic Mass Distributions versus Elliptic Potentials in Gravitational Lenses. *ApJ* **417**, 450–473.

Keeton, C. R. (2001a). A Catalog of Mass Models for Gravitational Lensing. *ArXiv:astro-ph/0102341* .

Keeton, C. R. (2001b). Computational Methods for Gravitational Lensing. *ArXiv:astro-ph/0102340* .

Keeton, C. R. (2009). Gravitational lensing with stochastic substructure: Effects of the clump mass function and spatial distribution. *ArXiv:astro-ph/0908.3001* .

Keeton, C. R., Burles, S., Schechter, P. L. & Wambsganss, J. (2006). Differential Microlensing of the Continuum and Broad Emission Lines in SDSS J0924+0219, the Most Anomalous Lensed Quasar. *ApJ* **639**, 1–6.

Keeton, C. R., Gaudi, B. S. & Petters, A. O. (2003). Identifying Lenses with Small-Scale Structure. I. Cusp Lenses. *ApJ* **598**, 138–161.

Keeton, C. R. & Kochanek, C. S. (1997). Determining the Hubble Constant from the Gravitational Lens PG 1115+080. *ApJ* **487**, 42.

Keeton, C. R., Kochanek, C. S. & Falco, E. E. (1998). The Optical Properties of Gravitational Lens Galaxies as a Probe of Galaxy Structure and Evolution. *ApJ* **509**, 561–578.

Keeton, C. R., Kochanek, C. S. & Seljak, U. (1997). Shear and Ellipticity in Gravitational Lenses. *ApJ* **482**, 604–620.

Keeton, C. R. & Moustakas, L. A. (2009). A New Channel for Detecting Dark Matter Substructure in Galaxies: Gravitational Lens Time Delays. *ApJ* **699**, 1720–1731.

Khamitov, I. M., Bikmaev, I. F., Aslan, Z., Sakhibullin, N. A., Vlasyuk, V. V., Zheleznyak, A. P. & Zakharov, A. F. (2006). Analysis of optical light curves for the components of the gravitationally lensed quasar SBS 1520+530 based on observations with the 1.5-m RTT-150 telescope in 2001-2005. *Astronomy Letters* **32**, 514–519.

Kneib, J.-P., Alloin, D. & Pello, R. (1998). Unveiling the nature of the Cloverleaf lens-system: HST/NICMOS-2 observations. *A&A* **339**, L65–L68.

Kneib, J.-P., Cohen, J. G. & Hjorth, J. (2000). RX J0911+05: A Massive Cluster Lens at z=0.769. *ApJL* **544**, L35–L39.

Kochanek, C. S. (1991). The implications of lenses for galaxy structure. *ApJ* **373**, 354–368.

Kochanek, C. S. (2002). What Do Gravitational Lens Time Delays Measure? *ApJ* **578**, 25–32.

Kochanek, C. S. & Dalal, N. (2004). Tests for Substructure in Gravitational Lenses. *ApJ* **610**, 69–79.

Kochanek, C. S., Falco, E. E., Schild, R., Dobrzycki, A., Engels, D. & Hagen, H.-J. (1997). SBS 0909+532: A New Double Gravitational Lens or Binary Quasar? *ApJ* **479**, 678,683.

Kochanek, C. S., Morgan, N. D., Falco, E. E., McLeod, B. A., Winn, J. N., Dembicky, J. & Ketzeback, B. (2006). The Time Delays of Gravitational Lens HE 0435-1223: An Early-Type Galaxy with a Rising Rotation Curve. *ApJ* **640**, 47–61.

Kochanek, C. S. & Schechter, P. L. (2004). The Hubble Constant from Gravitational Lens Time Delays. In W. L. Freedman, ed., *Measuring and Modeling the Universe*.

Komatsu, E., Dunkley, J., Nolta, M. R., Bennett, C. L., Gold, B., Hinshaw, G., Jarosik, N., Larson, D., Limon, M., Page, L., Spergel, D. N., Halpern, M., Hill, R. S., Kogut, A., Meyer, S. S., Tucker, G. S., Weiland, J. L., Wollack, E. & Wright, E. L. (2009). Five-Year Wilkinson Microwave Anisotropy Probe Observations: Cosmological Interpretation. *ApJS* **180**, 330–376.

Koopmans, L. V. E., Barnabe, M., Bolton, A., Bradac, M., Ciotti, L., Congdon, A., Czoske, O., Dye, S., Dutton, A., Elliasdottir, A., Evans, E., Fassnacht, C. D., Jackson, N., Keeton, C., Lasio, J., Moustakas, L., Meneghetti, M., Myers, S., Nipoti, C., Suyu, S., van de Ven, G., Vegetti, S., Wucknitz, O. & Zhao, H.-S. (2009a). Strong Gravitational Lensing as a Probe of Gravity, Dark-Matter and Super-Massive Black Holes. *Astronomy* **2010**, 159.

Koopmans, L. V. E., Bolton, A., Treu, T., Czoske, O., Auger, M. W., Barnabè, M., Vegetti, S., Gavazzi, R., Moustakas, L. A. & Burles, S. (2009b). The Structure and Dynamics of Massive Early-Type Galaxies: On Homology, Isothermality, and Isotropy Inside One Effective Radius. *ApJL* **703**, L51–L54.

Koopmans, L. V. E., de Bruyn, A. G. & Jackson, N. (1998). The edge-on spiral gravitational lens B1600+434. *MNRAS* **295**, 534–548.

Koopmans, L. V. E., de Bruyn, A. G., Xanthopoulos, E. & Fassnacht, C. D. (2000). A time-delay determination from VLA light curves of the CLASS gravitational lens B1600+434. *A&A* **356**, 391–402.

Koopmans, L. V. E. & Fassnacht, C. D. (1999). A Determination of H_0 with the CLASS Gravitational Lens B1608+656. II. Mass Models and the Hubble Constant from Lensing. *ApJ* **527**, 513–524.

Koopmans, L. V. E., Garrett, M. A., Blandford, R. D., Lawrence, C. R., Patnaik, A. R. & Porcas, R. W. (2002). 2016+112: a gravitationally lensed type II quasar. *MNRAS* **334**, 39–47.

Koopmans, L. V. E., Treu, T., Fassnacht, C. D., Blandford, R. D. & Surpi, G. (2003). The Hubble Constant from the Gravitational Lens B1608+656. *ApJ* **599**, 70–85.

Kozłovski, S., Morgan, N., Kochanek, C. S., Pointdexter, S., Falco, E. & Dai, X. (in preparation) .

Krist, J. & Hook, R. (2004). *The Tiny Tim User's Guide Version 6.3*.

Krolik, J. H. (1999). *Active galactic nuclei : from the central black hole to the galactic environment*. Julian H. Krolik. Princeton, N. J. : Princeton University Press.

Kundic, T., Hogg, D. W., Blandford, R. D., Cohen, J. G., Lubin, L. M. & Larkin, J. E. (1997). The External Shear Acting on Gravitational Lens B1422+231. *AJ* **114**, 2276–2283.

Lawrence, C. R., Neugebauer, G., Weir, N., Matthews, K. & Patnaik, A. R. (1992). Infrared observations of the gravitational lens system B1422+231. *MNRAS* **259**, 5P–7P.

Lehár, J., Falco, E. E., Kochanek, C. S., McLeod, B. A., Muñoz, J. A., Impey, C. D., Rix, H.-W., Keeton, C. R. & Peng, C. Y. (2000). Hubble Space Telescope Observations of 10 Two-Image Gravitational Lenses. *ApJ* **536**, 584–605.

Letawe, G. (2006). *Etude spectroscopique de galaxies hôtes de quasars lumineux*. Ph.D. thesis, Université de Liège, Belgium.

Lidman, C., Courbin, F., Kneib, J.-P., Golse, G., Castander, F. & Soucail, G. (2000). Exploring the gravitationally lensed system HE 1104-1805: VLT spectroscopy of the lens at z=0.729. *A&A* **364**, L62–L65.

Lopez, S., Wucknitz, O. & Wisotzki, L. (1998). Detection of the lensing galaxy in HE 2149-2745. *A&A* **339**, L13–L16.

Lubin, L. M., Fassnacht, C. D., Readhead, A. C. S., Blandford, R. D. & Kundić, T. (2000). A Keck Survey of Gravitational Lens Systems. I. Spectroscopy of SBS 0909+532, HST 1411+5211, and CLASS B2319+051. *AJ* **119**, 451–459.

Lynden-Bell, D. (1969). Galactic Nuclei as Collapsed Old Quasars. *Nature* **223**, 690.

MacLeod, C. L., Kochanek, C. S. & Agol, E. (2009). Detection of a Companion Lens Galaxy Using the Mid-Infrared Flux Ratios of the Gravitationally Lensed Quasar H1413+117. *ApJ* **699**, 1578–1583.

Magain, P., Courbin, F., Gillon, M., Sohy, S., Letawe, G., Chantry, V. & Letawe, Y. (2007). A deconvolution-based algorithm for crowded field photometry with unknown point spread function. *A&A* **461**, 373–379.

Magain, P., Courbin, F. & Sohy, S. (1998). Deconvolution with Correct Sampling. *ApJ* **494**, 472.

Magain, P., Surdej, J., Swings, J.-P., Borgeest, U. & Kayser, R. (1988). Discovery of a quadruply lensed quasar - The 'clover leaf' H1413+117. *Nature* **334**, 325–327.

Mao, S. & Schneider, P. (1998). Evidence for substructure in lens galaxies? *MNRAS* **295**, 587–594.

McKean, J. P., Koopmans, L. V. E., Flack, C. E., Fassnacht, C. D., Thompson, D., Matthews, K., Blandford, R. D., Readhead, A. C. S. & Soifer, B. T. (2007). High-resolution imaging of the anomalous flux ratio gravitational lens system CLASS B2045+265: dark or luminous satellites? *MNRAS* **378**, 109–118.

Mediavilla, E., Muñoz, J. A., Kochanek, C. S., Falco, E. E., Arribas, S. & Motta, V. (2005). The First Precise Determination of an Optical-Far-Ultraviolet Extinction Curve Beyond the Local Group (z=0.83). *ApJ* **619**, 749–754.

Metcalf, R. B. & Madau, P. (2001). Compound Gravitational Lensing as a Probe of Dark Matter Substructure within Galaxy Halos. *ApJ* **563**, 9–20.

Miller, J. S., French, H. B. & Hawley, S. A. (1978). The spectrum and magnitude of the galaxy associated with BL Lacertae. *ApJL* **219**, L85–L87.

Momcheva, I., Williams, K., Keeton, C. & Zabludoff, A. (2006). A Spectroscopic Study of the Environments of Gravitational Lens Galaxies. *ApJ* **641**, 169–189.

More, A., McKean, J. P., More, S., Porcas, R. W., Koopmans, L. V. E. & Garrett, M. A. (2009). The role of luminous substructure in the gravitational lens system MG 2016+112. *MNRAS* **394**, 174–190.

Morgan, C. W., Eyler, M. E., Kochanek, C. S., Morgan, N. D., Falco, E. E., Vuissoz, C., Courbin, F. & Meylan, G. (2008). Simultaneous Estimation of Time Delays and Quasar Structure. *ApJ* **676**, 80–86.

Morgan, N. D., Caldwell, J. A. R., Schechter, P. L., Dressler, A., Egami, E. & Rix, H.-W. (2004). WFI J2026-4536 and WFI J2033-4723: Two New Quadruple Gravitational Lenses. *AJ* **127**, 2617–2630.

Morgan, N. D., Kochanek, C. S., Falco, E. E. & Dai, X. (2006). Time-Delay Measurement for the Quadruple Lens RX J1131-1231. *ArXiv:astro-ph/0605321* .

Morgan, N. D., Kochanek, C. S., Pevunova, O. & Schechter, P. L. (2005). The Lens Redshift and Galaxy Environment for HE 0435-1223. *AJ* **129**, 2531–2541.

Motta, V., Mediavilla, E., Muñoz, J. A., Falco, E., Kochanek, C. S., Arribas, S., García-Lorenzo, B., Oscoz, A. & Serra-Ricart, M. (2002). Detection of the 2175 Å Extinction Feature at z = 0.83. *ApJ* **574**, 719–725.

Moustakas, L. A., Abazajian, K., Benson, A., Bolton, A. S., Bullock, J. S., Chen, J., Cheng, E., Coe, D., Congdon, A. B., Dalal, N., Diemand, J., Dobke, B. M., Dobler, G., Dore, O., Dutton, A., Ellis, R., Fassnacht, C. D., Ferguson, H., Finkbeiner, D., Gavassi, R., High, F. W., Jeltema, T., Jullo, E., Kaplinghat, M., Keeton, C. R., Kneib, J.-P., Koopmans, L. V. E., Koishiappas, S. M., Kuhlen, M., Kusenko, A., Lawrence, C. R., Loeb, A., Madae, P., Marshall, P., Metcalf, R. B., Natarajan, P., Primack, J. R., Profumo, S., Seiffert, M. D., Simon, J., Stern, D., Strigari, L., Taylor, J. E., Wayth, R., Wambsganss, J., Wechsler, R. & Zentner, A. (2009). Strong gravitational lensing probes of the particle nature of dark matter. *Astronomy* **2010**, 214.

Myers, S. T., Fassnacht, C. D., Djorgovski, S. G., Blandford, R. D., Matthews, K., Neugebauer, G., Pearson, T. J., Readhead, A. C. S., Smith, J. D., Thompson, D. J., Womble, D. S., Browne, I. W. A., Wilkinson, P. N., Nair, S., Jackson, N., Snellen, I. A. G., Miley, G. K., de Bruyn, A. G. & Schilizzi, R. T. (1995). 1608+656: A Quadruple-Lens System Found in the CLASS Gravitational Lens Survey. *ApJL* **447**, L5–L8.

Narayan, R. & Bartelmann, M. (1996). Lectures on Gravitational Lensing. *ArXiv:astro-ph/9606001* .

Navarro, J. F., Frenk, C. S. & White, S. D. M. (1996). The Structure of Cold Dark Matter Halos. *ApJ* **462**, 563–575.

Ofek, E. O. & Maoz, D. (2003). Time-Delay Measurement of the Lensed Quasar HE 1104-1805. *ApJ* **594**, 101–106.

Ofek, E. O., Maoz, D., Rix, H.-W., Kochanek, C. S. & Falco, E. E. (2006). Spectroscopic Redshifts for Seven Lens Galaxies. *ApJ* **641**, 70–77.

Orban de Xivry, G. (2009). *Etude des courbes de lumière d'un mirage gravitationnel*. Master's thesis, Université de Liège, Belgium.

Oscoz, A., Serra-Ricart, M., Mediavilla, E., Buitrago, J. & Goicoechea, L. J. (1997). Support for the Gravitational Lens Interpretation of SBS 0909+532. *ApJL* **491**, L7–L9.

Paraficz, D., Hjorth, J., Burud, I., Jakobsson, P. & Elíasdóttir, Á. (2006). Microlensing variability in time-delay quasars. *A&A* **455**, L1–L4.

Patnaik, A. R., Browne, I. W. A., King, L. J., Muxlow, T. W. B., Walsh, D. & Wilkinson, P. N. (1993). B0218+35.7 - A gravitationally lensed system with the smallest separation. *MNRAS* **261**, 435–444.

Patnaik, A. R., Browne, I. W. A., Walsh, D., Chaffee, F. H. & Foltz, C. B. (1992). B1422+231 - A new gravitationally lensed system at Z = 3.62. *MNRAS* **259**, 1P–4P.

Patnaik, A. R., Kemball, A. J., Porcas, R. W. & Garrett, M. A. (1999). Milliarcsec-scale polarization observations of the gravitational lens B1422+231. *MNRAS* **307**, L1–L5.

Patnaik, A. R. & Narasimha, D. (2001). Determination of time delay from the gravitational lens B1422+231. *MNRAS* **326**, 1403–1411.

Pelt, J., Hjorth, J., Refsdal, S., Schild, R. & Stabell, R. (1998). Estimation of multiple time delays in complex gravitational lens systems. *A&A* **337**, 681–684.

Pelt, J., Refsdal, S. & Stabell, R. (2002). Bias and consistency in time delay estimation methods: Case of the double quasar HE 1104-1805. *A&A* **389**, L57–L60.

Penzias, A. A. & Wilson, R. W. (1965). A Measurement of Excess Antenna Temperature at 4080 Mc/s. *ApJ* **142**, 419–421.

Pindor, B., Eisenstein, D. J., Inada, N., Gregg, M. D., Becker, R. H., Brinkmann, J., Burles, S., Frieman, J. A., Johnston, D. E., Richards, G. T., Schneider, D. P., Scranton, R., Sekiguchi, M., Turner, E. L. & York, D. G. (2004). SDSS J115517.35+634622.0: A Newly Discovered Gravitationally Lensed Quasar. *AJ* **127**, 1318–1324.

Poindexter, S., Morgan, N., Kochanek, C. S. & Falco, E. E. (2007). Mid-IR Observations and a Revised Time Delay for the Gravitational Lens System Quasar HE 1104-1805. *ApJ* **660**, 146–151.

Pooley, D., Rappaport, S., Blackburne, J., Schechter, P. L., Schwab, J. & Wambsganss, J. (2009). The Dark-matter Fraction in the Elliptical Galaxy Lensing the Quasar PG 1115+080. *ApJ* **697**, 1892–1900.

Raychaudhury, S., Saha, P. & Williams, L. L. R. (2003). Is B1422+231 a "Golden Lens"? *AJ* **126**, 29–36.

Refsdal, S. (1964). On the possibility of determining Hubble's parameter and the masses of galaxies from the gravitational lens effect. *MNRAS* **128**, 307.

Remy, M., Claeskens, J.-F., Surdej, J., Hjorth, J., Refsdal, S., Wucknitz, O., Sorensen, A. N. & Grundahl, F. (1998). Detection of the lensing galaxy for the double QSO HE 1104-1805. *New Astronomy* **3**, 379–390.

Remy, M., Surdej, J., Smette, A. & Claeskens, J.-F. (1993). Optical imaging of the gravitational lens system B 1422+231. *A&A* **278**, L19–L22.

Renn, J., Sauer, T. & Stachel, J. (1997). The origin of gravitational lensing: A postscript to Einstein's 1936 Science paper. *Science* **275**, 184–186.

Ros, E., Guirado, J. C., Marcaide, J. M., Pérez-Torres, M. A., Falco, E. E., Muñoz, J. A., Alberdi, A. & Lara, L. (2000). VLBI imaging of the gravitational lens MG J0414+0534. *A&A* **362**, 845–850.

Saha, P. (2004). Time-delay quasars: Scales and orders of magnitudes. *A&A* **414**, 425–428.

Saha, P., Courbin, F., Sluse, D., Dye, S. & Meylan, G. (2006). COSMOGRAIL: the COSmological MOnitoring of GRAvItational Lenses. IV. Models of prospective time-delay lenses. *A&A* **450**, 461–469.

Saha, P. & Williams, L. L. R. (1997). Non-parametric reconstruction of the galaxy lens in PG 1115+080. *MNRAS* **292**, 148.

Sandage, A., Tammann, G. A., Saha, A., Reindl, B., Macchetto, F. D. & Panagia, N. (2006). The Hubble Constant: A Summary of the Hubble Space Telescope Program for the Luminosity Calibration of Type Ia Supernovae by Means of Cepheids. *ApJ* **653**, 843–860.

Schechter, P. L., Bailyn, C. D., Barr, R., Barvainis, R., Becker, C. M., Bernstein, G. M., Blakeslee, J. P., Bus, S. J., Dressler, A., Falco, E. E., Fesen, R. A., Fischer, P., Gebhardt, K., Harmer, D., Hewitt, J. N., Hjorth, J., Hurt, T., Jaunsen, A. O., Mateo, M., Mehlert, D., Richstone, D. O., Sparke, L. S., Thorstensen, J. R., Tonry, J. L., Wegner, G., Willmarth, D. W. & Worthey, G. (1997). The Quadruple Gravitational Lens PG 1115+080: Time Delays and Models. *ApJL* **475**, L85–L88.

Schechter, P. L., Gregg, M. D., Becker, R. H., Helfand, D. J. & White, R. L. (1998). The First FIRST Gravitationally Lensed Quasar: FBQ 0951+2635. *AJ* **115**, 1371–1376.

Schechter, P. L., Udalski, A., Szymański, M., Kubiak, M., Pietrzyński, G., Soszyński, I., Woźniak, P., Żebruń, K., Szewczyk, O. & Wyrzykowski, Ł. (2003). Microlensing of Relativistic Knots in the Quasar HE 1104-1805 AB. *ApJ* **584**, 657–663.

Schmidt, M. (1963). 3C 273 : A Star-Like Object with Large Red-Shift. *Nature* **197**, 1040.

Schneider, P. (1984). The amplification caused by gravitational bending of light. *A&A* **140**, 119–124.

Schneider, P., Ehlers, J. & Falco, E. E. (1992). *Gravitational Lenses*. Springer-Verlag Berlin Heidelberg New York & Astronomy and Astrophysics Library.

Shannon, C. E. (1949). Communications in the presence of noise. In *Proc. of the IRE*, volume 37.

Sluse, D., Claeskens, J.-F., Altieri, B., Cabanac, R. A., Garcet, O., Hutsemékers, D., Jean, C., Smette, A. & Surdej, J. (2006). Multi-wavelength study of the gravitational lens system RXS J113155.4-123155. I. Multi-epoch optical and near infrared imaging. *A&A* **449**, 539–550.

Sluse, D., Claeskens, J.-F., Hutsemékers, D. & Surdej, J. (2007). Multi-wavelength study of the gravitational lens system RXS J1131-1231. III. Long slit spectroscopy: microlensing probes the QSO structure. *A&A* **468**, 885–901.

Sluse, D., Surdej, J., Claeskens, J.-F., Hutsemékers, D., Jean, C., Courbin, F., Nakos, T., Billeres, M. & Khmil, S. V. (2003). A quadruply imaged quasar with an optical Einstein ring candidate: 1RXS J113155.4-123155. *A&A* **406**, L43–L46.

Smette, A., Robertson, J. G., Shaver, P. A., Reimers, D., Wisotzki, L. & Koehler, T. (1995). The gravitational lens candidate HE 1104-1805 and the size of absorption systems. *A&AS* **113**, 199–236.

Soldner, J. G. v. (1804). Ueber die ablenkung eines lichtstrahls von seiner geradlinigen bewegung, durch die attraktion eines weltkörpers, an welchem er nahe vorbei geht. *Berliner Astronomisches Jahrbuch* , 161–172.

Stepanyan, D. A., Lipovetskii, V. A., Chavushyan, V. O., Erastova, L. K. & Shapovalova, A. I. (1991). Spectroscopic Investigations of Objects of the Second Byurakan Survey - Stellar Objects - Part Four. *Astrophysics* **34**, 1.

Stickel, M. & Kuehr, H. (1993). Spectroscopic observations of radio source identifications from the 1 Jy, S4 and S5 Surveys. III. *A&AS* **100**, 395–411.

STScI NICMOS Group, past & present members, i. S. A. E. B. T. B. H. B. D. C. L. C. M. D. S. H. L. M. B. M. K. N. A. N. E. R. C. S. A. S. A. S. M. S. A. S. A. S. C. X. (2007). *HST Data Handbook for NICMOS (Version 7.0)*, B. Mobasher, Baltimore, STScI edition.

Sugai, H., Kawai, A., Shimono, A., Hattori, T., Kosugi, G., Kashikawa, N., Inoue, K. T. & Chiba, M. (2007). Integral Field Spectroscopy of the Quadruply Lensed Quasar 1RXS J1131-1231: New Light on Lens Substructures. *ApJ* **660**, 1016–1022.

Sunyaev, R. A. & Zeldovich, Y. B. (1970). Small-Scale Fluctuations of Relic Radiation. *Ap&SS* **7**, 3–19.

Suyu, S. H., Marshall, P. J., Auger, M. W., Hilbert, S., Blandford, R. D., Koopmans, L. V. E., Fassnacht, C. D. & Treu, T. (2010). Dissecting the Gravitational lens B1608+656. II. Precision Measurements of the Hubble Constant, Spatial Curvature, and the Dark Energy Equation of State. *ApJ* **711**, 201–221.

Suyu, S. H., Marshall, P. J., Blandford, R. D., Fassnacht, C. D., Koopmans, L. V. E., McKean, J. P. & Treu, T. (2009). Dissecting the Gravitational Lens B1608+656. I. Lens Potential Reconstruction. *ApJ* **691**, 277–298.

Tewes, M. & et al. (in preparation) .

Tonry, J. & Schneider, D. P. (1988). A new technique for measuring extragalactic distances. *AJ* **96**, 807–815.

Tonry, J. L. (1998). Redshifts of the gravitational lenses B1422+231 and PG 1115+080. *AJ* **115**, 1–5.

Treu, T. & Koopmans, L. V. E. (2002). The internal structure of the lens PG1115+080: breaking degeneracies in the value of the Hubble constant. *MNRAS* **337**, L6–L10.

Tully, R. B. & Fisher, J. R. (1977). A new method of determining distances to galaxies. *A&A* **54**, 661–673.

Turnshek, D. A., Lupie, O. L., Rao, S. M., Espey, B. R. & Sirola, C. J. (1997). Hubble Space Telescope Observations of the Gravitationally Lensed Cloverleaf Broad Absorption Line QSO H1413+1143: Imaging. *ApJ* **485**, 100.

Ullán, A., Goicoechea, L. J., Zheleznyak, A. P., Koptelova, E., Bruevich, V. V., Akhunov, T. & Burkhonov, O. (2006). Time delay of SBS 0909+532. *A&A* **452**, 25–35.

van Dokkum, P. G. (2001). Cosmic-Ray Rejection by Laplacian Edge Detection. *PASP* **113**, 1420–1427.

Vanderriest, C., Schneider, J., Herpe, G., Chevreton, M., Wlérick, G. & Moles, M. (1989). Optical determinations of the time delay in 0957+561. In *Gravitational Lenses in Honor of Bernard F. Burke's 60th Birthday*.

Vuissoz, C. (2008). *Gravitational lenses: time delays and the Hubble constant*. Ph.D. thesis, Ecole Polytechnique Fédérale de Lausanne (EPFL), Switzerland.

Vuissoz, C., Courbin, F., Sluse, D., Meylan, G., Chantry, V., Eulaers, E., Morgan, C., Eyler, M. E., Kochanek, C. S., Coles, J., Saha, P., Magain, P. & Falco, E. E. (2008). COSMOGRAIL: the COSmological MOnitoring of GRAvItational Lenses. VII. Time delays and the Hubble constant from WFI J2033-4723. *A&A* **488**, 481–490.

Vuissoz, C., Courbin, F., Sluse, D., Meylan, G., Ibrahimov, M., Asfandiyarov, I., Stoops, E., Eigenbrod, A., Le Guillou, L., van Winckel, H. & Magain, P. (2007). COSMOGRAIL: the COSmological MOnitoring of GRAvItational Lenses. V. The time delay in SDSS J1650+4251. *A&A* **464**, 845–851.

Walsh, D., Carswell, R. F. & Weymann, R. J. (1979). 0957 + 561 A, B - Twin quasistellar objects or gravitational lens? *Nature* **279**, 381–384.

Warren, S. J. & Dye, S. (2003). Semilinear Gravitational Lens Inversion. *ApJ* **590**, 673–682.

Weymann, R. J., Latham, D., Roger, J., Angel, P., Green, R. F., Liebert, J. W., Turnshek, D. A., Turnshek, D. E. & Tyson, J. A. (1980). The triple QSO PG1115+08 - Another probable gravitational lens. *Nature* **285**, 641–643.

Williams, L. L. R. & Saha, P. (2000). Pixelated Lenses and H_0 from Time-Delay Quasars. *AJ* **119**, 439–450.

Willott, C. J., Delorme, P., Omont, A., Bergeron, J., Delfosse, X., Forveille, T., Albert, L., Reylé, C., Hill, G. J., Gully-Santiago, M., Vinten, P., Crampton, D., Hutchings, J. B., Schade, D., Simard, L., Sawicki, M., Beelen, A. & Cox, P. (2007). Four Quasars above Redshift 6 Discovered by the Canada-France High-z Quasar Survey. *AJ* **134**, 2435–2450.

Wisotzki, L., Christlieb, N., Bade, N., Beckmann, V., Köhler, T., Vanelle, C. & Reimers, D. (2000). The Hamburg/ESO survey for bright QSOs. III. A large flux-limited sample of QSOs. *A&A* **358**, 77–87.

Wisotzki, L., Koehler, T., Kayser, R. & Reimers, D. (1993). The new double QSO HE 1104-1805: Gravitational lens with microlensing or binary quasar? *A&A* **278**, L15–L18.

Wisotzki, L., Koehler, T., Lopez, S. & Reimers, D. (1996). Discovery of a new gravitationally lensed QSO with broad absorption lines. *A&A* **315**, L405+.

Wisotzki, L., Schechter, P. L., Bradt, H. V., Heinmüller, J. & Reimers, D. (2002). HE 0435-1223: A wide separation quadruple QSO and gravitational lens. *A&A* **395**, 17–23.

Wisotzki, L., Schechter, P. L., Chen, H.-W., Richstone, D., Jahnke, K., Sánchez, S. F. & Reimers, D. (2004). HE 0047-1756: A new gravitationally lensed double QSO. *A&A* **419**, L31–L34.

Wisotzki, L., Wucknitz, O., Lopez, S. & Sorensen, A. N. (1998). First estimate of the time delay in HE 1104-1805. *A&A* **339**, L73–L76.

Wucknitz, O. (2002). Degeneracies and scaling relations in general power-law models for gravitational lenses. *MNRAS* **332**, 951–961.

Wucknitz, O., Biggs, A. D. & Browne, I. W. A. (2004). Models for the lens and source of B0218+357: a LENSCLEAN approach to determine H_0. *MNRAS* **349**, 14–30.

Wyrzykowski, L., Udalski, A., Schechter, P. L., Szewczyk, O., Szymanski, M., Kubiak, M., Pietrzynski, G., Soszynski, I. & Zebrun, K. (2003). The Optical Gravitational Lensing Experiment. Optical Monitoring of the Gravitationally Lensed Quasar HE1104–1805 in 1997–2002. *Acta Astronomica* **53**, 229–240.

Yonehara, A., Hirashita, H. & Richter, P. (2008). Origin of chromatic features in multiple quasars. Variability, dust, or microlensing. *A&A* **478**, 95–109.

Yoo, J., Kochanek, C. S., Falco, E. E. & McLeod, B. A. (2005). The Lens Galaxy in PG 1115+080 is an Ellipse. *ApJ* **626**, 51–57.

Yoo, J., Kochanek, C. S., Falco, E. E. & McLeod, B. A. (2006). Halo Structures of Gravitational Lens Galaxies. *ApJ* **642**, 22–29.

York, T., Jackson, N., Browne, I. W. A., Wucknitz, O. & Skelton, J. E. (2005). The Hubble constant from the gravitational lens CLASS B0218+357 using the Advanced Camera for Surveys. *MNRAS* **357**, 124–134.

Zackrisson, E. & Riehm, T. (2009). Gravitational lensing as a probe of cold dark matter subhalos. *ArXiv:astro-ph/0905.4075* .

Zwicky, F. (1937). On the Masses of Nebulae and of Clusters of Nebulae. *ApJ* **86**, 217.

It is our choices... that show what we truly are,
far more than our abilities.

J. K. Rowling (1965 -)

List of publications

Refeered articles

- "COSMOGRAIL: the COSmological MOnitoring of GRAvItational Lenses. VIII. Deconvolution of high resolution near-IR images and simple mass models for 7 gravitationally lensed quasars ",
  Chantry,V.; Sluse, D.; Magain, P., submitted to *Astronomy & Astrophysics*

- "Multi-wavelength observations of the GRB 080319B afterglow and the modeling constraints",
  Pandey, S. B.; Castro-Tirado, A. J.; Jelínek, M.; Kamble, A. P.; Gorosabel, J.; de Ugarte Postigo, A.; Prins, S.; Oreiro, R.; **Chantry, V.**; Trushkin, S.; Bremer, M.; Winters, J. M.; Pozanenko, A.; Krugly, Y.; Slyusarev, I.; Kornienko, G.; Erofeeva, A.; Misra, K.; Ramprakash, A. N.; Mohan, V.; Bhattacharya, D.; Volnova, A.; Plá, J.; Ibrahimov, M.; Im, M.; Volvach, A.; Wijers, R. A. M. J., 2009, *Astronomy & Astrophysics*, Volume 504, pp.45-51

- "The QSO HE0450-2958: Scantily dressed or heavily robed? A normal quasar as part of an unusual ULIRG",
  Jahnke, K.; Elbaz, DK; Pantin, EK; Böhm, A.; Wisotzki, L.; Letawe, G.; **Chantry, V.**; Lagage, P.-O., 2009, *Astrophysical Journal*, Volume 700, pp.1820-1830

- "Near-infrared observations of the HE0450-2958 system: discovery of a second active galactic nucleus?",
  Letawe, G.; Magain, P.; **Chantry, V.**; Letawe, Y., 2009, *Monthly Notices of the Royal Astronomical Society*, Volume 396, pp.78-84

- "Redshifts and lens profile for the double quasar QJ 0158-4325",
  Faure, C.; Anguita, T.; Eigenbrod, A.; Kneib, J.-P.; **Chantry, V.**; Alloin, D.; Morgan, N.; Covone, G., 2009, *Astronomy & Astrophysics*, Volume 496, pp.361-364

- "COSMOGRAIL: the COSmological MOnitoring of GRAvItational Lenses. VII. Time delays and the Hubble constant from WFI J2033-4723",
  Vuissoz, C.; Courbin, F.; Sluse, D.; Meylan, G.; **Chantry, V.**; Eulaers, E.; Morgan, C.; Eyler, M. E.; Kochanek, C. S.; Coles, J.; Saha, P.; Magain, P.; Falco, E. E., 2008, *Astronomy & Astrophysics*, Volume 488, pp.481-490

- "Deconvolution of HST images of the Cloverleaf gravitational lens. Detection of the lensing galaxy and a partial Einstein ring",
  Chantry, V.; Magain, P., 2007, *Astronomy & Astrophysics*, Volume 470, pp.467-473

- "A deconvolution-based algorithm for crowded field photometry with unknown point spread function",
  Magain, P.; Courbin, F.; Gillon, M.; Sohy, S.; Letawe, G.; **Chantry, V.**; Letawe, Y., 2007, *Astronomy & Astrophysics*, Volume 461, pp.373-379

Articles in preparation

- "COSMOGRAIL: the COSmological MOnitoring of GRAvItational Lenses. XI. Study of 11 gravitationally lensed quasars: deconvolution of high resolution near-IR images, remeasurement of the time delays, simple models and the Hubble constant",
  Chantry, V., Sluse, D.; Eulaers, E.; Magain, P. et al.

- "COSMOGRAIL: the COSmological MOnitoring of GRAvItational Lenses. X. New time delays for the gravitational lens HE 0435-1223",
  Chantry, V.; Courbin, F.; Revaz, Y.; Faure, C.; Vuissoz, C.; Sluse, D.; Eulaers, E.; Tewes, M.; Dye, S.; Coles, J.; Saha, P.; Koleva, M.; Magain, P.; Folhmeister, J.; van Winckel, H.; Meylan, G.; Ibrahimov, M.

Participation to conferences

- Talk: "ISMCS: An iterative method well-suited to extract constraints from lensed quasars",
  Chantry, V., June 2009, *Strong Gravitational Lensing in the Next Decade*, Cogne (Aosta Valley), Italy

- Poster: "COSMOGRAIL, The COSmological MOnitoring of GRAvitational Lenses: New results on HE0435-1223",
  Chantry, V.; Magain, P.; Courbin, F.; Vuissoz, C., October 2008, *OZ Lens 2008: Dark Matter, Dark Energy and Dark Ages with Gravitational Lensing*, Institute of Astronomy, School of Physics, University of Sydney, Australia

- Poster: "Deconvolution of HST images of the Cloverleaf gravitational lens: detection of the lensing galaxy and an incomplete Einstein ring",

Chantry, V.; Magain, P., January 2008, *Science with the new HST after Servicing Mission 4*, CNR Conference Center, Bologna, Italy

- Poster: "Deconvolution of HST images of the Cloverleaf gravitational lens: detection of the lensing galaxy and an incomplete Einstein ring",
  Chantry, V.; Magain, P., October 2006, *Applications Of Gravitational Lensing: Unique Insights Into Galaxy Formation And Evolution*, KITP (UCSB), Santa Barbara (CA), USA

Publications in conference proceedings

- "DECPHOT: An Optimal Deconvolution-based Photometric Reduction Method", Gillon, M.; Magain, P.; **Chantry, V.**; Letawe, G.; Sohy, S.; Courbin, F.; Pont, F.; Moutou, C., 2007, *Transiting Extrapolar Planets Workshop*, Astronomical Society of the Pacific Conference Series, Volume 366, pp.113-118

Miscellaneous communications

- "GRB 080319B: second epoch imaging from canarias (correction to GCN7469)", Jelinek, M.; Castro-Tirado, A. J.; **Chantry, V.**; Pla, J., 2008, *GRB Coordinates Network*, Circular Service, Volume 7476, p.1
- "GRB 080319B: optical observations", Jelinek, M.; Castro-Tirado, A. J.; **Chantry, V.**; Pla, J., 2008, *GRB Coordinates Network*, Circular Service, Volume 7469, p.1
- "GRB 080315: optical observations", de Ugarte Postigo, A.; **Chantry, V.**; Castro-Tirado, A. J.; Jelinek, M.; Gorosabel, J.; Melo, C.; Smette, A., 2008, *GRB Coordinates Network*, Circular Service, Volume 7418, p.1

All we have to decide is what to do with the time that is given to us.

J. R. R. Tolkien (1892 - 1973)

Acknowledgments

First I want to start with a look on my future in thanking Manu Jehin and Mike Gillon for trusting me enough to offer me a great opportunity with this wonderful job in La Silla taking care of TRAPPIST. One of my dreams is actually coming true and I'm very grateful for that!

Of course I have many other thanks to formulate. Indeed, this work is far from being an individual achievment but is the result of great collaborations and sharings with astrophysicists, observers, informaticians but also family and friends whom I shared so much with, mostly on non-scientific matters.

Let me start with an enormous "thank you" to my supervisor for his patience and for having guided me. In particular thank you for the very enriching and inspiring conversations about image processing techniques.

I am also grateful to the members of the jury who accepted to read this thesis and to devote some of their precious time to examine my work.

Then of course I want to thank my family from the bottom of my heart, especially my parents and my sister: they have always been there for me in the good moments as in the bad ones. I owe so much to you. I hope you are as proud of me as I've always been of you. To "Domi de Fanatik" I'd say this: thank you for making my sister so happy... And, of course: long live the firemen!!!!! LOL. Then I want to thank my boyfriend Nikko, now part of this family no matter what, for his presence, his patience, his unconditional support and understanding: with him around, everything always seems to be easier. You have no idea how precious you are to me. To my godmother Ghislaine and my dear uncle Gianni as well as their two crazy sons, Peter Van Dexter (Pierre) and Lézard (François): thanks for all the good moments we've spent together and for the many more that are still to come! A special thought goes to MamYvette, one of the best grandmother of all times, for still bearing and supporting us after all these years and all she's been through: it's not always easy with eleven children and even more grandchildren and great-grandchildren... Then a very moved thought goes to Papy Henry, Nonna Chiara, Nonno Pietro, Zia Eugenia, Marraine Christine and Alain who left us too soon: I think about you a lot!

Afterwards I want to thank my friends who were, still are and will always be so

important in my life. I'll start with someone I wouldn't have met if I hadn't come back in Belgium to start this PhD thesis: my dear "office mate", Mélanie Godart. To you Méla, I'd say this: you are one of the best things that has happened to me these last years regarding my work, along with going to Chile of course... LOL! Thank you for the parties, the restaurants, the chats, the trip to Paris just to eat sushis, the BSG nights, the help for the PhD students' night at my place, and many more unforgettable moments. I would not have been able to go through this thesis without your friendship and support. Only you could understand the good, bad and sometimes weird phases I went through. You're the girl! :-)

When it comes to friends, there is no way not to mention the Stan sisters, PQ and Frede. I really don't know what my life would have been if I hadn't met you... Probably a lot sadder and emptier! So to you I'd simply say: "Merci les cailles!!!". Speaking of "cailles", I owe a lot to May, my dear old friend, for the many conversations and arguments because of our strong personalities, the memorable parties at "l'Escalier", and many more good times. A few other people I really want to mention are: Ana, Chuck (Jacques), Rodrigue, Cama (Syl), Annemine and Greg, Bono (Juju), Nico Georges or the man with the greatest tricky imagination, Cath, Mumu, Elise or the little dragonfly, Artémis and her two monsters, my dear Italian mates from Quara di Toano (my little spot of Paradise on Earth), i.e. Tommy (ti aspetto in Cile!!), Claudio, Mirko, Manuel, Lele, Robbie, Fabio, Daiana, Cristina, Andrea V., Marco (Ballotta), Guido, il mastro Cioccolataio (Matteo), Patti, Carlo and finally Daniela. I hope I didn't forget anyone! To all of you guys: thank you so much for being there in your own special way!

How could I not also thank my dear handball team in the persons of Kitty, Barbara, Caro, Sarah, Rox S., Rox M., Pauline and Loraine. I really appreciate that you gave me the opportunity to learn how to play that wonderful sport by your side. I hope that we still have many games and parties ahead of us. Speaking of sport, I also want to thank the Estudiantes Handball Club of Tournai for letting me be part of their wonderful family!

Then I owe my dear Swiss collaborators big time: Christel Vuissoz who taught me so much about programming and Malte Tewes who is always impressively full of ressources and ideas. To Fred Courbin: thank you so much for the interest you showed in my work and for your many precious advices. To Cécile Faure: thanks for your support and for showing me that Astrophysics means more than just Science. I'm so glad I met you also because I think we're very much alike and I took comfort in that thought! To stay amongst astronomers, I also want to thank Dominique Sluse for his support, availability and his kindness: I could not have learned to model a lens without your fast email answers! And thank you for your precious advices! Speaking of lens modeling: many thanks to Chuck Keeton for his commitment in LENSMODEL and his precious help to anyone who's willing to use it. I really hope to work with you on substructures in a close future! My Italian lensed friends: Matteo who invited me to Groningen for his defence where I had the time of my life, Simona who welcomed me at home like a childhood friend, Claudio who is always so nice and Marco who's so funny. I also want to thank a bunch of other people from the lensing community: John for listening to me whatever the topics, Sherry for her friendship and for being so nice to me, Alicia for her positive energy, Matt for his friendship and our little entertainting fights over anything,

Dan for his smile and good mood, Leon for letting me come to the workshop in Aosta (thank you so much!!!) and Chris for being nice to me and letting me sit next to him at the official dinner in Aosta (which must not have been easy... LOL). Without them all I would not have spent such a wonderful time at Santa Barbara 2006, OZ Lens 2008 and Aosta 2009, and the accomplishment of my thesis would not have had the same flavour!

Finally I would like to thank some coworkers from the Liège Institute as Yanoushka and Géraldine Letawe for their kindness and their joy in life (their door has always been open for me), Sandrine Sohy for her help and her availability, Angela Della Vecchia for her kindness and open-mindedness, Geneviève Parmentier for being a really sweet person, the first floor in general, and all the PhD students especially Davide for drawing me logos with a black background for my title page, Anthony, Denis, Charles, Jean-Christophe, Arnaud, Thomas, François, Bertrand and Mehdi for their friendship, the pops, the restaurants and many other activities (I still have a scar on my back remembering me to look behind me for Denis and his paint balls...). Thanks a lot also to Tanya, Virgi B., Olga, Géraldine G. and Manue for their support no matter when, their understanding no matter what and the great company and entertaining evenings. There are still a few other people from the Liège Institute that I want to mention: Oli and Mu, PG, Poulpynou, Pierre Warnant also called "the elfe of the forest", Valérie C., Nat the Alchimist and Benoît B. or the specialist of the "boulet sauce lapin". Last but not least, I want to express my gratefulness to Arlette Noels and Nicolas Grevesse for supporting me since the beginning of my passion for Astrophysics.